Propagative plasmons in graphene investigated by simulation method and infrared spectroscopy

David Legrand

David Legrand. Propagative plasmons in graphene investigated by simulation method and infrared spectroscopy. Micro and nanotechnologies/Microelectronics. Université de Technologie de Troyes; Nanyang Technological University (Singapour), 2018. English. NNT : 2018TROY0049 . tel-03609734

HAL Id: tel-03609734

https://theses.hal.science/tel-03609734

Submitted on 15 Mar 2022

Thèse
de doctorat
de l'UTT

David LEGRAND

Propagative Plasmons in Graphene Investigated by Simulation Method and Infrared Spectroscopy

Champ disciplinaire :
Sciences pour l'Ingénieur

2018TROY0049 **Année 2018**

Thèse en cotutelle avec Nanyang Technological University - Singapour

NANYANG
TECHNOLOGICAL
UNIVERSITY
School of Electrical and Electronic Engineering

utt
UNIVERSITÉ DE TECHNOLOGIE
TROYES

THESE

pour l'obtention du grade de

DOCTEUR
de l'UNIVERSITE DE TECHNOLOGIE DE TROYES

EN SCIENCES POUR L'INGENIEUR

Spécialité : MATERIAUX, MECANIQUE, OPTIQUE, NANOTECHNOLOGIE

présentée et soutenue par

David LEGRAND

le 11 décembre 2018

Propagative Plasmons in Graphene Investigated by Simulation Method and Infrared Spectroscopy

JURY

M. P.-M. ADAM	PROFESSEUR DES UNIVERSITES	Président
M. F. CHARRA	DIRECTEUR DE RECHERCHE - CEA	Rapporteur
M. S. GRÉSILLON	MAITRE DE CONFERENCES - HDR	Rapporteur
M. B. WANG	PROFESSOR	Rapporteur
M. J. PLAIN	PROFESSEUR DES UNIVERSITES	Examinateur
M. T.-K.-S. WONG	ASSOCIATE PROFESSOR	Examinateur

Abstract

English

Graphene physics and plasmonics are two fields which, once combined, promise a variety of exciting applications. One of those applications is the integration of active nano-optoelectronic devices in electronic systems, using the fact that plasmons in graphene are tunable, highly confined and weakly damped. Before achieving these active device, a crucial challenge remains : finding a platform enabling a high propagation of Graphene Plasmons Polaritons (GPPs).

In this framework, a full study of the propagation of plasmons through suspended graphene is addressed. This study start by reviewing the theoretical and experimental research achievement related to the really recent emerging field of graphene plasmonics. A numerical investigation by FDTD method is presented, and the conditions for a realisation of the study of graphene plasmons in suspended graphene are analysed. A design of the sample with an experimental process is proposed. Finally, an experimental study from the fabrication in clean room, then the characterisation of graphene and plasmonics structure, to the optical measurement through Scanning Near-field Optical Microscopie is presented.

Keywords— Surface plasmon resonance; Graphene; Simulation methods; Near-field microscopy; Infrared spectroscopy

French

La physique du graphène et la plasmonique sont deux domaines qui, une fois combinés, promettent une variété d'applications intéressantes. Une de ces applications est l'intégration de dispositifs nano-optoélectroniques actifs dans des systèmes électroniques, en utilisant le fait que les plasmons dans le graphène sont accordables, fortement confinés et faiblement amortis. Avant de réaliser ces dispositifs actifs, un défi crucial demeure : trouver une plateforme permettant une forte propagation des Polaritons Plasmons Graphène (GPP).

Dans ce cadre, une étude complète de la propagation des plasmons à travers le graphène en suspension est abordée. Cette étude commence par examiner les résultats de la recherche théorique et expérimentale liés au domaine émergent de la plasmonique du graphène. Une étude numérique par méthode FDTD est présentée, et les conditions pour la réalisation de l'étude des plasmons de graphène dans le graphène en suspension sont analysées. Une conception de l'échantillon avec un processus expérimental est proposée. Enfin, une étude expérimentale, de la fabrication en salle blanche, puis la caractérisation de la structure graphène et plasmonique, à la mesure optique par microscopie optique à champ proche à balayage, est présentée.

Mots Clés — Résonance plasmonique de surface; Graphène; Simulation, Méthodes de; Microscopie en champ proche; Spectroscopie infrarouge

Contents

List of Figures

Introduction

Over the past century, the field of infinitely small has started to be investigated, as the tools were developed and being available in the research centers. Nanoscience have been carrying the promises of revolution in many fields. Among other, huge effort are made in the fields of medicine and information technology, where progress are strongly demanded. Nanoscience is present in our daily life through the electronic devices, where the size of the component has been reduced steadily to the nanoscale. However, the nanoworld does not work with the same physical rules, where others phenomena take place. Many researches are directed toward the resolution of the arising problems, to make nano-device work in the way it works on our scale. Other research are driven in order to take advantage of those new rules and phenomena. This research aims at showing some recent results about electromagnetic waves appearing down to the atomic scale. This thesis work is taking place at the intersection of two fields, plasmonic and graphene.

Plasmonics is part of the general field of plasma. Plasma is a state of the matter, where collective electrons density waves can be manipulated. It exists on several forms, and one of them is the 2D collective oscillation of electrons at the surface of conducting materials. At the interface between a metal and an insulator, surface plasmons can be found. This electromagnetic wave can be coupled with light, and the latter can be confined at the subwavelength scale. The confinement of the light is an important research topic as photonic devices suffer from their size. This plasmonic phenomenon has been studied on 2D material and more particularly graphene.

In the quest of understanding and manipulating the infinitely small, graphene appears as a very promising material. It is in fact infinitely thin: the first single-atom-thick layer discovered. Moreover, the strong carbon-carbon bound allow the scientist to manipulate it with macroscopic tools. On the top of that, it is possible to isolate a graphene layer by the scotch-tape mechanical exfoliation technique. This technique is so simple and cheap that it can be reproduced by any research team all over the world. Finally, its peculiar properties open up new fields of research. In order to have an idea of the importance of the discovery, it took only 6 years to Andrei Geim and Kostya Novoselov to get their Nobel price after their famous publication. In this context appears the field of graphene plasmonics.

The field of graphene plasmonics emerged recently, within few years after the Nobel price. Graphene plasmons have shown their potential through their high confinement and tunability. This work is all about graphene plasmonics, which is introduced through this thesis. In the first chapter, some basic knowledges about plasmonics in general and graphene properties, mostly electronic, are presented. The second chapter is a literature review about graphene and graphene plasmonics, as well as the demonstration of a basic model explaining graphene plasmons properties. In the third chapter, a numerical study about plasmons propagating in suspended graphene is shown. In the fourth chapter, fabrication of samples as well as optical measurements through home-made SNOM are introduced. Finally, the main results of this thesis are summarized, as well as the possible research direction to consider, following this work.

Chapter 1

Theoretical background

This thesis takes place in the framework of a broad and not really intuitive field of science usually called nanotechnology. The name refers directly to the size (nanometres) of the systems studied because of the wide properties arising from this range of length. New properties arise from the confinement of the media in one or more dimensions. As an example, the ratio of surface atoms over core atoms vary dramatically when reducing the dimensions of an object to the nanometric scale. Figure 1.1 shows the ratio of surface atoms over core atoms in the case of a spherical bulk of palladium when the cluster diameter is reduced. In fact, surface atoms exhibit different properties as the forces applied on them differ, as well as chemical terminations. Therefore, surface atoms give to the structure new chemical properties, as they build the physical interface between the solid and its environment. The confinement of the structure also gives physical, mechanical, electromagnetic, and in particular plasmonic, remarkable new properties. That is noticiably the case for the 2 dimensions materials discovered quite recently [119], and among them graphene.

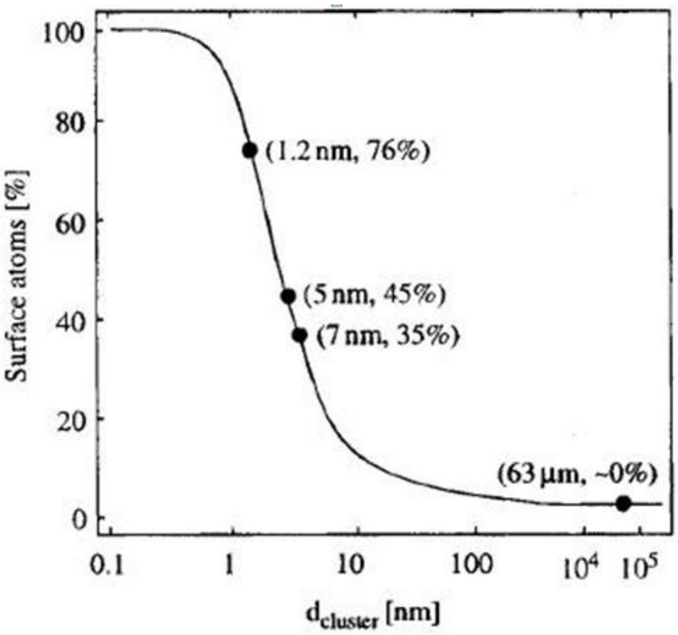

Figure 1.1: Variation of the percentage of surface atoms as a function of the size of a palladium cluster, adapted from [120]

In order to go deeper into the field of graphene plasmonics, the first chapter aims to expound the bases in plasmonics and about graphene. Therefore, in a first part, Maxwell's equations and the Drude model are introduced, which will give the keys for treating the second part of this chapter, i.e. the surface plasmons polaritons (SPPs). Finally, some of the graphene electronics properties will be explained.

1.1 Maxwell's equations and Drude model

Maxwell's equations are the bases of a revolution in physics [56, 71]. These equations couple the magnetic field $\mathbf{H}(\mathbf{r},t)$ and the electric field $\mathbf{E}(\mathbf{r},t)$. In space and time domain, the 6 scalar functions of these fields are interrelated by the Maxwell's equations, which give birth to the electromagnetic wave's equations. This set of partial differential equations is a part of the laws of science. There are four equations that it is possible to define depending on the surrounding media. In a medium, two additional vector fields are required, showing up in the Maxwell's equations : the electric flux density $\mathbf{D}(\mathbf{r},t)$ and the magnetic flux density $\mathbf{B}(\mathbf{r},t)$. To simplify the notations, the informations about time and space "$(\mathbf{r},t)$" will be omitted.

Maxwell's equation, in a medium without (and with) free charges ρ_f and currents density $\mathbf{J_f}$, are given by :

$$\nabla\cdot\mathbf{D}=0(+\rho_f)\quad\text{Gauss's law for electricity}\tag{1.1}$$

$$\nabla\cdot\mathbf{B}=0\quad\text{Gauss's law for magnetism}\tag{1.2}$$

$$\nabla\times\mathbf{E}=-\frac{\partial\mathbf{B}}{\partial t}\quad\text{Faraday's law}\tag{1.3}$$

$$\nabla\times\mathbf{H}=\frac{\partial\mathbf{D}}{\partial t}(+\mathbf{J_f})\quad\text{Ampère's law}\tag{1.4}$$

The two first Equations (1.1) and (1.2) are known as the Gauss's laws for electricity and magnetism respectively. They are related to the charge and magnetic sources. The two last equations, i.e. the Faraday's law (1.3) and the Ampère's law (1.4), are governing the time evolution of the electromagnetic fields. The relation between the fields and the flux densities are described by :

$$\begin{aligned}\mathbf{D}&=\epsilon_0\mathbf{E}+\mathbf{P}\\\mathbf{B}&=\mu_0\mathbf{H}+\mu_0\mathbf{M}\end{aligned}\tag{1.5}$$

where $\epsilon_0\approx 8.854187817.10^{-12}F/m$, or approximately $1/36\pi.10^{-9}F/m$, is the vacuum permittivity, $\mu_0=4\pi.10^{-7}V.s.A^{-1}m^{-1}$ is the vacuum permeability. The vectors fields $\mathbf{P}$ and $\mathbf{M}$ are related to the properties of the media. The first one is called the polarization density $[C/m^2]$ that corresponds to a volume density of dipole moments. The second one is the magnetisation density $[A/m]$. They are describing the reaction of the medium to external fields. In non-magnetic media, we have :

$$\mathbf{D}=\epsilon_0\mathbf{E}+\mathbf{P}=\epsilon_0\epsilon_r\mathbf{E}\tag{1.6}$$

$$\mathbf{B}=\mu_0\mathbf{H}\tag{1.7}$$

with $\epsilon=\epsilon_0\epsilon_r$ the absolute permittivity of the medium. The physical quantity ϵ_r refer to the relative permittivity, which can be written as $\epsilon_r(r)$ when highlighting a spacial dependence. ϵ_r is the sqaure of the refractive index of the medium.

1.1.1 Electromagnetic wave equation and dispersion relation

The electromagnetic wave equation is a second order partial equation, arising from the Maxwell's Equations (1.3) and (1.4). In fact, these equations can be combined in non magnetic media which gives, in absence of charge and current :

$$\nabla\times\nabla\times\mathbf{E}=-\mu_0\frac{\partial^2\mathbf{D}}{\partial t^2}\tag{1.8}$$

Then, using mathematical identities such as $\nabla\times\nabla\times\mathbf{E}\equiv\nabla(\nabla\cdot\mathbf{E})-\nabla^2\mathbf{E}$ as well as $\nabla\cdot(\epsilon_r(r)\mathbf{E})\equiv\mathbf{E}\cdot\nabla\epsilon_r(r)+\epsilon_r(r)\nabla\cdot\mathbf{E}$, and inserting Equation (1.1) in Equation (1.8), leads to :

$$\nabla\left(-\frac{1}{\epsilon_r(r)}\mathbf{E}\cdot\nabla\epsilon_r(r)\right)-\nabla^2\mathbf{E}=-\mu_0\epsilon_0\epsilon_r(r)\frac{\partial^2\mathbf{E}}{\partial t^2} \tag{1.9}$$

Latter the last equation will be solved in different media separately. In an homogeneous medium, the dielectric function can be considered as constant in space, which leads to : $\nabla\epsilon_r(r)=\nabla\epsilon_r=0$. Finally, the well known electromagnetic wave equation, named d'Alembert equation, can be deduced as :

$$\nabla^2\mathbf{E}-\frac{\epsilon}{c^2}\frac{\partial^2\mathbf{E}}{\partial t^2}=0 \tag{1.10}$$

where $c = 299792458 m/s$ is the speed of the light in vacuum. In order to simplify the model, the wave is assumed to be solution of the d'Alembert equation, i.e. this wave is a superposition of progressive harmonic plane waves. Such a wave has a plane wavefront orthogonal to its propagating direction. It is a solution of Maxwell's equations, which has 6 electromagnetic components, with a same pulsation w and wave vector $\mathbf{k}$. It is common to write the harmonic electric and magnetic fields with complex notations so that $\mathbf{E}(r,t)=\mathbf{E_0}e^{j(\mathbf{k}.\mathbf{r}-wt)}$. Using the partial derivative in time and in space, $\mathbf{E}$ is governed by :

$$\nabla\mathbf{E}=j\mathbf{k} \quad \text{and} \quad \frac{\partial\mathbf{E}}{\partial t}=-jw \tag{1.11}$$

Combining equations (1.10) and (1.11), leads to the dispersion relation :

$$k^2=\epsilon\frac{w^2}{c^2} \quad \text{i.e.} \quad k=\sqrt{\epsilon}\frac{w}{c} \tag{1.12}$$

This dispersion relation describes the dynamic of a plane wave in a medium. If the medium is said to be dispersive, its dielectric function is function of the light wavelength. The dielectric function is usually noted $\epsilon(w)$. In the vacuum, $\epsilon(w)=1$ and the well known linear dispersion relation becomes :

$$k=\frac{w}{c} \tag{1.13}$$

1.1.2 Boundary conditions

Maxwell's equations are valid for a continuous medium. However, they can be used in the case of interfaces, where they constrain the behavior of electromagnetic fields leading to the so-called boundary conditions. As a result, a part of the energy is generally reflected, and another transmitted. It is also possible to deduce from it directions and angles of the resultant fields, depending on the incident beam, its polarisation as well as the media properties. More specifically for this study, the dispersion relation of graphene plasmons (see section 2.3.2) arises from the boundary conditions applied on the magnetic field (see below).

The boundary conditions for electromagnetic fields can be derived from integral forms of the Maxwell's equations expounded in the introduction of Section 1.1. Let's consider an interface between two homogeneous media. In the following description, the notation $\mathbf{E_{1i}}$ will be used, with $i = x, y, z$ (cartesian coordinate) or $i = t$ (tangential to the boundary i.e. in the plane (x,y)), for the component of the electric field lying in the medium 1 (see Figure 1.2). Four boundary conditions arise from the 4 Maxwell's equations seen above. They are demonstrated in the four paragraphs below.

From the Ampère's law Starting from Equation (1.4), which is integrated over a surface bounded by a loop (see Figure 1.2), Stokes' theorem is applied :

$$\int_S \nabla\times\mathbf{H}\cdot \mathrm{d}\mathbf{S}=\oint_C \mathbf{H}\cdot \mathrm{dl}=\frac{\partial}{\partial t}\int_S \mathbf{D}\cdot \mathrm{d}\mathbf{S} \tag{1.14}$$

Following Figure 1.2, where the Roman numbers are defining the edges of a rectangle loop perpendicular to the interface, and assuming a constant electric flux $\mathbf{D}$ over the surface S, it is possible to develop :

$$(I)+(II)+(III)+(IV)=\frac{\partial}{\partial t}\mathbf{D}\cdot\mathbf{e_y}\int_S \mathrm{d}S \tag{1.15}$$

with $\mathbf{e_y}$ the unit vector in the y direction. The Roman numbers are directly related to the terms on the left side in the next equation. The electric flux density $\mathbf{D}$ is oriented through the loop, and is directly proportional to the surface involved in the experiment. Therefore, it is possible to re-write Equation (1.15) as:

$$\mathbf{H_{1x}} \cdot \mathrm{d}\mathbf{x} + (\mathbf{H_{1z}} + \mathbf{H_{2z}}) \cdot \mathrm{d}\mathbf{z} - \mathbf{H_{2x}} \cdot \mathrm{d}\mathbf{x} - (\mathbf{H_{1z}} + \mathbf{H_{2z}}) \cdot \mathrm{d}\mathbf{z} = \frac{\partial}{\partial t}\mathbf{D} \cdot \mathbf{e_y}(\mathrm{d}x\mathrm{d}z) \tag{1.16}$$

If the distance dz tends to zero, Equation (1.16) becomes :

$$(\mathbf{H_{1x}} - \mathbf{H_{2x}}) \cdot \mathrm{d}\mathbf{x} = 0 \tag{1.17}$$

$$\mathbf{H_{1x}} = \mathbf{H_{2x}} \tag{1.18}$$

Equation (1.18) can be generalized for all the magnetic field compounds in plane as follow :

$$\mathbf{H_{1t}} = \mathbf{H_{2t}} \tag{1.19}$$

As it has been mentioned in introduction, a key equation for obtaining graphene plasmons relation dispersion is lying in the boundary condition applied on the magnetic field. That comes from the fact that graphene is a semi-metal (see Section 1.3.2), which has quasi-free electrons (see Section 1.3). Therefore, taking into account surface currents at the interface of two media, with dz tending to zero and the use of Equations (1.17) and (1.16)), Equation (1.14) becomes :

$$\oint_C \mathbf{H} \cdot \mathrm{d}\mathbf{l} = (\mathbf{H_{1x}} - \mathbf{H_{2x}}) \cdot \mathrm{d}\mathbf{x} = \int_S \left(\frac{\partial \mathbf{D}}{\partial t} + \mathbf{J_f}\right) \cdot \mathrm{d}\mathbf{S} = \mathrm{d}x\mathbf{J_S} \cdot \mathbf{e_y} \tag{1.20}$$

and therefore

$$H_{2x} - H_{1x} = -J_{Sy} \tag{1.21}$$

with J_f the volumetric density of current ($A.m^{-2}$) and J_S the surface density of current ($A.m^{-1}$). When an electric field is applied to the object, electrons will move. The Ohm's law states that :

$$\mathbf{J} = \sigma \mathbf{E} \tag{1.22}$$

Plugging Equation (1.22) in Equation (1.21) leads to :

$$H_{2t} - H_{1t} = -\sigma E_{t\perp} \tag{1.23}$$

with σ the surface conductivity. This key equation will be used in order to obtain the dispersion relation of graphene plasmons in section 2.3.2, in the case of TM (Transverse Magnetic) modes.

From the Faraday's law Using the same development as in the previous paragraph, Equation (1.3) leads to :

$$\mathbf{E_{1x}} = \mathbf{E_{2x}} \tag{1.24}$$

Generalised to all the tangential components, it is possible to write :

$$\mathbf{E_{1t}} = \mathbf{E_{2t}} \tag{1.25}$$

From the Gauss's law (electricity) The schema helping to solve this boundary condition problem is illustrated in Figure 1.3. We can see there an interface, plane in blue, separating two media (medium 1 and 2). The Roman numbers represent surfaces delimiting a pillbox, in red, which is crossing the interface. (I) represents the surface of the pillbox parralel to the interface in the medium 1. (II) represents the surface of the pillbox parralel to the interface in the medium 2. (III) represents the surface of the pillbox which is perpendicular and crossing the interface. The electric flux density $\mathbf{D_{i,n}}$ normal to the interface is represented in the two media (i=1,2) with an arrow. Let's take the Maxwell equation (1.1), integrate over the pillbox and apply Gauss' theorem in the absence of charge :

$$\int_V \nabla \cdot \mathbf{D} \quad \mathrm{d}V = \oint_S \mathbf{D} \cdot \mathrm{d}\mathbf{S} = 0 \tag{1.26}$$

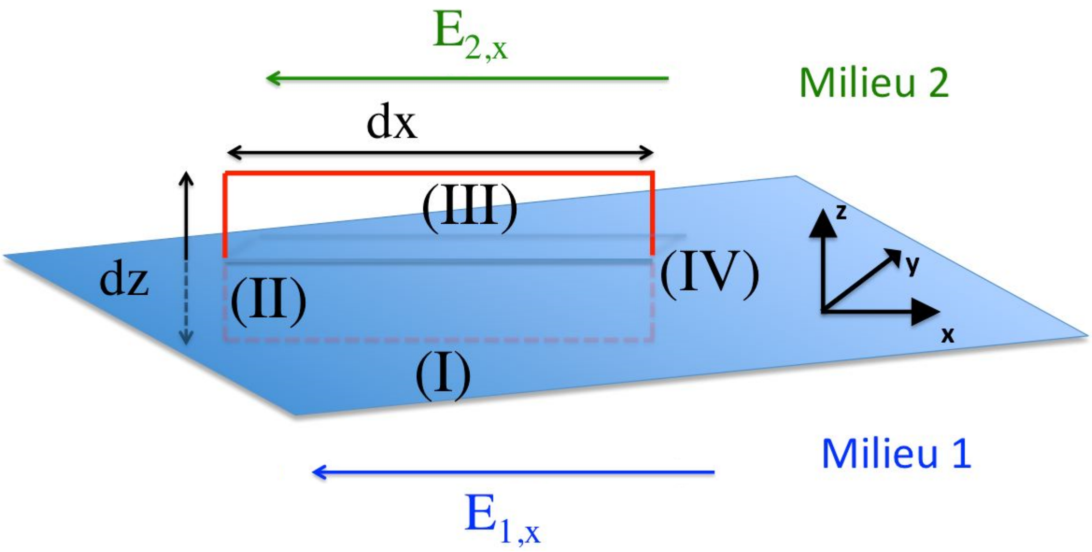

Figure 1.2: Schema describing the interface (in blue) between two media, medium 1 and the medium 2. Two electric field tangential to the interface are displayed. A rectangle loops crossing perpendicularly the interface is also shown in red, used for getting the boundary condition using the Maxwell's Equations (1.3) and (1.4)

where V and S are respectively the volume and the surface of the pillbox. The surface integral can be separated into three parts :

$$\oint_S \mathbf{D}\cdot \mathrm{d}\mathbf{S} = \int_{S_I} \mathbf{D_{1,n}}\cdot \mathrm{d}\mathbf{S_I} + \int_{S_{II}} \mathbf{D_{2,n}}\cdot \mathrm{d}\mathbf{S_{II}} + \int_{S_{III}} \mathbf{D_t}\cdot \mathrm{d}\mathbf{S_{III}} \tag{1.27}$$

where (I) and (II) are the flat ends, and (III) is the curved surface as shown on Figure 1.3. It can be noticed first of all notice that $S_I = S_{II} = S$. Then, let's take the limit in which the pillbox height tends to zero, to obtain :

$$-\mathbf{D_{1n}}\cdot S + \mathbf{D_{2n}}\cdot S = 0 \tag{1.28}$$

$$\mathbf{D_{1n}} = \mathbf{D_{2n}} \tag{1.29}$$

From the Gauss's law for magnetism Starting from Maxwell's equation (1.2), and using the same development as in the previous paragraph, we have :

$$\mathbf{B_{1n}} = \mathbf{B_{2n}} \tag{1.30}$$

1.1.3 Review of the Drude model and the free electrons gas equations of motion

The Drude model was constructed three years after Thomson's discovery of electrons. In a metal, Drude considers a sea of electrons and uses the theory of gases to describe the electrical and thermal conductions. In this model, it is assumed that electrons are spherical solids identically moving along a straight line. A time average ($t = \tau$) known as the collision time is set delimiting two collisions. The electrons will emerge with a random direction and random speed after each collision (no particular initial condition). There is no force applied on electrons except the one occurring when they collide: no electron-electron interaction (independent electrons approximation), no electron-ion interaction (free electrons approximation).

Case of a uniform and constant perturbation. In the case where a uniform and constant electrical field ($\mathbf{E}$) is applied, electrons feel the electrostatic force $\mathbf{F_{el}}$:

$$\mathbf{F}_{el} = -e\mathbf{E} \tag{1.31}$$

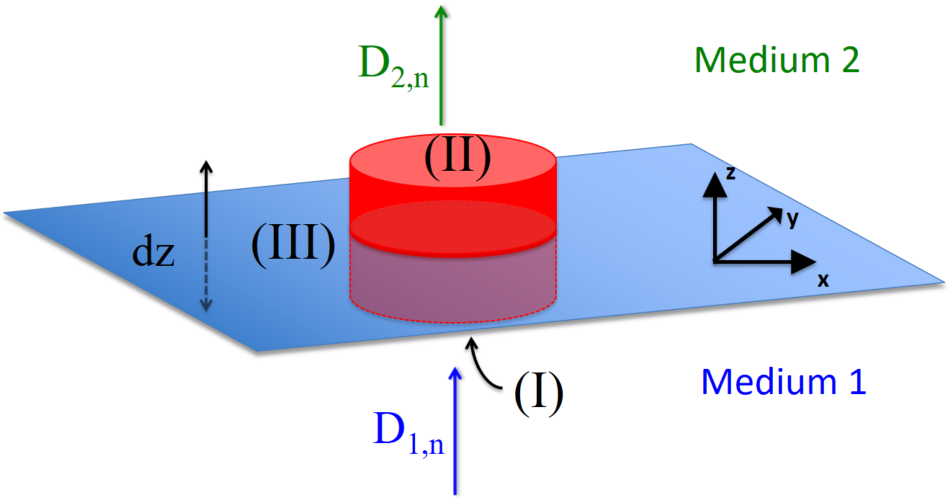

Figure 1.3: Schema describing the interface (in blue) between two media, medium 1 and the medium 2. Two electric flux density normal to the interface are displayed. A pillbox crossing perpendicularly the interface is also shown in red, used for getting the boundary condition using the Maxwell's Equations (1.1) and (1.2)

with the electronic charge $e = 1.6021765 \times 10^{-19}$ C. With m_e the mass of a free electron (9.11×10^{-31}kg), the fundamental principle of dynamic gives:

$$m_e \frac{d\mathbf{v}}{dt} = \mathbf{F}_{el} = -e\mathbf{E} \tag{1.32}$$

Since the electron past move is unknown (direction, velocity), all prior contribution to the electron motion is ignored and the average of the electronic velocity is defined as following :

$$\mathbf{v}_{avg} = \frac{-e\mathbf{E}}{m_e}\tau \tag{1.33}$$

The current density $\mathbf{J}$ is expressed as:

$$\mathbf{J} = -ne\mathbf{v} \tag{1.34}$$

with n the charge carrier density. Combining the last equation with the Ohm law, $\mathbf{E} = \rho\mathbf{J}$, leads to the resistivity ρ:

$$\rho = \frac{m_e}{ne^2\tau} \tag{1.35}$$

This first result is interesting because it gives an order of magnitude of the collision time for metals.

Dielectric function of the electron gas. The optical response of a Drude metal, in absence of drag force, can also be established. Plugging the electron displacement $\mathbf{x}(\omega) = \mathbf{x_0}e^{-i\omega t}$ in Equation (1.32), and linking the polarisation density $\mathbf{P}(\omega)$ with $\mathbf{x}(\omega)$ through $\mathbf{P}(\omega) = -ne\mathbf{x}(\omega)$ lead after a little algebra to :

$$\mathbf{P}(\omega) = \frac{-ne^2}{m\omega^2}\mathbf{E} \tag{1.36}$$

The frequency dependent dielectric function of Drude metal can be expressed, using Equation (1.5) as:

$$\epsilon(\omega) = 1 - \frac{ne^2}{\epsilon_0 m\omega^2} = 1 - \frac{\omega_p^2}{\omega^2} \tag{1.37}$$

with ω_p the plasma frequency. At this angular frequency, the collective motion of electrons in a conducting medium, such as a metal, is resonant. Under this frequency, the medium is reflecting the electromagnetic wave, whereas above it, the wave are propagating through the medium.

Equations of motion for a free charge carrier. It is possible to describe the dynamic of a free charge carrier adding a damping term. An electron has a velocity $\mathbf{v}_0(t)$ at time t and the probability $\frac{dt}{\tau}$ to collide at t+dt. Therefore $1-\frac{dt}{\tau}$ is the probability to avoid a collision. While an electron does not experience collision, it moves following Equation (1.32) and will get a velocity:

$$d\mathbf{v} = \frac{\mathbf{F}_{el}dt}{m_e} \tag{1.38}$$

Thus, an electron has a probability of $1-\frac{dt}{\tau}$ to not collide at a time t+dt and add to its own velocity ($\mathbf{v}_0(t)$ at the time t) a velocity $d\mathbf{v}$. Considering a metal with free electrons, all the electrons which collide can be neglected. Thus, the contribution to the velocity per electron added by all the electrons which survive during a time dt, $\mathbf{v}(t+dt)$, can be calculated as:

$$\mathbf{v}(t+dt) = \left(1-\frac{dt}{\tau}\right)\left(\mathbf{v}_0(t)+\frac{\mathbf{F}_{el}dt}{m_e}\right) = \left(1-\frac{dt}{\tau}\right)\left(\mathbf{v}_0(t)+d\mathbf{v}\right) \tag{1.39}$$

The second magnitude order (dt^2) in the development of the following equation is not taken into account:

$$\mathbf{v}(t+dt) = \mathbf{v}_0(t)+\frac{\mathbf{F}_{el}dt}{m_e}-\frac{dt}{\tau}\mathbf{v}_0(t) \tag{1.40}$$

To obtain finally the equations of motion for a free charge carrier when $dt \to 0$:

$$\frac{\mathbf{v}(t+dt)-\mathbf{v}_0(t)}{dt} = \frac{d\mathbf{v}(t)}{dt} = \frac{\mathbf{F}_{el}}{m_e}-\frac{\mathbf{v}(t)}{\tau} \tag{1.41}$$

It is possible to re-write the last equation with $\mathbf{p}$ the momentum of the electron:

$$\frac{d\mathbf{p}}{dt} = -\frac{\mathbf{p}}{\tau}-e\mathbf{E} \tag{1.42}$$

Equation (1.42) is the other significant result of the Drude model, with Equation (1.35). When an external perturbation $\mathbf{E}(\omega)$ oscillates periodically such as $\mathbf{E}(\omega) = \mathbf{E_0}e^{-i\omega t}$, the solution of Equation (1.42) is of the form $\mathbf{p}(\omega) = \mathbf{p_0 e^{-iwt}}$, and we get :

$$\mathbf{p}(w) = -\frac{ie\mathbf{E}(w)}{w+i/\tau} \tag{1.43}$$

Taking Equation (1.22), with $\mathbf{J} = -ne\mathbf{p}/m_e$ the current density and n the carrier density, the optical conductivity $\sigma(w)$ as a function of the pulsation can be deduced as:

$$\sigma(w) = \frac{ine^2}{m(w+i/\tau)} \tag{1.44}$$

From the optical conductivity to the permittivity. Let's take the case where a free current takes place at an interface between two media, characterized by their relative permittivity ϵ_1 and ϵ_2. $\epsilon_s = (\epsilon_1+\epsilon_2)/2$ is defined as the surrounding permittivity. Taking Maxwell Ampère's law, it is possible to write :

$$\begin{aligned} \nabla\times\mathbf{H} &= \frac{\partial\mathbf{D}}{\partial t}+\mathbf{J_f} && (1.45)\\ &= \epsilon_0\epsilon_s\frac{\partial\mathbf{E}}{\partial t}+\sigma\mathbf{E} = (-i\omega\epsilon_0\epsilon_s+\sigma)\mathbf{E} && (1.46)\end{aligned}$$

Using equation (1.9), it follows :

$$\begin{aligned} \nabla\times\nabla\times\mathbf{E} = -\nabla^2\mathbf{E} &= -\mu_0\frac{\partial\nabla\times\mathbf{H}}{\partial t} && (1.47)\\ &= -\mu_0(-i\omega)(-i\omega\epsilon_0\epsilon_s+\sigma)\mathbf{E} && (1.48)\end{aligned}$$

After some rearranging, using the partial derivative in space (1.11), the dispersion relation can be found :

$$k^2 = \left(\epsilon_s + \frac{i\sigma}{\omega\epsilon_0}\right)\frac{\omega^2}{c^2} \tag{1.49}$$

The relative permittivity of a metal-like material (Drude conductivity) as a function of the optical conductivity can thus be written as:

$$\epsilon(w) = \epsilon_s + \frac{i\sigma(w)}{\epsilon_0 w} = \epsilon_s - \frac{ne^2}{m\epsilon_0(w^2 + iw/\tau)} = \epsilon_s - \frac{w_p^2}{w^2 + iw/\tau} \tag{1.50}$$

with $w_p = ne^2/m\epsilon_0$ the plasma frequency of the free electron gas. Because the Drude model doesn't take into consideration interband transition in its model, the description is not valid for high frequency, relatively to the plasma frequency w_p and the relaxation time τ. In this case, the sign of the real part of the relative permittivity change and its optical response is not anymore metallic. However, in the scope of this thesis, we would like to work in the infrared range, where no interband transition may appear.

The permittivity is a really interesting intrinsic property of materials because it gives access to the optical answer of a material under perturbations. Unfortunately, this property is convenient only for 3D materials modeling. Graphene being a one atom thick carbon sheet, we will more likely use 2D conductivity. However, as a first approach, the Drude model can convert the 2D conductivity into a 3D permittivity, giving us a good idea about the optical response of graphene in the infrared range. Its optical properties via materials permittivity has been widely used at first for graphene, thus enabling FDTD simulation.

This 3D approach implies to model materials with a finite thickness arbitrary set as $2a$, for the sake of simplicity in the next section. In this model, graphene surroundings, characterized by a permittivity ϵ_s, also plays a crucial role :

$$\epsilon_g(\omega) = \epsilon_s(\omega) + \frac{i\sigma_{2D}(w)}{\omega 2a\epsilon_0} \tag{1.51}$$

In the case of suspended graphene, $\epsilon_1 = \epsilon_2 = \epsilon_{air} = 1$ and thus $\epsilon_s = 1$, and Equation (1.51) leads to :

$$\epsilon_g(\omega) = 1 + \frac{i\sigma_{2D}(w)}{\omega 2a\epsilon_0} \tag{1.52}$$

1.2 Surface plasmon polaritons

In the framework of the study of electromagnetic waves, Surface Plasmons Polaritons (SPPs) can be seen as a particular result of the Maxwell's equations at the interface of two media with specific properties [101, 128, 130]. In order to give a picture about plasmonics, it is interesting to go back to its physical origin. It can be seen as a collective motion of electron reacting to an electric field. However, they tend to travel slightly too far and as a result, a restoring force pulls them back in order to screen the charge disturbance created by their displacement. This first collective motion is repeated such that a weakly damped oscillation occurs. Therefore, a plasmon can be defined as a coherent collective oscillations of free electrons. When the excitation of the plasmon is light, a coupling between plasmons and the eletromagnetic wave takes place, resulting in a Surface Plasmon Polariton (SPPs).

1.2.1 Surface plasmon polaritons at a single interface in absence of free current

We can start the description of surface plasmons by solving the problem of a plane wave crossing an interface separating two media defined by their dielectric function ϵ_1 and ϵ_2.

An arbitrary polarized plane wave $\mathbf{E} = \mathbf{E_0} e^{i(\mathbf{k}.\mathbf{r}-wt)}$ can always be split up into two orthogonally polarized plane waves. Basing our problem on the interface between the two medium ϵ_1 and ϵ_2, the electric field is moving parallel to the interface for the first case, and in the other case, we set the magnetic field parallel to the interface. In the first case, we speak about a transverse electric (TE or s) polarization. In the second case, we speak about a transverse magnetic polarization (TM or p), which is illustrated in Figure 1.4.

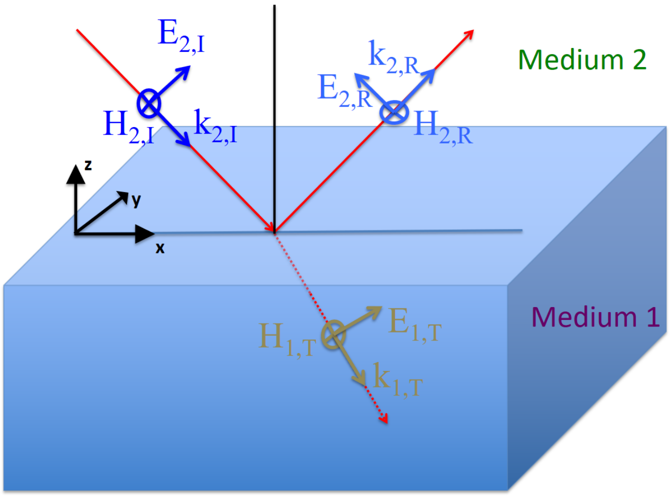

Figure 1.4: Schema of an incident TM polarized wave propagating in the plane xz, crossing an interface (from medium 2 to medium 1). A part of this incident electromagnetic wave is reflected back in the medium 2, and a part is transmitted in the medium 1. The wave is characterized by a wavector $\mathbf{k_{i,j}}$, with i=1,2 stands for the medium, and j=I,R,T in case where we are looking at the Incident, Reflected of Transmitted component. As well, the electric field $\mathbf{E_{i,j}}$ and the magnetic field $\mathbf{B_{i,j}}$ are illustrated.

In our case, we are interested in surface plasmons, only appearing in TM mode (for the TE case, see [101]). In TM mode, the non-zero components are H_y, E_x and E_z. Let's write the fields in the media (1) and (2) as follows :

$$\begin{aligned} \text{For z>0} \quad \mathbf{H_2} &= (0, \mathbf{H_{y2}}, 0)e^{i(k_{x2}x+k_{z2}z-wt)} \\ \mathbf{E_2} &= (\mathbf{E_{x2}}, 0, \mathbf{E_{z2}})e^{i(k_{x2}x+k_{z2}z-wt)} \\ \text{For z<0} \quad \mathbf{H_1} &= (0, \mathbf{H_{y1}}, 0)e^{i(k_{x1}x-k_{z1}z-wt)} \\ \mathbf{E_1} &= (\mathbf{E_{x1}}, 0, \mathbf{E_{z1}})e^{i(k_{x1}x-k_{z1}z-wt)} \end{aligned} \tag{1.53}$$

At the interface between two media, in the absence of free charges and currents, the tangential components of the electric and magnetic fields, $\mathbf{E_t}$ and $\mathbf{H_t}$, as well as the normal components of the electric and magnetic flux densities, $\mathbf{D_n}$ and $\mathbf{B_n}$, must be continuous (see sub-section 1.1.2) :

$$\begin{cases} \mathbf{E_{1t}} = \mathbf{E_{2t}} & \text{for the electric field} \\ \mathbf{H_{1t}} = \mathbf{H_{2t}} & \text{for the magnetic field} \\ \mathbf{D_{1n}} = \mathbf{D_{2n}} & \text{for the electric flux density} \\ \mathbf{B_{1n}} = \mathbf{B_{2n}} & \text{for the magnetic flux density} \end{cases} \tag{1.54}$$

Let's start from the fact that the boundary conditions must be satisfied everywhere on the interface. Let us consider a point p(x,y,0) such as it belongs to the plane z=0. It means that the electric field can be written :

$$\mathbf{E_{x1}}e^{i(k_{x1}x-wt)} = \mathbf{E_{x2}}e^{i(k_{x2}x-wt)} \text{ so } \mathbf{E_{x1}} = \mathbf{E_{x2}} = \mathbf{E_x} \text{ and } k_{x1} = k_{x2} = k_p \tag{1.55}$$

And the magnetic field :

$$\mathbf{H_{y1}}e^{i(k_px-wt)} = \mathbf{H_{y2}}e^{i(k_px-wt)} \text{ so } \mathbf{H_{y1}} = \mathbf{H_{y2}} \tag{1.56}$$

The time dependence is assumed to be harmonic ($\frac{\partial}{\partial t} = -iw$). The harmonic time dependence, applied to the magnetic field via the d'Alembert Equation (1.10) thus yields to the Helmholtz equation :

$$\nabla^2\mathbf{H_i} + k_0^2\epsilon\mathbf{H_i} = \frac{\partial^2\mathbf{H_i}}{\partial z^2} + (\epsilon k_0^2 - k_p^2)\mathbf{H_i} = 0 \tag{1.57}$$

If this equation is applied to the media (1) and (2), the following relations are obtained:

$$(-ik_{z1})^2 + (\epsilon_1 k_0^2 - k_p^2) = 0 \text{ and } (ik_{z2})^2 + (\epsilon_2 k_0^2 - k_p^2) = 0 \tag{1.58}$$

which yield to the general equation :

$$k_{zi} = \sqrt{\epsilon_i k_0^2 - k_p^2} \tag{1.59}$$

It is important to keep in mind that the wave is polarized TM ($E_y = H_x = H_z = 0$) and that homogeneity is maintained in the y-direction, such that ($\frac{\partial}{\partial y} = 0$). Maxwell's Equation (1.4) can now be applied to obtain the electric field :

$$iw\epsilon_0\epsilon_i E_{xi} = \frac{\partial H_{yi}}{\partial z} \tag{1.60}$$

either

$$E_{xi} = \frac{-i}{w\epsilon_0\epsilon_i}\frac{\partial H_{yi}}{\partial z} \tag{1.61}$$

for each media. Applying Equation (1.61) at the boundary, plugging the Equations (1.53) in and using the results found in the Equations (1.55) and (1.56) lead to:

$$\frac{k_{z1}}{\epsilon_1} = \frac{-k_{z2}}{\epsilon_2} \text{ or } \frac{\epsilon_2}{\epsilon_1} = -\frac{k_{z2}}{k_{z1}} \tag{1.62}$$

Inserting Equation (1.59) into Equation (1.62) leads to the dispersion relation of the SPs in a single interface system :

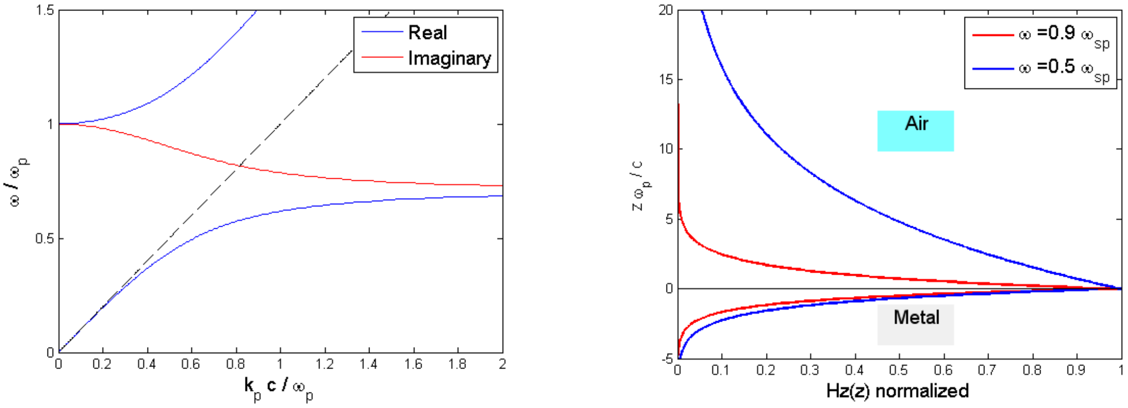

(a) Dispersion relation of plasmons.

(b) Magnetic field profile of SPPs at ω = 0.35 ω_{SP} and ω = 0.57 ω_{SP}.

Figure 1.5: Dispersion relation and magnetic field profile of SPPs at a planar interface between air and a Drude-metal with no damping.

$$k_x = k_p = k_0 \sqrt{\frac{\epsilon_1 \epsilon_2}{\epsilon_1 + \epsilon_2}} \tag{1.63}$$

k_p is the surface plasmon wavevector. The component k_{zi} can also be developed combining Equation (1.59) and Equation (1.63), to find :

$$k_{zi} = k_0 \sqrt{\frac{\epsilon_i^2}{\epsilon_1 + \epsilon_2}} \tag{1.64}$$

From these results, it is possible to describe the appropriate environment for surface plasmon mode at the interface between two media. Indeed, surface plasmon propagate parallel to the surface, vanishing in the z-direction. Hence, as it has been seen previously, k_{zi} should be purely imaginary. Therefore, following Equation (1.64), the condition becomes $\epsilon_1 + \epsilon_2 < 0$. Then, considering a wave that propagates along the interface, k_p should be real. Therefore, following Equation (1.63), we shall have $\epsilon_1 \epsilon_2 < 0$.

This means that one medium must exhibit a negative dielectric function, with an absolute value exceeding that of the other. Such materials can be found among noble metals, which exhibit a large negative real part. It is also the case of graphene in the infrared range (see Figure 2.13), using the model described Section 3.2. The second medium should have a positive real dielectric value, not too large. Dielectric media such as SiO_2 or air are good candidates.

In the case of a system presented in Figure 1.4, with a medium 2 which is air, $\epsilon_2 = 1$. Defining the medium 1 as a Drude metal, neglecting the damping (Equation (1.37)), Equation (1.63) becomes :

$$\frac{k_p c}{\omega_p} = \frac{\omega}{\omega_p} \sqrt{\frac{\epsilon_1(\omega/\omega_p)}{\epsilon_1(\omega/\omega_p) + 1}} \tag{1.65}$$

Equation (1.65) is plotted in Figure 1.5a. For real k_p (in blue) and $\omega < \omega_p$ (half bottom part), $\omega/\omega_p \to 1/\sqrt{2}$. The black dashed curve represents the limit for the incident photon dispersion relation. The lack of overlapping between the incident photon relation dispersion and the SPPs relation dispersion poses problems regarding to the excitation of SPPs, where a third structure is needed for the coupling. For k_p pure imaginary, in red, the plasmons are localized. For $\omega > \omega_p$, so-called Brewsters modes are supported.

Going further, Figure 1.5b displays the magnetic field profile at this interface, using Equation (1.64) and $H_y = H_0 e^{-ik_{zi}z}$, with $H_0 = 1$. We can observe that SPPs are more confined to the interface as we approach $\omega_{SP} = \omega_p/\sqrt{2}$. As ω tends to ω_{SP}, the group velocity $v_g = \partial\omega/\partial k$ of the SPPs decreases.

Finally, coming back to Equation (1.65), the plasmons wavevector k_p can give interesting information such as the propagation length :

$$L = \frac{1}{2Im[k_p]} \tag{1.66}$$

as well as the effective surface plasmon wavelength and the penetration depth in the medium :

$$\lambda_p = \frac{2\pi}{Re[k_p]} \tag{1.67}$$

$$\delta = \frac{1}{Im[k_{zi}]} = \frac{1}{|k_{zi}|} \tag{1.68}$$

The propagation length is the length at which the intensity, proportional to the square of the electromagnetic field modulus, fall to 1/e. The penetration depth gives a direct information about the confinement of the electromagnetic field in its surrounding. Finally, the wavelength of the plasmons is the effective wavelength that can be measured, for example, by Scanning Near-Field Optical Microscopy (SNOM). This last physical quantity can be normalized by the excitation field and is called in this case the localization factor. It gives also, indirectly, a good idea of the confinement of the electromagnetic field in the materials.

1.2.2 Surface plasmon polariton in a multilayer system

In the multi-layer model (illustrated in Figure 1.6), a thin metallic layer (in blue) sandwiched between two (infinitely) thick dielectric claddings (media 1 and 2). This system is often refereed as an insulator/metal/insulator (IMI) heterostructure. Here the simplest case is considered, such as the same insulator above and below is sandwiching the metallic layer.

A multilayer system is defined when an interaction/coupling between the surface plasmon of different interfaces takes place. This means that the thickness of the metal is comparable to or smaller than the decay of the surface plasmon.

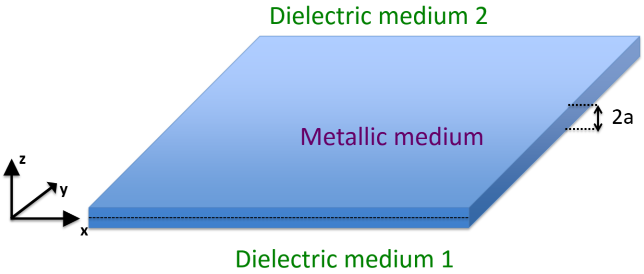

Figure 1.6: Geometry of a two-interface system consisting of a thin layer (metallic medium with a thickness of Δ = 2a) sandwiched between two infinite half spaces (dielectric medium).

The vectorial base being centred in the middle of the metallic thin layer (with a thickness of Δ = 2a), we will distinguish three parts of the system : for $z > a$, a medium with a permittivity ϵ_2, for $a > z > -a$, a medium with a permittivity ϵ_m and for $z < a$, a medium with a permittivity ϵ_1.

Following the same path as in Section 1.2.1, and taking into account the symmetry of the system, the boundary conditions imply that $k_{x1} = k_{x2} = k_p$.

Let's assume that for $z > a$, the magnetic field can be simplified as follow :

$$H_{y_2} = Ae^{ik_{z2}z}e^{ik_px} \tag{1.69}$$

with an harmonic time dependence, and A the amplitude of the $\mathbf{H_{y2}}$ field. It must be noticed below that the notation for the wavevector in the z direction is the following : $k_i \equiv k_{zi}$ for i=1,2 in the dielectric medium and m for the metallic one. Using Equation (1.61), it is possible to write :

$$E_{x_2} = \frac{k_2}{w\epsilon_0\epsilon_2}Ae^{ik_2z}e^{ik_px} \tag{1.70}$$

In the same way, we can write for $z < -a$:

$$H_{y_1} = Be^{-ik_1z}e^{ik_px} \tag{1.71}$$

$$E_{x_1} = -\frac{k_1}{w\epsilon_0\epsilon_1}Be^{-ik_1z}e^{ik_px} \tag{1.72}$$

with B the amplitude of $\mathbf{H_{y1}}$. While for $-a < z < a$, we have a combination of the modes from the media upon and below and we can write, with C^+ and C^- the amplitude of the field for respectively z positive and z negative :

$$\begin{aligned} H_{y_m} =& C^+e^{i(k_px+k_mz)} + C^-e^{i(k_px-k_mz)} \\ =& (C^+e^{ik_mz} + C^-e^{-ik_mz})e^{ik_px} \end{aligned} \tag{1.73}$$

$$\begin{aligned} E_{x_m} =& \frac{-i(ik_m)}{w\epsilon_0\epsilon_m}C^+e^{ik_mz}e^{ik_px} + \frac{-i(-ik_m)}{w\epsilon_0\epsilon_m}C^-e^{-ik_mz}e^{ik_px} \\ =& \frac{k_m}{w\epsilon_0\epsilon_m}(C^+e^{ik_mz} - C^-e^{-ik_mz})e^{ik_px} \end{aligned} \tag{1.74}$$

H_y has to fulfill the wave equation which gives again (see Equation (1.59)) :

$$k_i = \sqrt{\epsilon_i k_0^2 - k_p^2} \tag{1.75}$$

Here, we have $k_i \equiv k_{zi}$ for i=1,2 and m, and $k_p \equiv k_x$. The boundary continuity requirement seen in the subsection 1.1.2 implies that $H_{y_2} = H_{y_m}$ at $z = a$ as well as $H_{y_1} = H_{y_m}$ at $z = -a$:

$$Ae^{ik_2a} = C^+e^{ik_ma} + C^-e^{-ik_ma} \quad \text{at z=a} \tag{1.76}$$

$$Be^{ik_1a} = C^+e^{-ik_ma} + C^-e^{ik_ma} \quad \text{at z=-a} \tag{1.77}$$

While for E_x, we have :

$$\frac{k_2}{\epsilon_2}Ae^{ik_2a} = \frac{k_m}{\epsilon_m}(C^+e^{ik_ma} - C^-e^{-ik_ma}) \quad \text{at z=a} \tag{1.78}$$

$$-\frac{k_1}{\epsilon_1}Be^{ik_1a} = \frac{k_m}{\epsilon_m}(C^+e^{-ik_ma} - C^-e^{ik_ma}) \quad \text{at z=-a} \tag{1.79}$$

Those four equations can be seen as a linear system. Let's take first Equations (1.76) and (1.78), which lead to :

$$C^- = C^+e^{2ik_ma}\frac{k_m/\epsilon_m - k_2/\epsilon_2}{k_m/\epsilon_m + k_2/\epsilon_2} \tag{1.80}$$

Then, doing the same for Equations (1.76) and (1.78) results in :

$$C^+ = C^-e^{2ik_ma}\frac{k_m/\epsilon_m - k_1/\epsilon_1}{k_m/\epsilon_m + k_1/\epsilon_1} \tag{1.81}$$

Finally, multiplying Equation (1.80) by Equation (1.81) yields to the general equation :

$$e^{i4k_m a} = \frac{k_m/\epsilon_m + k_2/\epsilon_2}{k_m/\epsilon_m - k_2/\epsilon_2} \frac{k_m/\epsilon_m + k_1/\epsilon_1}{k_m/\epsilon_m - k_1/\epsilon_1} \tag{1.82}$$

This equation is a general equation for a two interfaces system. It is interesting to notice that if the thickness a is infinite, Equation (1.62) for a single interface is retrieved (keeping in mind that k_m is pure imaginary). In the case of this thesis, the study of suspended graphene requires to set the two media above and below the graphene as the same dielectric one, with a permittivity ϵ_d. Therefore, the simplest case of a symmetric structure will be solved and Equation (1.82) becomes :

$$e^{2ik_m a} = \pm \frac{k_m/\epsilon_m + k_d/\epsilon_d}{k_m/\epsilon_m - k_d/\epsilon_d} \tag{1.83}$$

Here, it is really interesting to realize that two solutions arise and therefore two branches on the dispersion relation will appear. Going back to Equations (1.81) and (1.80), and replacing k_1/ϵ_1 and k_2/ϵ_2 by k_d/ϵ_d, yield to $C^- = \pm C^+$. This result can be plugged in Equation (1.73) which becomes :

$$H_{y_m} = (e^{ik_m z} \pm e^{-ik_m z}) C e^{i(k_p x - wt)} \tag{1.84}$$

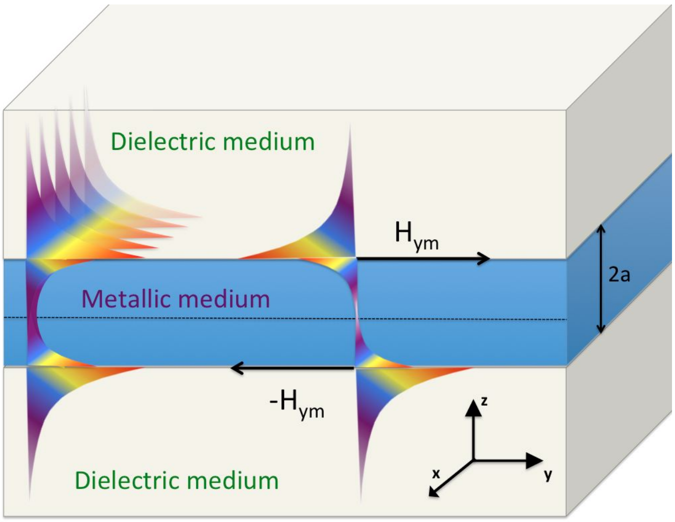

Figure 1.7: The magnitude of the field H for the symmetric (left) and anti-symmetric (right) modes while surface plasmon is propagating in a symmetric structure

It is possible to solve Equation (1.83) knowing that $tanh(z) = (e^{2z} - 1)/(e^{2z} + 1)$ which leads to the two following solutions :

$$tanh(ik_m a) = \frac{\epsilon_d k_m}{\epsilon_m k_d} \quad \text{for the symmetric mode where} \quad C^- = -C^+ \tag{1.85}$$

$$tanh(ik_m a) = \frac{\epsilon_m k_d}{\epsilon_d k_m} \quad \text{for the anti-symmetric mode where} \quad C^- = C^+ \tag{1.86}$$

These results are shown in Figure 1.7 where the magnetic field profile for the symetric modes is shown on the left and for the anti-symetric modes on the right. Using the result of Section 1.2.1, i.e. k_{z_i} should be a pure imaginary, it is possible to replace it as $k_{z_i} = iq_{z_i}$ with q_{z_i} real positive and $q_{z_i} = \sqrt{k_p^2 - \epsilon_i k_0^2}$. Finally, the dispersion relations for the symmetric modes and anti-symmetric modes in a thin slab of metal m sandwiched between a dielectric d turn into their most known forms :

$$tanh(a\sqrt{k_p^2 - \epsilon_m k_0^2}) = -\frac{\epsilon_d \sqrt{k_p^2 - \epsilon_m k_0^2}}{\epsilon_m \sqrt{k_p^2 - \epsilon_d k_0^2}} \tag{1.87}$$

$$tanh(a\sqrt{k_p^2 - \epsilon_m k_0^2}) = -\frac{\epsilon_m \sqrt{k_p^2 - \epsilon_d k_0^2}}{\epsilon_d \sqrt{k_p^2 - \epsilon_m k_0^2}} \tag{1.88}$$

When d tends to infinity, Equation (1.85) and Equation (1.86) are reduced to the equation of dispersion of surface plasmons at a single interface, Equation (1.63), since tanh tends to 1.

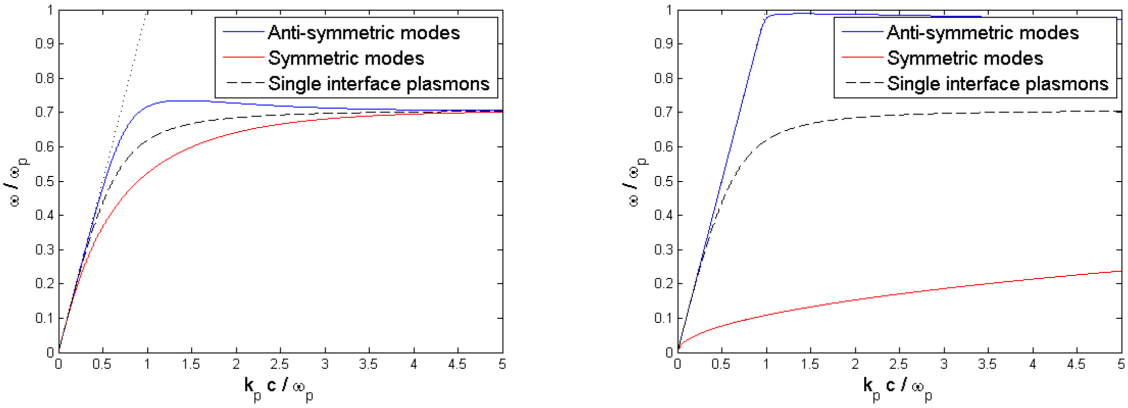

(a) The thickness of the core is chosen as a =0.5*c/wp. For typical value of $f_p = 2.10^{15} Hz$ (silver and gold), we get a thickness around 12 nm.

(b) The thickness of the core is chosen as a =0,012*c/wp. For typical value of $f_p = 2.10^{15} Hz$ (silver and gold), we get a thickness around 0.3 nm.

Figure 1.8: Dispersion relations of symmetric and antisymmetric modes in a Metal-Insulator-Metal waveguide. The metal is modeled as a lossless Drude dispersion. The black dotted lines indicate the dispersion relation of the light in air, whereas the dashed line represent decoupled SPPs.

The two branches of the dispersion relations of plasmons for a IMI hetero-structure are shown in Figure 1.8, for two different thicknesses. It is interesting to notice that the anti-symmetric modes vanish as the thickness of the metal gets atomically thin. It can be explained as follow. When the metallic core becomes thinner and tends to atomic thickness, we can express the hyperbolic tangent as Taylor serie as :

$$tanhx = x - \frac{x^3}{3} + \frac{2x^5}{15} + \mathcal{O}(x^7) \tag{1.89}$$

Taking Equations 1.85 and 1.86, we find :

$$-\frac{\epsilon_d}{\epsilon_m k_d} \to 0 \quad \text{for the symmetric mode} \tag{1.90}$$

$$-\frac{\epsilon_m k_d}{\epsilon_d k_m^2} \to 0 \quad \text{for the anti-symmetric mode} \tag{1.91}$$

For the symmetric modes, k_d tends to infinity which means that $k_p >> k_0$. For the anti-symmetric modes, k_d tends to 0 and therefore $k_p \to k_0$. Therefore, the antisymmetric modes tend to become radiative, as it follows the dispersion relation of the light in air. Therefore, for graphene which is a one atom thick material, only the symmetric dispersion relation remains. As it can be observed in Figure 1.8b, a significant mismatch between the light wave-vector (black dotted line) and the plasmons wave-vector takes place. In fact, at a certain frequency, the mismatch is higher than in conventional noble material, as it can be observed in Figure 2.19b. As $q_{z_i} = \sqrt{k_p^2 - \epsilon_i k_0^2}$ is really high, the penetration depth get small (Equation (1.68)), which leads to very high confinement.

Coming back to Equation (1.84), the magnetic field for the symmetric modes and for the anti-symmetric modes can be obtained applying the boundary conditions at $z = \pm a$:

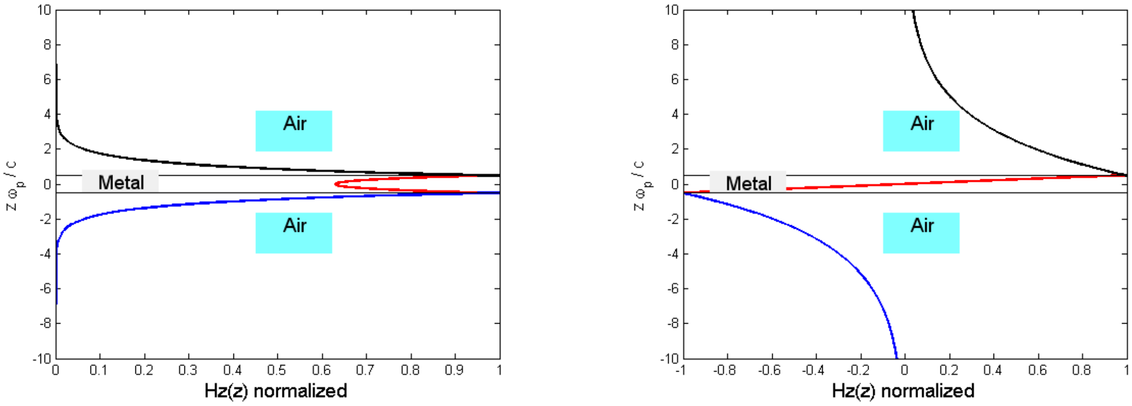

(a) Y component of the magnetic field H_y as a function of z, the normal space axis, in the case of the symmetric modes

(b) Y component of the magnetic field H_y as a function of z, the normal space axis, in the case of the anti-symmetric modes

Figure 1.9: Magnetic field profile in a Metal-Insulator-Metal waveguide. The thickness of the core is chosen as a =0.5*c/wp. For typical value of $f_p = 2.10^{15} Hz$ (silver and gold), we get a thickness around 12 nm.The metal is modeled as a lossless Drude dispersion. The black lines indicate the interface between the air and the metal.

$$H_y^s(x,z) = \begin{cases} A\frac{cosh(k_m z)}{cosh(k_m a)}e^{ik_p x}, & \text{where } |x| < a \\ Ae^{-k_d(|z|-a)}e^{ik_p x}, & \text{where } |x| > a \end{cases}$$

$$H_y^a(x,z) = \begin{cases} A\frac{sinh(k_m z)}{sinh(k_m a)}e^{ik_p x}, & \text{where } |x| < a \\ \frac{z}{|z|}Ae^{-k_d(|z|-a)}e^{ik_p x}, & \text{where } |x| > a \end{cases}$$

, which gives modes with the shape drawn in Figure 1.9.

The study done in this chapter have been conducted toward plamonics in extremely thin metal. Graphene, which is a semi-metal, has plasmonics behaviour remarkably close to the SPPs arising from extremely thin layer of common noble metal. However, its 2D crystalline structure as well as its electrons dynamic make Graphene Plasmons (GPs) a bit different. In the next section, we will therefore focus on graphene crystalline and electronics properties, before going deeper into graphene plasmonics, in Chapter 2.

1.3 Properties of Graphene

1.3.1 A sheet of carbon atom

Graphene is the mother of all graphitic forms: it is a sheet of carbon atoms in a honeycomb lattice. It possesses unique physical properties: graphene is the strongest and the most stretchable known material, it has the record of thermal conductivity, and is completely impermeable [50, 8]. Moreover, from the opto-electronic point of view, its carriers (both electrons and holes) exhibit ultra-high mobility and long mean free path. Graphene has gate-tunable carrier densities, anomalous quantum Hall effects, fine structure constant defining optical transmission, and so on. Also, this two dimensional one atom thick membrane is a perfect example of a two-dimensional electron system for a physicist. According to [62], "When the quantum theory of solids was developed, graphite was one of the earliest materials to which it was applied. The first calculations of the energy band structure of graphite appears to have been made by Hund and Mrowska in 1937 as an academic exercise."

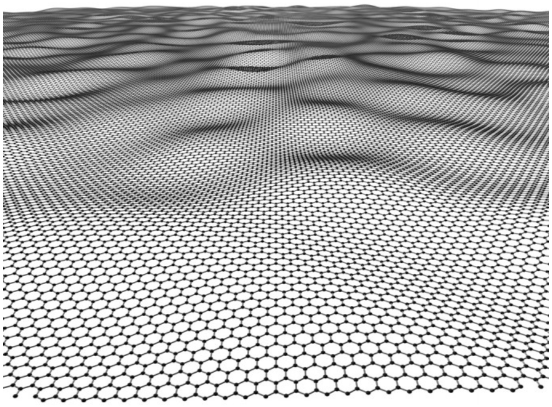

Figure 1.10: Artistic representation of graphene

In order to study graphene opto-electronic properties in detail, it is important to look at its crystalline structure. It is a monolayer of sp_2 bounded carbon atoms in a honeycomb lattice. Each carbon atom is attached to three neighbours by covalent bounds with a length of about $a_0 = 0.142nm$. This lattice configuration comes from the atomic orbitals interferences between neighbouring carbon atoms (orbital hybridisation).

Let's first zoom on the smallest unit of its structure: the carbon atom. This chemical element has six electrons, four of the electrons are in its valence shell (outershell). Carbon's ground state configuration is $1S^2 2S^2 2P^2$ which can also be written in order to show the valence electrons $[He]2S^2 2P^2$, or more easily read :

$$\boxed{\uparrow\downarrow}_{1S} \quad \boxed{\uparrow\downarrow}_{2S} \quad \begin{array}{|c|c|c|}\hline \uparrow & \uparrow & \\ \hline \end{array}_{2P} \tag{1.92}$$

Here we can see the six electrons represented by arrows (the direction of the arrow represents the electron spin). The electrons located the closest to the nucleus are found in the 1s orbital. These electrons are usually considered as "frozen" in the pseudo-potential approximation, which takes place in many models. The pseudopotential model is a way of replacing the complicated effects of the motion of the core (i.e. non-valence) electrons of an atom and its nucleus with an effective potential, or pseudopotential. Those electrons are not involved in bounding. The next two will go into the 2s orbital. The remaining ones will be in two separate 2p orbitals. The p orbitals have the same energy and the electrons would rather be in separate orbitals.

In graphene, carbon atom rearranges its valence electrons so as to create bounds with its three neighbours. In fact, creating a bound decreases the energy of the system. The first step is to describe the atom in one of its excited state, which can be displayed as

$$\left\{ \begin{array}{c} s \\ p_x \\ p_y \\ p_z \end{array} \right\} \text{ with a electronic configuration : } \boxed{\uparrow}_{2S} \quad \begin{array}{|c|c|c|}\hline \uparrow & \uparrow & \uparrow \\ \hline \end{array}_{2P} \tag{1.93}$$

Then, these orbitals will mix in a special manner in order to create three covalent bounds. This concept of mixing atomic orbitals into new hybrid orbitals is called hybridisation. A more intuitive way to look at the carbon atom and its hybridisation is to use an energy level graph shown in Figure 1.11. One s orbital is hybridized with two p orbitals. The orbital p_z remains unchanged.

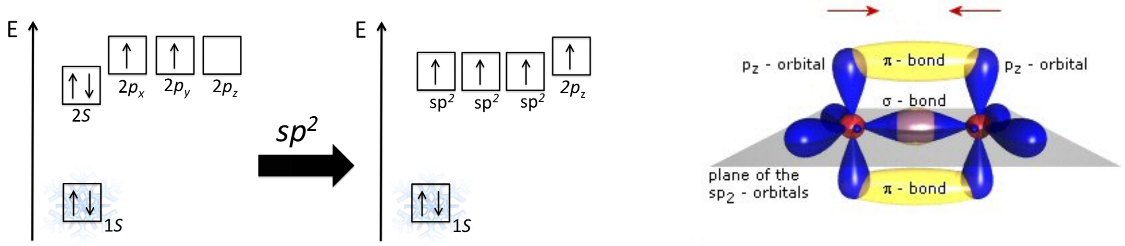

(a) Hybridisation

(b) Illustration of the carbon atom after sp^2 hybridisation

Figure 1.11: Illustration of the three hybridised orbitals : as an energy diagram (a) and as a picture on the right (red sphere represent Carbon atoms).

The three orbitals sp^2 form a triangular base with 120° angle in the hexagonal plane and will create σ bounds. The last orbital p_z is the only one electron which does not belong to the core neither to the covalent bounds and form a π bound perpendicular to the plane. Its interaction with the lattice will give the main electronic properties of the graphene at relatively low energy, such as the massless fermion behavior (see section 1.3.2)

Crystal structure in the real space and in the reciprocal space

Carbon atoms in a graphene plane are located at the vertices of a hexagonal lattice (Figure 1.12a). This triangular lattice has two atoms per unit cell (in green), A atom (in red) and B atom (in blue). The atoms A form a sublattice, and each atom A is surrounded by three atoms B, and vice versa. The basis vectors of this honeycomb lattice are $\mathbf{a_1}$ and $\mathbf{a_2}$, defined with the unit vector $\mathbf{x}, \mathbf{y}$ by :

$$\mathbf{a_1} = a_0\sqrt{3}\left(\frac{\sqrt{3}}{2}, \frac{1}{2}\right) \quad \text{and} \quad \mathbf{a_2} = a_0\sqrt{3}\left(\frac{\sqrt{3}}{2}, -\frac{1}{2}\right) \tag{1.94}$$

with $a_0 = 1.42\text{Å}$ the nearest-neighbour distance.

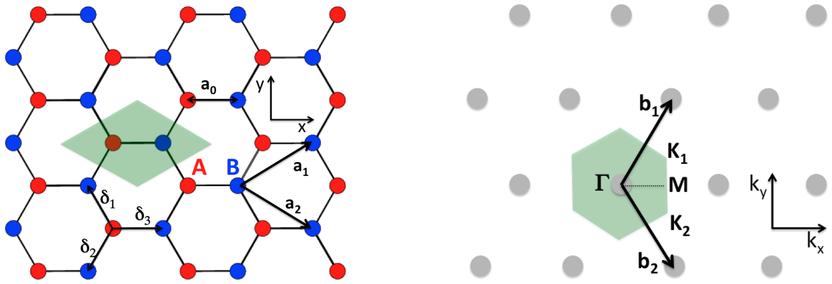

(a) Hexagonal lattice of graphene

(b) Reciprocal lattice of graphene

Figure 1.12: Graphene lattice (a) in the real space and (b) in the reciprocal space with the main parameters described in the text.

It is also interesting to describe the sub-lattice B starting from one A atom. We can build in this case three vectors :

$$\delta_{\mathbf{1}} = a_0\left(-\frac{1}{2}, \frac{\sqrt{3}}{2}\right) \quad \text{and} \quad \delta_{\mathbf{2}} = a_0\left(-\frac{1}{2}, -\frac{\sqrt{3}}{2}\right) \quad \text{and} \quad \delta_{\mathbf{3}} = a_0\,(1,0) \tag{1.95}$$

Then, it is interesting to go a bit further into the description of graphene by defining the concept of reciprocal space. This is an important concept because every crystalline structure have a particular reciprocal network. This signature of a structure can be recorded experimentally with diffraction pattern that give valuable informations about the reciprocal space .

We define the reciprocal space vectors by :

$$\mathbf{b_i}.\mathbf{a_j} = 2\pi\delta_{ij} \quad \text{therefore we get} \quad \begin{array}{ll} \mathbf{b_1}.\mathbf{a_1} = 2\pi & \mathbf{b_1}.\mathbf{a_2} = 0 \\ \mathbf{b_2}.\mathbf{a_2} = 2\pi & \mathbf{b_2}.\mathbf{a_1} = 0 \end{array} \tag{1.96}$$

We can then deduce the reciprocal vectors, drawn on the Figure 1.12b :

$$\mathbf{b_1} = \frac{2\pi}{3a_0}\left(1, \sqrt{3}\right) \quad \text{and} \quad \mathbf{b_2} = \frac{2\pi}{3a_0}\left(1, -\sqrt{3}\right) \tag{1.97}$$

In Figure 1.12b, we have drawn in green the Brillouin zone, which is the the primitive cell of the reciprocal space. It is a really interesting notion because it makes possible to study the lattice vibration as well as the electronic properties of the crystal by its symmetries. The three high symmetry points of the Brillouin zone, Γ , K and M are the center, the corner, and the center of the edge of the hexagon, respectively. More in detail, there are two non-equivalent corners, here noted K_1 and K_2, like in the real space :

$$\mathbf{K_1} = \frac{2\pi}{3a_0}\left(1, \frac{1}{\sqrt{3}}\right) \quad \text{and} \quad \mathbf{K_2} = \frac{2\pi}{3a_0}\left(1, -\frac{1}{\sqrt{3}}\right) \tag{1.98}$$

This results will be important for the next section, where the main electronic properties of graphene are expounded through the tight binding model. This model will give the so peculiar band structure of graphene in the reciprocal space. In between a semi-conductor and a metallic behavior, graphene can be considered as a zero-gap semi-conductor, or a semi-metal.

1.3.2 The tight binding model : a study about the dynamics of the electrons

Modelling the dynamics of electrons, a set of hypothesis

In order to study in detail the opto-electronic properties of graphene, giving rise to plasmons, it is important to have a look at the electron dynamics in this 2D material.

This problem is well known and can be solved by mixing solid states physics with quantum mechanics. The first point is to realize that such a n-body system cannot be solved exactly, due to the huge interactions and degrees of freedom which take place. In fact, electrons and holes are charge carriers, therefore their dynamic depends on all the others particles (electrons, holes, nuclei and defects) in the media. Exact computation on such systems requires power of calculus that is not available nowadays. This is the reason why physicists set up methods of calculus based on approximations which enable to get results close to the experimental ones.

Here, the goal is to understand the electronic properties of graphene via the tight binding model which gives a result in a form of band energy structures [23, 54]. In this approach, electrons are moving through a periodic potential that is very strong in the vicinity of the the lattice atoms (see Figure 1.13). In general, the tight-binding approximation [10, 82] can handle the case where the overlapping of atomic wave functions is significant enough to require corrections to the representation of isolated atoms, but not enough to make inappropriate atomic description.

Looking at the dynamics of electrons in a lattice is somehow looking at the delocalization of the electrons caused by the neighboring atoms. This system is a many-electron problem which requires us to make the following assumptions to solve it.

The π-band approximation. In a single atom, electrons belong to atomic orbitals. The atomic orbitals can be seen as a mathematical function which describes the wave-like behaviour of an electron in an atom. In a crystalline solid, the atomic orbitals interact with each others to form bounds. As seen before, the electrons which are involved in the low energy range of electronic properties, are those that can be found in the π band. The p_z orbitals do not overlaps with the sp_2 orbitals (see Figure 1.11b), therefore, other electrons belonging to the σ band should not be taken into account. This unsaturated orbital p_z can be described by a wave-function that is noted $P_z^s(\mathbf{r})$ with s being the index for the two sub-lattice (s= A or B). s can also be seen as the number of bands or the number of atomic wave-functions used in a unit cell.

The frozen heart. We will consider the approximation of "frozen heart", which assumes that all the electrons belonging to the core shell (1S), which are not involved in bounding, are not disrupting. As well, we consider the nuclei as entities positively charged (cations) and immobile (in reality, the atoms vibrate). This approximation gives rise to a positive pseudo-potential emerging from the lattice nucleus.

The perfect crystal. The perfect crystal will not suffer any defects. In order to build a description of the behaviour of electrons delocalizing from π to π bands, we need to take into account all the π-bounded electrons of the graphene lattice. We will first consider one unit cell (in green in Figure 1.12a), which is composed of two carbon atoms, A and B. Then, the process will be duplicated in order to recover a perfect lattice.

The single and independent electron approximation. In this approximation, the electron-electron interaction is not taken into account. Indeed, the electron-electron interaction does not give rise to a periodic potential, which could complexify the model. The tight-binding model is a one-electron model, which is not suitable for electron-electron interaction. Fortunately, electron-electron interaction is usually weaker than ion-electron interactions.

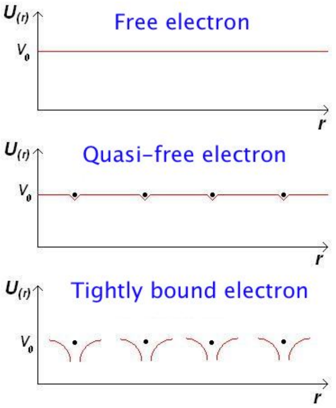

Figure 1.13: Representation of the potential for the three models described here

The time independent periodic potential. From the previous approximations, we can now assume that electrons will be subjected to a periodic and static potential. Therefore, the wave functions Ψ describing the dynamics of electrons form standing waves called stationary states, which are the physical quantities defining orbitals. They are solutions of the time independent Schrödinger equation :

$$\hat{H}\Psi = E\Psi \tag{1.99}$$

$\hat{H}$ is the Hamiltonian, which can be seen as a matrix which gives us the possible energy of the system when it is operating on the wave-function of the graphene lattice. E is the energy eigen-values of the system, which constitute a discrete set of solutions that would be found if the energy of the system was measured. In order to get the energy of delocalized electrons in the honeycomb lattice of graphene, the Schrödinger equation should be solved for all the π-bonded electrons of the 2D lattice. In our perfect lattice, we will sum the orbitals wave-function of the atoms belonging to each sub-lattice $\Phi_s(\mathbf{r},\mathbf{k}) \propto \sum P_z^s(\mathbf{r})$, and then build the total wave-functions $\Psi(\mathbf{r},\mathbf{k}) \propto \Phi_A(\mathbf{r},\mathbf{k})+\Phi_B(\mathbf{r},\mathbf{k})$ describing the whole lattice. $\mathbf{k}$ is the wave vector, which is related to the quantized crystal momentum $\mathbf{p}$, by $\mathbf{p} = \hbar\mathbf{k}$.

The Bloch's theorem. We know that the eigenstates of an electron in a periodic potential can be written as Bloch waves, according to the Bloch theorem. Those eigenstates are characterized by a wave-vector $\mathbf{k}$ that belongs to the first Brillouin zone. Assuming a perfect pristine graphene sheet, an orbital wave-function $P_z^s(\mathbf{r})$ should satisfy the Bloch's theorem, which gives us :

$$T_R P_z^s(\mathbf{r}) = e^{i\mathbf{k}.\mathbf{R}} P_z^s(\mathbf{r}) \tag{1.100}$$

with $\mathbf{R}$ the periodicity of the underlying lattice and T_R the translation operator along the periodicity. This means that we have a translational symmetry of the unit cells in the direction of a lattice vector. We can notice that the eigenfunctions assessed at two different lattice locations, 1 and 2 associated to respective position vectors r_1 and r_2, differ from each other in just a phase factor, $e^{i\mathbf{k}.(\mathbf{r_1}-\mathbf{r_2})}$. Finally, it is possible to write the Bloch function, which is a sum of the Bloch wave-function over the lattice, for one sub-lattice :

$$\Phi_s(\mathbf{r},\mathbf{k}) = \frac{1}{\sqrt{N}} \sum_{R_s} e^{i\mathbf{k}.\mathbf{R_s}} P_z^s(\mathbf{r}-\mathbf{R_s}) \tag{1.101}$$

with N the number of cells that are taken into account in the model.

Therefore, we can write the total wave-function for the lattice as a sum of the Bloch wave-functions of the lattice A and B, which will give :

$$\Psi(\mathbf{r},\mathbf{k}) = \sum_s C_s \Phi_s(\mathbf{r},\mathbf{k}) = C_A \Phi_A(\mathbf{r},\mathbf{k}) + C_B \Phi_B(\mathbf{r},\mathbf{k}) \tag{1.102}$$

with C_s the weight associated to sum of the atomic orbitals ($\Phi_s(\mathbf{r},\mathbf{k})$) of the sub-lattice s. With the Dirac notations, the wave-function Ψ can finally be described by :

$$|\Psi\rangle = \sum_s C_s |\Phi_s\rangle \tag{1.103}$$

The tight binding model : solving the Schr*ö*dinger time independent equation

Let's come back on the time independent Schrödinger equation (Equation (1.99)), and insert the equation describing the wavefunction seen in Equation (1.103). We obtain using bra and ket notation :

$$\hat{H}|\Psi\rangle = E|\Psi\rangle \tag{1.104}$$

$$\sum_s C_s \hat{H}|\Phi_s\rangle = E \sum_s C_s |\Phi_s\rangle \tag{1.105}$$

In order to work with a scalar equation, the last equation is multiplied by its conjugate, which leads to :

$$\sum_{s,s'} C_s C_{s'}^* \langle \Phi_{s'}|\hat{H}|\Phi_s\rangle = E \sum_{s,s'} C_s C_{s'}^* \langle \Phi_{s'}|\Phi_s\rangle \tag{1.106}$$

$$\sum_{s,s'} C_s C_{s'}^* H_{s's} = E \sum_{s,s'} C_s C_{s'}^* S_{s's} \tag{1.107}$$

where $H_{s's}$ is the matrix representation of the Hamiltonian in the orbitals $|\Phi_s\rangle$ base. $S_{s's}$ is the overlapping orbitals matrix, which is a quantitative measurement of the overlap of two atomic orbitals belonging to two different atoms. The last equation can be re-written more compactly in matrix form as :

$$HC = ESC \tag{1.108}$$

This matrix equation leads to the following condition for non-trivial solutions:

$$det[H - ES] = 0 \tag{1.109}$$

This equation will give us the dispersion relation of the graphene and provides n energy eigen-value as a function of $\mathbf{k}$, with n the number of bands for n orbitals in the unit cell. Since the unit cell contains two atoms, n=2 and the Hamiltonian matrix will have a dimension of 2×2.

Diagonal matrix elements. The Hamiltonian $H_{\alpha,\beta}$, with ($\alpha,\beta \in$ A,B), when $\alpha = \beta = A$ is given as follows:

$$H_{AA} = \frac{1}{N}\sum_{i}^{N}\sum_{j}^{N} e^{i\mathbf{k}\cdot(\mathbf{R_{A,j}}-\mathbf{R_{A,i}})}\langle P_z^A(\mathbf{r}-\mathbf{R_{A,i}})|\hat{H}|P_z^A(\mathbf{r}-\mathbf{R_{A,j}})\rangle \tag{1.110}$$

with i and j defining different unit cell. Here we will only consider the nearest neighbour (i=j), the others being neglected so that the equation becomes :

$$H_{AA} = \frac{1}{N}\sum_{i}^{N}\langle P_z^A(\mathbf{r}-\mathbf{R_{A,i}})|\hat{H}|P_z^A(\mathbf{r}-\mathbf{R_{A,i}})\rangle = \frac{1}{N}\sum_{i}^{N}\epsilon_{2P} = E_{2P} \tag{1.111}$$

with E_{2P} being the reference energy. The reference energy is usually set to zero, in order to have the junction (Dirac point) between the upper band and the lower band of the p_z orbital at 0. The atoms of the second sub-lattice being chemically identical, it is possible to write :

$$H_{AA} = H_{BB} = E_{2P} \tag{1.112}$$

For the overlap matrix, regarding the A sublattice, it is assumed that there is no contribution from the other A atoms, which leads to :

$$S_{AA} = \frac{1}{N}\sum_{i}^{N}\langle P_z^A(\mathbf{r}-\mathbf{R_{A,i}})|P_z^A(\mathbf{r}-\mathbf{R_{A,i}})\rangle = 1 \tag{1.113}$$

This means that the wave-function does not overlap any other wave-function of another same sub-lattice atom.

Off-diagonal matrix elements. The Hamiltonian $H_{\alpha,\beta}$, with ($\alpha,\beta \in$ A,B), when $\alpha \neq \beta$ is given as follows:

$$H_{AB} = \frac{1}{N}\sum_{i}^{N}\sum_{j}^{N} e^{i\mathbf{k}\cdot(\mathbf{R_{B,j}}-\mathbf{R_{A,i}})}\langle P_z^A(\mathbf{r}-\mathbf{R_{A,i}})|\hat{H}|P_z^B(\mathbf{r}-\mathbf{R_{B,j}})\rangle \tag{1.114}$$

In the approximation of the nearest-neighbours, only the three nearest atoms will be taken into account, belonging to the other sub-lattice. In this case of an atom A belonging to the unit cell i, the three neighbours atoms B will be considered and they will be indexed with l=1,2,3. This can be written as:

$$H_{AB} = \frac{1}{N}\sum_{i}^{N}\sum_{l}^{3} e^{i\mathbf{k}\cdot(\mathbf{R_{B,l}}-\mathbf{R_{A,i}})}\langle P_z^A(\mathbf{r}-\mathbf{R_{A,i}})|\hat{H}|P_z^B(\mathbf{r}-\mathbf{R_{B,l}})\rangle \tag{1.115}$$

For each neighbouring pair (atoms A-B), we will have the same matrix element that we can note:

$$\gamma_0 = -\langle P_z^A(\mathbf{r}-\mathbf{R_{A,i}})|\hat{H}|P_z^B(\mathbf{r}-\mathbf{R_{B,l}})\rangle \tag{1.116}$$

Therefore

$$H_{AB} = -\frac{\gamma_0}{N}\sum_{i}^{N}\sum_{l}^{3} e^{i\mathbf{k}\cdot\delta_{\mathbf{l}}} \equiv -\gamma_0 f(\mathbf{k}) \tag{1.117}$$

and since the Hamiltonian is also hermitian,

$$H_{BA} \equiv -\gamma_0 f^*(\mathbf{k}) \tag{1.118}$$

with

$$\begin{aligned} f(\mathbf{k}) = \frac{1}{N}\sum_{i}^{N}\sum_{l}^{3} e^{i\mathbf{k}\cdot\delta_{\mathbf{l}}} = \sum_{l}^{3} e^{i\mathbf{k}\cdot\delta_{\mathbf{l}}} &= e^{ia_0k_x} + e^{-ia_0\frac{1}{2}k_x}e^{-ia_0\frac{\sqrt{3}}{2}k_y} + e^{-ia_0\frac{1}{2}k_x}e^{ia_0\frac{\sqrt{3}}{2}k_y} \\ &= e^{ia_0k_x} + 2cos\left(a_0\frac{\sqrt{3}}{2}k_y\right)e^{-ia_0\frac{1}{2}k_x} \end{aligned} \tag{1.119}$$

using Equations (1.95). The overlap matrix will be treated in the same way, and for the neighbouring atoms pair (A-B), we expect the same matrix element:

$$s_0 = -\langle P_z^A(\mathbf{r} - \mathbf{R_{A,i}}) | P_z^B(\mathbf{r} - \mathbf{R_{B,l}}) \rangle \tag{1.120}$$

which leads to :

$$S_{AB} = -s_0 f(\mathbf{k}) \quad \text{and} \quad S_{BA} = -s_0 f^*(\mathbf{k}) \tag{1.121}$$

To summarize, the Hamiltonian matrix and the overlapping matrix become:

$$H = \begin{pmatrix} E_{2P} & -\gamma_0 f(\mathbf{k}) \\ -\gamma_0 f^*(\mathbf{k}) & E_{2P} \end{pmatrix} \tag{1.122}$$

$$S = \begin{pmatrix} 1 & -s_0 f(\mathbf{k}) \\ -s_0 f^*(\mathbf{k}) & 1 \end{pmatrix} \tag{1.123}$$

which can be pugged in Equation (1.109) :

$$det[H - ES] = det \begin{pmatrix} E_{2P} - E & -(\gamma_0 + Es_0) f(\mathbf{k}) \\ -(\gamma_0 + Es_0) f^*(\mathbf{k}) & E_{2P} - E \end{pmatrix} = 0 \tag{1.124}$$

to obtain:

$$E_{2P} - E = \pm(\gamma_0 + Es_0)|f(\mathbf{k})| \tag{1.125}$$

which leads to the final dispersion relation for the dynamic of electrons in graphene, taking into account the three nearest neighbour:

$$E^{\pm} = \frac{E_{2P} \pm \gamma_0 |f(\mathbf{k})|}{1 \mp s_0 |f(\mathbf{k})|} \tag{1.126}$$

with (+) for the π band and (-) for the π^*, and

$$|f(\mathbf{k})| = \sqrt{4cos^2(\frac{a_0\sqrt{3}}{2}k_y) + 4cos(\frac{a_0\sqrt{3}}{2}k_y)cos(\frac{3a_0}{2}k_x) + 1} \tag{1.127}$$

E_{2P}, γ_0 and s_0 are three parameters used to fit the experiments. E_{2P} is usually set to 0 in order to have the Fermi energy at 0ev. Indeed, taking the point of high symmetry K_1 and K_2 seen in Equation (1.98), the calculation gives $E^{\pm}$=0 : graphene is a semi-conductor with a bandgap null. According to [136], the parameters E_{2P}=0, γ_0=3.033eV and s_0=0.129eV should be used in order to get the best fit of the first principles calculations. The plot is displayed in Figure 1.14a as well as zoom on the high symmetry point K_1/K_2 in Figure 1.14b.

It is also possible to make approximations in order to simplify Equation (1.126). For the overlap matrix of the neighbouring atoms pair (A-B), it can be reasonably supposed that the overlap of the A and B wavefunctions is very low and can be neglected. As a matter of fact, the electrons which account for transport are in p_z orbitals which exhibit a small spatial extension in the x,y plane. Therefore, we can ignore non-diagonal terms and set $s_0 = 0$. It is interesting to note that by setting $s_0 = 0$, the π and π^* bands will become symmetrical. Hence, we find the widely spread equation describing the band structure of the graphene layer :

$$E^{\pm} = \pm\gamma_0 \sqrt{4cos^2(\frac{a_0\sqrt{3}}{2}k_y) + 4cos(\frac{a_0\sqrt{3}}{2}k_y)cos(\frac{3a_0}{2}k_x) + 1} \tag{1.128}$$

The band structure. The orbitals p_z being half filled, each energy band is either full or empty. The valence band and the conduction band touch at two points in the Brillouin zone (Figure 1.14a), K_1 and K_2 in our model (Figure 1.12a). As a consequence, graphene is often refereed to as a zero-gap semi-conductor or a semi-metal. It is interesting to observe that at low energy, the dispersion relation around the K points is linear (Figure 1.14b), which gives to graphene electronic band structure this peculiar shape of cone at the vicinity of the Dirac point.

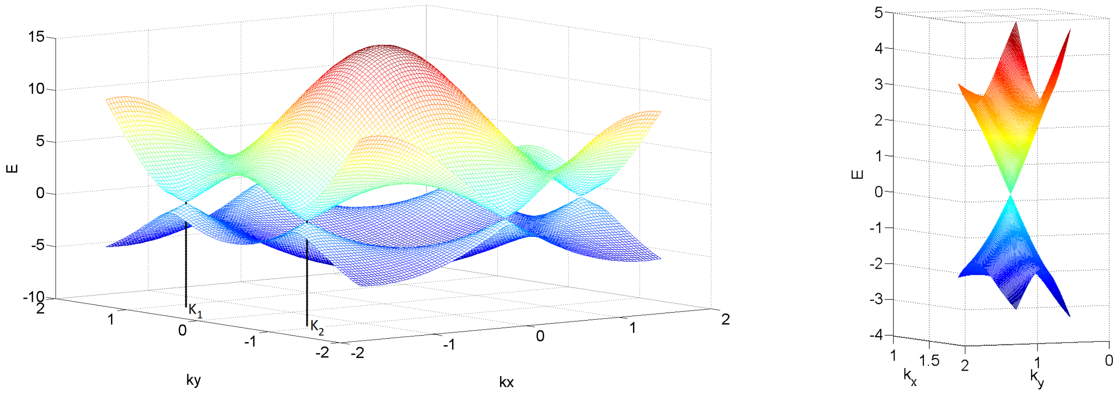

(a) Electronic dispersion relation of graphene single layer drawn in the first brillouin zone with the fitting value from [136].

(b) Zoom at the point of high symmetry K, for low energy we have a linear dispersion

Figure 1.14: Illustration of the dispersion relation of graphene electrons (a) in the first brillouin zone and (b) at the vicinity of the high symmetry point K.

The Dirac equation for low energy. The dispersion relation of graphene tends to be linear for low energy, around the Dirac cones. In the model developed before, it happens therefore at the points K_1 and K_2 on Figure 1.12a (see Equations (1.98)). The best fit at low energy is given with E_{2P}=0, γ_0=2.7eV and s_0=0 according to [132], which gives $E^{\pm} = \pm\gamma_0|f(\mathbf{k})|$. In order to demonstrate it, let's go back to Equation 1.119 and insert $\mathbf{q} = \mathbf{K_1} + \delta\mathbf{k}$. Using Taylor serie for trigonometric functions and keeping only the first order term, it is possible to write:

$$\begin{aligned} f(\mathbf{q}) &= e^{ia_0 q_x} + 2cos\left(a_0\frac{\sqrt{3}}{2}q_y\right)e^{-ia_0\frac{1}{2}q_x} \\ &= \left(-\frac{1}{2}+i\frac{\sqrt{3}}{2}\right)(1+ia_0\delta k_x) + \left(1-\frac{3}{2}a_0\delta k_y\right)\left(\frac{1}{2}-i\frac{\sqrt{3}}{2}\right)\left(1+ia_0\frac{1}{2}\delta k_x\right) + \mathcal{O}(\delta k^2) \\ &= \frac{3a_0}{2}\left(-\frac{1}{2}+i\frac{\sqrt{3}}{2}\right)(i\delta k_x + \delta k_y) + \mathcal{O}(\delta k^2) \\ &= \frac{3a_0}{2}e^{i\frac{2\pi}{3}}(i\delta k_x + \delta k_y) + \mathcal{O}(\delta k^2) \end{aligned} \tag{1.129}$$

Therefore, in the vicinity of the K points, the dispersion relation can be approximated as

$$E^{\pm} = \pm\gamma_0|f(\mathbf{q})| = \pm\gamma_0\frac{3a_0}{2}|\delta\mathbf{k}| = \pm\hbar v_F|\delta\mathbf{k}| \tag{1.130}$$

where the Fermi velocity has been defined as $v_F = \gamma_0\frac{3a_0}{2\hbar} \approx 10^6 m.s^{-1}$. Moreover, the Fermi speed does not depend on the mass. We will therefore speak about the electron as massless Fermions of Dirac in graphene. One of the consequence is the ultra-high mobility of the carrier in graphene, leading to a high conductivity of this material even at room temperature. It is also a really interesting behaviour to study in quantum mechanics.

1.3.3 Graphene electron-hole excitation spectrum

The electron hole excitations in the low energy range can be explained looking carefully at the cone-like band structure (Figure 1.14b). Those excitations are really important in the study of graphene plasmonics because there is a possibility of an energy transfer between plasmons and single particle excitation resulting in plasmons damping. This damping is called the Landau damping, which is a loss of collective electronic motion from the plasmons to the excitation of electron-hole pairs, a single particle excitation.

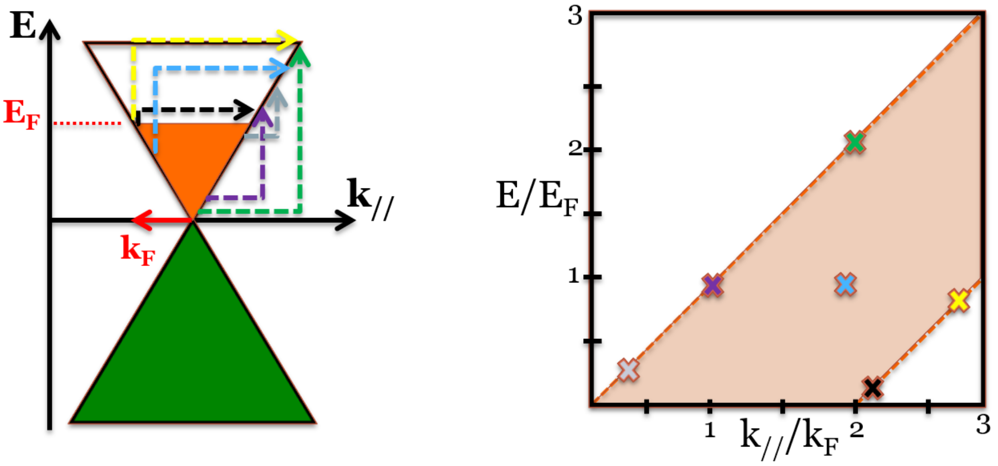

Figure 1.15: Illustration of the construction of the intraband excitation zone in graphene (on the right), from its electronic band structure (on the left). Here it has been considered a n-doped graphene (conduction band half filled in orange on the electronic band structure). Each arrow on the band structure represent a couple energy-wavevector of a specific electronic transition. The crosses on the corresponding map represent the different transitions illustrated by the arrows on the band structure.

Figure 1.15 illustrates the construction of the single particle excitation zone $\mathbf{SPE_{intra}}$ (on the right in orange on the map E($k_{\|}$)) where intraband excitation takes place. In this case, both the electrons and holes taking place in the excitations of electron-hole pairs, are located in the conduction band (for E positive, upper cone, on the left of Figure 1.15). The different possible excitations are represented by the coloured arrows on a graphene n-doped electronic band structure, on the left of Figure 1.15. Each arrow is defined by a particular energy/wavenumber couple $(E, k_{\|})$. Picking up all the possible couple $(E, k_{\|})$ of intraband electron-hole excitations, it is possible to plot a map displaying the wavenumber and the energy, in x and y axis respectively (on the right Figure 1.15). A region in orange appears on the dispersion relation graphic, where each coloured arrow has been replaced by a corresponding cross. This region is called the intraband single particle excitation zone ($\mathbf{SPE_{intra}}$).

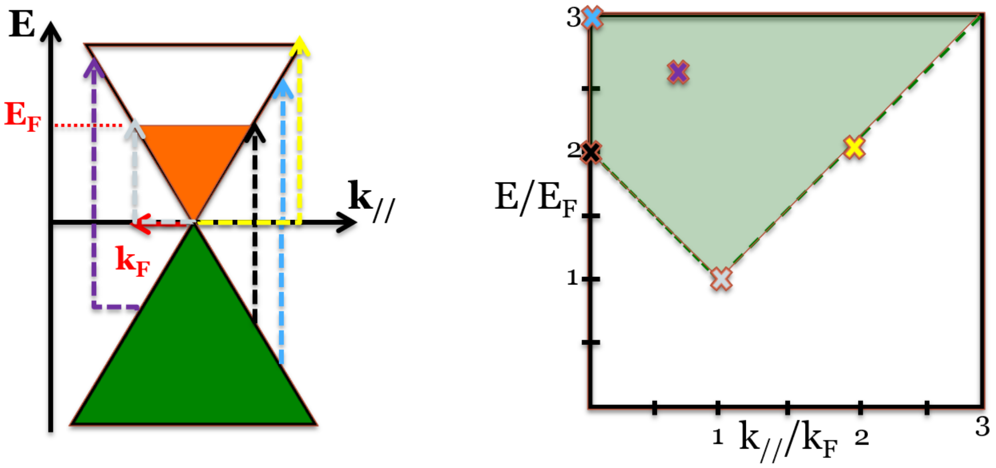

Figure 1.16: Possible interband single particle excitation (electron-hole-excitations) in graphene n-doped and illustration of the interband transition zone. The conduction band is illustrated by the orange zone, whereas the valence band is illustrated in green. The arrow represent the couple energy-wavevector of a specific transition. The cross represent the different transitions illustrated on the band structure.

Figure 1.16 illustrates the interband excitation, in which electrons participating to the excitations are located in the valence band, whereas holes are located in the conduction band. The electron is promoted from the valence band to the conduction band when the condition $(E, k_{||})$ is met. In the same way than above, a region in green appears, which is called the interband single particle excitation zone ($\mathbf{SPE_{inter}}$). The interband transition are only possible above an energy threshold of $\mathbf{E_F}$, where an electron at the dirac crossing can get promoted with a couple of energy-wavevector $(\mathbf{E_F}, \mathbf{k_F})$. An interesting point is to realize that a photon can excite an electron only at the energy of $2\mathbf{E_F}$ and above. This $2\mathbf{E_F}$ is usually called the Pauli-blocking threshold. Therefore, at energy below this threshold, the interband contribution to the optical response of graphene becomes insignificant as compare to the intraband one. This will be see section 2.2.1, where the optical conductivity of graphene is demonstrated.

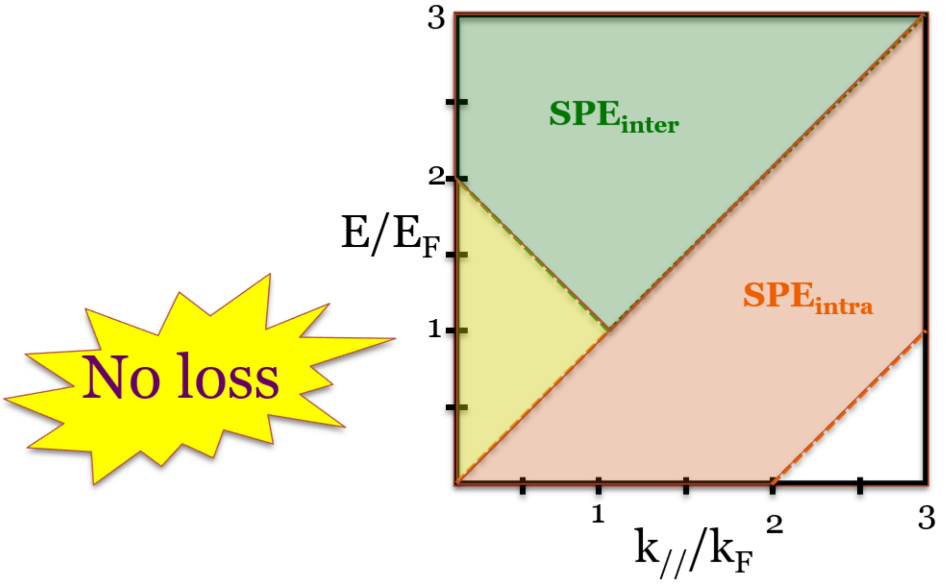

Figure 1.17: Illustration of the zone where there is no Landau damping in the ideal case, in yellow. The orange zone on the spectrum illustrates the intraband excitation, whereas the green zone illustrates the interband single particle excitation.

Figure 1.17 summarize the figure 1.15 and 1.16. In yellow is highlighted the zone in which there should be a weak Landau damping for the surface plasmons to propagate. However, outside this triangular zone, plasmons experience high dampings due to electron-hole excitations. Therefore, when studying graphene plasmons, it is important to carefully choose the energy of excitation.

1.4 Conclusion

In this first chapter, the fundamental principles have been presented in order to cover both fields, plasmonics and graphene. The physics principles of electromagnetism have been used to understand the basis of plasmonics, in the general case as well as in the case of thin films. Then, the main properties of graphene are introduced. Particularly, the tight binding model provides an understanding on the behavior of electrons in graphene. It leads to the construction of a graphic representing the possible excitation of electrons-holes as a function of a given energy and momentum. This latter is a necessity in order to work on a long propagation of plasmons in graphene.

In the next chapter, the knowledge gathered here will be utilized to study the field of graphene plasmonics.

Chapter 2

Graphene plasmonics

Electronic devices, used in telecommunication and information processing, exhibit inherent limitations due to materials electronic losses and noises which have consequences on their conductivity and associated energy consumption. To remove this barrier and keep on increasing electronic devices performances, the technological trend is to find another information carrier that is able to replace or complete electrons, among which photons appear to be the ideal candidate. Until now, however, despite recent promising demonstrations of strong near-field confinement in hybrid Silicon on Insulator structures, e.g [99], photonic devices have been diffraction-limited by the light wavelength which leads to some difficulties when components are scaled down to nanoscale.

Recently, graphene [50] has been proposed as a good candidate to bridge the gap between electrons and photons for a new generation of optoelectronic devices [14]. While many promising properties like its ultimate thickness, transparency, ultra-high electronic mobility or mechanical strength have concentrated the efforts of numerous groups, a few pioneering groups have recently started considering and studying graphene for its optoelectronic [20] and plasmonic properties [57], opening new routes to ultimate optoelectronic nanodevices based on electron-photon interactions.

From all the pioneering theoretical [159, 58, 66, 59] and experimental [117, 114] studies, it now appears feasible to use light as an information carrier by manipulating it through Graphene Plasmons Polaritons (GPPs).

The promises of graphene for plasmonics lie in the high confinement and weak damping [49] of sustained plasmons as well as in the possibility to electrostatically tune them simply by applying a voltage. The main asset would be to enable miniaturization of photonic component without facing usual thermal limitations thanks to low graphene electronic losses. The applications could therefore be numerous.

This chapter aims to expound the literature review of graphene and graphene plasmonics, as well as the properties of graphene plasmons. At first, the discovery of graphene will be traced as well as its limits in term of transport properties. Then, the optical properties of graphene will be introduced and an overview of graphene plasmonics state of the art will be presented. Subsequently, the dispersion relation of graphene plasmons will be demonstrated. Afterwards, the graphene plasmonics properties will be reviewed in details and finally, a conclusion through the objectives of this study will be made.

2.1 Litterature review on graphene and its transport properties

2.1.1 The discovery of graphene and the synthesising process

In october 2004, two papers were published [17, 117] and showed some properties of few layers of carbon on different substrates. Despite the common thought [105], such extremely thin films are thermodynamically stable. Two different ways of fabrication were used : on silicon carbide by thermal desorption of Si [17] (Figure 2.1a, STM image), and by mechanical exfoliation [117] (Figure 2.1b, AFM image).

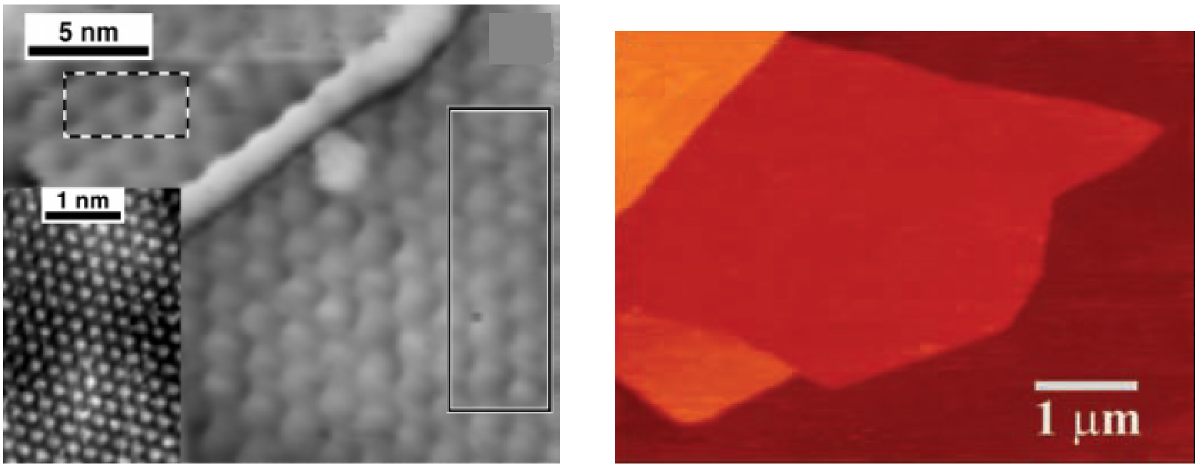

(a) STM image of few layers graphene grown by carbon segregation on SiC [17]

(b) AFM image of a single layer graphene mechanically exfoliated [117]

Figure 2.1: The two first papers published in October 2004 reporting graphene monolayer with different fabrication process

The behavior of 2D electron gas properties in such thin film have been demonstrated, opening wild area of research in domain such as quantum mechanics. It has also been shown shown that graphene is a semi-metal and can sustain huge current. The transport of electrons in this medium shows small electrical resistivity (ballistic transport), limited by scattering effect, and a significant mobility. Finally, the most important feature discovered is the possibility to inject carriers in graphene (doping) which changes its conductivity/resistivity and exhibits an ambipolar electric field effect (conductivity carried by electron or hole depending on the applied voltage). This discovery led to a Physics Nobel price and many promising applications. In the next paragraphs, the different ways of producing graphene will be reviewed.

Mechanical exfoliation. This method [117] consists in a repeated peeling of highly oriented pyrolytic graphite with the use of clean room tape (Figure 2.2). The advantage of this method is a high quality of single layer graphene deposited on various substrate. The mono-cristaline flake can be up to millimetre scale and shows excellent electronic properties. Although this method have been widely used for fundamental studies, it is impractical for large scale application.

Carbon segregation. It is possible to get graphene from silicon carbide [17] or other metal substrates, through carbon segregation. At high temperature, on SiC, silicon desorption occurs leaving on the substrate few to one layer of graphene. It is possible to obtain free standing graphene of high quality via, among others, hydrogen treatment [134].

Chemical Vapour Deposition. Another way for graphene synthesis emerged in 2008/2009 [166, 93]. This process has drawn a lot of interest in the industry because of the possibility to grow it on a large scale basis at low cost. Hydrocarbon species are introduced in a high temperature chamber, where is lying a metal substrate. Two type of metals are widely used : Nickel (Figure 2.3a) and Copper (Figure 2.3b). The choice of metal is important because it determines the growth mechanism and eventually the quality of the graphene.

It has been demonstrated [169] that the graphene growth on Ni (Figure 2.3a) is a segregation process, where carbon is first dissolved in the metal substrate at high temperature. Then, the substrate is cooled down to a temperature for which the carbon is less soluble in Nickel, forming at the surface multi layer and polycristalline graphene.

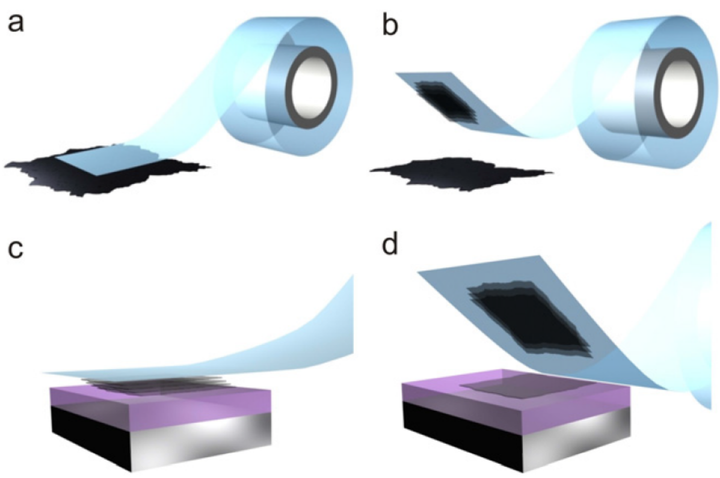

Figure 2.2: Illustration of Micro exfoliation (a)A pressure is applied to stick the tape to the surface of the material. (b) Few layers of the material are attached to the tape. (c) The tape is then pressed against the substrate. (d) One or few layers remain on the substrate once the tape is withdrawn [118]

On Cu substrate (Figure 2.3b), the metal acts as a catalyst and graphene is formed at its surface from the decomposition of the hydrocarbon precursor. This comes from the fact that carbone solubility in copper is low. Two consequences arise: only one layer can be form, because the metal underlying is the catalyst, and once it is covered by a first layer, no other reaction can take place. The second consequence is that it is possible to get large monocrystalline flakes of graphene. The quality of the copper substrate is crucial in order to get low defects in CVD graphene [171].

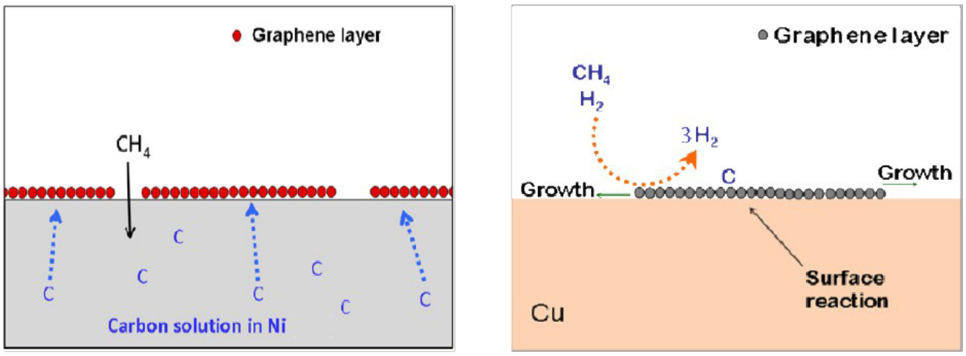

(a) Growth of graphene on Nickel substrate by segregation reaction process, leading to muliti-layer and polycristalline graphene

(b) Growth of graphene on Copper substrate by surface reaction process, leading to single layer monocristalinne graphene

Figure 2.3: Growth of graphene by Chemical Vapour Deposition on different substrate [169]

Chemical methods and chemically modified graphene. It is possible to fabricate graphene through colloidal suspension of graphite [31]. In the presence of strong acids and oxidants, oxidation of graphite occurs with the intercalation of epoxide and hydroxyl groups. The hydrophilic properties of these chemical end points facilitate the introduction of water and the dispersion of graphene layers in solution. This method is inexpensive and produce large flakes but the remaining graphene have a poor conductivity with significant amount of defects. Research groups [126] have been trying to reduce the graphene oxide (Figure 2.4) but obtaining pristine graphene properties remains a challenge.

Liquid phase exfoliation of graphene. By using different types of solvent (aqueous or not), it is possible to disperse graphene flakes from powdered graphite via ultrasonication. In that way, unoxidised,

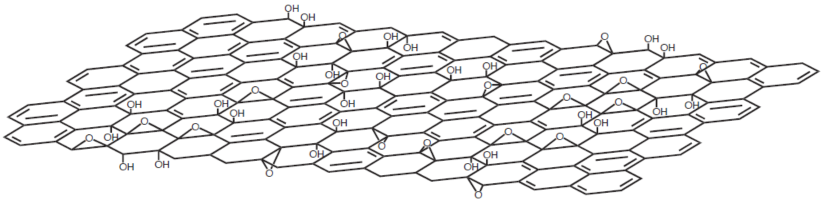

Figure 2.4: Illustration of a flake of graphene oxide with epoxide (-O-) and hydroxyl (-OH) groups [126]

high quality, scalable graphene has been obtained [61] , which can be for example deposited by spray coating. This inexpensive method, as compared to CVD graphene, and the high quality of graphene obtained, as compared to the chemically modified graphene, attract wide interest in the scientific community.

Transfer of graphene on a targeted area. The potential possibilities od devices offered by graphene through its opto-electronic properties require the ability to deposit it on a targeted area where electrodes are located. However, the manipulation of an atomic layer is not trivial. The main challenge is to keep the sheet undamaged and its opto-electronic properties intact. Several ways have been studied [20], and the most popular one is based on the use of PMMA layer [133] (see Figure 2.5).

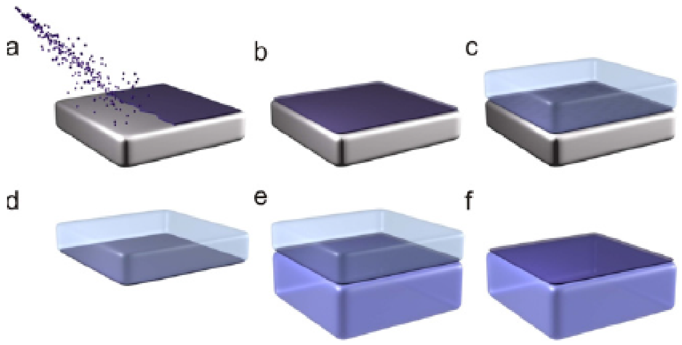

Figure 2.5: Illustration of the transfer of a CVD graphene layer by the use of PMMA. (a) and (b), the graphene is grown on metal substrate. (c) A thin film of PMMA is deposited on the metal+graphene sample. (d) The metal is then etched, and graphene+PMMA is remaining. (e) Graphene+PMMA is transfered on the chosen substrate and (f) the PMMA layer is removed. [118]

One of the most challenging step is then to clean the graphene. Acetone is widely used to remove the PMMA layer, but it also contaminates the graphene layer [68]. In general, any chemical component in contact with graphene can potentially affect its opto-electronic, and thus transport properties. Therefore, many groups have been working on the measurement, the identification and the quantification of the limit of graphene transport properties. This issue will be discussed in the next section.

2.1.2 Limits on the transport properties of graphene

The transport properties of graphene are limited by different scattering mechanisms. The magnitude of the carrier scattering can be expressed in term of mobility μ, which links the average drift velocity of a charge carrier to an applied electric field. Graphene on SiO_2 substrate exhibits a mobility of more than $1m^2V^{-1}s^{-1}$, one order of magnitude higher than the silicon that is the most common electronic material [57]. However, the scattering rate remains an obstacle and limits potential application in opto-electronic, as well as in fundamental physics [19].

Scattering can be divided into two categories. The first one concerns intrinsic scattering mechanisms, such as graphene defects, grain boundaries, intrinsic ripples or graphene phonons, emerging from the graphene itself. The second one involves the extrinsic mechanisms, arise from the surrounding materials, like charged impurities in the substrate or trapped under/above the graphene, corrugations and strains induced by the substrate, and remote interfacial phonon. All these scattering sources influence the mobility of the charged carriers and we are going to enumerate and quantify their weight through a literature review.

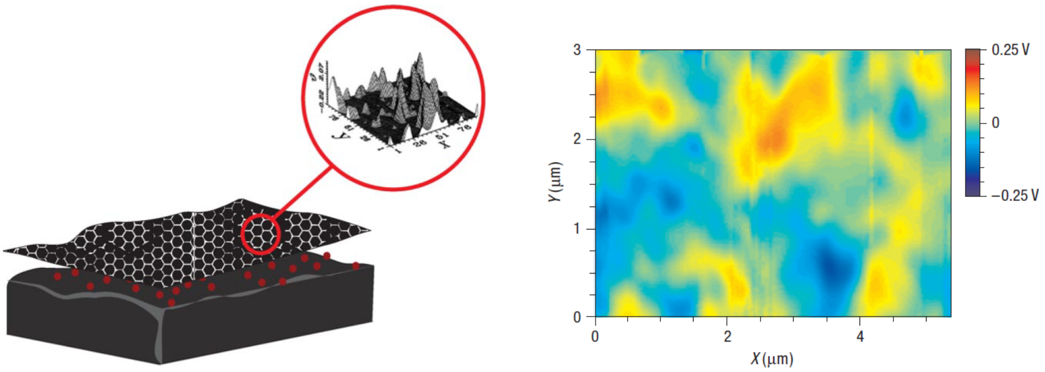

(a) Artistic illustration of the model of charged impurities sandwiched in between graphene and substrate [4]. It creates a local inhomogeneous voltage fluctuation, illustrated in inset [4].

(b) Fluctuation of the density of carriers from the substrate with E_F close to zero, as observed by scanning single-electron transistor [104]

Figure 2.6: Charged impurities as an explanation of the limitation of experimental transport properties of graphene

Charged impurities. Graphene being confined ultimately in one dimension, it is natural to speak about two-dimensional electron systems. As other two-dimensional systems, the electrons in graphene do not move as independent particles, but rather by pair, where the distance between two electrons have a central role [57]. Electrons are strongly interacting with each other, and we speak about an interaction potential $u(r) = e^2/\epsilon_s\mathbf{r}$. Their motion are therefore correlated and the potential $u(r)$ created by their separation distance $\mathbf{r}$ is really sensitive to the surrounding media, $\epsilon_s = (\epsilon_1 + \epsilon_2)/2$ [57] (see section 1.1.3). Therefore, the effects of the substrate and any chemical component in the vicinity of the carbon sheet should be taken into account carefully.

Scattering from charged impurities by the substrate [7, 116, 173] was pointed out as the limiting factor of the transport properties. Located near the interface between graphene and substrate (Figure 2.6a), or in the substrate (Figure 2.8), charged impurities generate charged puddles in the graphene layer which influence the transport properties, being a dominant source of scattering [65]. At high Fermi level, the density of impurities impact linearly graphene carrier transport, whereas it could explain why there is a finite conductivity near the Dirac point [4]. Although the local density of charges from the substrate have been imaged (see Figure 2.6b) using a scanning single-electron transistor [104], the study emphasis that it is not sufficient to explain the emerging electron-holes puddles on graphene. It would rather come from the pollution by resist and other chemical post treatments exposing graphene. The resist residue have been imaged [68] by scanning tunnelling microscopy (STM) which showed a layer of photo-resist remaining despite a careful treatment of the sample. On the other hand, molecules from air, such as H_2O or N_2 trapped in between the substrate and graphene during the transfer of the carbon layer have been suggested [170] as potential charged impurities creating charged puddles.

By adding potassium atoms as impurity centers, a study [27] showed that the conductivity gets lower as the density of impurities gets higher. It could be possible, according to [28], to get a mobility as high as $4m^2V^{-1}s^{-1}$, provided one gets rid of charged impurities. However, an alternative explanation have been pointed out through the study of suspended graphene [105]: corrugation of graphene layer (see section below).

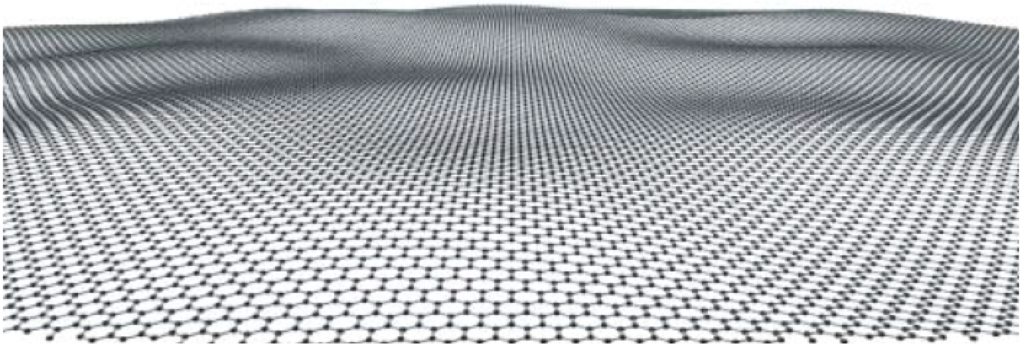

Figure 2.7: Artistic illustration of what a real graphene should look like, with the presence of ripples [105]

Corrugation. Using Transmission Electronic Microscope (TEM) technique, it was shown that graphene is not flat [105], in agreement with the theory predicting that perfect 2D material are unstable under ambient condition. Suspended graphene exhibits microscopic corrugation in the three dimensions as illustrated on Figure 2.7. On SiO_2 substrate, perturbations and fractures of the hexagonal lattice symmetry have been imaged [68] by scanning tunnelling microscopy (STM). The authors demonstrated a correlation between the graphene lattice perturbation and the underlying substrate. However, it was suggested that in their study, there was no independent intrinsic graphene corrugations, but rather extrinsic corrugations caused by the lattice mismatch with the substrate. The presence of corrugations partially matching the underlying SiO_2 substrate, inducing stiffness in the graphene sheet, are more likely to create strain-induced disorder, and dramatically affect the electronic transport properties in graphene. Both extrinsic and intrinsic ripples have been observed on SiO_2 substrate [52], meaning that the graphene would be partially suspended in between the sample surface relief (see Figure 2.8).

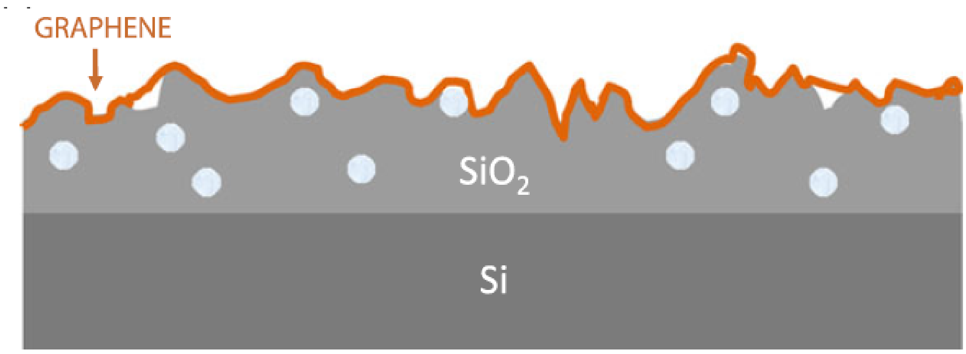

Figure 2.8: Schema drawn from STM and AFM data, showing how graphene wraps a substrate. Graphene is represented in orange, charged impurities in light grey dots [9].

Following these investigations, studies demonstrated that intrinsic [78] as well as extrinsic [80] corrugations could be an alternative explanation to the scattering rate observed experimentally in graphene. In fact, such scattering mechanisms produce similar effects on the conductivity, as compared to the charges impurities, and could be confused with charge impurities effect. However, it was shown, by STM-based dI/dV mapping, that there is no correlation between corrugations and scattering centers.[170]

Lattice disorder. The structure of graphene, made of sp^2 covalent bond in between carbon (see Figure 1.11), make lattice defects relatively rare, according to [19]. However, several types of defect can still be found, such as grain boundaries (Figure 2.9b, 2.9c), vacancies or atoms substitution(point defect, Figure 2.9a), mechanical distortion of the lattice, etc... Studies have allowed one to analyze the influence of

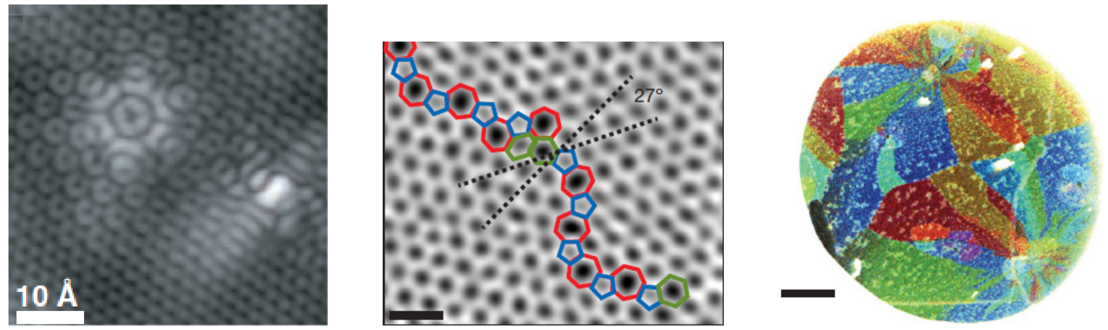

(a) STM image of a point defect of bilayer graphene grown on SiC From [135]

(b) TEM image of CVD graphene grown on copper. Two grain boundary meeting each other at an angle of 27 deg. Scale bar 5 Å from [64]

(c) TEM image of CVD polycristalline graphene grown on copper. Fake color representing different grain orientation. Scale bar 500nm from [64]

Figure 2.9: (a) STM image of point defects, (b) TEM image of a grain boundary and (c) TEM image of a polycristalline CVD graphene.

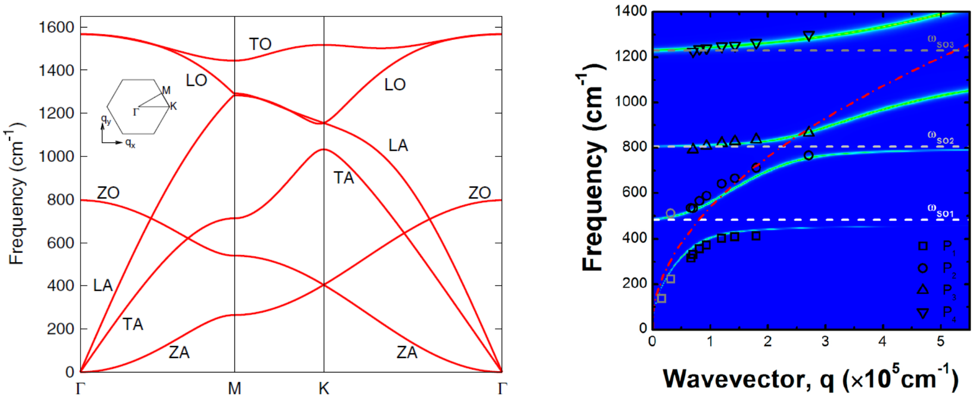

(a) Numerical phonon dispersion in graphene from the Long-range Carbon Bond Order Potential (LCBOPII) [77].

(b) Graphene plasmons coupling with SiO2 surface optical phonon revealed through extinction measurement, with ω_{SO1} = 485 cm^{-1} (≈ 20.6 μm), ω_{SO21} = 806 cm^{-1} (≈ 12.4 μm), ω_{SO3} = 1229 cm^{-1} (≈8.1 μm) [100].

Figure 2.10: Intrinsic phonon of a monolayer graphene and extrinsic phonon-plasmons coupling at the interface between graphene and SiO2 substrate

such defects on the opto-electronic properties of graphene [127]. They have been imaged through various techniques. As an example, bilayer graphene grown epitaxially on SiC have been investigated by STM technique, where it is possible to see different perturbation and point defect of the lattice structure [135]. It puts into evidence the critical influence of the substrate and the substrate quality on the transport properties of graphene.

More specifically, CVD graphene, which has been used in this study, presents many defect types, depending on the type and the quality of the substrate [171], as well as on the process of growth and transfer. One of the most common defects is grain boundaries (Figure 2.9b), that have been imaged through STM [33], TEM [81, 64], but also Raman spectroscopy [75] and later with SNOM [43] (Figure 2.18b). In general, grain boundaries tend to reduce the electrical conductivity of polycrystalline graphene [75], even if larger grain does not coincide with higher conductivity [64]. Comparing the influence on the conductivity of three types of defects (point defect, surface contamination and line defects), grain boundary seems to be the main factor [142] limiting the electronic transport in CVD graphene.

Electron-Phonon interactions. Several types of phonon can interact with electrons in graphene, which are as many possible energetic channel leading to the scattering of charge carrier.

The intrinsic phonons, three optical and three acoustic phonons, are present in this 2D material (see Figure 2.10a). The optical phonons are energetically too high for IR-SNOM to be taken into account, and are usually studied by spectroscopy. The intrinsic acoustic phonons have been studied for their unusual heat transport properties [115] as well as for their impact on the conductivity. They are nowadays pointed to be one of the main graphene plasmons scattering mechanism, limiting their propagation in h-BN/graphene heterostructure [153, 114].

A first study analysing the transport in high quality graphene [110] predicted an extremely low electrons-phonons scattering, even at high temperature. The limitation of the mobility would stand as high as $20m^2V^{-1}s^{-1}$ if extrinsic scattering are eliminated. A second one discussed theoretically in plane acoustic phonons [67]. The authors show that those phonons would limit the mobility of graphene at more than $10m^2V^{-1}s^{-1}$. Therefore, according to these studies, in plane phonon would not be a significant scattering mechanism. However, flexural phonon could be significant in suspended membrane [102]. These out-of-plane quasi-particles would be present in any samples due to intrinsic ripples [78], and more particularly in suspended graphene [122].

This scattering process involves two flexural phonons [22], excited simultaneously, and limits the mobility in suspended graphene around $1m^2V^{-1}s^{-1}$. However, strain induced mechanically or by back gate potential could reduce the influence of this scattering in suspended graphene, to be analogous to the in plane one [103]. Further experimental data agreed [88] with the theory for a value of mobility in suspended graphene at room temperature around $1.5m^2V^{-1}s^{-1}$ [37]. However, recently, it has been recorded a mobility as high as $24m^2V^{-1}s^{-1}$ in CVD suspended graphene at room temperature. In bilayer graphene, the electron-phonon coupling mechanism is different. As a consequence, the mobility could be found as high as $10 - 20m^2V^{-1}s^{-1}$ [121].

The Remote Interfacial Phonon (RIP) is a phonon of the substrate excited by the charge carriers in graphene. In the presence of a polar substrate, such as $Si0_2$ or SiC, the carriers in graphene couple with the polarisation field at the interface graphene-substrate. This scattering mechanism is known to limit electronic transport in 2D-like Si structure [48]. Plasmons-phonon coupling have been observed experimentally on SiC substrate [95] as well as on SiO2 substrate ([100], Figure 2.10b). Others high-k dielectric substrates have been investigated, stuying mobility in presence of charged impurities [83]. The advantage of dielectric screening effect of impurities, thanks to high-k substrate, is lost by RIP arising. So it has been predicted not much improvement of the mobility at room temperature . A numerical study [123] of graphene on SiO_2 and HfO_2 (high-k substrate) at room temperature predicted a limitation for the mobility between 0.55 to 2.4 $m^2V^{-1}s^{-1}$ due to RIP (with E_F from approximately 0.1eV to 0.3eV).

Dc scattering approximation. As it has been seen in this section, the sources of scattering are multiple. Usually, the mobility is evaluated for a Direct Current, which is a good starting point. Following this rule, the mobility can be expressed as $\mu = \frac{\tau_{DC} e v_F^2}{E_F}$. Here, τ_{DC} is the relaxation time of the electrons in the DC approximation. However, it has been observed values relatively different when coming to optical frequency. At first, electrons-electrons scattering has been pointed [70] to be responsible for unexpected increased of scattering rate [42]. In the case of the study of plasmons, authors in ref. [57] emphasized that "The plasmon lifetime, τ_{pl}, however, should not be confused with the d.c. transport scattering time, τ_{DC}".

In another study [129] focusing on the plasmons losses in h-BN/graphene heterostructures, the authors compare the contributions of graphene's acoustic phonons and h-BN optical phonons to GPs damping. In the introduction, the authors reminded the Boltzman-transport theory, which demonstrates that the mobility μ is inversely proportional to the charge carrier density n. The Fermi level E_F beeing proportional to the square roots of the density of charge carrier, $\tau_{DC} \propto \frac{1}{\sqrt{n}}$. However, it was claimed that the plasmons lifetime should be increasing for increasing carrier density. τ_{pl} would therefore be anticorrelated with the mobility. However, recent imaging of plasmons in encapsulated h-BN, heterostructure known to enhance greatly the mobility, gives the best results [153]. In any case, increasing the Fermi level should increase the plasmons lifetime. Working with high-k dielectric material, in order to gate electrostatically the graphene and obtain high Fermi level, is one direction where research teams have been looking at recently.

Relationship between Fermi level and mobility. As a conclusion of what was seen above, the mobility, which aims to measure scattering mechanism, is limited by numerous factors. To summarize mobility, we can divide the different contribution in two categories [158], the intrinsic mechanisms or short range scattering (μ_{short} in the Figure 2.11 : lattice disorder e.g. vacancies, adatoms, absorbed molecules, grain boundaries) and the extrinsic mechanisms or coulumb scattering ($\mu_{coulumb}$ in the Figure 2.11 : charged impurities from substrate, interfacial phonons). According to [158], the former depends on carrier concentration in graphene. The dependence of the carrier concentration/Fermi level versus the mobility ($\mu_{coulumb}$, μ_{short} and μ_{total}) is plotted Figure 2.11. The chemical doping, with H_3PO_4, increase the carrier concentration (Fermi level), but increase also the short range scattering.

Maximizing the propagation length L_p of plasmons in graphene is a complexe task. In one hand, a high Fermi level seems to be a rather good target for getting long propagation, which is in agreement with recent experiment (will be seen section 2.3). In the other hand, plasmons being a collective oscillation of free charge carriers, a high mobility seems to be necessary. Moreover, h-BN, which is the support for the longest propagation, maximized the mobility [153]. However, high Fermi energy does not always match with high mobility, and uncertainties remain [129].

Beside the electronic transport, the optical behavior of graphene is of the first importance in order to understand graphene plasmons properties. Therefore, in the following section, the optical properties of graphene will be reviewed.

2.2 Litterature review on optics and plasmonics graphene properties

As it has been seen in Section 1.3 , graphene exhibits exotic properties. Among others, the massless dirac particule behavior of electrons leads to a really high mobility of the charged carriers (see Section 2.1.2). Moreover, the possibility to tune the Fermi level of graphene, and thus its optical properties, leads to a wide interest in the scientific community for graphene plasmonics. In fact, charge carriers can be injected up to 0.01 per atom of carbone for back gate system ($1 \times 10^{13} cm^{-2}$), and up to 0.1 per atoms for solid gel electrolyte [97]. Although much below the doping concentration that can be achieve in noble metal (up to 1 per atom), the injection of charges in graphene results in a significant change of optical properties of graphene.

The tunability of optical properties of graphene compared to a bulk of metal one can be understood

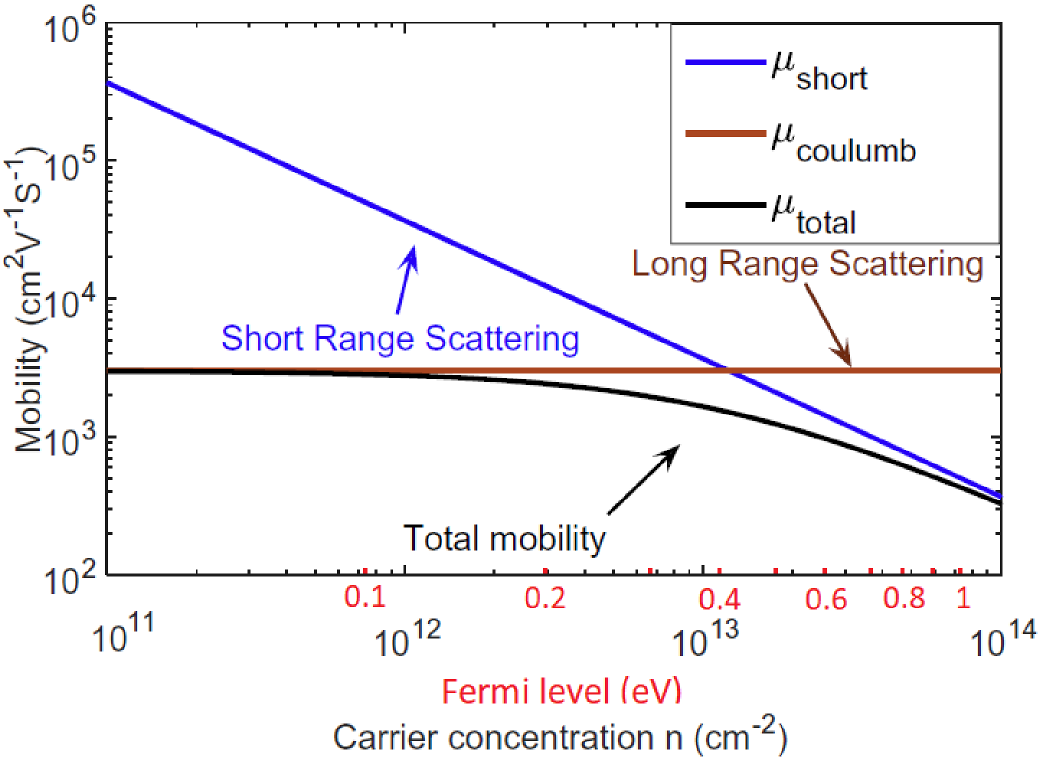

Figure 2.11: Mobility as a function of carrier concentration for graphene deposited on SiO_2 when graphene is doped chemically with H_3PO_4[158]

as follow. When a bulk of metal stands in a strong electric field, the electrons accumulate along the surface and shift the state of all the electrons inside the bulk. However, the total Fermi level is not changed and therefore, the property of the metal is not changed. At the contrary, in a single layer of carbon atoms, there is an effective change of the electrons/holes density in the material, which changes the conductivity and then the optical response [69]. Therefore, it is possible to modulate the dispersion relation of plasmons (see Section 2.3), which attracts considerable interest in the scientific world.

In the following section, the theory of the optical properties of graphene will be introduced, and then, the predicted opto-electronic devices emerging subsequently through simulation will be expounded. In a second part, an overview of what have been experimentally done in the graphene plasmonics field will be presented.

2.2.1 Theory of the optical properties and simulation of graphene-based devices

Graphene is a promising material for opto-electronics, but remain challenging to manipulate and control, because of its one atom thickness. However, the possible applications coming out have attracted wide interest and many groups worked on the theory and simulated devices based on graphene to design future opto-electronic platform. In this sub-section, a semi-classical way to treat the graphene optical properties will be given, based on the Kubo formula [59]. Subsequently, devices based on graphene, predicted through different simulation methods, will be enumerated.

The optical properties of graphene

The needs of understanding graphene peculiar electro-optics behaviour through the theory have been motivated early by the discovery and the characterisations of a monolayer graphene sheet [17, 117]. The tight binding approach (see Section 1.3.2) applied to this 2D honeycomb lattice enables to understand most of the unusual electronic properties [54]. However, the interaction of graphene with light is not trivial and many research groups have been working on different approaches to model it [58, 40, 59, 106]. Here, a first look will be taken at the semi-classical formalism, starting from the Kubo formula [59], which represents graphene as a conductive surface. Ryogo Kubo introduced an electronic transport formalism in order to describe the conductivity, based on linear response theory. It gives the conductivity depending on the electric field applied. To express the intrinsic conductivity of the graphene, the magnetic effect will be ignored. It is then possible to obtain the conductivity as a function of the radian frequency ω, the chemical potential μ, the scattering rate Γ and the temperature T[41]:

$$\begin{aligned}\sigma(\omega,\mu,\Gamma,T) = -\frac{ie^2(\omega+i2\Gamma)}{\pi\hbar^2}\Bigg[&\frac{1}{(\omega+i2\Gamma)^2}\int_0^\infty E\left(\frac{\partial f(E)}{\partial E}-\frac{\partial f(-E)}{\partial E}\right)\mathrm{d}E \\ &-\int_0^\infty \frac{f(-E)-f(E)}{(\omega+i2\Gamma)^2-4(E/\hbar)^2}\mathrm{d}E\Bigg]\end{aligned} \tag{2.1}$$

where

$$f(E) = \frac{1}{1+e^{\frac{E-\mu}{k_bT}}} \tag{2.2}$$

is the Fermi distribution. Equation (2.1) can be expressed as a sum of the intraband term (first integral term) and the interband term (second integral term), i.e $\sigma = \sigma_{intra} + \sigma_{inter}$.

$$\sigma_{intra}(\omega,\Gamma,T,\mu_c) = \frac{-ie^2}{\pi\hbar^2(\omega+i2\Gamma)}\int\limits_0^\infty E\left(\frac{\partial f(E)}{\partial E}-\frac{\partial f(-E)}{\partial E}\right)\partial E \tag{2.3}$$

$$\sigma_{inter}(\omega,\Gamma,T,\mu_c) = \frac{ie^2(\omega+i2\Gamma)}{\pi\hbar^2}\int\limits_0^\infty \frac{f(-E)-f(E)}{(\omega+i2\Gamma)^2-4(E/\hbar)^2}\partial E \tag{2.4}$$

It is interesting to notice that σ_{intra} (Equation (2.3)) is responsible for the intraband transitions that can be seen as the electron-phonon scattering process [98], whereas the second term (Equation (2.4)) is about the interband electron transitions. The scattering rate Γ can also be expressed as a function of relaxation time τ, by $\Gamma = 1/2\tau$.

It is possible to solve analytically the intraband term which gives :

$$\sigma_{Intra}(w,E_F,\tau,T) = \frac{ie^2E_F}{\pi\hbar^2(w+i/\tau)}\left[1+2\frac{k_BT}{E_F}ln(e^{-E_F/k_BT}+1)\right] \tag{2.5}$$

, where the chemical potential μ has been replaced by the Fermi energy. It is possible to do so when the chemical potential is much higher than k_BT [98]. It is also interesting to note that the intra-band term turns to a Drude like form when $E_F >> k_BT$:

$$\sigma_{intra}(w,E_F,\tau,T) = \frac{ie^2E_F}{\pi\hbar^2(w+i/\tau)} \tag{2.6}$$

However, the interband contribution is more difficult to evaluate analytically. At finite, but low temperature ($E_F,\omega >> k_BT$), several interband contribution part of the conductivity have been proposed. According to [40]:

$$\sigma_{inter}(w,E_F,\tau,T) = \sigma_0\left[\frac{1}{2}+\frac{1}{\pi}arctan\left(\frac{\hbar w-2E_F}{2k_BT}\right)-\frac{i}{2\pi}ln\left(\frac{(\hbar w+2E_F)^2}{(\hbar w-2E_F)^2+4(k_BT)^2}\right)\right] \tag{2.7}$$

with $\sigma_0 = e^2/4\hbar$. According to [84], the electron disorder scattering processes $i\hbar/\tau$ can be added to the second part of the equation to get at any temperature :

$$\sigma_{inter}(w, E_F, \tau, T) = \sigma_0 \left[\frac{1}{2} + \frac{1}{\pi} arctan\left(\frac{\hbar w - 2E_F}{2k_B T} \right) - \frac{i}{2\pi} ln \left(\frac{(\hbar w + 2E_F + i\hbar/\tau)^2}{(\hbar w - 2E_F + i\hbar/\tau)^2 + 2(k_B T)^2} \right) \right] \quad (2.8)$$

According to [24], the inter band term of the optical conductivity in a single layer of graphene can be writen as :

$$\sigma_{inter}(w, E_F, \tau, T) = \frac{\sigma_0}{2} \left[tanh\left(\frac{\hbar w + 2E_F}{4k_B T} \right) + tanh\left(\frac{\hbar w - 2E_F}{4k_B T} \right) - \frac{i}{\pi} ln \left(\frac{(\hbar w + 2E_F)^2}{(\hbar w - 2E_F)^2 + 4(k_B T)^2} \right) \right] \quad (2.9)$$

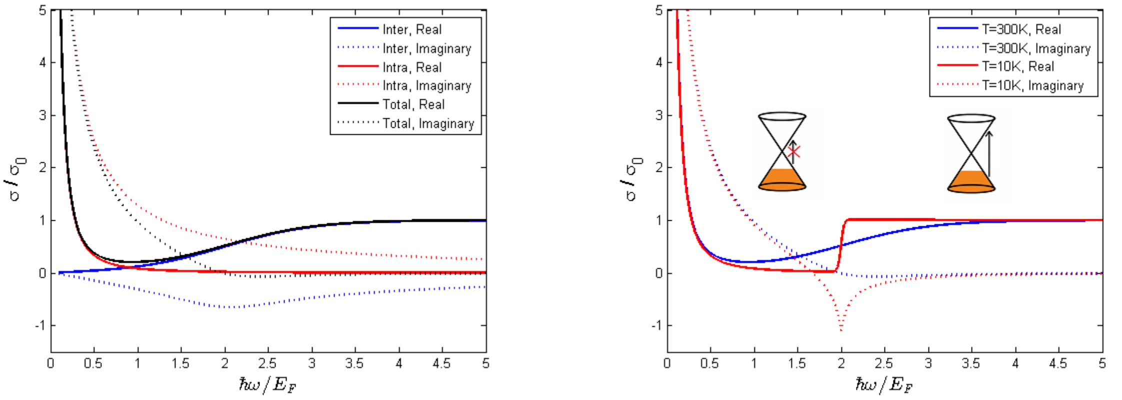

(a) σ/σ_0 of graphene details term by term

(b) σ/σ_0 of graphene for two different temperature

Figure 2.12: Optical conductivity of graphene using the Equations (2.9) and the full intraband term, Equation (2.5) as a function of the pulsation ω. The mobility of graphene (unit $e^2/4\hbar$) is set at $1m^2V^{-1}s^{-1}$.

Plots of the optical conductivity σ/σ_0 is shown Figures 2.12, where σ_{inter} has been taken from Equation (2.9) and σ_{intra} is computed through the Equation (2.5). The conductivity is plotted as a function of the energy of the electromagnetic wave, normalized by the Fermi energy. In Figure 2.12a, the different terms of the conductivity are plotted separately. It is interesting to observe that the intraband terms of the conductivity (in red) approach the total term (in black) when $\hbar\omega << E_F$. Therefore, the intra band term is dominating in the infrared region, while in the near-infrared and the visible regions, the interband term dominates. In figure 2.12b, as expected from Equations (2.7), (2.8), (2.9), the real part of the interband contribution displays a step at $\hbar\omega = 2E_F$, which represents the losses due to the interband excitation of carriers. Two electronic band structures of graphene are shown in inset. The Fermi level is illustrated by the interface between the orange and the white. The black arrow represents the interband transition, not possible for $\hbar\omega < 2E_F$, and possible above the threshold of $2E_F$.

Finally, it is worth speaking about the 3D approach based on a convenient 3D permittivity for graphene. As seen in the Section 1.1.3, Equation (1.51) gives a conversion of the 2D optical conductivity into a 3D electrical permittivity, to represent graphene as a 3D material with a finite thickness. Let's write the optical conductivity of the graphene as a sum of a Real part and an Imaginary part, $\sigma = \sigma_R + i\sigma_I$, which leads to :

$$\epsilon(\omega) = \epsilon_s(w) - \frac{\sigma_I(\omega)}{\omega 2a\epsilon_0} + i\frac{\sigma_R(\omega)}{\omega 2a\epsilon_0} \quad (2.10)$$

It is interesting to notice that the positive imaginary part of the optical conductivity at low frequency (see Figure 2.12b) will give a negative real part of the graphene permittivity when $\epsilon_s(w) - \frac{\sigma_I(\omega)}{\omega 2a\epsilon_0} < 0$. In this case, graphene layer has a metallic behavior and plasmons can be supported. The positive real part of the conductivity corresponds to the imaginary part of the permittivity, which is related to losses experienced by an electromagnetic field. This last term will be determinant for the dissipation losses of surface plasmons in graphene.

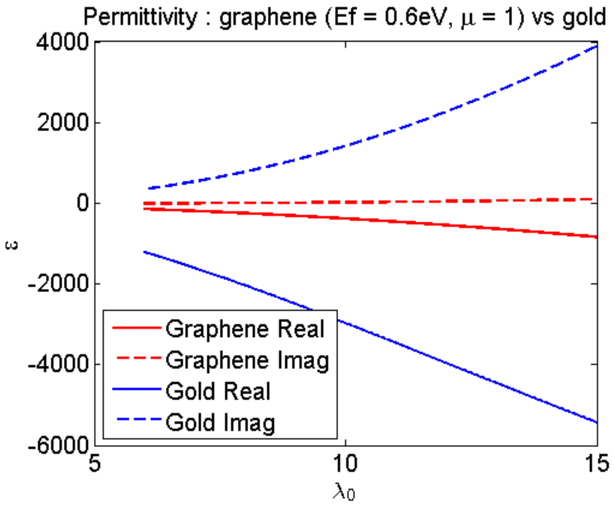

Figure 2.13: Permittivity of graphene ($E_f = 0.6eV, \mu = 1m^2V^{-1}s^{-1}$) compare to Gold in the infrared range, using Equation (1.51) and the Drude-like conductivity Equation (2.6), valid under these conditions (see Section 3.2.1)

Simulations of devices based on graphene plasmonics

Early, the power of graphene local tunability has shown the possibility to create exotic devices. As an exemple, at a p-n junction of graphene layers, it is theoretically possible to get a Veselago lens. This type of lens act like a slab of material with negative refractive index, giving counter intuitive properties. [25]. Therefore, graphene based device could lead to electronic lenses, but also graphene-based transistors. Soon after, the p-n junction applied for graphene plasmonics have been studied [108] and a plasmon transistor has been envisaged.

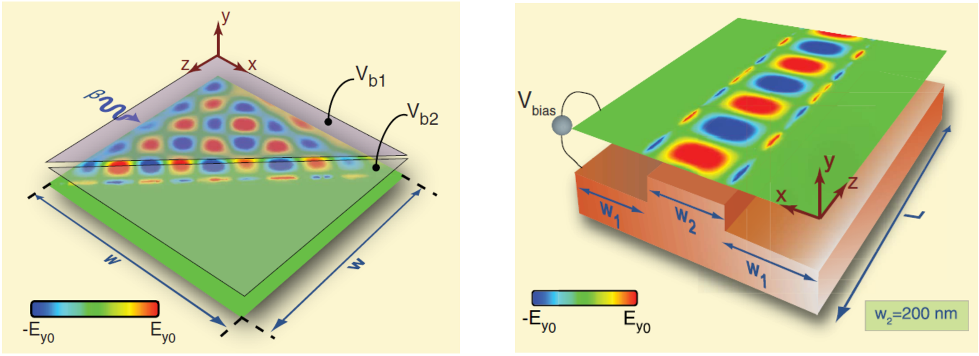

(a) Simulation showing an almost total reflection of plasmons at an interface of two graphene layer with different conductivity.

(b) AFM image of a single layer graphene mechanically exfoliated

Figure 2.14: Two snapshot in time showing the y component of the electric field at low temperature (T=3K) on free standing graphene. From [148]

An interesting study has shown [148] that the local modulation of optical properties in a single layer of suspended graphene could lead to complex photonic function and eventually transfomative optics device (Figures 2.14). It is due to the low-loss plasmonic properties and to its intrinsic two dimensional structure. Playing with local electrostatic potential applied to graphene, they demonstrated total reflection of plasmons (Figure 2.14a) and plasmonics waveguide (Figure 2.14b). From this starting point emerged a lots of new device proposals based on the control of the Fermi level in graphene (electrostatic gatting). Plasmonic switches and transistors [3, 32, 55, 26], light modulators [94, 163, 35, 167], photodetectors [172], ring filters [91, 92], plasmonic lens [149], logic gates [125, 164] and waveguides [124, 86] have been predicted numerically.

In most of the cases cited above, the studies suppose to have an excellent control over the amount of charge carrier located in different part of the layer, by applying electric field. Unfortunately, it remains a big challenge since the electric field needed locally is really important. Therefore, many research groups are working on finding an experimental system that could lead to variation of graphene optical and electronical properties on micrometric scale on demand. In fact, the substrate plays a key role (see section 2.1.2) in order to get optimal eletro-optic properties [57].

2.2.2 Experimental observation of plasmons in graphene

Several techniques enable researchers to access to a direct proof of the existence of plasmons in graphene. The first experimental evidence showing the phenomenon has been performed by Electron Energy Loss Spectroscopy (EELS) [111, 39, 96], where electrons are used to probe the graphene properties. In this method, an incident beam of electrons strikes the carbon sheet. Some of the electrons will transfer a part of their energy, through inelastic scattering, to the graphene plasmons. Their energy will be eventually recorded after the reflection or the transmission through the sample, and an electrons energy loss spectrum is obtained (see Figure 2.15). In graphene, it is known that there are two kinds of valences electrons : the π electrons responsible for the covalent bounds between carbone atoms, and the σ electrons, quasi free, which are creating bounds over p_z orbitals (see Figure 1.11b). Therefore, several types of plasmons may exist [36]:

- The low energy plasmons, usually refereed as 2D plasmons, with energy lower than 3 eV, which is the field of interest of this thesis.
- The high energy plasmons, corresponding to the π (around 4.7 eV) and $\pi + \sigma$ (around 14.6 eV) plasmons.

In Figure 2.15, the signature of two different plasmons can be observed : one of high energy ((b) on the Figure), corresponding to a $\pi + \sigma$ plasmon, and one with lower energy ((a) on the Figure), corresponding to the 2D plasmons [111]. However, 2D plasmons are difficult to probe because they appear with relatively high doping (Fermi level), beeing highly dependent to it. They are also dependent on other parameters like the substrate and the temperatures [98].

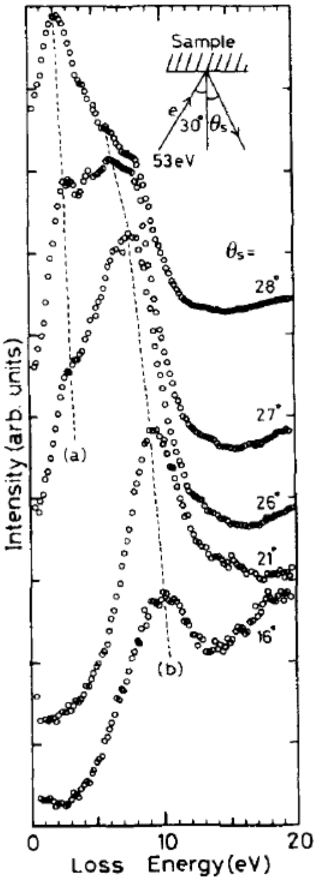

Figure 2.15: Electrons energy loss spectra obtained in 1992 for graphene grown on TiC surface [111]

It is also possible to record plasmonic effects in graphene by confining the carbon sheet in a second dimension, which leads to structures so-called ribbons. As for noble materials, a resonance peak can be observed with an infrared light polarized perpendicularly to the ribbon axis, function of its width. The resonance in graphene ribbons is characteristic of 2D electrons gas (Figure 2.16b). It is worth mentioning that this property is also present at room temperature, compared to other 2D materials [76]. But the most interesting feature in graphene as a plasmonic material is, one more time, the possibility to tune its optical properties, and therefore to tune the absorption peak of the device through electrostatic gating (see Figure

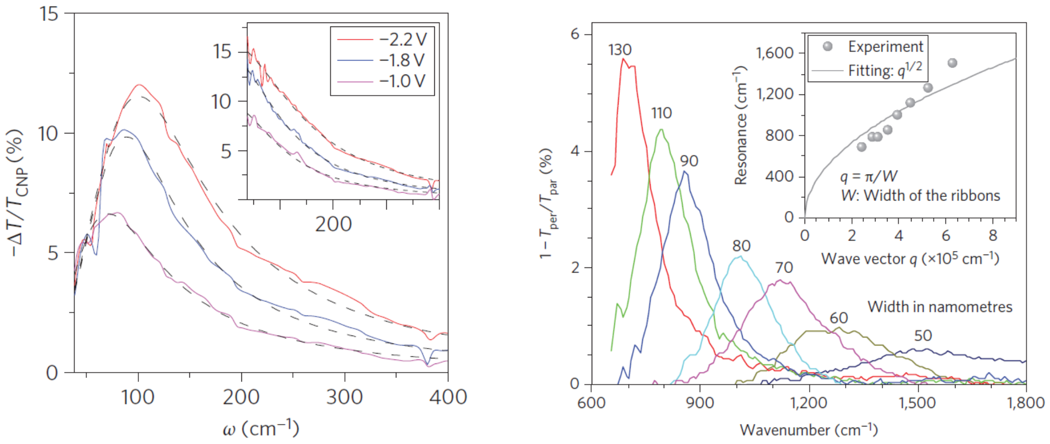

(a) Tuning of the transmission of an array of graphene ribbons on SiO_2 through electrostatic gating [76]. $\Delta T = T - T_{CNP}$ with CNP Charge Neutral Point. Inset the transmission for a parallel polarisation. Ribbons width of $4\mu m$.

(b) Tuning of the transmission of an array of graphene ribbons on SiO_2 varying the width of the ribbons [161].

Figure 2.16: Intrinsic graphene plasmons confined by designing ribbons

2.16a).

Confining the graphene in 3 dimensions gives also interesting results. Micro-disk of graphene+insulators, deposited on quartz for its transparency in the infrared region, have been engineered in order to create plasmonics resonators. Stacks of several layers have been fabricated enhancing the plasmonics resonance frequency and magnitude, and far-infrared notch filters as well as polarisers are demonstrated [160].

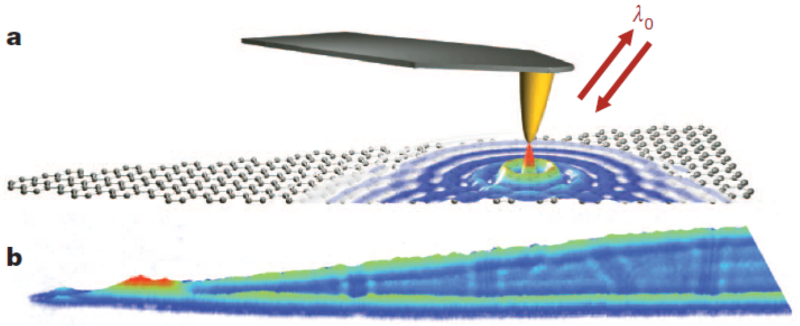

Figure 2.17: Illustration of the experimental configuration describing the SNOM tips launching and detecting simultaneously the Graphene plasmon in (a), and the obtained near field amplitude on graphene nanoribbon on top of 6H-SiC. [29]

In 2012, two papers [42, 29] have been published simultaneously describing the first real-space imaging of surface plasmons propagating on a substrate Si/SiO_2 for the first one (Fig 2.18a), and on graphene nanoribbon on the top of 6H-SiC substrate for the second (Fig 2.17). It has been a challenge to record the signature of such a wave because of its nonradiative nature. In order to visualize those evanescent waves, a Scanning Near-field Optical Microscope has been used (SNOM, Fig. 2.17) in the infrared region.

An infrared beam is focused on an Atomic Force Microscope (AFM) metal tip (apertureless). The tip scatters the light and a fraction of the resulting angular spectrum will excite a plasmon in graphene with the correct wave-vector. The plasmon will propagate in the 2D sheet of carbone and be reflected by a grain boundary, or graphene edge (Figure 2.18b). This reflected plasmon will interfere with the incoming one, resulting in an interference pattern, creating a standing wave, (Figure 2.18a). It is possible to extract from the standing wave the effective wavelength of the graphene plasmons, which agree with the theory to be much smaller than the excitation one. These two papers are the starting point of nano-imaging of plasmons in graphene by SNOM technique.

Following the previous studies, in 2013, a study [43] demonstrates that the SNOM technique is able to highlight the grain boundary (Figure 2.18b) in CVD graphene, and could be applied in order to characterize graphene cristallinity. The key point here is that the grain boundaries, that were challenging to image, are scattering centers that obstruct the electronic transport as well as the plasmon propagation. In the meanwhile [30], nano-defects in graphene on silicon carbide have been revealed by the same technique and surface roughness of the substrate such as SiC terraces have been studied. It is shown that plasmons in graphene are highly disturbed by substrate and substrate discontinuities.

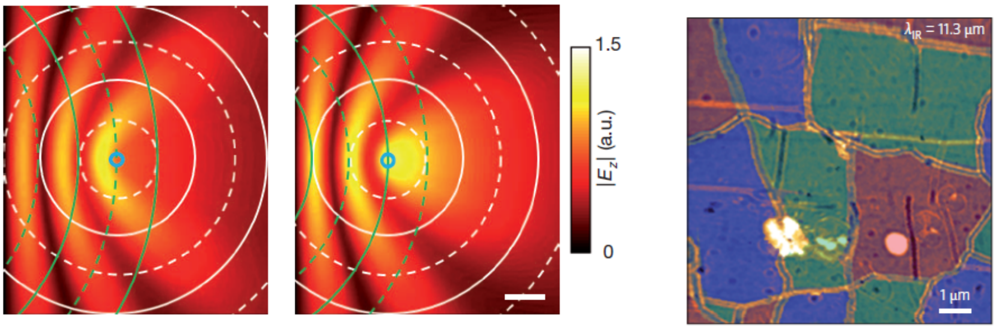

(a) Image of the interference occurring between the tip-launched plasmon (in green) and the edge reflected plasmon (in white), creating the standing waves. [42]

(b) Mapping of grain in a single layer graphene through the interferences created by the grain boundary and/or grain overlap under SNOM tips [43]

Figure 2.18: Interferometric image of graphene layer using SNOM technique at graphene edges and grain boundary

The next step was the development of h-BN/graphene structure, predicted to be one of the best platform for optimizing transport properties of graphene [19, 174]. Low plasmons damping as well as high confinement have been shown [153]. Intriguing behaviour of this heterostructure have been studied [34] showing hybrid plasmons-phonons polariton phenomenon with low losses. The properties of infrared plasmons have been shown by pump-probe technique [114]. It must be underlined that the high quality of such structure is able to sustain high propagation of plasmons, which can be switched by electrostatic gating.

2.3 Properties of Graphene Plasmons

It is interesting to notice two things when speaking about plasmons in graphene. They show a lot of similarities with the surface plasmons at an interface between a dielectric and a metal (see section 1.2.1). However, two properties of the system imply different characteristics of plasmon in graphene. The first one is that electrons are frozen perpendicular to the surface, and the second is about the dispersion relation of electrons in graphene (see Section 1.3.2), as compared to the parabolic one in metals [70]. Those two major differences lead to different dispersion relations in between those two systems, that will be studied below.

This study aims to focus on longitudinal modes, where the electric field associated with the plasmons are in the plane, parallel to the wave vector. Those modes are known as Transverse Magnetic modes. They appear at a frequency below the Pauli-blocking energy. A transverse electric mode of plasmon exists also in graphene, where a collective oscillation of electrons transverse to the graphene plane can be found [15]. However, the dispersion curve of those modes seems to be too close to the one of the light.

As a results, on the energy confinement point of view, it seems less interesting than the TM modes are[70].

In 2007, it has been proposed several ways to study the transverse electric and magnetic plasmonic modes on graphene. [66, 106]. In the following sections two semi-classical approaches will be proposed in order to get the dispersion relation of plasmon in graphene. One is based on a volume approach, and the other one consists of a surface approach. Then the different parameters that matter in the propagation of graphene plasmons will be analysed.

2.3.1 Dispersion relation by the volume approach

In this section, graphene will be considered as a material with a finite thickness. Therefore, graphene will be described as an extremely thin metallic slab with a complex permittivity ϵ_m. The results that have been found in section 1.2.2 will be extensively used, where the system can be described as a multilayer and graphene is embedded in a dielectric media with dielectric permitivity ϵ_d. Graphene being a material which is one-carbone atom thick, the thickness $\Delta = 2a$ can be approximated as tending towards 0. Introducing Equation (1.87) and using a finite expansion of $tanh$ when z tends to 0, $tanh(z) = z + o(z^2)$, it is possible to write :

$$tanh(a\sqrt{k_p^2 - \epsilon_m k_0^2}) = -\frac{\epsilon_d \sqrt{k_p^2 - \epsilon_m k_0^2}}{\epsilon_m \sqrt{k_p^2 - \epsilon_d k_0^2}} \approx a\sqrt{k_p^2 - \epsilon_m k_0^2} \tag{2.11}$$

$$-\frac{\epsilon_d}{a\epsilon_m} \approx \sqrt{k_p^2 - \epsilon_d k_0^2} \tag{2.12}$$

$$k_p^2 \approx \epsilon_d k_0^2 + \frac{\epsilon_d^2}{a^2 \epsilon_m^2} \tag{2.13}$$

In order to further simplify this equation, let's suppose that the graphene sheet is suspended, and therefore $\epsilon_d = 1$. Let's insert Equation (1.52), in the last equation to find :

$$k_p^2 \approx k_0^2 + \frac{1}{a^2} \frac{(\epsilon_0 w 2a)^2}{(\epsilon_0 w 2a)^2 - \sigma_{2D}^2 + 2iw2a\epsilon_0 \sigma_{2D}} \tag{2.14}$$

In the vanishing thickness limit, we finally get :

$$k_p^2 \approx k_0^2 - \left(\frac{2\epsilon_0 w}{\sigma_{2D}}\right)^2 \tag{2.15}$$

$$k_p \approx k_0 \sqrt{1 - \left(\frac{2\epsilon_0 w}{k_0 \sigma_{2D}}\right)^2} \tag{2.16}$$

Knowing that $k_0 = w/c$ and inserting the impedance of the surrounding medium $\eta = \sqrt{\mu_0/\epsilon_0}$, it leads to :

$$k_p \approx k_0 \sqrt{1 - \left(\frac{2}{\eta \sigma_{2D}}\right)^2} \tag{2.17}$$

In section 3, an introduction to the simulation of material-light interaction will be given. In order to study graphene via numerical tools, a material model is needed. As a first approach, the results obtained above has been implemented in Lumerical FDTD software, where graphene was treated as a 3D material (3D permittivity, Equation (2.10)), with finite thickness. However, the meshing required is very small compare to the infrared wavelength, and some aberration may occur (see Section 3.2.2). Therefore, a second model had been developped, with graphene seen as a 2D material, defined by its 2D conductivity. This second approach is demonstrated hereafter.

2.3.2 Dispersion relation by the surface approach

Another way to get the dispersion relation of plasmons in graphene is to describe the system as an interface of two dieletric media, with a free current laying in between. Therefore, the same method as in Section 1.2.1 will be used. The same TM mode, using Equations (1.53), will be considered. The boundary conditions on the electric field lead to $\mathbf{E_{x1}} = \mathbf{E_{x2}} = \mathbf{E_x}$ and $k_{x1} = k_{x2} = k_p$. Let's take Equation (1.61) and apply it in the two media, which leads in media 1:

$$\frac{E_x w \epsilon_0 \epsilon_1}{k_{z1}} = -H_{y1} \tag{2.18}$$

and in media 2:

$$\frac{E_x w \epsilon_0 \epsilon_2}{k_{z2}} = H_{y2} \tag{2.19}$$

Combining with Equation (1.23), the boundary equation for $\mathbf{H_x}$ in the case of surface current, it becomes :

$$E_x w \epsilon_0 \left(\frac{\epsilon_2}{k_{z2}} + \frac{\epsilon_1}{k_{z1}} \right) = H_{y2} - H_{y1} = -\sigma E_x \tag{2.20}$$

And the dispersion relation is finally obtained for TM mode:

$$\frac{\epsilon_2}{k_{z2}} + \frac{\epsilon_1}{k_{z1}} = -\frac{\sigma}{w \epsilon_0} \tag{2.21}$$

It has been seen previously that k_{z_i} should be pure imaginary. It is therefore possible to replace it as $k_{z_i} = i q_{z_i}$ with q_{z_i} real positive and $q_{z_i} = \sqrt{k_p^2 - \epsilon_i k_0^2}$. The dispersion relation is revealed in its most known form :

$$\frac{\epsilon_2}{\sqrt{k_p^2 - \epsilon_2 k_0^2}} + \frac{\epsilon_1}{\sqrt{k_p^2 - \epsilon_1 k_0^2}} = -\frac{i\sigma}{w \epsilon_0} \tag{2.22}$$

If graphene is sandwiched in air, $\epsilon_1 = \epsilon_2 = 1$, the dispersion relation of plasmons in graphene seen in Equation (2.15) can be found easily.

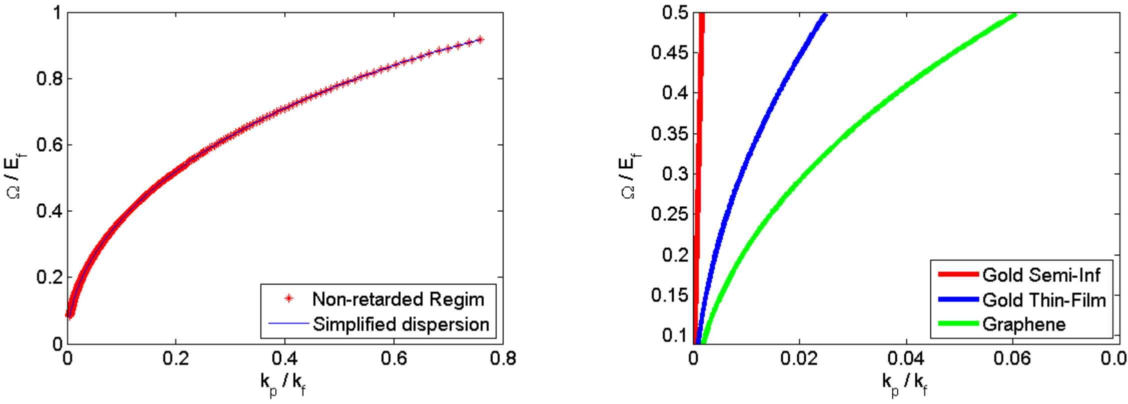

(a) Plot of the full dispersion relation of graphene plasmons (Equation (2.22)) Vs the non-retarded approximation for graphene (Equation (2.23))

(b) Plot of the dispersion relation of plasmons for a single interface Gold/air (in red, Equation (1.63)), for a thin film of gold (1nm) sandwiched in air (in blue, Equation (1.87)) and graphene sandwiched in air (in green, Equation (2.23)). Frequency is taken from 8.3 microns to 50 microns. Gold is set as a Drude metal with $\omega_p = 2,15.10^{15} Hz$ and $\Gamma = 17,14.10^{12} Hz$

Figure 2.19: Dispersion relation of graphene plasmons without and with non-retarded approximation, and comparison with Gold. The substrate is set as a pure dielectric with $\epsilon = 5$. Graphene is set with $E_F = 0.3eV$ and a mobility of $\mu = 1 m^2 V^{-1} s^{-1}$.

2.3.3 Graphene plasmons propagation and damping rate

Considering a non retarded regime, in the case where $k_p >> k_0$, Equation (2.22) can be simplified:

$$k_p \approx \frac{i\omega\epsilon_0}{\sigma}(\epsilon_1 + \epsilon_2) \tag{2.23}$$

This approximation validity is demonstrated in Figure 2.19a. As an example, the plasmonic dispersion relation of a sheet of graphene with a Fermi level $E_F = 0.3eV$ and a mobility of $\mu = 1m^2V^{-1}s^{-1}$ is computed using the full Equation (2.22), and the simplified Equation (2.23). As we can see, the two curves fit really well and we can safely use the simplified equation (2.23). The next step is to plug in this equation the optical conductivity (seen Section 2.2.1). Let's start with a graphene which is highly doped, $E_F >> k_bT$ and an excitation energy below the optical phonon in graphene, $\hbar\omega \approx 0.2eV$. We can therefore use the Drude-like expression of the conductivity, Equation (2.6), and we find:

$$k_p = \frac{1}{\lambda_0}\frac{\pi\hbar}{2\alpha\tau E_F}(\epsilon_1 + \epsilon_2)(\omega\tau + i) \tag{2.24}$$

Therefore, using Equation (1.130) ($E_F = \hbar v_F k_F$), we obtain finally:

$$\frac{\hbar\omega}{E_F} = \sqrt{\frac{c}{v_F}\frac{4\alpha}{(\epsilon_1 + \epsilon_2)(1 + \frac{i}{\omega\tau})}\frac{k_p}{k_F}} \tag{2.25}$$

, where $\alpha = e^2/4\pi\epsilon_0\hbar c \approx 1/137$ is the fine structure constant. Figure 2.19b shows a comparison between graphene plasmons dispersion relation and gold plasmon relation dispersion. The graphene is free standing (sandwiched in air); it is represented in green in Figure 2.19b. Two cases have been taken into account for gold. The red curve corresponds to a semi infinite system, where surface plasmons take place at an interface between gold and air. The second case, in blue, is a free-standing thin film of gold of 1-nm thickness (sandwiched in air). Comparing dispersion relation of graphene with gold, we can observe that GPs wavevectors k_p are generally much higher in graphene than for the gold, which means that we have a higher spatial confinement.

Dispersion relation of GPs is also calculated via the Random Phase Approximation (RPA) model. This model comes from the wish of researchers to introduce in the theory quantum mechanical interactions between the electrons. It takes into account the weak screening Coulomb interaction, so the electrons are driven by a total potential summing the external potential and the coulomb potential. Several groups [66, 159] worked on doped graphene at 0 temperature in order to get the dielectric function of graphene as a function of q and ω. The graphene plasmons are derived directly from it (Figure 2.20). For small values of q, the dispersion relation $w_{sp}(q)$ is proportional to $\sqrt{q}$ and remains really close to the semi-classical model. But for finite values, it is really interesting to notice that the square roots behaviour vanishes. Instead, the dispersion relation converges to the boundary line between the two SPE region (section 1.3.3, Figure 1.17) without entering in the intraband SPE zone. In any cases, in the mid-infrared region, the dispersion relation lies in the weakly damped area and therefore can theoretically propagate on long distance. Some high-resolution electron energy-loss spectroscopy are fitted well by the RPA theory [139], but the approximation of infinite electron relaxation time coupled with the complicated case of graphene plasmon limits the scope of this model [98].

As it has been seen in Section 1.2.1, the wavelength of the plasmon in the graphene can be obtained using Equation (1.67). It is also possible to get the propagation distance with the Equation (1.66), as well as the penetration depth (Equation (1.68)) of the field in the dielectric medium. All this physical quantities can be derived from the real and the imaginary parts of the wave vector k_p (see Equation (2.24)). Let's take into consideration the case of a graphene layer sandwiched in between a dielectric and the air. Therefore, we can define $\epsilon_1 = \epsilon_{sub} = \epsilon' + i\epsilon''$ and $\epsilon_2 = \epsilon_{air} = 1$. The wavelength of the plasmons λ_p^{sup} can be therefore established, as well as its propagation distance L_p^{sup} and the penetration depth for supported graphene as follow :

$$\lambda_p^{sup} = \lambda_0 \frac{4\alpha\tau E_F}{\hbar((\epsilon' + 1)\omega\tau - \epsilon'')} \tag{2.26}$$

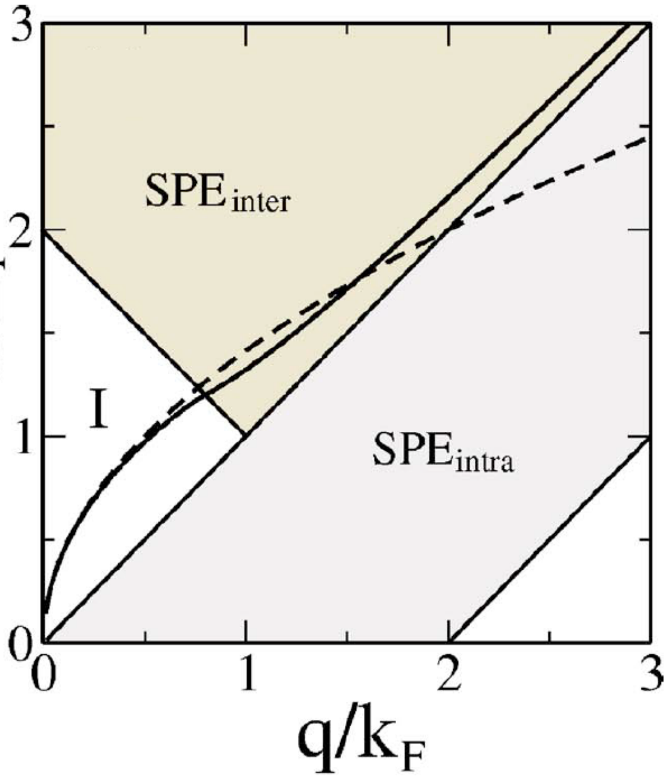

Figure 2.20: Dispersion relation of graphene plasmon calculated by RPA (solid line), and by the classical model (dashed line). The graphene is lying on SiO2 substrate. The two kind of SPE zone are drawn in background (see Figure 1.17)

$$L_p^{sup} = \lambda_0 \frac{\tau\alpha E_F}{\pi\hbar(\epsilon' + 1 + \epsilon''\omega\tau)} \tag{2.27}$$

$$\delta_p^{sup} = \frac{1}{Re(k_p)} = \frac{\lambda_p^{sup}}{2\pi} \tag{2.28}$$

From Equation (2.27), it is interesting to notice that the propagation of plasmons in graphene depend on three main factors. The first one is the lifetime of the plasmons τ_{pl}, which is a phenomenology parameter. This factor takes into account mechanism of scattering in graphene seen section 2.1.2. The second interesting parameter is the Fermi energy. The Fermi energy in graphene vary with the process of fabrication and transfer of graphene, but can also be tuned electrostatically. The third parameter is the permittivity of the dielectric medium surrounding graphene. The propagation distance of plasmons in graphene being inversely proportional to those dielectric permittivity, it is interesting to work with substrate having really low permittivity. For example, working in a configuration of suspended graphene, the Equations (2.26) and (2.27) become :

$$\lambda_p^{susp} = \lambda_0^2 \frac{\alpha}{\hbar\pi c} E_F \tag{2.29}$$

$$L_p^{susp} = \lambda_0 \frac{\tau\alpha E_F}{2\pi\hbar} \tag{2.30}$$

It is interesting to notice that the plasmons wavelength in suspended graphene is a direct measurement of the Fermi level in this graphene sheet. An other interesting parameter is the quality factor, also called figure-of-merits, which is usually used to compare a phenomenon applied to different materials [151]. It takes into account the complex permittivity of a substrate at differents wavelength. The imaginary part of the permittivity is responsible for the loss, and the real part of the permittivity is describing the distribution of the field in a material. The inverse of this physical quantity is more common in graphene

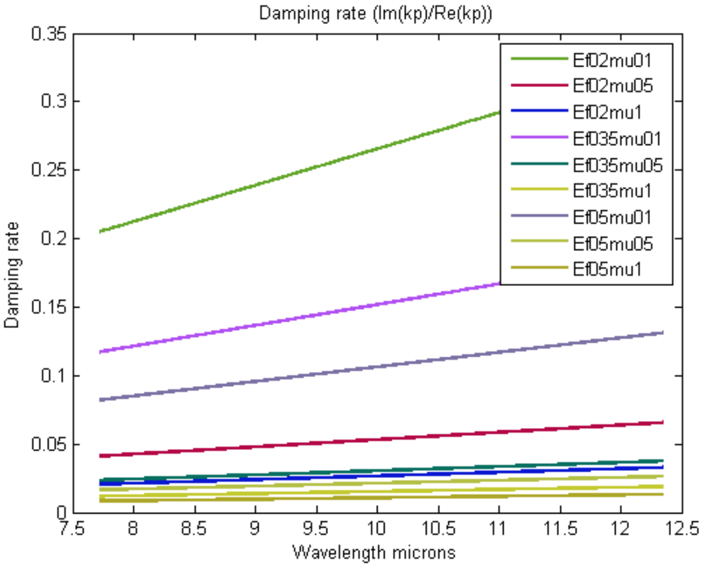

Figure 2.21: Plot of the damping rate of graphene plasmons for suspended monolayer graphene

plasmonics field [42] and it is called the damping rate, or propagation loss. Let's take the general case of a monolayer sheet of carbon deposited on a substrate. Therefore, we can define $\epsilon_1 = \epsilon_{sub} = \epsilon' + i\epsilon''$ and $\epsilon_2 = \epsilon_{air} = 1$. The damping rate can be written as :

$$\gamma = \frac{Im(k_p)}{Re(k_p)} = \frac{\epsilon' + 1 + \epsilon''\omega\tau}{(\epsilon' + 1)\omega\tau - \epsilon''} \approx \frac{1}{\omega\tau} + \frac{\epsilon''}{\epsilon' + 1} \tag{2.31}$$

The last approximation made on the right side of the equation above is true as long as we remain far enough from the intrinsic phonon of the substrate. In the case of suspended graphene, $\epsilon' = 1$ and $\epsilon'' = 0$ and it is possible to plot the damping rate for graphene plasmons in the range of interest. Figure 2.21 shows the damping rate of graphene plasmons as a function of the wavelength in the mid-infrared range. The lifetime τ is set as a approximation as the DC relaxation time of electrons (see Section 2.1.2). The different curves correspond to different Fermi level and different mobility. As expected, higher is the mobility/Fermi level, and lower is the damping rate. From this Figure, it is possible to see that the damping rate is increasing as the wavelength does (as long as the wavelength is above the intrinsic phonon in plasmons, around 6.5 μm). However, for high quality of graphene and high doping, the plasmons loss is less and less dependant of the wavelength.

Taking the case of graphene deposited on a SiO_2/Si wafer(Optical constant from Palik Handbook, Figure 2.22a), we can plot the damping rate in the same range, Figure 2.22b. Here again the graphene parameter such as the Fermi level and the mobility have been varied. Figure 2.22b shows a minimum around 11 μm, which correspond to the litterature [42].

However, the values obtained here, are relatively low compared to the literature review. As mention in the papers [42, 43], it is probably due to a many-body interaction at the edge and grain boundary of the graphene sheet, where other scattering mechanisms (electrons-electrons) take place.

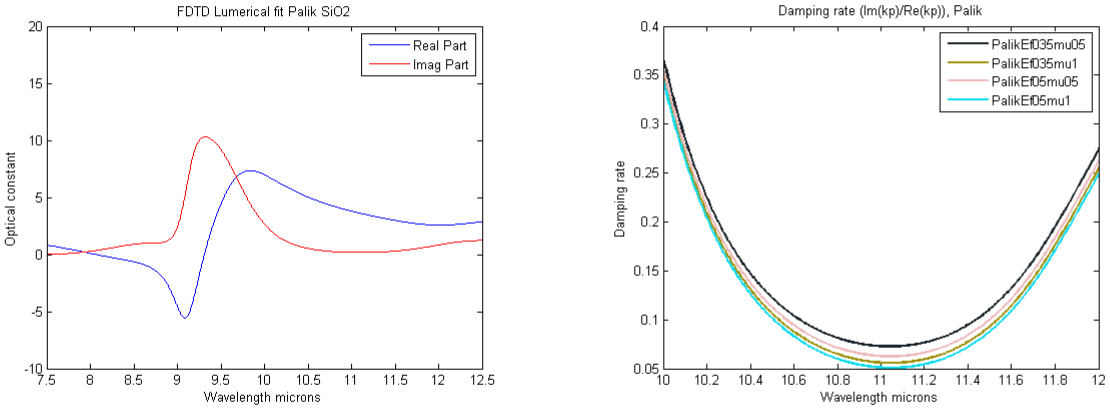

(a) Permittivity of SiO_2 substrate using Palik Handbook.

(b) Zoom on the minimum of the damping rate

Figure 2.22: Damping rate of graphene plasmons for suported graphene

2.4 Aim of this study

The initial aim of this study is to lay the foundations of plasmon propagation for the development of future graphene-based optoelectronic devices. Ideally, graphene plasmons in the infrared suffer low metallic losses as compared to noble metals. This is due to its excellent electronic properties. However, substrate implies impurities and defects that affect the transport properties of graphene. Also, the use of a substrate induces a strong damping due to a high optical energy dissipation. In this context, suspended graphene appears to be a promising route for the design of future opto-electronic devices.

The scope of this work is the study of plasmons in free standing graphene. Free standing graphene enable to get rid of the interaction of graphene charges with the substrate. Under special condition, graphene plasmons could reach interesting propagation length. Therefore, a numerical study is detailed in the chapter 3. In the chapter 4, experimental results are presented. The fabrication of samples, the characterizations as well as optical measurements are introduced in the chapter 4. The optical measurement are performed with an home made Scanning Near-field Optical Microscope (SNOM) in the infrared range.

Chapter 3

FDTD Simulation of the propagation of plasmons in suspended graphene

The work of a researcher is to undertake creative investigation on a systemic, organized basis. Therefore, numerical tools have been developed to help scientists to predict interesting roads to explore, before experimental demonstrations. The finite-difference time-domain (FDTD) method is a numerical analysis technique which gives to the community of optics the possibility to simulate various interaction between light and matter. Surface Plasmons excitation is one phenomenon taking place in the scope of those interactions, appearing theoretically after rearranging Maxwell's equations. These equations are the basis of the FDTD method, which aims to solve them in discretized space and time. Therefore, plasmons can be computed and study through this numerical method.

First of all, the basic idea of the FDTD method will be introduced briefly. Then, the modelization of graphene through FDTD will be discussed. Finally, the case of the plasmons propagation in suspended graphene will be detailed: at first, the use of an in plane nano-antenna for Graphene Plasmons (GPs) excitation will be investigated. Then, a system taking into account the constrain induced by the goal of a long propagation is designed. Finally, some critical remarks are addressed.

3.1 Basic idea of the Finite-Difference Time-Domain (FDTD)

FDTD method is based on an algorithm proposed by Kane Yee, who used second-order central difference [146]. The key steps of the algorithm are summarized in the following, with some references to the 1D case that will be developed subsequently.

1. Replace all the time and space derivatives of the Ampère (Equation (1.3)) and Faraday laws (Equation (1.4)) by finite differences (see Equation (3.2)). Doing so, the space and time are discretized and the electric and magnetic fields are staggered in the four dimensions.

2. Solve the different equations (Equation (3.1)), using second-order central differences (Equations (3.6) and (3.5)), and express the future unknown fields in terms of known past fields (Equation (3.7)).

3. Evaluate the magnetic fields one time-step into the future so they are now known (effectively they become past fields).

4. Evaluate the electric fields one time-step into the future so they are now known (effectively they become past fields).

5. Repeat the previous two steps until the fields have been obtained over the desired duration.

Let's have a more detailed look at the simplest case : the one dimension case.

3.1.1 1-D FDTD

From the Maxwell's equations, the wave equation for electromagnetic waves can be obtained (Equation (1.8)). To simplify, the wave equation in free space with no current and source can be expressed in 1D as follow:

$$\frac{\partial^2 u}{\partial x^2} - \frac{1}{v^2}\frac{\partial^2 u}{\partial t^2} = 0 \tag{3.1}$$

with u as a scalar field to be described. A gaussian wave can be seen as a possible solution. Let's assume this wave propagating from left to right (increasing x), so it is possible to draw the following schema (Figure 3.1). It represents snapshots of the field at different time steps t_n and position x_i, where i and n are intergers. $x_i \equiv i\Delta x$ is defined to dicretize the space and $t_n \equiv n\Delta t$ is defined for the time.

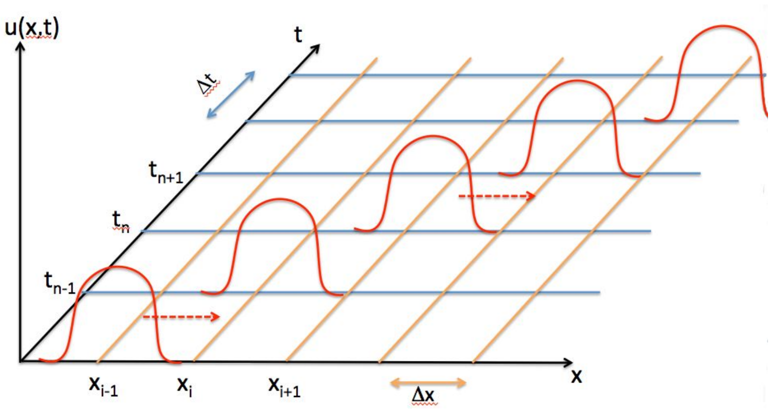

Figure 3.1: Skecth of the discretization in time and space of a gaussian wave propagating towards the right

Then, the new wave equation taking into account these discrete variables is written as :

$$\left.\frac{\partial^2 u}{\partial x^2}\right|_{x_i}^{t_n} - \frac{1}{v^2}\left.\frac{\partial^2 u}{\partial t^2}\right|_{x_i}^{t_n} = 0 \tag{3.2}$$

Let's freeze the time. Taylor series expansion on the term $u_{x_{i+1}}^{t_n} \equiv u_{i+1}^n$ can be written as :

$$u_{i+1}^n = u_i^n + \Delta x \left.\frac{\partial u}{\partial x}\right|_{x_i}^{t_n} + \frac{(\Delta x)^2}{2!}\left.\frac{\partial^2 u}{\partial x^2}\right|_{x_i}^{t_n} + \frac{(\Delta x)^3}{3!}\left.\frac{\partial^3 u}{\partial x^3}\right|_{x_i}^{t_n} + \frac{(\Delta x)^4}{4!}\left.\frac{\partial^4 u}{\partial x^4}\right|_{x_i}^{t_n} + ... \tag{3.3}$$

From the space-step $i-1$ to the step i, Equation 3.3 becomes :

$$u_{i-1}^n = u_i^n - \Delta x \left.\frac{\partial u}{\partial x}\right|_{x_i}^{t_n} + \frac{(\Delta x)^2}{2!}\left.\frac{\partial^2 u}{\partial x^2}\right|_{x_i}^{t_n} - \frac{(\Delta x)^3}{3!}\left.\frac{\partial^3 u}{\partial x^3}\right|_{x_i}^{t_n} + \frac{(\Delta x)^4}{4!}\left.\frac{\partial^4 u}{\partial x^4}\right|_{x_i}^{t_n} - ... \tag{3.4}$$

Adding Equations (3.3) and (3.4) gives :

$$\left.\frac{\partial^2 u}{\partial x^2}\right|_{x_i}^{t_n} = \frac{u_{i+1}^n - 2u_i^n + u_{i-1}^n}{\Delta x^2} + \mathcal{O}(\Delta x^2) \tag{3.5}$$

The same method can be used to get the partial derivative in time :

$$\left.\frac{\partial^2 u}{\partial t^2}\right|_{x_i}^{t_n} = \frac{u_i^{n+1} - 2u_i^n + u_i^{n-1}}{\Delta t^2} + \mathcal{O}(\Delta t^2) \tag{3.6}$$

Substituting Equations (3.5) and (3.6) to Equation (3.2) leads to:

$$u_i^{n+1} \backsimeq \left(\frac{v\Delta t}{\Delta x}\right)^2 (u_{i+1}^n - 2u_i^n + u_{i-1}^n) + 2u_i^n - u_i^{n-1} \tag{3.7}$$

Equation (3.7) is said to be fully explicit. On the right side of the equation, all the fields values are at the time step n or $n-1$, therefore already computed because referring to the present and to the past time steps respectively. On the left side, however, the value of the field corresponds to the future, at the time t_{n+1}. The full explicit equation enables to compute the future value of the field from the previous value, already stored in the computer (at the current time step n and the past step time n-1).

Numerical dispersion relation In order to have an idea about the numerical accuracy of FDTD, the Maxwell dispersion relation (Equation (3.1)) can be pluged in. Let's write the field as a plane wave:

$$u_i^n = U_0 e^{j(wt_n - kx_i)} \tag{3.8}$$

with $t_n = n\Delta t$ and $x_i = i\Delta x$. Substituting this to the Equation (3.7), and simplifying with the common factor $U_0 e^{j(wn\Delta t - ki\Delta x)}$, it becomes :

$$e^{jw\Delta t} = \left(\frac{v\Delta t}{\Delta x}\right)^2 (e^{-jk\Delta x} - 2 + e^{jk\Delta x}) + 2 - e^{-jw\Delta t} \tag{3.9}$$

It can be also written as :

$$\frac{e^{jw\Delta t} + e^{-jw\Delta t}}{2} - 1 = \left(\frac{v\Delta t}{\Delta x}\right)^2 \left(\frac{e^{jk\Delta x} + e^{-jk\Delta x}}{2} - 1\right) \tag{3.10}$$

Recognizing the Euler's identity, the so-called numerical dispersion relation appears as :

$$\cos(w\Delta t) - 1 = \left(\frac{v\Delta t}{\Delta x}\right)^2 (\cos(k\Delta x) - 1) \tag{3.11}$$

Two cases have to be considered:

First case : if $\left(\frac{v\Delta t}{\Delta x}\right) \to 1$, Equation (3.11) becomes $\cos(w\Delta t) = \cos(k\Delta x)$ and finally the exact dispersion relation $w = kv$ will be approached. Unfortunately, it is only occurring in 1-D, but it is not the case in 2D and 3D [146]. Let's therefore look at the second case.

Second case : if $\Delta t \to 0$ and $\Delta x \to 0$ Using the Taylor series for cosine expressed as $\cos(x) = 1 - \frac{x^2}{2!} + \mathcal{O}(x^3)$, Equation (3.11) tends to the exact dispersion relation $w = kv$. The discrete dispersion relation in time and space converges to the exact analytical solution for $\Delta t \to 0$ and $\Delta x \to 0$, which is intuitively what is expected.

Numerical accuracy in FDTD Two numerical factors are defined. They have to be considered in order to avoid numerical errors and aberrations, which are :

$$S \equiv v\frac{\Delta t}{\Delta x} \quad \text{and} \quad N_\lambda \equiv \frac{\lambda}{\Delta x} \tag{3.12}$$

The first one is the FDTD stability factor, or Courant number. It plays a role in determining the stability of the simulation. In fact, let's assume that the simulation takes place in the vacuum. Therefore, v=c, with c the speed of the light. For one time step Δt, a Gaussian pulse (Figure 3.1) will therefore travel over length $L = c \times \Delta t = S\Delta x$. If $S > 1$, the pulse will propagate to more than one spatial step. Therefore, Equation (3.7) which takes into account the first neighbour cells, would not solve the future field accurately. In fact, it produces unstable results and numerical errors. According to [146], when the Courant number is all but 1, the FDTD grid is dispersive, which means that different frequencies travel at different speeds. In practice, the dispersive effect is something to avoid.

The second one is the grid sampling density in the case of free space. According to [2], in order to keep reasonable errors, the size of Δx should be 10 times smaller than the wavelength. Here, it is important to notice that the wavelength of graphene plasmons can be more than 100 times smaller than the excitation in free space [70]. Therefore, the meshing size should be at least 1000 times smaller than the excitation. This leads to extremely small meshing, huge computation resources and possible numerical aberrations (see Section 3.2.2).

Let's come back to the dispersion relation found above. It is possible to re-write the numerical dispersion relation, Equation (3.11), with the two numerical factors introduced above (Equation (3.12)), as follow :

$$k = \frac{N_\lambda}{\lambda} cos^{-1}\left(1 + \frac{1}{S^2}\left(cos\left(\frac{2\pi S}{N_\lambda}\right) - 1\right)\right) \tag{3.13}$$

It is interesting to notice that we recover the exact wave-number when S=1. More detailed examples and analysis for different value of S and N_λ can be found in the literature [146], which shows percentages errors and non-physical behavior of waves using not appropriated values of these two parameters. In practice, we will play with these two parameters to minimize the time of simulations whereas converging to a solution which agrees with the theory.

3.1.2 FDTD in 3 dimensions

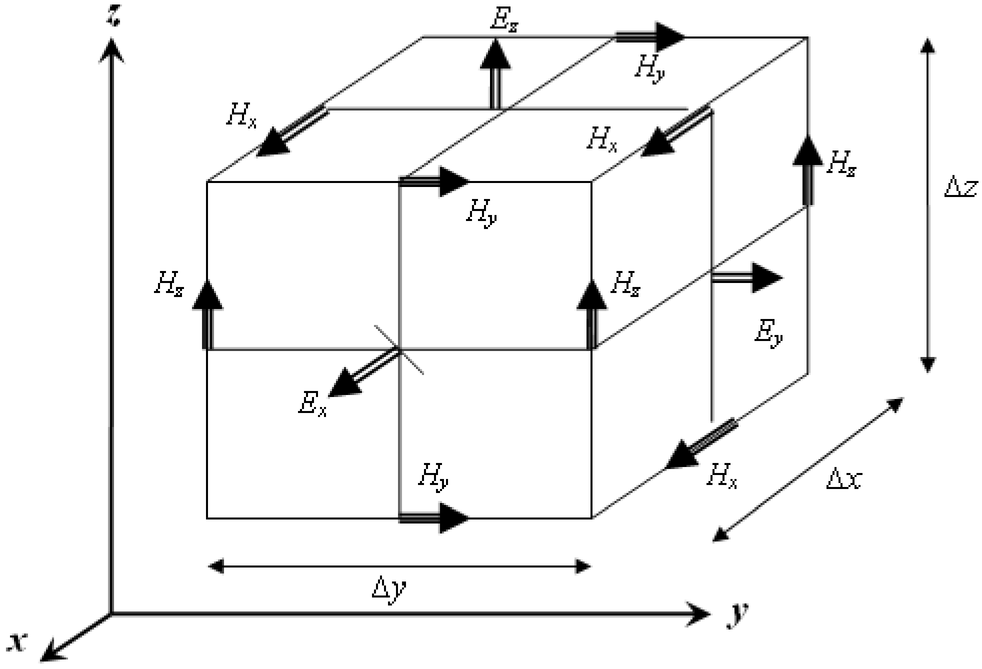

Figure 3.2: Yee cell with the representation of the different component of the **E** and **H** field

In 3 dimensions, the FDTD technique, which is a time-domain method, solves the Maxwell's curl equations (Equations (1.3) and (1.4)) in a discretised space. This gives rise to a set of 6 scalar equations for 6 vector field components, $\mathbf{E_x}$, $\mathbf{E_y}$, $\mathbf{E_z}$, $\mathbf{H_x}$, $\mathbf{H_y}$, $\mathbf{H_z}$, that are computed within a Yee cell. The Yee cell, from the name of its inventor, is a staggered and uncollocated grid, which means that **E** and **H** are not sampled on the same location, and each 3 vectorial components of the two fields are not computed on the same location, respectively.

In 40 years of existence, many other meshing structures have been proposed, but none of them has been able to replace it. Some of the reasons are enumerated subsequently. At first, the Yee algorithm solves simultaneously the electric field and the magnetic field, rather than solving only one of them through the wave equation (Equation (3.7)). Therefore, it makes the computation more robust and enlarges the field of possible simulations, including singularities near edges and corners.

Secondly, the E-fields and H-fields components are placed particularly, such that each E-field component is surrounded by four circulating H-field components, and inversely. This makes easier to maintain the boundary conditions (see section 1.1.2, Figure 1.2), where the Faraday's law and the Ampère's law are interlinked. The only requirement is to set the optical properties of the different materials at an interface. The interface will be set parallel to a Yee cell face. Therefore, the interface will have a staircase form with a space resolution of the size of the meshing. Finally, in absence of charges and currents, the location of the E-field and H-field, combined with the second-order differences, enforces the Gauss's laws, making the simulations divergence free.

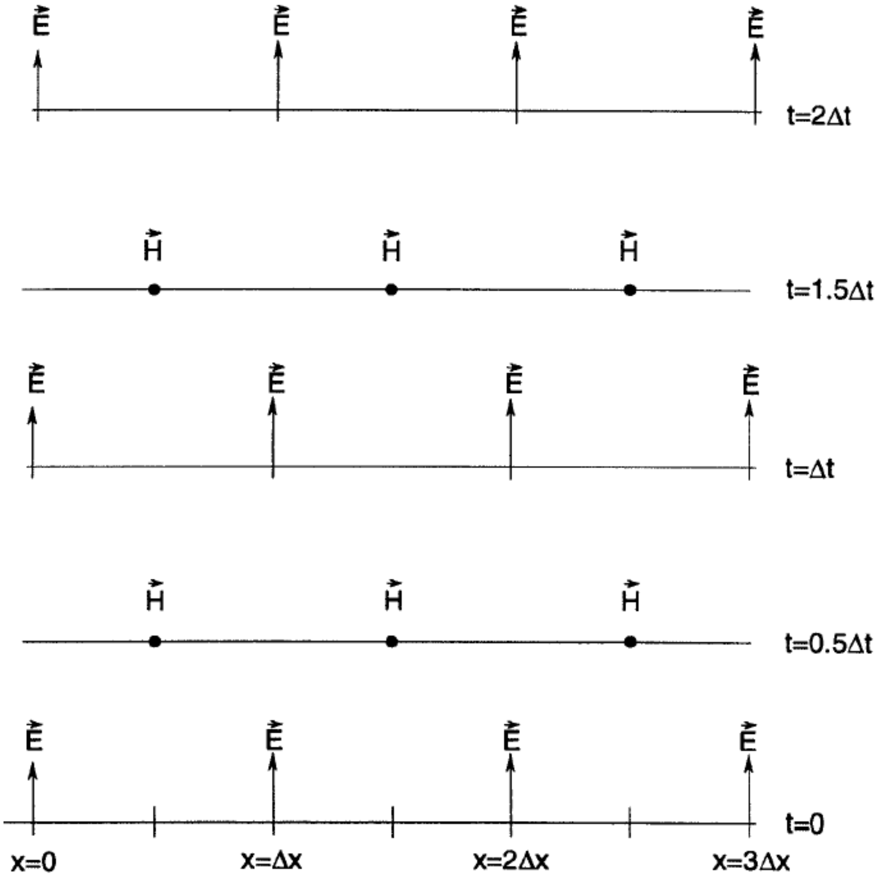

Figure 3.3: Yee Cell with the representation of the **E** and **H** field, each of them calculated at different time step : the leapfrog arrangement

Finally, the 6 components of the magnetic and electric fields are also centered in time. Figure 3.3 shows the so-called leapfrog arrangement, where the H-field (and E-field) are solved alternatively, in different time steps, using the previous results stored for the E-field (H-field). The time stepping process is centred and second order accurate, as seen Equations (3.5) and (3.6). It is robust because the fields do not dissipate due to the time-stepping algorithm, which could arise from numerical artefacts. It is also called "fully explicit", therefore avoiding again errors and aberrations. For more information, see [146].

For a same amount of error, the Yee cell enables to use a smaller number of cells, as comprared to the others possibilities, namely unstaggered-collocated and staggered-collocated cells [73].

The dispersion relation in 3 dimensions is a little bit more complex and it is possible to obtain it as :

$$\left[\frac{1}{c\Delta t}sin\left(\frac{w\Delta t}{2}\right)\right]^2 = \left[\frac{1}{\Delta x}sin\left(\frac{k_x\Delta x}{2}\right)\right]^2 + \left[\frac{1}{\Delta y}sin\left(\frac{k_y\Delta y}{2}\right)\right]^2 + \left[\frac{1}{\Delta z}sin\left(\frac{k_z\Delta z}{2}\right)\right]^2 \tag{3.14}$$

It is interesting to notice that when Δt, Δx, Δy and Δz tend to zero, we find the analytical dispersion relation :

$$\left(\frac{w}{c}\right)^2 = k_x^2 + k_y^2 + k_z^2 \tag{3.15}$$

Therefore, this means that it is possible to recover any degree of accuracy, as far as the mesh grid and time step are set at the right value. As a rule of thumb [2], the spacial step should be set as :

$$maximum(\Delta x, \Delta y, \Delta z) \leq \frac{\lambda_{min}}{10n_{max}} \quad \text{or} \quad N_\lambda \geq 10n_{max} \tag{3.16}$$

where n_{max} is the maximum value of the different refractive index found in the system. On the other hand, the time step should be set as :

$$\Delta t \leq \frac{1}{c\sqrt{\frac{1}{(\Delta x)^2} + \frac{1}{(\Delta y)^2} + \frac{1}{(\Delta z)^2}}} \tag{3.17}$$

in the case where the light is propagating through vacuum at the speed c. Again, those parameters are used to minimize the duration of the simulation whereas converging to an acceptable solution. In the next section, the way to deal with graphene as a material is presented.

3.2 Modeling graphene in FDTD

Graphene is a 2D material, and as such it is not trivial to simulate using FDTD. First of all, the theory which gives us the dispersion equation for graphene optical properties is based on the Kubo formula (see Section 2.2.1). The Kubo formula gives two integral terms to be solved, which represent the intraband term and the interband term. The former is solved analytically whereas the second can be accurately solved numerically. Because the interband term can be solved only numerically, several approximations exist.

Secondly, graphene optical properties, usually presented in term of 2D optical conductivity, is not trivial to solve for FDTD 3D numerical simulation. Two methods exist: a 3D approach based on a 3D virtual permittivity, defining graphene with a finite very weak thickness, and a 2D approach using the 2D optical conductivity, using special algorithm for modelising graphene as a 2D material [1]. In fact, in the case of the 3D approach, meshing a layer of graphene with a thickness of the order of magnitude around the Angstrom gives a significant amount of Yee cells to be computed. The electro-magnetic excitation is the infrared, which makes system structures of the order of the micrometer. Coupled with effective wavelength of graphene plasmons which is really small, it makes the computation region huge, relatively to the meshing.

This section will be divided into two sub-sections. At first, the different approximations using different terms of the conductivity are presented and tested. The conditions to apply the different approximations are given. Finally, the two main methods existing to implement graphene as a material in FDTD are shown. The first is to modelize graphene in 3 dimensions via the permittivity. The second, implemented recently, aims to use a special algorithm to modelize graphene as a 2D material, taking place on one face of the cubic Yee cell.

3.2.1 How to deal with the interband term of graphene conductivity

As it has been seen in Section 2.2.1, the optical properties of graphene can be described thanks to its optical conductivity given by the Kubo formula (Equation (2.1)). However, some problems arise when dealing with the interband term that can be solved only numerically.

Let's evaluate the optical conductivity of graphene. The starting point is to express the optical conductivity of graphene, thanks to the kubo formula (Equation (2.1)). We can therefore express the conductivity as a sum of the intraband term $\sigma_{intra}(\omega, \Gamma, T, \mu_c)$ and the interband term $\sigma_{inter}(\omega, \Gamma, T, \mu_c)$ as follow :

$$\sigma_{intra}(\omega, \Gamma, T, \mu_c) = \frac{-ie^2}{\pi\hbar^2(\omega + i2\Gamma)} \int_0^\infty E \left(\frac{\partial f_d(E)}{\partial E} - \frac{\partial f_d(-E)}{\partial E} \right) \partial E \tag{3.18}$$

$$\sigma_{inter}(\omega, \Gamma, T, \mu_c) = \frac{ie^2(\omega + i2\Gamma)}{\pi\hbar^2} \int_0^\infty \frac{f_d(-E) - f_d(E)}{(\omega + i2\Gamma)^2 - 4(E/\hbar)^2} \partial E \tag{3.19}$$

with f_d the Fermi-Dirac distribution, μ_c the chemical potential, e the elementary charge, Γ the scattering rate and ω the excitation pulsation. The scattering rate is a phenomenological physical quantity related to the relaxation time of electron in graphene by $2\Gamma = \tau^{-1}$. The interband term is determined numerically whereas the intraband term of the conductivity is solved analytically as:

$$\sigma_{intra}(\omega, \Gamma, T, \mu_c) = \frac{ie^2\mu_c}{\pi\hbar^2(\omega + i\tau^{-1})} \left[1 + \frac{2k_BT}{\mu_c} \ln(e^{-\mu_c/k_BT} + 1) \right] \tag{3.20}$$

As seen before, the intraband term can be also reduced to a Drude-like expression, in the case where $E_F >> k_bT$:

$$\sigma_{intra}(w, E_F, \tau, T) = \frac{ie^2E_F}{\pi\hbar^2(w + i/\tau)} \tag{3.21}$$

These two equations, Equations (3.20) and (3.21) will be used later on as first approximations of the optical conductivity in the infrared range. In fact, as shown in Figure 2.22b, the ideal wavelength for low plasmons damping lies around 11 microns, in the middle infrared. As seen with Figure 2.12a, in the infrared range, the optical conductivity of graphene tends to the intraband terms, and the interband terms can be neglected (no electron-hole excitation between valence and conduction band, see section 1.3.3). This case would make the analitically solved intraband terms a good approximation for the optical conductivity of graphene.

Let's come back to the Kubo formula and the resolution of its second term, namely the interband term. For numerical evaluation of this term, it is interesting to rearrange the difference of the Fermi function. Using an arbitrary function $G(E)$, it is possible to write [40] :

$$G(E) = \frac{sinh(E/k_bT)}{cosh(\mu/k_bT) + cosh(E/k_bT)} \tag{3.22}$$

Then the interband term can be re-written as :

$$\sigma_{inter} = \frac{ie^2(\omega+i2\Gamma)}{\pi\hbar^2}\int_0^\infty \frac{G(E)}{(\omega+i2\Gamma)^2-4(E/\hbar)^2}\partial E \tag{3.23}$$

$$= \frac{ie^2(\omega+i2\Gamma)}{\pi\hbar^2}\left[\int_0^\infty \frac{G(E)-G(\omega/2)}{(\omega+i2\Gamma)^2-4(E/\hbar)^2}\partial E + \int_0^\infty \frac{G(\omega/2)}{(\omega+i2\Gamma)^2-4(E/\hbar)^2}\partial E\right] \tag{3.24}$$

$$= \frac{ie^2(\omega+i2\Gamma)}{\pi\hbar^2}\left[\int_0^\infty \frac{G(E)-G(\omega/2)}{(\omega+i2\Gamma)^2-4(E/\hbar)^2}\partial E - iG(\omega/2)\frac{\hbar\pi}{4(\omega+i2\Gamma)}\right] \tag{3.25}$$

$$= \frac{e^2}{4\hbar}\left[G(\omega/2) + \frac{i4(\omega+i2\Gamma)}{\hbar\pi}\int_0^\infty \frac{G(E)-G(\omega/2)}{(\omega+i2\Gamma)^2-4(E/\hbar)^2}\partial E\right] \tag{3.26}$$

This mathematical simplification removes the singularity from the integrals. Figure 3.4 shows the real part (solid line) and imaginary part (dashed line) of the optical conductivity of graphene. As it can be seen in Figure 3.4, the conductivity (σ_{intra}+ σ_{inter}) plotted with the function G(E) introduced above (in red on the graph) removes the singularity at high energy (low wavelength on the graphic), as compared to the conductivity plotted with the integral (in blue on the figure), Equation (3.19).

It is then possible to compare the optical responses of a graphene sheet for different Fermi level, corresponding to different densities of charge. In Figure 3.5, the optical conductivity of graphene is plotted as function of the wavelength, for different Fermi levels (colour). The dash lines correspond to the imaginary part of the conductivity, whereas the solid lines correspond to the real part. As expected, the wavelength threshold between the interband and intraband domains takes place at $2E_F$, and diminishes as the Fermi level gets higher (Figure 3.5).

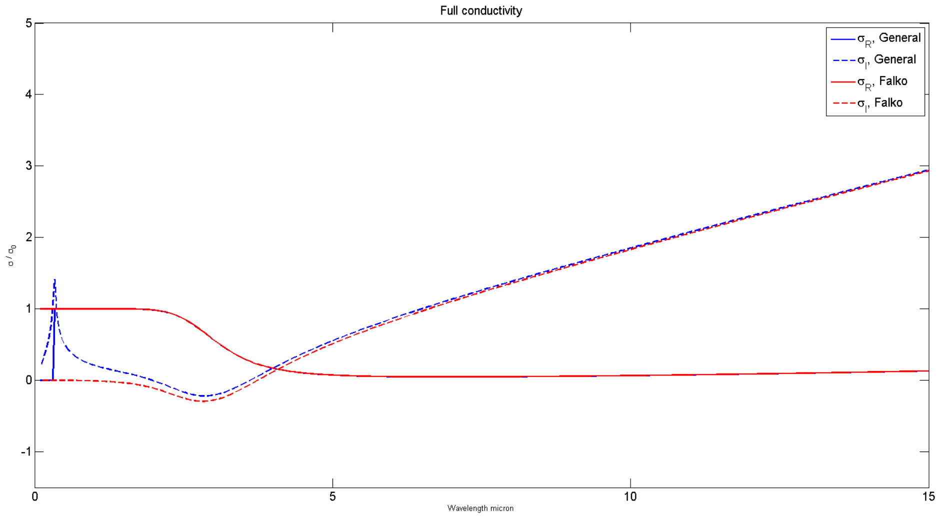

Figure 3.4: Conductivity numerically calculated with (in red) and without (in blue) the functions $G(E)$ and $G(\omega/2)$ [40]

Graphene has been implemented in FDTD at first by using only the Drude-like intraband approximation (Equation (3.21)). This approximation is known to be valid at high Fermi level. Figure 3.6 displays four graphs of graphene optical conductivity, corresponding to four different Fermi energies. On each graph, three sets of conductivity obtained in three different ways : the two approximations of the conductivity via the intraband term (Equations (3.20) and (3.21)), compared to the full conductivity

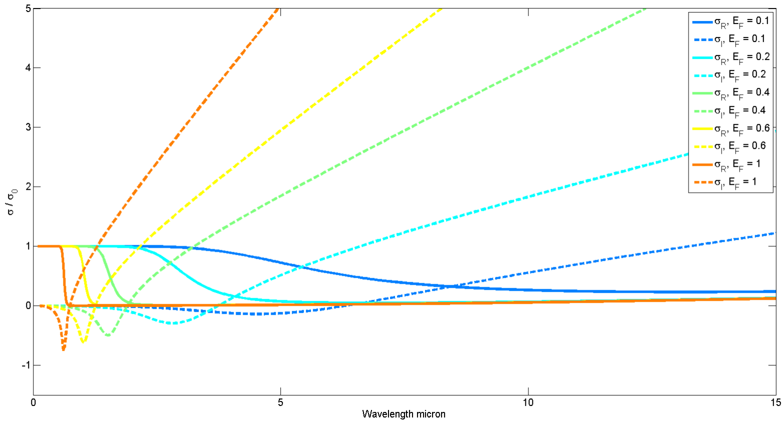

Figure 3.5: Comparison of the optical conductivity for different Fermi energy (0.1,0.2,0.4,0.6,1eV), using numerical calculation for σ_{inter} and Equation (2.5) for σ_{intra}. The conductivity is plotted as a function for the wavelength λ running from 100nm to 15 μm. The optical conductivity of graphene (unit $e^2/4\hbar$) of a graphene layer with a mobility of $1m^2V^{-1}s^{-1}$.

(interband calculated numerically), in the infrared range. In red is shown the Drude-like intraband conductivity approximation, using Equation (3.21). In blue is displayed the complete intraband term approximation, from Equation (3.20). Finally, in green is shown the full conductivity, with the interband term computed numerically with the method shown above. The solid lines correspond to the real part of the optical conductivity, whereas the dashed line+symbol correspond to the imaginary part of the conductivity.

First, let's have a look on the two intraband terms, in red and blue for the partial and complete terms respectively. At low Fermi energy, with $E_F = 0.05eV$ (Figure 3.6a), both approximations (in blue and red) give graphene conductivity with a strong bias (as compared to the green). Unexpectedly, the Drude-like conductivity (in red), which is an approximation only for high E_F as compared to the full intraband term approximation (in blue), tends to be closer to the one obtain with full conductivity (in green). The approximations tend to be correct at a Fermi level $E_F \geq 0.3eV$ (Figures 3.6c and 3.6d). Therefore, the Drude-like approximation can be used in this infrared region for Fermi level higher than 0.3eV. Below 0.3eV, the full conductivity should be considered.

As we will see later (see Section 3.4), an undoped bare suspended graphene sheet can be electrostatically doped only until 0.25eV. For this reason, the intraband approximation is not valid for the study of suspended graphene. We will therefore use the full conductivity when simulating suspended graphene with FDTD method. However, as it will be shown below, the graphene optical properties have been implement at first in FDTD taking only into account Drude-like approximation. Moreover, graphene was only available as a 3D material (permittivity) with finite thickness. We will see in the next section the limit of the 3D approach, as compared to the 2D one.

3.2.2 Two methods to compute graphene in FDTD : 3D vs 2D approach

Graphene is a 2D material, and as such it is not trivial to simulate its properties using FDTD. Its optical properties are usually presented in terms of optical conductivity, which can be expressed using the Kubo formula (Equation 2.1). Two main methods exist to implement it in FDTD.

The first one attempts to use full Yee cells to describe it, but difficulties arise due to their inherent 3D nature. This approach requires converting the 2D conductivity (sections 2.2.1 and 3.2.1) into a volume anisotropic permittivity (Equation (2.10)), assuming that graphene has a finite thickness. A study

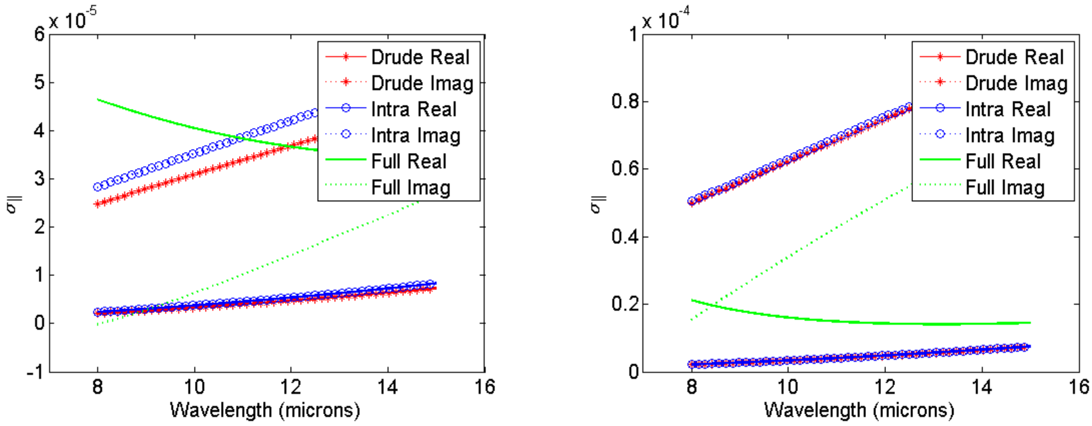

(a) Fermi energy $E_f = 0.05eV$ (b) Fermi energy $E_f = 0.1eV$

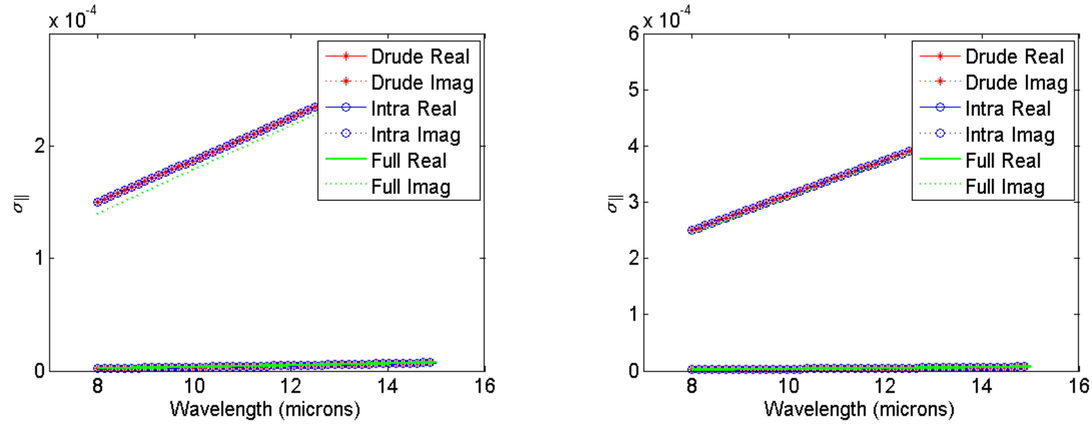

(c) Fermi energy $E_f = 0.3eV$ (d) Fermi energy $E_f = 0.5eV$

Figure 3.6: Comparison of the conductivity $\sigma_{||}$ of the graphene obtained using different approximations from the Kubo formula. In red, $\sigma_{||}$ obtained by the use of the Drude-like intraband term from equation 2.6. In blue, $\sigma_{||}$ obtained by the use of the full intraband conductivity from equation 2.5. In green, the full conductivity obtained by the use of the full intraband conductivity from equation 2.5 and the interband term obtain numerically. The mobility is set at $1m^2V^{-1}s^{-1}$.

[140] has been done in order to know if this procedure is safe or if it will profoundly change the optical properties of the graphene sheet. We first tried following this path, and numerical results confirmed the accuracy of this approach.

A second approach aims at describing graphene as a charged surface boundary condition applied only to a fraction of a Yee cell [112, 59]. This condition is of the general form:

$$\vec{n} \times \left(\vec{H_1} - \vec{H_2}\right) = \sigma \vec{E_t} \tag{3.27}$$

where $\vec{n}$ is the vector normal to the graphene sheet, $\vec{H_1}$ and $\vec{H_2}$ the magnetic fields on each side of the sheet, σ the conductivity and $\vec{E_t}$ the tangent electric field. Through this, there is no need to discretize space (and time) to extreme sizes, and this was found to lead to an increased stability of our simulations. This is the method that will be used in this study.

Let's come back to the 3D method. Using Equation (2.10), it is possible to plug in different models of optical conductivity of graphene. As a first approximation the Drude-like conductivity is used (Equation (2.6)) valid in the infrared range at Fermi level $E_F \geq 0.3eV$ (Section 3.2.1). The permittivity is obtained as follow :

$$\epsilon_{||} = \epsilon_s - \left(\frac{E_F e^2 w}{\pi \hbar^2 (w^2 + \tau^{-2})}\right) \frac{1}{w \epsilon_0 \Delta} + i \left(\frac{E_F e^2}{\pi \hbar^2 (w^2 + \tau^{-2}) \tau}\right) \frac{1}{w \epsilon_0 \Delta} \tag{3.28}$$

$$\epsilon_{\perp} = \epsilon_s \tag{3.29}$$

Equation 3.28 is then implemented directly as an analytical material and several parameter have to be set. At first, the surrounding permittivity, ϵ_s (see Section 1.1.3), which is chosen to be at 2.5 for graphene on SiO_2 [57] and 1 for suspended graphene. Then, the Fermi level E_F and the mobility μ values have to be chosen carefully. In fact, they are function of each others, but they are also function of the system and phenomenon to be studied.

As seen in Section 2.2.1, the Kubo formula which gives the optical conductivity of graphene is function of the relaxation time τ (with $\Gamma = 1/2\tau$). In section 2.1.2, the Boltzmann-transport approximation ($\tau_D C = \mu E_F / e^2 v_f$), linking the relaxation time with the Fermi level and the mobility, has been presented as a good approximation. However, it usually remains too low as compared to the experiment. Different reasons have been put forward. It is possible to enumerate dielectric losses of the substrate, electron-hole scattering and thermal intrinsic phonon of the graphene. The FDTD commercial software used in this study enables user to set graphene parameter only with τ_{DC}.

Therefore, it has been chosen to work with conservative values of the DC mobility. It artificially lows down the relaxation time of graphene, being directly proportinal to it. In fact, mobility in suspended graphene has been recently recorded up to 40 times the value of $1m^2V^{-1}s^{-1}$ that has been taken in this study [150]. The graphene mobility limited only by acoustic phonon would be 20 times more important than the value used here. Litterature mentions a relaxation time which would be smaller by a factor of 3-4 times as compared to the DC [42].

Finally, it is important to look at the main parameter emerging from this method : the thickness of the graphene Δ. A straight forward way to have an idea about the range of validity of the thickness Δ is to use a mode solver. A mode solver enable to determine all the E-field and H-field components corresponding to the normal mode supported by an optical system. Defining the materials with complex permittivity, it is possible to deal with a wide range of materials, including graphene.

To investigate the effect of the thickness Δ to the TM plasmons mode of graphene in the infrared range, we consider a Fermi level of $E_F = 0.5eV$, in order to safely use Equations (3.28) and (3.29), and a mobility of about $1m^2V^{-1}s^{-1}$, which are realistic properties that have been reported in the literature [158]. That gives a relaxation time $\tau = 50ps$ and a scattering rate $\Gamma = 6,58.10^{-4}eV$ ($\tau_{DC} = \mu E_F / e^2 v_f$). The mode solver computation gives the effective index $n_{eff} = k_p / k_0$ which has a real part, related to

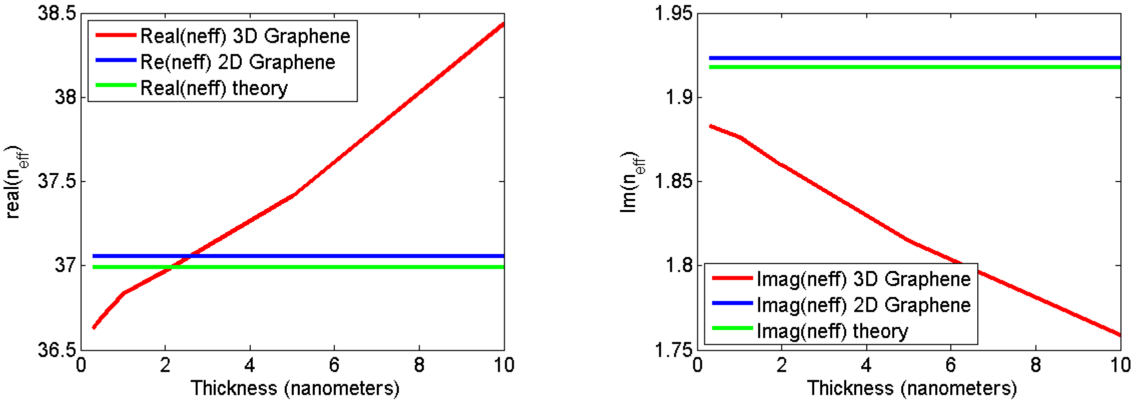

(a) Real part of the effective index n_{eff} of the GPs

(b) Imaginary part of the effective index n_{eff} of the GPs

Figure 3.7: Comparison of the (a) real part of the effective index n_{eff} and (b) the imaginary part of the effective index n_{eff} of the plasmons modes for 2D (in blue) vs 3D (in red) graphene (Drude-like approximation) vs theory (in green) using Equation (2.23). The optical conductivity as well as the permittivity of the SiO_2 substrate in the case of the computation of theoretical n_{eff} is taken from the 2D simulation. The mobility of the graphene is set at $1m^2V^{-1}s^{-1}$ whereas the Fermi level is about 0.5eV.

the effective wavelength of the GPs, and an imaginary part, related to the optical loss of the mode.

Figures 3.7 show a comparison of the real part and the imaginary part of the effective index n_{eff}, solved with a mode solver for graphene deposited on SiO_2, at a wavelength of 11 microns, in the following cases:

1. in red, 3D graphene (Equations (3.28) and (3.29)) where n_{eff} is function of the graphene thickness (x axis)
2. in blue, 2D graphene with the full conductivity (analytical intraband term and numerical interband term)
3. in green, a theoretical n_{eff} based on the dispersion relation of graphene plasmons, Equation (2.23)

We can first observe that the theoritical n_{eff} in green is relatively close to the one obtained from 2D graphene, in blue. We realise also here a strong bias for the simulation using the 3D permittivity for describing graphene. An exact value can be obtained for the real part of the effective index for $\Delta = 2nm$, but not for the imaginary part. The error on the latter one decreases for Δ getting thinner. Therefore, this model, which is a good first approach, is not enough accurate to study graphene plasmons.

Replacing the optical conductivity model (Drude like model) used for 3D graphene by the full conductivity, with the interband term calculated numerically, it is possible to solve the mode for different thickness, following the same process. Figure 3.8 shows a comparison of the normal modes obtained for 3D graphene using the full conductivity, 2D graphene with the full conductivity and using the theoritical equation, as seen above. The comparison shows this time that smaller is the thickness, and higher is the accuracy. This is summarized by the absolute error of the two cases seen Figure 3.7 and Figure 3.8, plotted Figure 3.9.

Figure 3.9 shows the absolute error of the effective index n_{eff} of the TM GPs mode computed for 3D graphene (with the Drude-like approximation Figure 3.7, and the full conductivity Figure 3.8) as compared to the theory (Equation (2.23)). The Drude like approximation gives more accurate results for thickness higher than 2nm, but does not tend to the exact solution, as the errors on the real part of the effective index increase for thinner layer. When using the full optical conductivity, the results seem to converge to the exact solution when the thickness of graphene vanishes. In any case, a really small

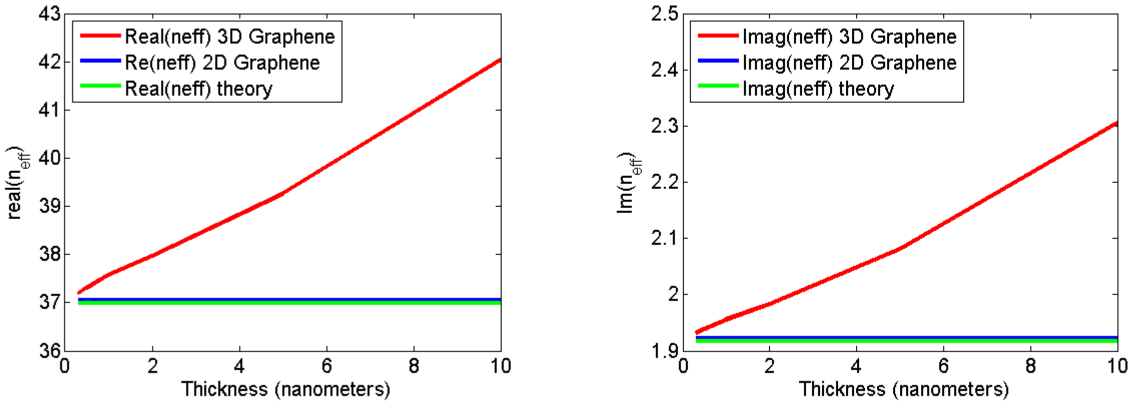

(a) Real part of the effective index n_{eff} of the GPs (b) Imaginary part of the effective index n_{eff} of the GPs

Figure 3.8: Comparison of the (a) real part of the effective index n_{eff} and (b) the imaginary part of the effective index n_{eff} of the plasmons modes for 2D (in blue) vs 3D (in red) graphene (using full conductivity) vs theory (in green) using Equation (2.23). The optical conductivity as well as the permittivity of the SiO_2 substrate in the case of the computation of theoretical n_{eff} is taken from the 2D simulation. The mobility of the graphene is set at $1m^2V^{-1}s^{-1}$ wheras the fermi level is about 0.5eV.

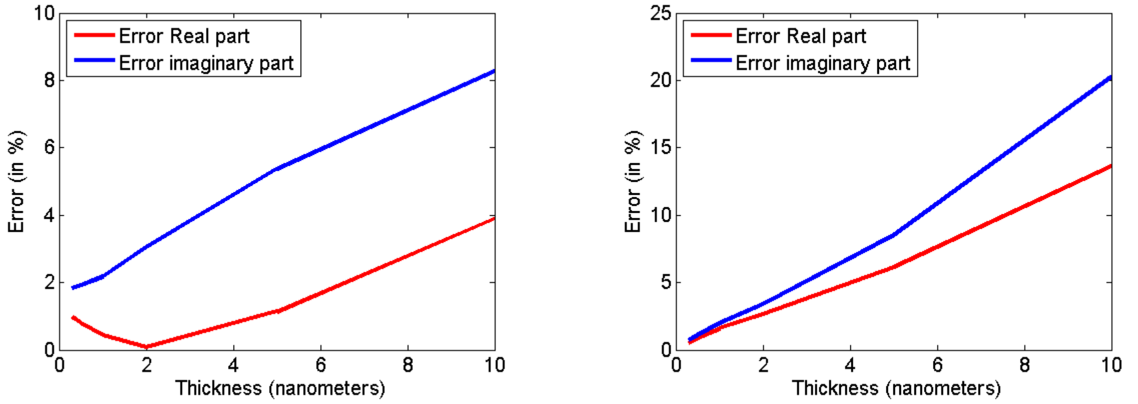

(a) Absolute errors $(n_{eff}(3D)$-$n_{eff}(theo))/n_{eff}(theo)$ applied for the real part and the imaginary part, of the results obtained Figure 3.7

(b) Absolute errors $(n_{eff}(3D)$-$n_{eff}(theo))/n_{eff}(theo)$ applied for the real part and the imaginary part, of the results obtained Figure 3.8

Figure 3.9: Absolute value of the errors on the effective index n_{eff} found in Figures 3.7 and 3.8, as compare to the theory

thickness is required for accurate simulation.

Therefore, this 3D graphene method requires a local spatial discretization of the order or thinner than the nanometer, while our simulations involve wavelengths and structures bigger than the micron, leading to huge computational domains and non-uniform meshing. Moreover, the stability criterion of the FDTD then requires an extremely short time discretization, and a huge number of iterations is thus needed to complete a single simulation. Therefore, this method is highly CPU-intensive and numerical aberration may occur.

In order to illustrate a case where numerical errors may occur, Figures 3.10 show an attempt to simulate graphene plasmons launched by a nanorod, using 3D graphene. This approach will be described in the next section. Figure 3.10a is an illustration of the system studied. A 3D graphene layer is lying on the top of a Si/SiO_2 substrate. A gold nanorod is deposited on the top of it and acts as a plasmons launcher. The five other figures, described below, show a serie of snapshots of the electric field recorded inside the graphene layer.

Figure 3.10b shows a half top-view of the simulation illustrated in Figure 3.10a, at t=0. Taking advantages of symmetry, we simulate the right-side half of the full 3D system. The light is normal to the plan of the simulation, exciting only the nanorod via Total-Field Scattering-Field source. Half of the gold nanoantenna is also shown. At $t = \Delta t$ (Figure 3.10d), the incident X-polarized light excites typically the dipolar mode of the rod. At $t = 2\Delta t$, the plasmons is spreading in the graphene layer, mainly in the y direction (see next section). At $t = 3\Delta t$ and $t = 4\Delta t$, it is possible to observe a field remaining in the nanoantenna, following the grid which is about $5nm \times 5nm \times 1nm(x, y, z)$. The graphene is set with a thickness of 2nm, using the Drude like approximation. This kind of aberration becomes more serious as the grid becomes smaller. The total energy in the box did not vanish after the time of the simulation. This kind of aberration adds a significant errors when studying the properties of the plasmons, like its effective wavelength λ_p or its propagation length L_p. Therefore, it has been chosen to study Graphene plasmons with the 2D model.

The 2D material modelization, which is the second approach seen above, aims to describe graphene as a charged surface, where the boundary conditions are applied only to a fraction of a Yee cell [6]. As such, there is no need to discretize space (and time) to extreme sizes, and this was found to lead to an increased stability of our simulations. Moreover, it leads to results fitting really well the theory for graphene plasmons, as shown Figures 3.8 and 3.7. This is the method that will be used hereafter. The numerical study of graphene has been made possible thanks to the use of the super-calculator Romeo in Reims, France.

3.3 Use of a plasmonic antenna for GPPs excitation

Originally, excitation of GPPs was achieved by the use of a laser illuminated metal tip in the scanning near-field optical microscopy configuration [42, 29]. Although the resulting scattered angular spectrum was broad, a small part of it was exploited for successfully launching the GPs (see section 2.2.2).

Another way for launching plasmons at metal/dielectric interfaces lies on the use of prisms or gratings [143] to efficiently convert the incident wave-vector into the in plane graphene plasmon one. In our simulations, we use Au nanorod as nanoantenna to study the GPPs launched perpendicularly to the main axis of the nanorod in order to anticipate the possibility to maximize the power of the GPPs launched using a grating. It is indeed possible to place side by side many nanoantenna together, and obtain an enhancement effect thanks to the grating configuration. As a first step, we will only rely on the angular spectrum generated by a single rod. Compared to an out-of-plane tip, the in-plane resonant launchers allow us to envisage future integrated chips. Additionally, the longitudinal resonance enables the enhancement of the angular spectrum components.

As a preliminary study, a gold nano-antennas with a length L acting as a resonant dipole along L

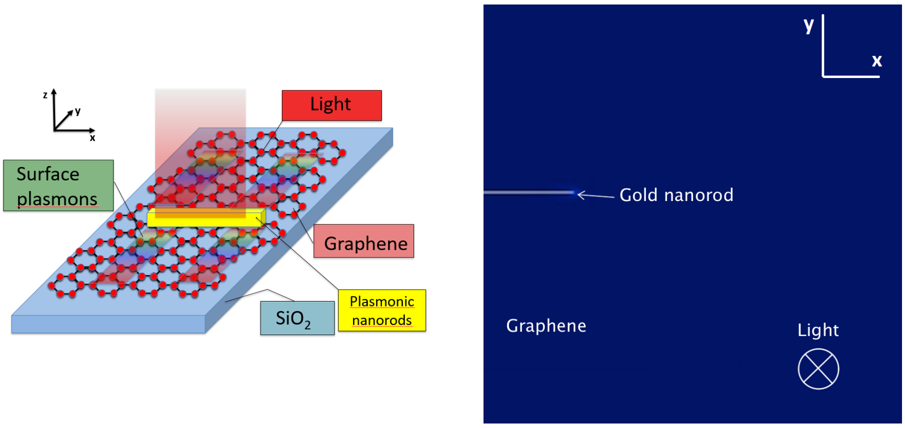

(a) Design of the simulation (b) Top view of the simulation at t=0

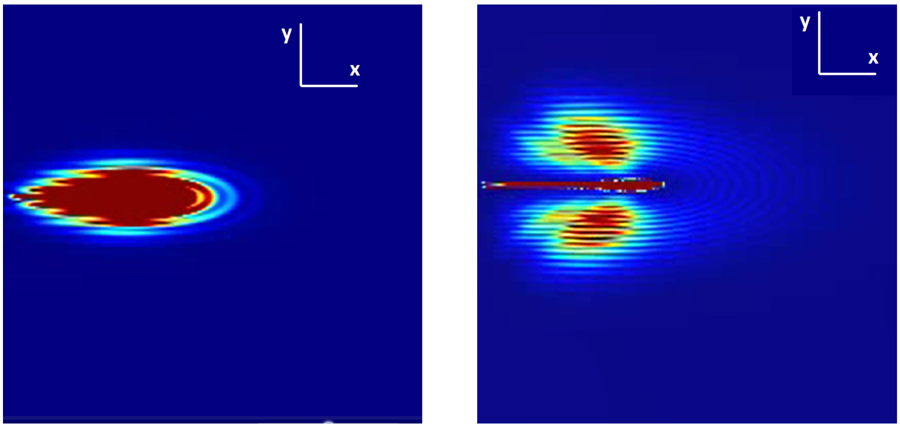

(c) Top view of the simulation at t= $1\Delta t$ (d) Top view of the simulation at t= $2\Delta t$

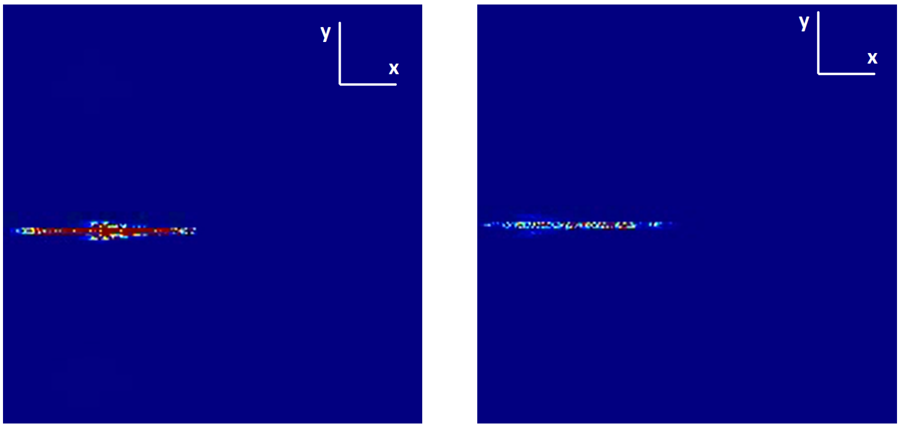

(e) Top view of the simulation at t= $3\Delta t$ (f) Top view of the simulation at t= $4\Delta t$

Figure 3.10: Snapshot of the propagation of surface plasmons, resolved in time using an arbitrary Δt, and the 3D graphene model. The monitor is located in the graphene. The launcher is a gold nanorod of 4 μm. The exciting source is a pulse of light, with a spectrum range from $9\mu m$ to $13\mu m$, normal to the images. The polarisation of the light follow the big axis. The graphene is lying under the gold nanorod, on the entire surface ($5\mu m \times 5\mu m$). The substrate is made of 300nm of SiO_2 and 7 μm of Si. The graphene is set with a Fermi level of 0.5eV and a mobility of $1 m^2 V^{-1} s^{-1}$.

is considered. The section of the nano-rods is rectangular, 80nm large and 50nm height. The shape is needle-like, to fit the fabrication via e-beam lithography. The nanorod was illuminated with a pulse that propagates perpendicular to the sample plane, along z (see configuration on Figure 3.10a). The incident light was linearly polarized with the electric field parallel to the rod long axis (x axis). This pulse has a wide-band spectrum going from 8 μm to 12 μm, with a central wavelength around 10 μm.

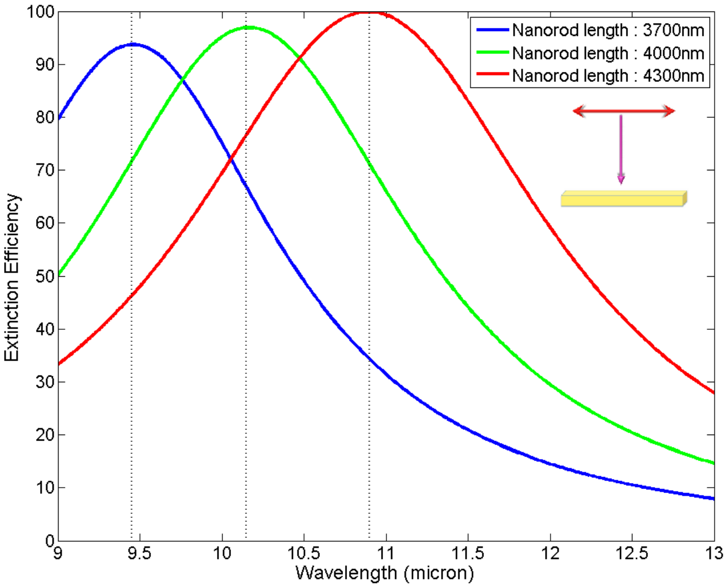

Figure 3.11: Calculated extinction efficiency of gold nano-rods with a length of 3700 nm, 4000nm and 4300nm, for a width of 80nm and height of 50nm. Nanorods are standing in air.

Figure 3.11 shows the calculated extinction efficiency spectrum of three nanorods without graphene, in air, for different lengths: 3700nm, 4000nm and 4300nm. The extinction efficiency is the sum of the absorption and scattering efficiency. The efficiency are dimensionless properties, and can be directly converted to the cross section by multiplying with the cross-sectional area of the nano-rods [72, 63]. It is well-known [147] that changing the shape of the rods shifts the resonance wavelength, as a result of a change of the oscillation length travelled by the free electrons along the long axis. When we increase the long axis of the nano-rod, we can see a red shift in the optical spectra. We can notice that the resonance is engineered to lie in the mid-infra-red region, in order to avoid plasmons losses and damping when travelling through graphene, at 11 μm.

Simulations have shown a red shift when the nanorods are lying on SiO_2 substrate with a monolayer of graphene deposited on it. This effect results from an increase of the effective surrounding medium. In order to discuss the possible momentum matching between the antenna and GPs, it is interesting to have a look to the Fourier transform of the antenna near field. Figure 3.12 shows this Fourier space at the wavelength of 11 microns both in air and on a SiO_2 substrate.

In the case of suspended graphene, the theory (Equation (2.23)), shows a large wavevector mismatch between the incident light and the Graphene Plasmons in this range of frequencies. At 11 microns, we can calculate the localization parameter λ_0/λ_p,which varies as a function of the graphene layer Fermi level. For $E_F = 0.3$eV and a mobility $\mu = 1m^2V^{-1}s^{-1}$, using the DC relaxation time approximation, $n_{eff} \approx 26$.

The momentum of the near field of the nanorods in the air, enhanced by the LSPR, matches the GPs, shown on figure 3.12(a). However, when the rod is deposited on SiO_2 substrate, we expect a lower near field intensity due to the absorption of the energy by the substrate. As seen figure 3.12(b), the system nanorods-susbtrate is able to excite the GPs. For graphene with E_F=0.3eV, it matchs well the

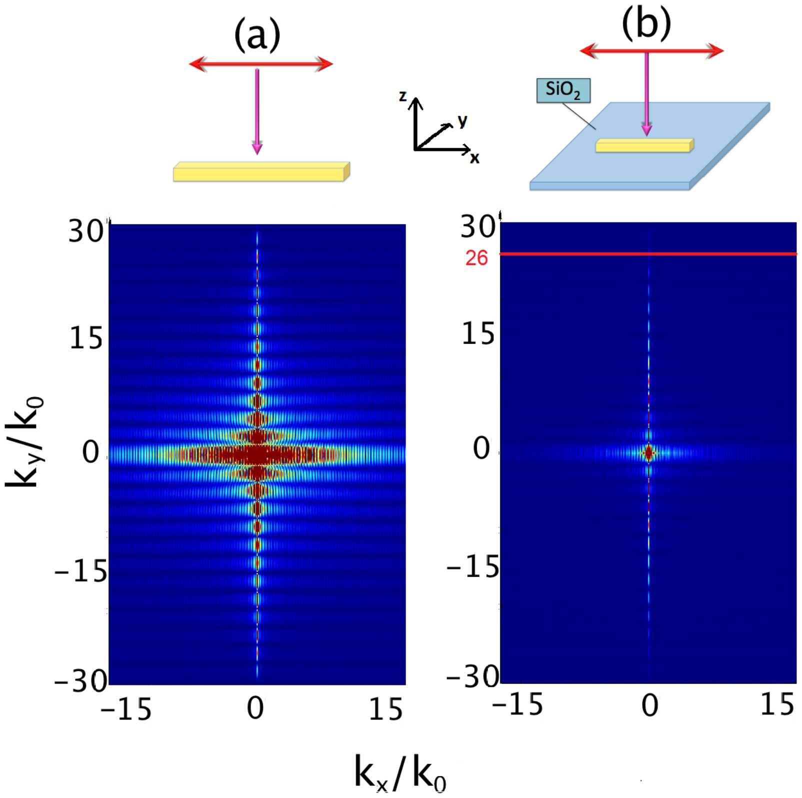

Figure 3.12: Fourier transform of the near field of different systems at 11 microns with the system's illustrations on the top. The red arrows represent the polarisation and the magenta arrow represent the direction of the light. In (a) case of a nanorod in air, in (b) case of a nanorod on a SiO2 substrate.

angular momentum of the nanorod on substrate. It is also interesting to note that the small width of the nanorods along y results in enhanced wavevector components perpendicular to the nanorod axis and not much along the long axis, which would make it integrable in a grating. To go further, a comparison of the near-field of an antenna with and without graphene is studied.

The local near field enhancement of single rods, with and without graphene, is investigated for a wavelength of 11 microns. It has been shown that the plasmons damping from SiO$_2$ substrate is the lowest [42] around this wavelength. The configuration with graphene is depicted in Fig. 3.13. A gold nanorod having a rectangular cross section lays on a $Si0_2$/Si substrate. The nanorod is surrounded by both suspended and supported graphene for comparison. Again, a pulse is exciting the nano-antenna, with a propagation direction normal to the surface of the sample, along z. The incident light was linearly polarized with the electric field parallel to the rod long axis (x axis). This pulse wavelength spectra is going from 8 μm to 12 μm, with a central wavelength around 10 μm. The optical properties of the gold nanoantenna are characterized numerically in order to fit the energy and momentum conditions of GPs.

Following [5, 107], the length L and the width W of the rod are first set to 2.9μm and 0.6μm respectively. The nanoantenna section is therefore rectangular, and its thickness is set to 100 nm. Figures 3.14 show maps of electric field intensity around the rod under illumination, without any graphene (Fig. 3.14(a)), and with graphene (Fig. 3.14(b)). The near-field distributions displayed on these figures unambiguously show the dominant mode excited at this wavelength is dipolar in nature. On Figure 3.14(b), two calculated top-view half-maps of the electric field intensity at the graphene layer plane are shown. For y $>$ 0, graphene is suspended, meaning that the graphene is surrounded by air. For y $<$ 0, graphene is sandwiched between air and the SiO$_2$ substrate. The rod is localized at y=0 nm, acting as a resonant dipole along L. The graphene is defined *via* its 2D conductivity by a Fermi level of 0.2eV, a temperature of 300K and a mobility 1 m^{2}s^{-1}V^{-1}. The parameters set for the graphene will be discussed in the next

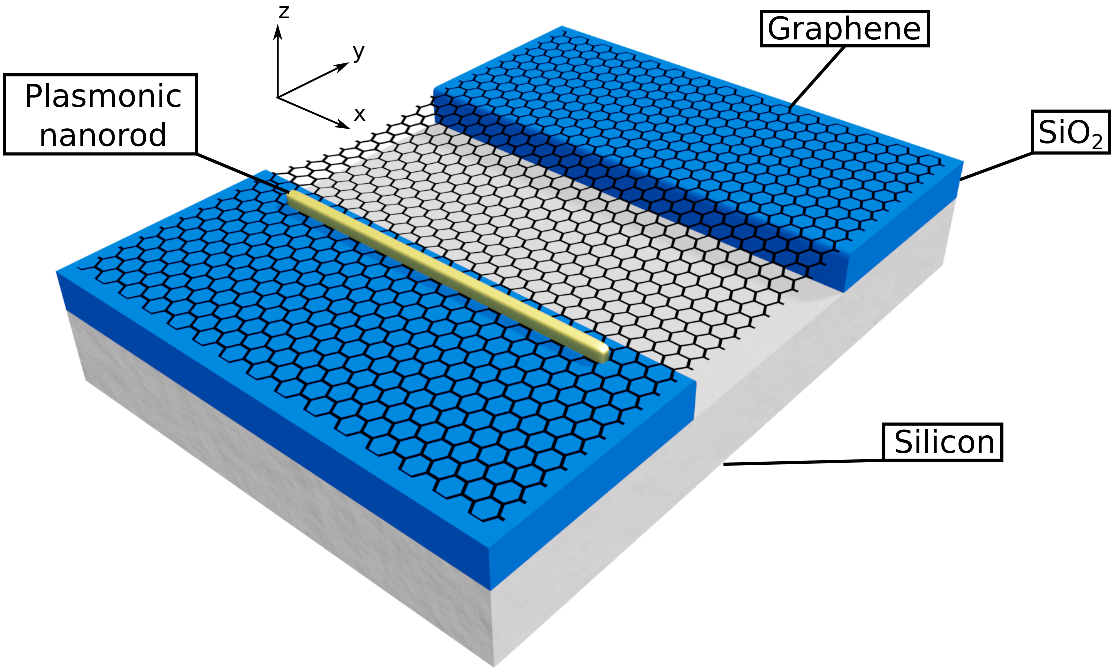

Figure 3.13: Illustration of a plasmonic antenna lying on a SiO_2/Si substrate + graphene. A trench is etched at the vicinity of the golden rod through the SiO_2/Si substrate. A monolayer of graphene is deposited on the top of the trench, and a gold nanoantenna is deposited on the edge of the trench. A part of the graphene is therefore suspended.

section.

In Figure 3.14(b) the spatial decay of the intensity of propagating plasmons in graphene can be observed. Whereas suspended graphene leads to clear propagation of GPPs (Fig. 3.14(b), top), it is not possible to distinguish this propagation in the case of graphene supported by SiO_2 substrate (Fig. 3.14(b), bottom). In the latter case, we clearly see a dipole-like resonance of the antenna at 11 μm, comparable to the one observed in Figure 3.14(a), that does not launch any efficient GPP (in terms of propagation length).

It is interesting to notice that the intensity tends to vanish along a vertical line (x=0) where destructive interference occurs between the phase shifted graphene plasmons that have been launched by the two out-of-phase antenna extremities. Such effects could open new routes to GPPs designing and engineering.

Over a second phase, the question of the dimension of the nanostructure have been addressed. So far, the geometrical parameters were chosen by considering recent studies [5, 107], where the main parameter used for optimizing the coupling is the electric field average. This factor reflects the significant near-field enhancement, consequence of the Local Surface Plasmons Resonance (LSPR) of the antenna, that is most likely to launch strong plasmons in graphene. As shown before, the current geometry could be used for our purpose, but [5] only optimized the GPPs coupling efficiency through variations of the antenna length. The rod width is another parameter that could be explored to increase the coupling efficiency even further. As such, we followed the same path as [5], but performed a parametric study of the near-field average $|E|/|E_0|$ for different lengths and widths of rods lying on a $Si0_2$/Si substrate without graphene. The results are shown on Fig. 3.15. The near-field average $|E|/|E_0|$ was taken at a 10 nm distance from the rod surface. The big axis L was set from 1.6 to 3.2μm, whereas the width W was chosen from 0.05 to 1.15 μm. A maximum of the electric near-field average is found for a micro antenna length of 2.5μm and a width of 50nm. Taking advantage of this results, simulations with suspended graphene are done to compare the new geometrical parameters coupling efficiency to the literature, and to study GPPs modes in details.

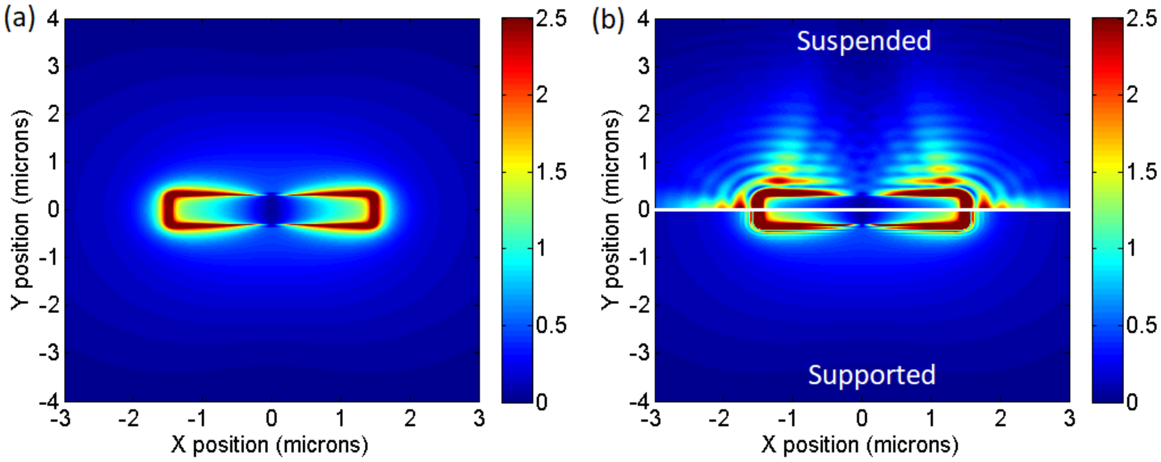

Figure 3.14: Comparison of the response of a gold nanoantenna, lying on Si/SiO_2 substrate, without (a) and with (b) graphene, through electric field intensity maps. (b) The graphene is suspended on the half-top, and supported on SiO_2 substrate for the half-bottom. The color scale is clamped in order to see the plasmon propagating through graphene. The 2.9 μm long, 600nm width, gold nanoantenna is in the center of the maps, at y=0, from x=-1.45 to x=1.45 μm. The wavelength excitation is 11μm.

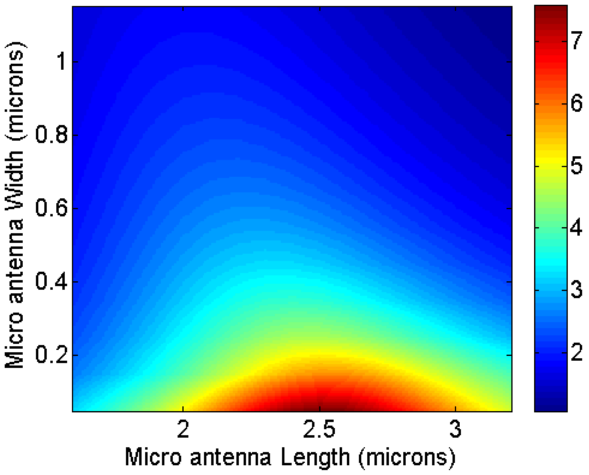

Figure 3.15: Map of the electric near-field average, $|E|/|E_0|$, calculated at the vicinity of rods of length L and width W, without graphene, for an excitation at $\lambda_0 = 11\mu m$.

Figure 3.16 shows $\sqrt{|fft(E_x)|^2 + |fft(E_y)|^2 + |fft(E_z)|^2}$, the spatial Fourier Transform of the near-field for the case of two different antenna geometry, with suspended graphene. Figure 3.16(a) shows the case of geometry dimension taken from [5, 107], that is the Fourier transform of the near field plotted in Fig. 3.14(b) top-half, for positive (k_x,k_y). It turns out that the nanorod launches two main surface plasmons: one in the x direction (peak 2), parallel to the antenna axis, and one in the y direction (peak 1), perpendicular to the nanorod axis. They are illustrated by the two maxima along the quarter-circle of radius $\sqrt{k_x^2 + k_y^2/k_0} = |k_p|/k_0 = \lambda_0/\lambda_p = 43$. These results were easily predictable from Fig. 3.14(b), where the two main GPPs propagations can also be observed, parallel and perpendicular to the rod long axis.

Figure 3.16(b) is using the geometry found in our parametric study (Fig. 3.15). It can be observed a strong enhancement of the peak 1, corresponding to GPPs launched in the y direction, whereas the peak 2 disappears (GPPs launched in the x direction). It is concluded that the new dimensions of the rod, following the investigation of the electric near field average (Fig. 3.15), lead to a stronger coupling to the GPPs launched in the y direction, resulting in an increased effective propagation length in this direction. In the future, the coupling efficiency of graphene plasmon propagating along the y direction could be also strongly enhanced by using a set of parallel nanoantennae to form a resonant grating.

However, the coupling may still not be optimal. After all, the optimization was performed without graphene, by using the average field exaltation as a criterion. Yet as shown here, the true value of the coupling efficiency can only be found by actually computing the whole system, and investigating the Fourier transform. As such, we decided to refine our optimisation once again.

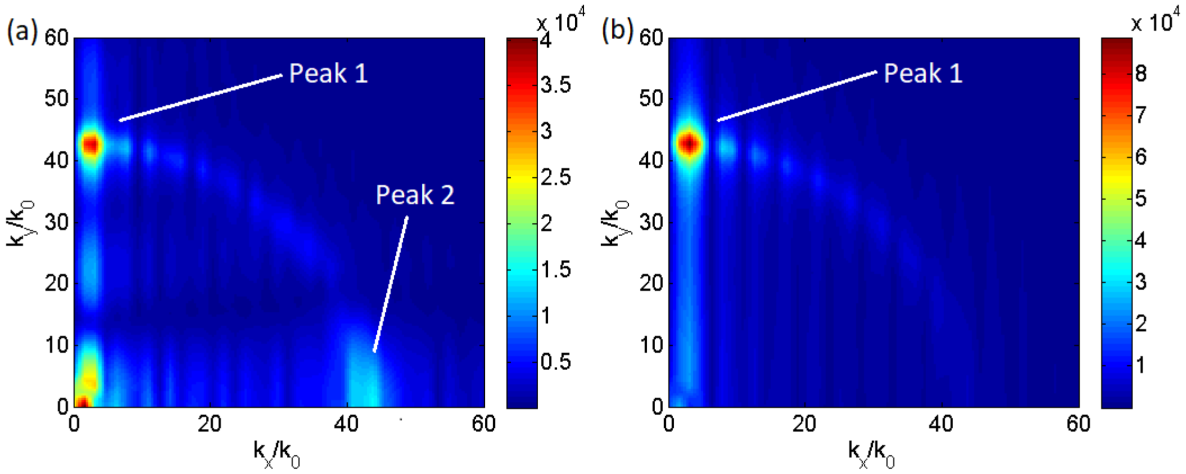

Figure 3.16: Maps representing $\sqrt{|fft(E_x)|^2 + |fft(E_y)|^2 + |fft(E_z)|^2}$, the spatial Fourier Transform of the near field in the reciprocal space, with positive (k_x,k_y), for suspended graphene, in the case of two different rods. (a) The rod length and width are set as L=2.9μm and W=600nm, according to [5, 107]. (b) A rod of length L=2.5μm and width W=50nm is chosen from the parametric study Fig. 3.15. The graphene is set with a Fermi energy about 0.2 eV and a mobility of 1 $m^2 s^{-1} V^{-1}$.

For this purpose, spatial Fourier Transforms of the electric fields maps at 11 microns were performed for different lengths and widths of nanorod (the height remained fixed at 100 nm). The results of this final parametric study are shown in Fig. 3.17. Figure 3.17(a) displays the intensity of the Fourier transform peak (Fig. 3.16(a), peak 2) of the graphene plasmons launched towards the x direction and Fig. 3.17(b) is the one for the y direction (figure 3.16(a) and 3.16(b), peak 1). We conclude that the best shape for the gold nanoantenna is to be as thin as possible (needle-like, see white crosses in Fig. 3.17), 50 nm here, with a length around 2.75 μm, in order to efficiently launch a plasmon perpendicular to rod long axis. While the average near field intensity enhancement of the antenna may not be the highest for this shape (see Fig. 3.15), it gives a stronger coupling with the plasmons in y direction. For comparison, the black crosses in Fig. 3.17 indicate the geometry used in the papers [5, 107], Fig. 3.16(a), while the grey crosses correspond to Fig. 3.16(b) and are the result of our first parametric study (Fig. 3.15). As far as plasmon propagation is concerned, the initial geometry (black cross) constitutes an intermediate case where both x and y directions are possible, and the field energy is thus distributed into both.

In the case of suspended graphene, the theory, from Equ. (2.24), shows a large wavevector mismatch between the incident light (characterized by k_0) and the Graphene Plasmons (characterized by k_p) in this range of frequency, illustrating the need for an antenna. At 11 μm, we can calculate the localization parameter, or effective index, λ_0 / λ_p, which varies as a function of the Fermi level of the graphene layer. For E_F = 0.2eV and a mobility of 1 $m^2 s^{-1} V^{-1}$, we find $real(n_{eff})$ = 42.3 from the dispersion relation (Equ. (1.65)), whereas the FDTD simulation gives an average value of 43 (±1.1) from the Fourier transform maps. Moreover, the propagation length L_p is about 558nm theoretically (from expression

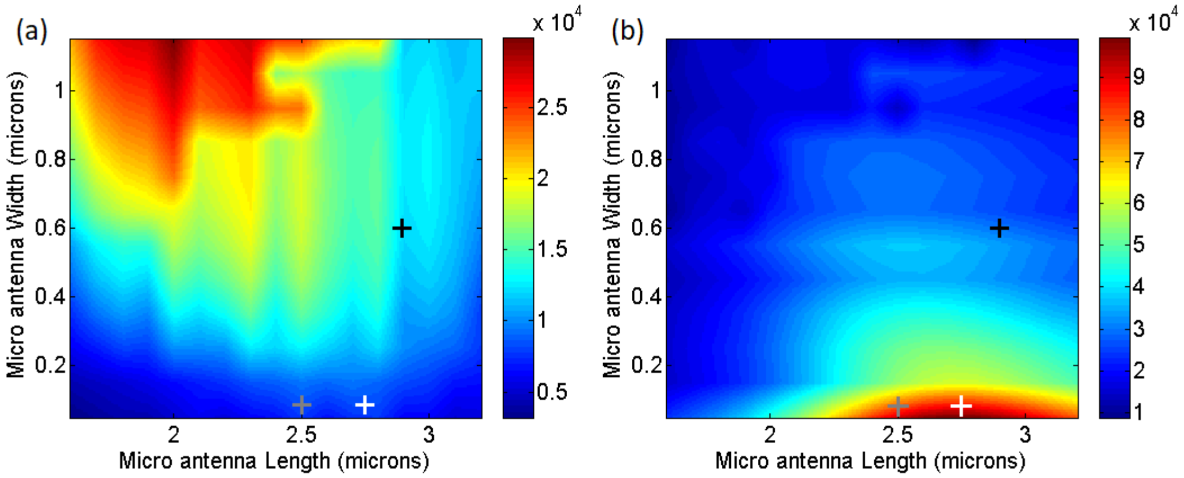

Figure 3.17: Maximum intensity of (a) the peak 2 and (b) the peak 1, the plasmons wavenumber k_p (see Fig. 3.16(a) as an example), in the x direction and in the y direction respectively, as a function of the length and the width of the nanorod. The black cross indicates the dimension of nanoantenna used in papers [5, 107], picked up from Fig.3.16(a). Grey cross corresponds to the antenna dimensions resulting from the parametric study Fig. 3.15. White cross is showing optimum dimensions for launching plasmon in y direction.

(1.65)) whereas we find 532nm in our simulation. It is interesting to notice that we have here already a longer propagation length as compared to SiO_2 supported graphene. Using data from [158], the longest propagation length would be less than 300nm for $\mathrm{SiO_2}$-supported graphene.

Figure 3.18 shows the optimized system for GPPs launched along the y axis, with the antenna geometry defined in Fig. 3.17 (white crosses). Compared to figure 3.14(b), figure 3.18 shows clearly that a rod with a length of 2.75μm and a width of 50nm can launch stronger GPPs that propagates on suspended graphene over a distance nearly 3μm away from the rod, normalized on the incident excitation. Again, supported graphene (y<0) does not enable significant GPP propagation.

As we have shown in this study, the geometry used in [5, 107] does allow for a non-negligible GPP coupling efficiency. Yet, that geometry had a fixed rod width, which could be optimized. Ultimately, our work showed that an accurate optimization of the coupling efficiency requires simulating the full system, and investigating the energy the plasmon actually carries through Fourier Transforms of the near field. Quantitatively speaking, this method is superior to investigating the average field only, as the average near field contains many k components that cannot be coupled to a GPP.

However, the average field criterion needs not to be dismissed entirely. As we showed here, it still leads to a good first order approximation of the optimal coupling efficiency. Unlike our criterion that requires numerical methods to compute the full system, the average field criterion can be used with analytical or pseudo-analytical models, or numerical methods or softwares that are unable to simulate the full system, graphene being fairly hard to simulate.

A third parameter that has not been explored is the nanoantenna thickness, but this parameter also affects the distance between the graphene sheet and the substrate, and can then not only affect the antenna behavior, but also the properties of graphene itself.

3.4 Designed system based on GPP

In equation (2.30), we can notice the importance of the Fermi energy for achieving a long propagation. However, it has been shown that suspended graphene is free of intrinsic doping [16]. Suspended graphene

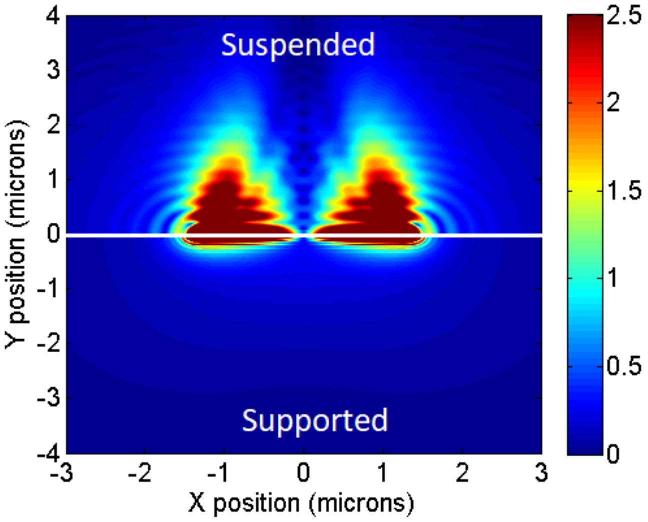

Figure 3.18: Map of the electric near-field intensity, for an excitation of $11\mu m$, with a limit up on the color scale in order to see the plasmon propagating through graphene. The nanoantenna is on the center of the map. The graphene is set with a fermi energy about 0.2eV and a mobility of 1 $m^2s^{-1}V^{-1}$. The dimensions of the rod are optimized for strong plasmons in y-direction : L=2750nm and W=50nm.

is thus characterized by a limited value for E_F while high mobility constitutes a clear asset that has been discussed in many published papers [37, 109, 150]. The design of a nano-opto-electronic system based on suspended graphene should take into account this issue. Therefore, it is important to engineer a system offering the possibility to inject charges through electrostatic gating. On SOI substrates with 300nm of SiO_2 layer, it has been shown the possibility to apply a difference of potential Vg higher than 100 V [117]. Modeling a capacitor between graphene and a Si-doped substrate, with two dielectric layers in between (SiO_2 300 nm, air 100 nm, see inset of Fig. 3.19), we can estimate a Fermi energy through:

$$E_F = \hbar v_f \sqrt{\pi n} = \hbar v_f \sqrt{\pi \frac{C_g V_g}{e}} \tag{3.30}$$

$$C_g = \left(\frac{1}{C_{air}} + \frac{1}{C_{SiO_2}} \right)^{-1} \tag{3.31}$$

$$C_{air} = \frac{\epsilon_{air}\epsilon_0}{t_{air}} \quad \text{and} \quad C_{SiO_2} = \frac{\epsilon_{SiO_2}\epsilon_0}{t_{SiO_2}} \tag{3.32}$$

Where t_{air} and t_{SiO_2} are the thicknesses of the air gap and the SiO_2 layer respectively and C_g is the total capacitance. We find $E_F \approx 0.2$eV, which justifies the value used in the previous section. In addition, the gate potential that is applied between the graphene and the substrate will bend the graphene, resulting in a deflection height h_0 that is a function of C_g, and therefore of the dielectric used. It is also a function of the potential applied V_g, and of the length of suspension L. At high V_g, we can obtain the deflection as [14] :

$$h_0 = \left(\frac{3PL^4}{64Et} \right)^{1/3} \tag{3.33}$$

$$P = \frac{c_g^2 V_g^2}{2\epsilon_0} \tag{3.34}$$

With E the Young's modulus in graphene which is about 1TPa, L the length of the trench, t the thickness of graphene, which is taken as 3.410^{-10}m, and P the electrostatic pressure.

Let us consider the case where the graphene is suspended straight over a 100 nm deep gap, (therefore with a maximum deflection h_0 of 100nm), and a gate voltage V_g of 100V. This enables us to design

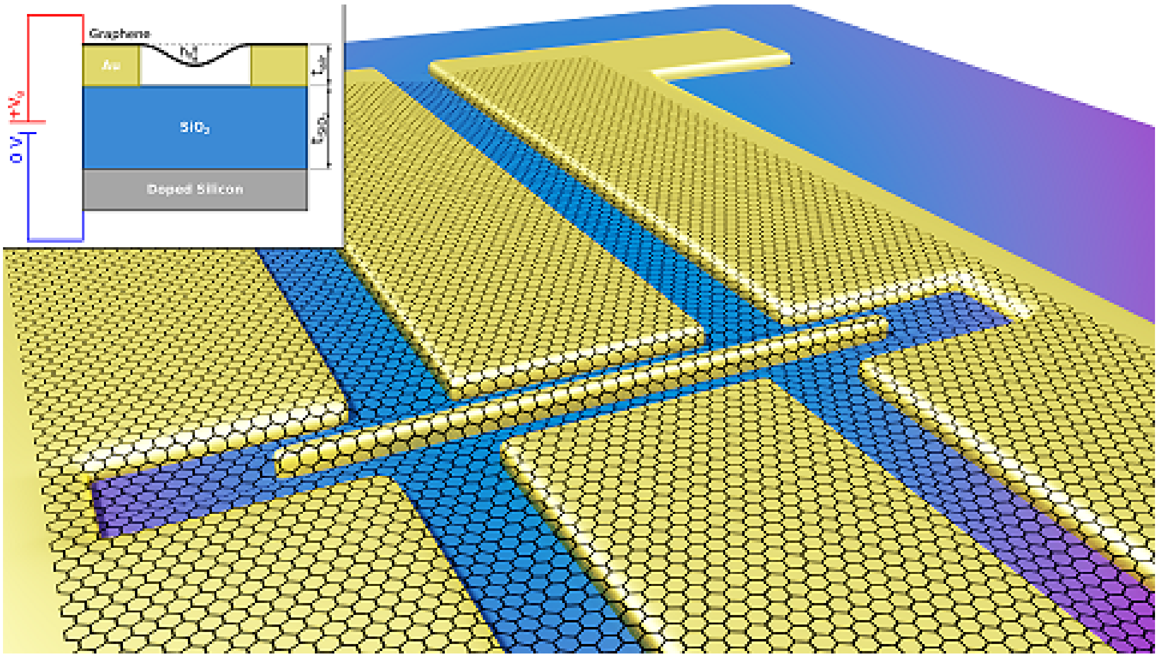

Figure 3.19: Illustration of the system studied. A plasmonic antenna is lying on a SiO_2/Si substrate. Gold nano-slots gather and propagate the plasmons on suspended graphene. The slab has also a function of electrode for doping suspended graphene. Gold, Si and $Si0_2$ are represented in yellow, gray and blue respectively. Inset : a schematic side view along the x axis of the graphene, golden slot and substrate. The deflection height h_0 is also represented.

a trench of L=1.5μm, using Equ. (3.33). Taking into account the penetration depth of the plasmons in air which is $1/Re(k_p) \approx 41$nm, we have a maximum deflection depth $h_0 = 60$ nm, and a maximum suspension length around $L = 1\mu$m so that the plasmon experiences damping from the subtrate that is as weak as possible.

As a result, we propose the design (see Fig. 3.19) of a realistic sample taking into account the different experimental parameters discussed above. On a SiO_2(300nm)/Si substrate are lying gold structures, which will also play the role of suspension support for graphene, including a nanorod (antenna) for launching GPPs. The thickness of the gold support and the gold antenna is set at 100nm. The gold nanoantenna is embedded in a gold nano-slots system perpendicular to the rod long axis. Gold slots, of 300nm of width, are designed to both suspend graphene and guide GPPs perpendicular to the rod long axis, opening the route to future nanophotonic circuitry based on suspended graphene.

Four slots are designed: two per extremities, in positive and negative y-directions. The extreme left and right parts of the gold constituting the slots are designed to be used as electrodes, in-between which voltage can be applied to generate current in gold. High temperature induced in graphene by high current (joule effect) have shown an improvement of the mobility in suspended graphene, by evaporating the thin layer of pollutants stuck on the carbon sheet after graphene transfer. In fact, electric current is one of the most efficient way to heat the graphene up and clean it, in order to get the best mobility in suspended graphene [150]. Finally, a difference of potential V_g is applied between the Si doped substrate and the graphene, in order to raise the Fermi energy.

Suspended graphene should be free of charge impurities, strain, corrugation and remote interfacial phonons induced by the substrate. The mobility, which is the physical value taking into account those effects, would increase up to one order of magnitude [137] in suspended graphene, as compared to the one on Si/SiO_2 substrate. However, studies predicted that the graphene mobility at T>10K could not exceed 4 $m^2s^{-1}V^{-1}$ [22, 103] due to flexural phonon. Recent reports measured a mobility of 1.5 $m^2s^{-1}V^{-1}$ [37], up to 38 $m^2s^{-1}V^{-1}$ [150] in CVD suspended graphene at low Fermi level. Therefore, 1 $m^2s^{-1}V^{-1}$ for a Fermi energy of 0.2eV in suspended graphene is reliable.

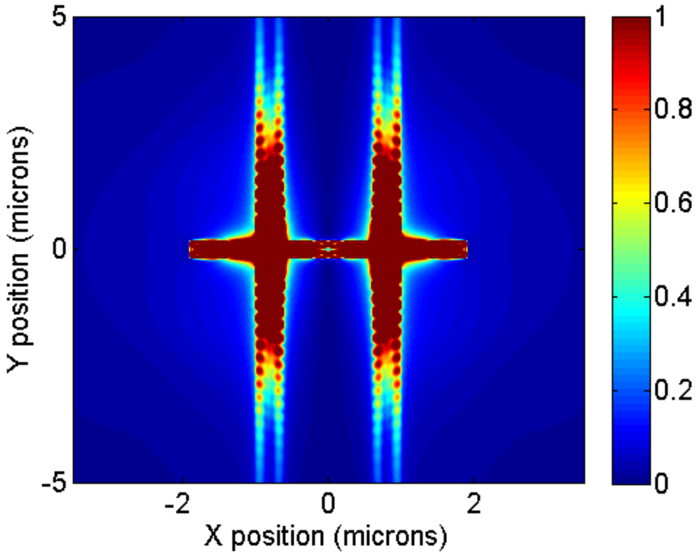

Figure 3.20: Map of the electric field intensity, for an excitation of $11\mu m$, with a limit up on the color scale in order to see the plasmon propagating through graphene. The nanoantenna is on the center of the map (y=0). We have set the graphene with a Fermi energy of 0.2eV and a mobility of 1 $m^2 s^{-1} V^{-1}$.

Similarly to Fig. 5, we simulated this system, and obtained the map of the electric field intensity shown in Fig. 3.20. In the middle of the map is laying a gold nanorod of $2.75\mu m$ of length, 80 nm of width, and 100nm high which is launching plasmons perpendicular to the long axis (x axis) of the antenna, i.e. along the y axis. As we have seen in Fig. 3.17, the width of the rods should be as small as possible. However, the height of the nanorods is set to 100nm in order to safely suspend graphene. For mechanical stability reasons when the rod is fabricated from e-beam lithography, it is better to consider a width comparable to the height of the structure. Therefore, we choose a width of about 80nm. The length of the rod corresponds to a resonance around 11 microns, where graphene plasmons exhibit an optimal propagation.

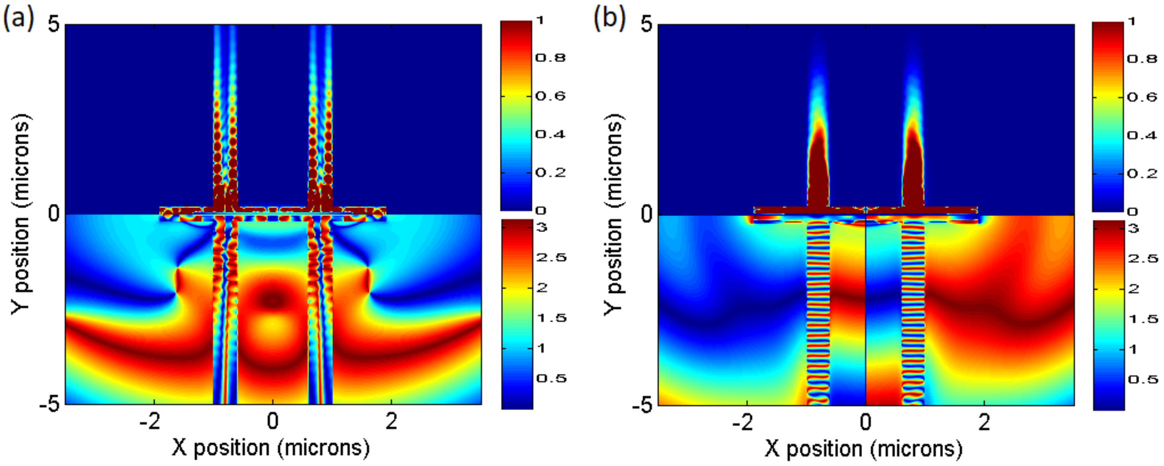

Figure 3.21: Maps of the intensity (on the top) and the phase (on the bottom) of the (a) x component of the electric field, and the (b) y component of the electric field of the system described in Fig. 3.19

While figure 3.20 reveals the micronic propagation of the total photonic intensity, Fig. 3.21 provides more informations. Two modes are appearing in the channel.

Figure 3.21(a) shows a TE-like mode where we have a strong intensity of the x component of the electric field. This mode is partly supported by the edges of the gold slots and is likely to result from coupling between GP and sharp metal edges. Properly speaking, it does not correspond to any pure GP modes.

Figure 3.21(b) shows a TM-like mode, which is the GP mode, with a strong intensity of the y component of the electric field. That is the surface plasmon mode of interest. It is worth noticing that the associated wavefronts, shown in the bottom of Fig. 3.21(b), are clearly defined by the phase giving a GPPs wavelength $\lambda_p \approx 265nm$, that is to say an effective index $n_{eff} \approx 41.5$. Again, the plasmons propagation length can be calculated using the exponential decay of the electric field along the slab. In case of Fig. 3.21(b) we find L_p higher than 525nm. The reduction of the propagation length is due to the confinement of the GPs path by the golden slots. Reducing the width of the slot decrease the propagation length.

As pointed out above, higher propagation length in supported CVD graphene, fabricated on industrial scale, could be achieved with higher Fermi energy. In the case of chemically doped graphene, taking data from [158], we find a propagation length of 1 micron in suspended graphene, as compared to the 300nm with graphene on SiO_2, using the same data.

Moreover, it is worth noticing that the propagation length is a conservative value. For example, the propagation length for the system described above is about 540nm. However, as we can observe Fig. 3.21(b), the intensity of the electric field decreases to the intensity of the incident light at a distance of 2 microns, that is to say about 4 times the propagation length. This phenomenon results from the field enhancement at the launching resonant nanoantenna.

Finally, it is important to notice that the simulations here do not take into account the interaction between graphene and metal. It is known that metal can transfer charges at the vicinity of graphene, which could lead locally to highly doped graphene, as high as 0.4eV [141]. As we have seen in Equ. (2.30), the propagation length of graphene plasmons is directly proportional to the Fermi energy. Therefore, it could lead to a strong increase of the GPPs propagation.

3.5 Discussion on the applied electric field

An issue uncovered by this study may arise at the experimental step. Indeed, the FDTD does not take into account electro-static phenomenon, such as electrostatic gating. To implement the injection of charge in graphene, the Fermi level parameter has to be changed. However, the electric and magnetic fields in the different materials are not taken into account.

In order to inject charges in graphene, the effective electric field applied to the graphene is huge. Therefore, the dielectric materials in between graphene and the back gate conductive layer should tolerate high electric field amplitude. The property related to the maximum electric field that a material can withstand without breakdown is called the dielectric strength. The dielectric strength of air is about 3MV/m. For a good thin film of SiO_2, it is possible to have 500MV/m. H-BN dielectric breakdown has been recorded as high as 1GV/m [60, 74]. Diamond can theoretically reach higher value [51, 156]. And finally, ideal vacuum would withstand electric field as high as 10^9GV/m.

Coming back to the case of the study developed in this chapter, Section 3.4, the system is made of a double layered dielectric sandwiched in between graphene and conductive substrate (Figure 3.22). In order to be effectively accumulating charge in graphene, it has been anticipating breakdown phenomenon. As such, the amplitude of the electric field inside the SiO_2 have been kept away from its dielectric strength, 0.5GV/m. Doing so, the capacitor effect would take place. Unfortunately, the thin layer of air would be able to disrupt the injection of charge in graphene.

When looking at the electric field in the different materials i for such system composed of a serie of capacitor, it is possible to write :

$$\mathbf{E_i} = \frac{C_{tot}}{d_i C_i} Vtot \tag{3.35}$$

with $\mathbf{E_i}$ the electric field amplitude in the dielectric i, d_i the thickness of the dielectric layer i, C_{tot} and C_i the capacitance of the total system in Farad per square meter $F.m^{-2}$, and V_{tot} is the difference of potential at the extremities of the multilayer.

$$C_i = \frac{\epsilon_0 \epsilon_i}{d_i} \tag{3.36}$$

Inserting Equation 3.36 into Equation 3.35 leads to :

$$\mathbf{E_i} = \frac{C_{tot}}{\epsilon_0 \epsilon_i} Vtot \tag{3.37}$$

The electric field amplitude in the dielectric medium i is therefore given by Equation (3.37). Higher is the static dielectric constant, and lower is the electric field. To come back to our system made of SiO_2 and air, the electric field will be much higher in the air. However, in order to get significant injection of charge in graphene, we stand at the limit of voltage breakdown in the SiO_2. The disruptive electric field in air being lower than the one in SiO_2, it will ionized the air. The air will become a plasma that will bring the charges down to the surface of the SiO_2, instead of staying in the suspended graphene. The graphene will therefore be screened and will not be significantly impacted by the electrostatic gating.

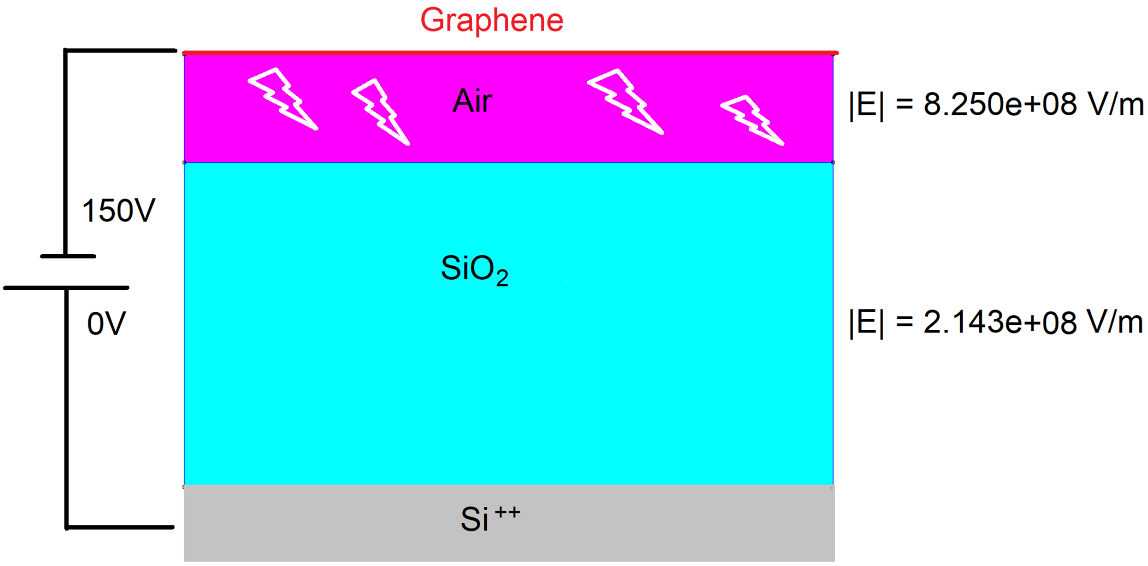

Figure 3.22: Schema illustrating the double layer capacitor used in the study of suspended graphene in Section 3.4. Two thin dielectric layer, air and SiO_2, are sandwish in between two electrode which are the graphene and heavily doped silicon substrate Si^{++}. A potential of 150V is applied in order to preserve the system of breakthrough, in a part of the sample where graphene is supported on SiO_2. The amplitude of the electric field in the two dielectric layers are displayed on the right.

3.6 Conclusion

In this chapter, a numerical study have been presented. After a brief history of the FDTD method, the solution for a one-dimensional wave problem have been solved, and then applied to the 3D case. The technique to modalize graphene in a 3D simulation have been discussed. Finally, a design is proposed, using antenna, to study the propagation of plasmons in suspended graphene.

Some concerns about the feasibility of such experiment at ambient condition are giving rise to a final discussion. A set up using a vacuum chamber would be probably required to obtain the measurement expected in laboratory.

Chapter 4

Experimental procedure

In this chapter, the experimental achievements are described. Chronologically, the fabrication of the first samples have been done in parallel with the numerical simulation work presented in Chapter 3. Therefore, a part of the work explained below was in fact a first try in order to record plasmons in suspended graphene and the design may be a bit different than the one shown in the previous chapter. Also, it did not take into some issues evoked in section 3.5, where it is explained why a high vacuum Scanning Near-field Optical Microscope (SNOM) set up is required for recording plasmons on suspended graphene.

Therefore, as a first step, the process to fabricate sample with suspended graphene is described, as well as the different designs that we wanted to study. Then, characterisation of the graphene based on Raman spectroscopy is discussed. Finally, preliminary SNOM data will be shown and commented.

4.1 Fabrication of sample

The samples with suspended graphene have been fabricated in Singapore, at the Center for Advanced 2D Materials.

4.1.1 Fabrication process of suspended graphene samples

Hereafter are presented the patterns fabricated with the goal to observe and measure the propagation distance of Graphene Plasmons.

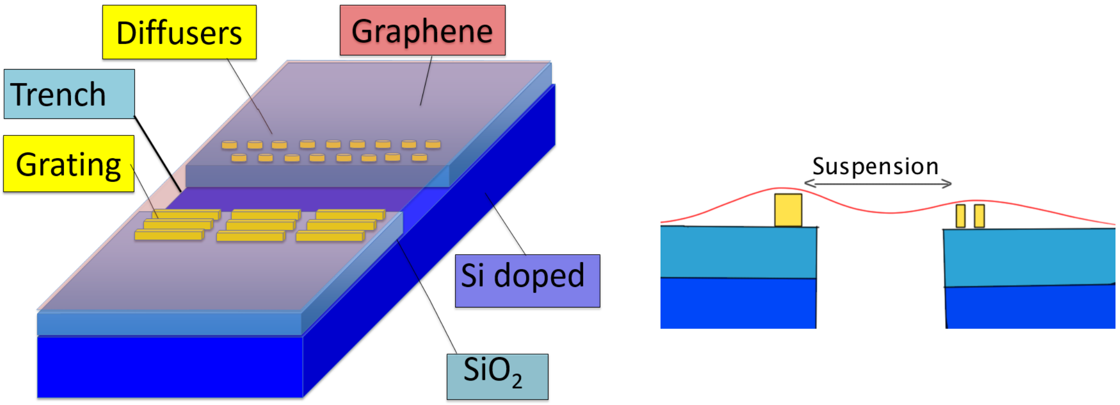

(a) A perspective view of the sample

(b) Cross-section view of the sample

Figure 4.1: Illustration of the design for the study of graphene plasmons through suspended graphene. The graphene monolayer (red) is on the top of the system. The gold nanostructures are in yellow and the substrate is made of SiO_2(300nm, light blue)/Si(dark blue) doped wafer.

A preliminary set of simulations have shown the possibility to excite graphene plasmons with plasmonic structures (see Section 3.3). The shape that was theoritically studied is that of the simple rectangular antenna, and the first results gave micrometric length and several tens of nanometers for the width and height. An illustration of the sample is showed Figure 4.1a. The graphene layer is deposited on the top of the system that is made of the substrate, the gold plasmonic nano-structures and the holes.

One of the challenges of fabrication process was to place the antenna really close to the holes in order for plasmonic structures to launch plasmons in suspended graphene (see Figure 4.1b). Gold scatterers were placed on the opposite side of the holes: small gold disks were designed to perturb in propagating graphene plasmons and to scatter them into the far field.

In order to avoid the pollution of the graphene layer, it has been decided to deposit it on the sample at the last step. Therefore, the fabrication process of such samples begins by etching holes and depositing plasmonic structures as close as possible to the edges. Since the structures need to be firmly bounded to the surface when the graphene is added at last, colloidal suspension has been dismissed. The rod being needle-like from the simulations results (section 3.3), e-beam lithography has been used. The holes are micrometric because the propagation length of the plasmons is expected to be micrometric. Therefore, photo-lithography (laser writer) has been used to pattern the holes, as the resolution of this technique is a bit less than a micron.

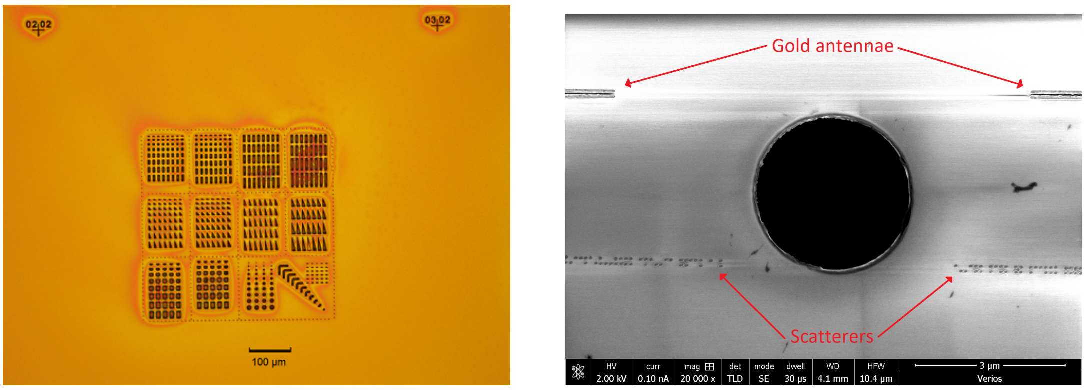

(a) Optical image of a pattern of holes, designed by laser writer and etched through RIE process. A thin layer of PMMA have been then deposited on the surface in order to perform e-beam lithography. The difference of colors represent gradient of the PMMA layer thickness.

(b) MEB image of a disk shaped hole with gold antenna (rods) and scatterers (dots)

Figure 4.2: Optical (a) and electronic (b) image from microscope of the samples fabricated for the study of Graphene plasmons in suspended Graphene

At first, micrometric markers (crosses with number) and holes have been designed on samples through laser writer technique (see Figure 4.2a). In fact, the resolution of the system LW405-A is about 700nm and has been tested. The wavelength of the writing beam is 405 nm (GaN solid state laser). The markers have been added in order to make possible a nanometric alignment with the e-beam lithography process. This technique is used to deposit the plasmonic nano-antenna close to the holes.

Thanks to a laser interferometer system that guides the stage of the laser writer, the markers are aligned with a resolution below 100 nm. The holes were designed with different shapes, including rectangles, disks and triangles. Finally, the biggest issue was to find out a way to deposit plasmonic structures as close as possible from the hole edge.

As it can be observed in Figure 4.2b, the nanostructures are not present (neither diffusers nor antennas) near the hole edge. They are present few microns away from the holes (red arrows). However, it is possible to observe carefully on the Figure 4.2b those structures left "footprint" near the holes.

This is the first major issue when fabricating the samples. When looking at the PMMA resin before the e-beam lithography process (Figure 4.2a), it is possible to see different color at the vicinity of the holes. It is supposed that the following scenario happened.

When the PMMA is spin coated on the whole pattern, it is deposited on all the surface of the sample. As we get closer to the holes, the thickness of the resin is getting thinner (Figure 4.3(a)). Then, during the development step, the PMMA exposed at the vicinity of the holes is removed (Figure 4.3(b)). Finally, the gold is deposited on the top of the sample (Figure 4.3(c)). But the problem is that the gold layer thickness is of the same height than the PMMA layer at the vicinity of the hole. This is the reason why, during the lift-off step, the structure closer to the holes were removed (Figure 4.3(d)). However, the footprint let by the antenna and diffusers at the end of the process can still be observed in Figure 4.2b.

Therefore, the deposition of the plasmonic structures has to be done at first, and then, the holes have been etched through Reactive Ion Etching (RIE).

In order to reduce the duration of e-beam lithography process, the markers have to be done at first by laser writer. Therefore, the main steps of the process have been plan as follows :

1. Markers designed by photo-lithography (laser writer)
2. Deposition of metal for the markers
3. Nano-structures designed by e-beam lithography
4. Deposition of metal for the nano-antenna
5. Pattern of holes designed by photo-lithography (laser writer)
6. Etching of the holes through RIE

The six steps listed above are detailed in the following pages.

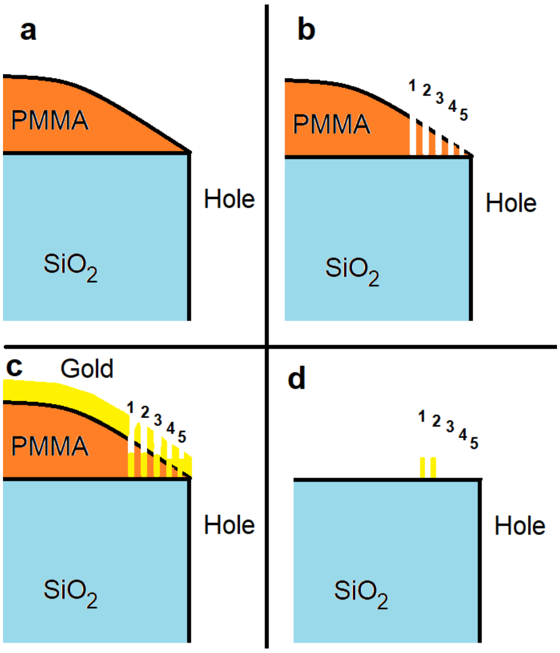

Figure 4.3: Illustration of the main problem that was encountered during the fabrication of the samples dedicated to the study of graphene plasmons.

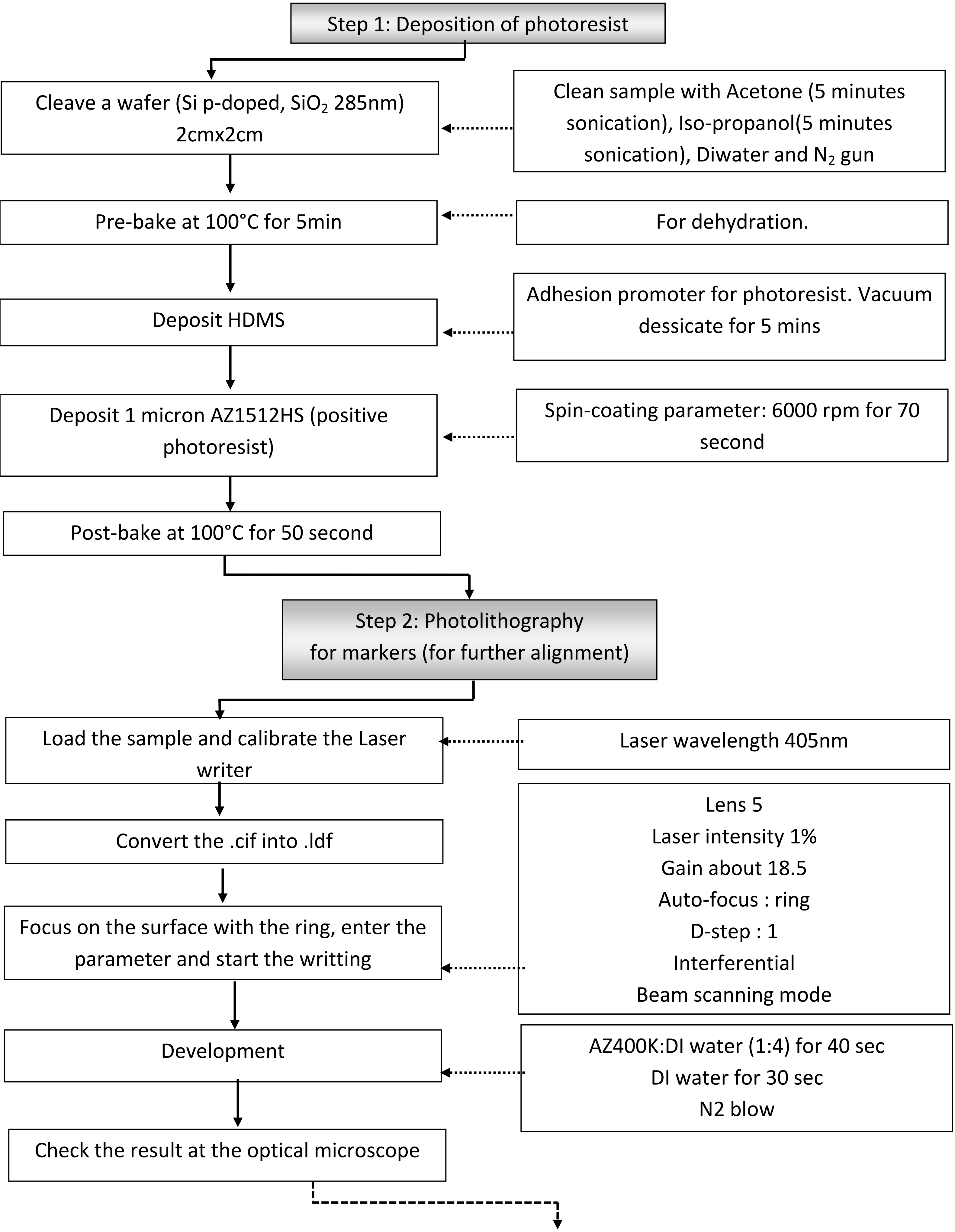

Step 1: Deposition of photoresist

Cleave a wafer (Si p-doped, SiO_2 285nm) 2cmx2cm

Clean sample with Acetone (5 minutes sonication), Iso-propanol(5 minutes sonication), Diwater and N_2 gun

Pre-bake at 100°C for 5min

For dehydration.

Deposit HDMS

Adhesion promoter for photoresist. Vacuum dessicate for 5 mins

Deposit 1 micron AZ1512HS (positive photoresist)

Spin-coating parameter: 6000 rpm for 70 second

Post-bake at 100°C for 50 second

Step 2: Photolithography for markers (for further alignment)

Load the sample and calibrate the Laser writer

Laser wavelength 405nm

Convert the .cif into .ldf

Focus on the surface with the ring, enter the parameter and start the writting

Lens 5
Laser intensity 1%
Gain about 18.5
Auto-focus : ring
D-step : 1
Interferential
Beam scanning mode

Development

AZ400K:DI water (1:4) for 40 sec
DI water for 30 sec
N2 blow

Check the result at the optical microscope

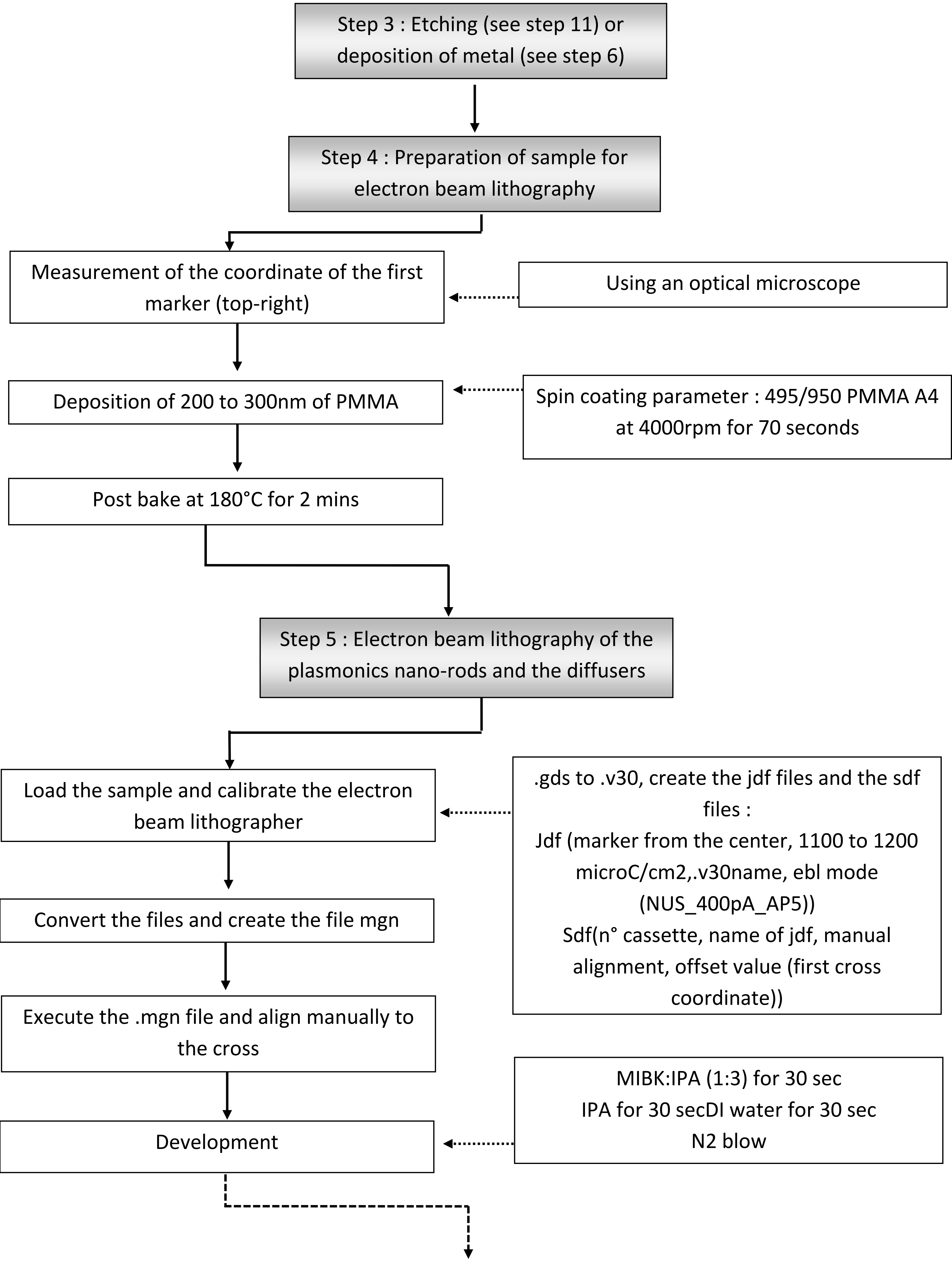

Step 3 : Etching (see step 11) or deposition of metal (see step 6)

Step 4 : Preparation of sample for electron beam lithography

Measurement of the coordinate of the first marker (top-right)

Using an optical microscope

Deposition of 200 to 300nm of PMMA

Spin coating parameter : 495/950 PMMA A4 at 4000rpm for 70 seconds

Post bake at 180°C for 2 mins

Step 5 : Electron beam lithography of the plasmonics nano-rods and the diffusers

Load the sample and calibrate the electron beam lithographer

.gds to .v30, create the jdf files and the sdf files :
Jdf (marker from the center, 1100 to 1200 microC/cm2,.v30name, ebl mode (NUS_400pA_AP5))
Sdf(n° cassette, name of jdf, manual alignment, offset value (first cross coordinate))

Convert the files and create the file mgn

Execute the .mgn file and align manually to the cross

Development

MIBK:IPA (1:3) for 30 sec
IPA for 30 secDI water for 30 sec
N2 blow

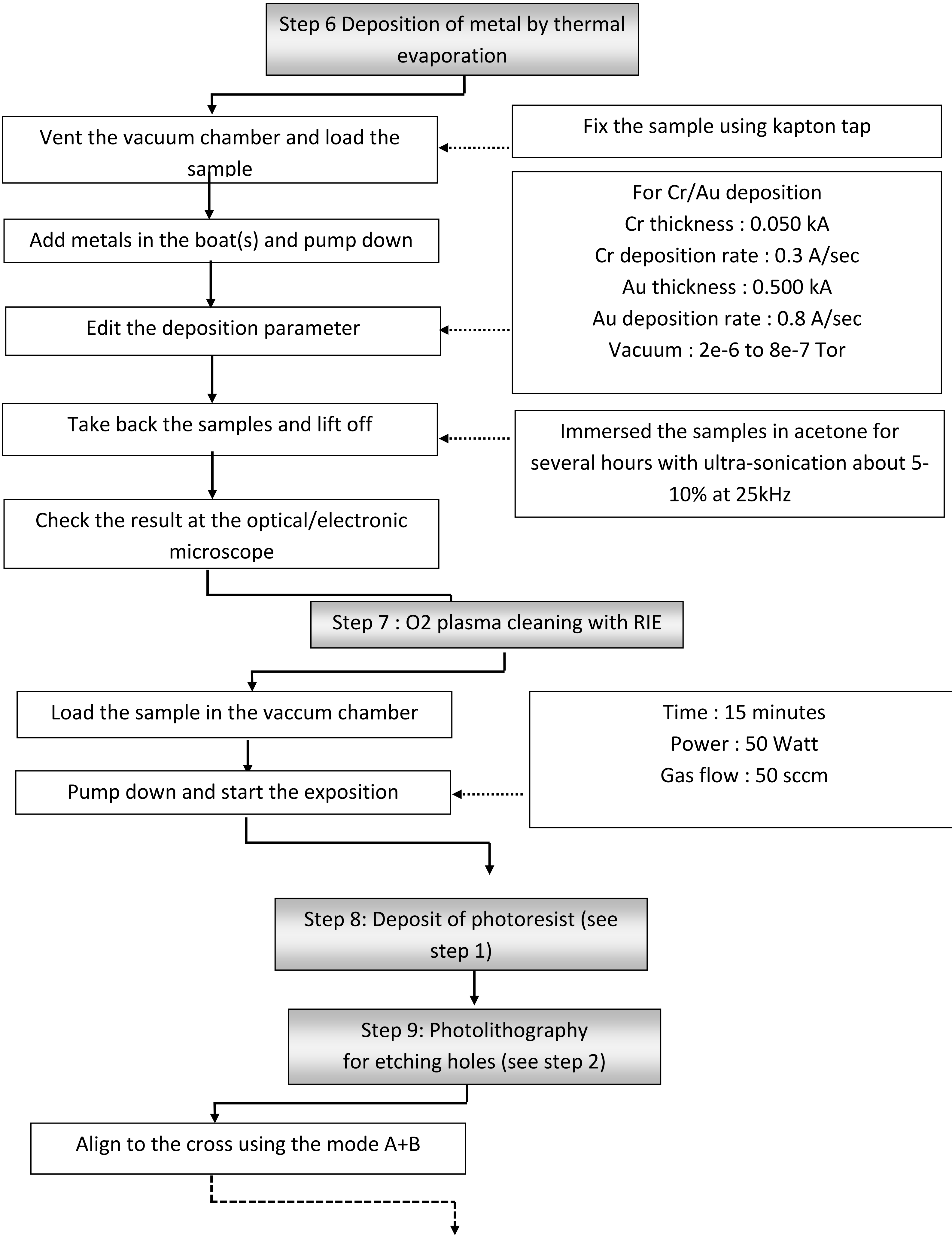
Step 6 Deposition of metal by thermal evaporation
Vent the vacuum chamber and load the sample
Fix the sample using kapton tap
Add metals in the boat(s) and pump down
Edit the deposition parameter
For Cr/Au deposition
Cr thickness : 0.050 kA
Cr deposition rate : 0.3 A/sec
Au thickness : 0.500 kA
Au deposition rate : 0.8 A/sec
Vacuum : 2e-6 to 8e-7 Tor
Take back the samples and lift off
Immersed the samples in acetone for several hours with ultra-sonication about 5-10% at 25kHz
Check the result at the optical/electronic microscope
Step 7 : O2 plasma cleaning with RIE
Load the sample in the vaccum chamber
Time : 15 minutes
Power : 50 Watt
Gas flow : 50 sccm
Pump down and start the exposition
Step 8: Deposit of photoresist (see step 1)
Step 9: Photolithography for etching holes (see step 2)
Align to the cross using the mode A+B

Step 11 : Deep RIE etching for digging holes

Vent the vaccum chamber and fix the samples on the bare Si wafer

Fix the samples using oil for better temperature transfer

Pump down the chamber and edit the duration in order to etch 300nm of SiO2

Edit : time 02min 36 sec

STEPS	DESCRIPTION	RF	ICP	CHF3	Ar	Press	Time	HC
		W	W	sccm	sccm	mT	min	T
Step 1	Pump down	0	0	0	0	0	1'	0
Step 2	Preheat	0	0	0	40	5	3	8
Step 3	Etch	100	650	25	40	5	xxx	8
Step 4	Pump down	0	0	0	0	0	1'	0

Vent the vaccum chamber and fix the samples on the SiO_2 wafer

Fix the samples using oil for better temperature transfer

Pump down the chamber and edit the number of loops in order to etch 20 µm of Si

Edit : repeat 38

STEPS	DESCRIPTION	RF	ICP	C4F8	SF6	Press	Time	HC
		W	W	sccm	sccm	mT	min	T
Step 1	Pump down	0	0	0	0	0	1	0
Step 2	Temp stable	0	0	50(O2)	0	15	3	8
Step 3	Strike	100	1000	50(O2)	0	15	5"	8
Step 4	Repeat xx							
Step 5	Dep	3	1300	100	5	40	5"	8
Step 6	Etch	30	1150	5	100	30	7"	8
Step 7	Loop							
Step 8	Pump down	0	0	0	0	0	1	0

Take back the samples and lift off

Immersed the samples in acetone for several hours with ultra-sonication about 5-10% at 25kHz

Check the result at the optical/electronic microscope

4.1.2 Patterns for the study of GPs propagation

Different patterns have been fabricated in order to investigate different platforms for the propagation of graphene plasmons. Several hole designs have been made. The shape of the trench have been made triangular (figures 4.4a and 4.4b), circular (4.4c and 4.4d) and rectangular (4.5a and 4.5b).

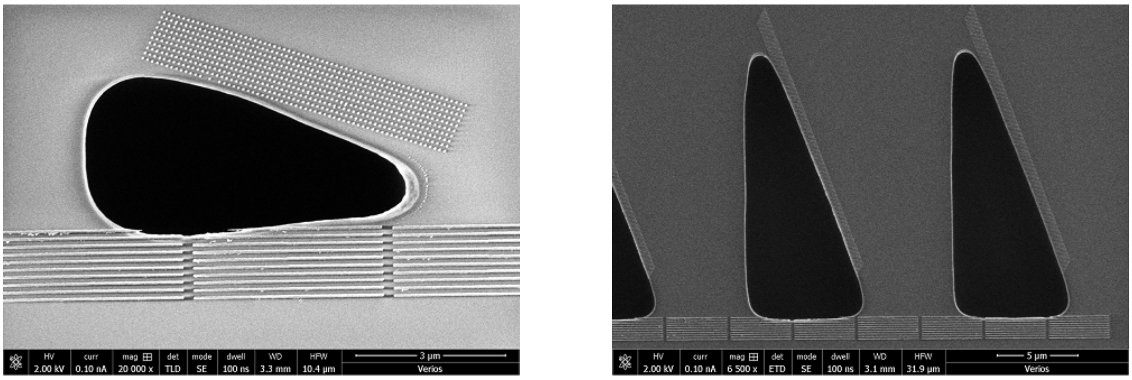

(a) Hole with small trianglular shape (b) Hole with large trianglular shape

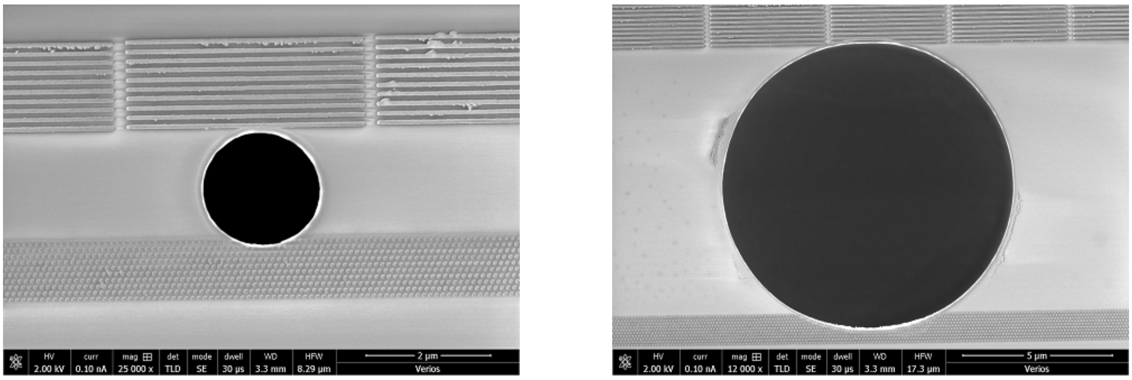

(c) Hole with small circular shape (d) Hole with large circular shape

Figure 4.4: SEM pictures of the samples fabricated in the clean room following the simulation set up. We can see on the different images gold nano rods of 4 μm on one side of the holes, and gold diffusers, tubular shape, on the other side of the holes.

These holes are designed to suspend graphene on them. Thanks to a highly accurate alignment between e-beam lithography and photo-lithography, plasmonics nano rods and scatterers are placed very near the edges of the holes. As already emphasized, one of the most challenging part of the fabrication were to deposit the nano structures as close as it is possible from the holes. In fact, once the graphene is deposited on the whole structure, shown in picture 4.1b, it is important that the monolayer does not touch the substrate in between the gold structures and the holes. As we can see on the different SEM pictures (Figures 4.4a, 4.4b, 4.4c, 4.4d, 4.5a, 4.5b, 4.6a, 4.6b), the final results is promising and we can expect graphene to be suspended over the whole structures.

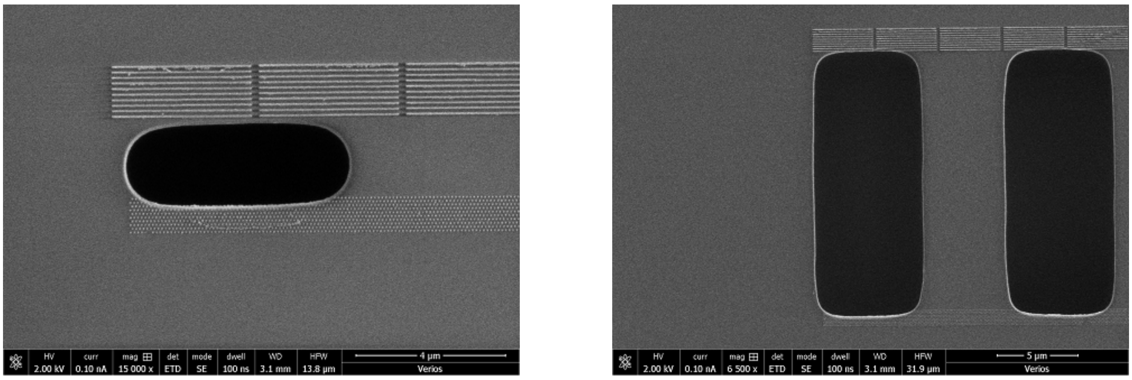

(a) Hole with small rectangular shape (b) Hole with large rectangular shape

Figure 4.5: SEM pictures of the samples fabricated in the cleanroom following the simulation data. We can see on the different images gold nano rods of 4 μm on one side of the holes, and gold scaterrer, circular shape, on the other side of the holes.

4.1.3 Patterns to study the wavelength of the SPPs

A second set of patterns have been made to study the wavelength of the SPPs through graphene via interferences phenomena.

With the patterns shown Figures 4.6a and 4.6b, we have the possibility to launch two plasmons from two different points.

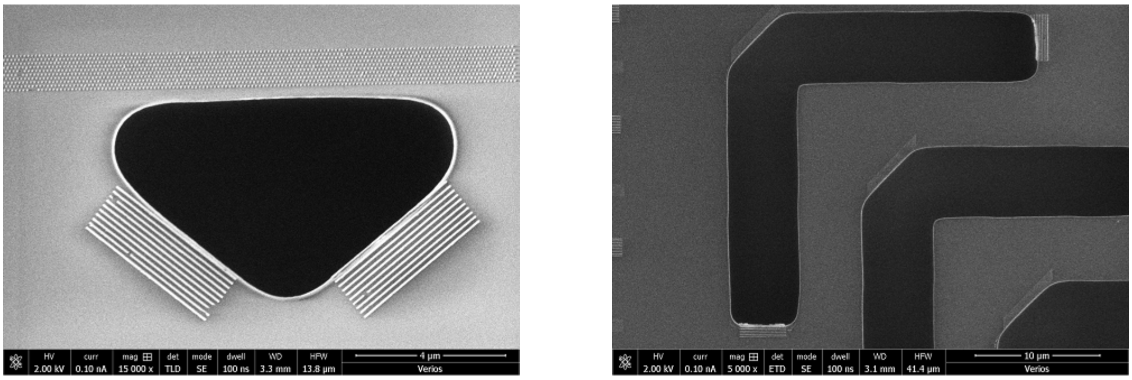

(a) Small trianglular shape of hole (b) Small trianglular shape of hole

Figure 4.6: SEM pictiures of the samples fabricated in the clean room following the simulation set up. We can see on the different images gold nanorods of 4 μm on one side of the holes, and gold scatterers, circular shape, on the other side of the holes.

These two surfaces waves would interfere with each other and an interference pattern may appear at the scatterers. In fact, we would expect to have an interference pattern that would be sampled by the scatterers, showing intense hot spots at the constructive interference location, and weak response at the destructive interference location. Similarly to the double-slit experiment (referred to as Young's experiment), we can describe our experience as shown in Figure 4.7.

Assuming that a plane wave excites the two stacks of nano rods with the same phase, at the same time, two SPPs will be launched as illustrated in Figure 4.7. Simplifying the problem to a two slits problem (see figure 4.7 on the right), the phase of the waves at the position x on the observation screen

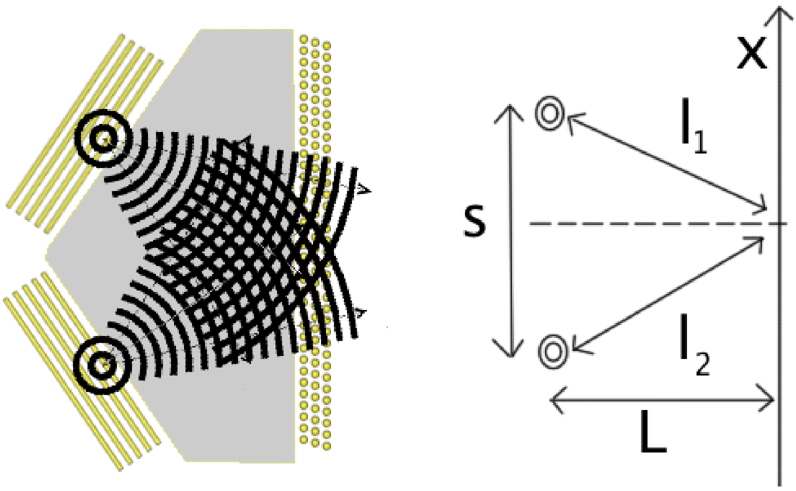

Figure 4.7: Illustration of the interference pattern. Left: realistic representation wih the fabricated sample. Right the problem simplified

(at the scatterers plane) relative to the phase at the slit (at the plasmonic nano rods) can be written as :

$$\Phi_{1,2} = kl_{1,2} = \frac{2\pi l_{1,2}}{\lambda_{SPP}} = \frac{2\pi}{\lambda_{SPP}}\sqrt{L^2 + (\frac{s}{2} \mp x)^2} \tag{4.1}$$

Therefore, the phase difference between the two waves can be written as:

$$\Delta\Phi = \frac{2\pi}{\lambda_{SPP}}\left(\sqrt{L^2 + (\frac{s}{2} - x)^2} - \sqrt{L^2 + (\frac{s}{2} + x)^2}\right) \tag{4.2}$$

For a period of $\Delta\Phi = 2\pi$, we should find the inter distance between the interference fringes via the following equation to be solved :

$$\left(\sqrt{L^2 + (\frac{s}{2} - x)^2} - \sqrt{L^2 + (\frac{s}{2} + x)^2}\right) = \lambda_{SPP} \tag{4.3}$$

There is no trivial solution to this equation, but we can estimate numerically the results using the experimental design. According to Figure 4.6a, we can take L=4 μm and s=6 μm. According to the numerical studied explained Chapter 3, we can suppose that $\lambda_{SPP} = 0.3\mu m$ (see also on the phase of the y component of the electric field, in Figure 3.21). These assumptions lead to the plot shown shown in Fig. 4.1a

From y=0.3 ($\lambda_{SPP} \approx 0.3\mu m$), we get that the period $x \approx 0.25\mu m$. The distance between diffuser being 100 nm (see Figure 4.8b), we could expect to have 2.5 scatterers, and then 2.5 measurements of the intensity for one period of the diffraction pattern. In vacuum condition, the induced density of charge in suspended graphene could be higher. The wavelength would therefore be higher, according to Equation (2.29). And finally, Equation (4.3) would give a larger period, where the number of diffusers would be more important. For example, for $E_F = 0.4$eV, $\lambda_{SPP} \approx 0.6\mu m$ and we get a period of interference about 0.5 μm.

4.1.4 Pattern to study the grating effect

Finally, in order to have the higher plasmons intensity possible, it would be promising to exploit the grating phenomenon, in addition to the resonance phenomenon of the nano rods. For this reason, it has been fabricated for each sample 4 different patterns with different spacings between the nano rods. In fact, the grating period of nano rods can be calculated to have an enhancement of the near field for a particular wave vector, which gives in terms of momentum (see Figure 4.9):

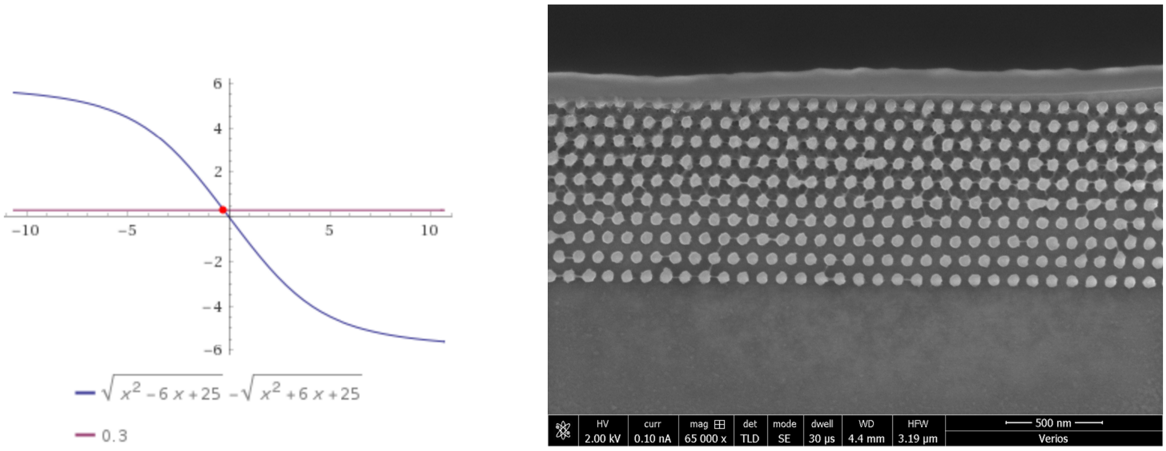

(a) Plot of the function $y = \left(\sqrt{x^2-6x+25}-\sqrt{x^2-6x+25}\right)$

(b) SEM picture of diffusers : small tubular gold structures spaced from each other by 100nm

Figure 4.8: Plot of the Equation (4.3) using experimental data from Figure 4.6a and SEM picture of the scatterers presented Figure 4.1a

$$k_{SPP} = k_0 \sin\theta + n\frac{2\pi}{d} \tag{4.4}$$

As we have seen previously in our simulation, we plan to illuminate our samples perpendicular to it. Therefore, $\sin\theta = 0$ and we find :

$$d = \frac{n2\pi}{k_{SPP}} = n\lambda_{SPP} \approx n300nm \tag{4.5}$$

So for a multiple of 300 nm, we should get a grating effect which should enhance the plasmons strength launched through the graphene. It has been therefore decided to fabricate several samples with different designs changing the spacing between the nanorods which are about 150 nm, 300 nm, 450 nm and finally 600 nm.

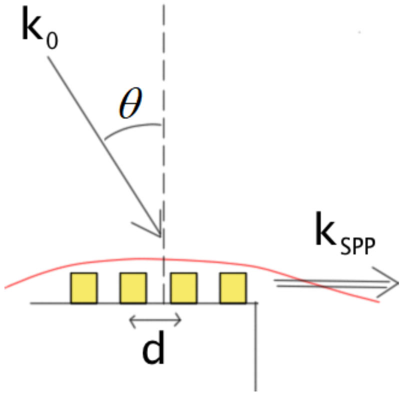

Figure 4.9: Illustration of the nano rods grating

4.2 Deposition of graphene and characterisation of the samples

It has been chosen to use CVD graphene which has been proved to sustain graphene plasmons [43].

As it has been explained before, the plasmons of graphene are highly sensitive to the surrounding. One of the main issue is to get really pure and clean graphene for low optical losses and high electrons mobility. At first, CVD graphene has been deposited in Singapore (see Figure 4.10).

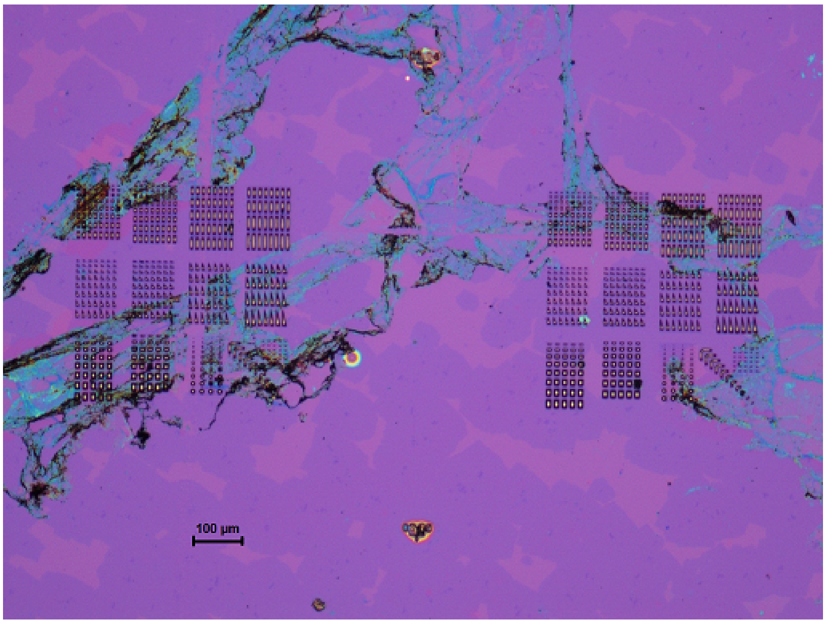

Figure 4.10: Optical image of the first sample where graphene has been deposited

As a first observation, it is interesting to notice that we can observe the presence of graphene on the sample, which appears to be dark blue in Figure 4.10 . This apparent color results from the interference of the incident visible light occurring in the multilayer Si/SiO2/graphene. A second remark is that the graphene is not homogeneously deposited on the surface. Instead, it covers sample with isles. Finally, the samples are covered by pollution chemical rest from the transfer process.

To address this issue, the samples have been chemically washed in order to remove impurities. Three baths have been prepared, one of acetone, one of isopropanol and one of deionized (DI) water.

Unfortunately, the results were not good enough and a lot of pollution remained, even after many washing cycles. A big part of the contamination is most probably coming from the PMMA. In order to have more information about the contaminant, Energy Dispersive X-Ray Spectroscopy (EDS) investigation has been performed.

This method consists in illuminating a sample with an incident x-ray light. Electrons in the inner shell of the atoms gets excited and the subsequent de-excitation of the particle is radiative. The photons emitted by the excited atoms are recorded and give spectra corresponding to a chemical entity. The results of this study is presented Figure 4.11.

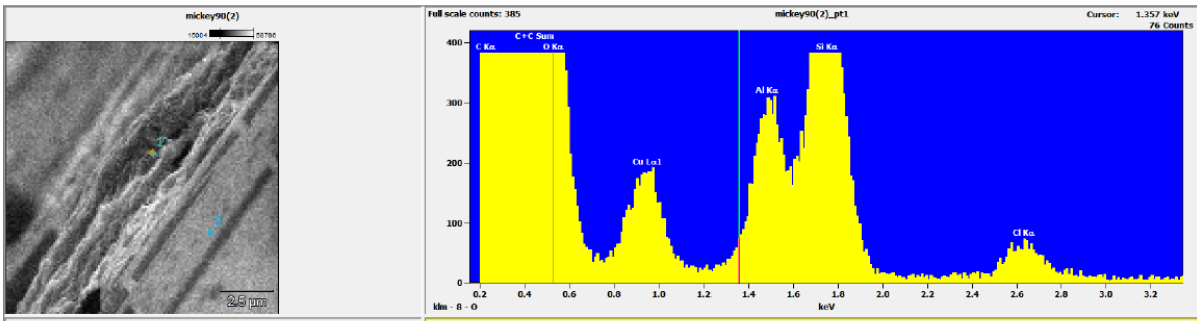

Figure 4.11: EDS screen shot where we have : on the left, a SEM picture of the zone studied, on the right, the spectrum obtained.

On the left of Figure 4.11, a SEM picture of the sample with a strong tilt. The tilt is important in order to maximized the response of the impurities. On the right side, the obtained spectrum is displayed, with the different chemical elements indicated above the different peaks. A high peak of carbon is visible, which comes from a carbon tape covering the sample holder. Carbon tape has been used in order to screen the response of the metallic holder where part of the electrons beam could land. Pronounced peaks corresponding to Silicon and Oxygen can be seen too. Both of them come from the substrate made of heavily doped silicon and a thin layer of silicon oxide. Additionally, even if the holder has been protected, it still gives an optical response as the aluminum and the copper are present on the spectrum. Finally, Chlorine is much more unexpected here, and it is not possible to remove it easily.

A washing attempt has been performed, using Reactive Ion Etching (RIE). RIE is a technique that uses a plasma to etch the sample surface. In our case, oxygen plasma has been used. It removed partly the impurities. However, graphene turned out to be removed too. As a backup strategy, new samples have been sent to our partner in Korea (Thanks to Rafael Salas (UTT, France) et Heejun Yang from Sungkyunkwan University (Korea)) for a successful deposition of graphene layer.

Figure 4.12 shows an optical image of a new sample with CVD graphene from Korea on the top of it.

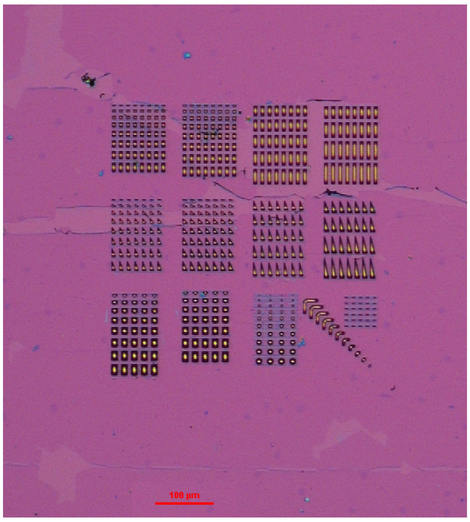

Figure 4.12: Optical microscope image of a pattern for the study of plasmons in suspended graphene with graphene deposited on the top from Korea

Here we can not distinguish any impurities, and graphene (that looks blue) is deposited homogeneously on the top of the sample, in many locations. The next step is to characterize it.

4.2.1 General presentation of Raman spectra in graphene

With Electron-Beam Microscopie (MEB) and Atomic Force Microscopie (AFM), Raman spectroscopy is a routine technique used to characterize graphene [155]. Whereas MEB and AFM may give physical images of the graphene, Raman spectroscopy can provide significantly more information based on the lattice vibration of the material. In fact, Raman spectroscopy is based on inelastic scattering of photons by matter (see Figure 4.13a), the difference of energy being recorded as the vibration of the lattice, or phonons. It is therefore a transfer of energy between the photon and phonon modes in a particular lattice, ie a kind of signature of each crystal. Because Raman spectra provide information about the lattice vibration, it is a technique that is really sensitive to the lattice structure and crystallinity. [47], the number of graphene layers[45], strain, defect and density of charges [89], among others [46]. Moreover, it is a technique that can be performed at room temperature, which is reliable, and non-destructive.

The conservation of the momentum tells us that we cannot probe phonons far from the centre of the Brillouin zone. This is due to the fact that the momentum of a photon is approximately three order of magnitude less important than the one of a phonon (wavelength of the light compared to the lattice

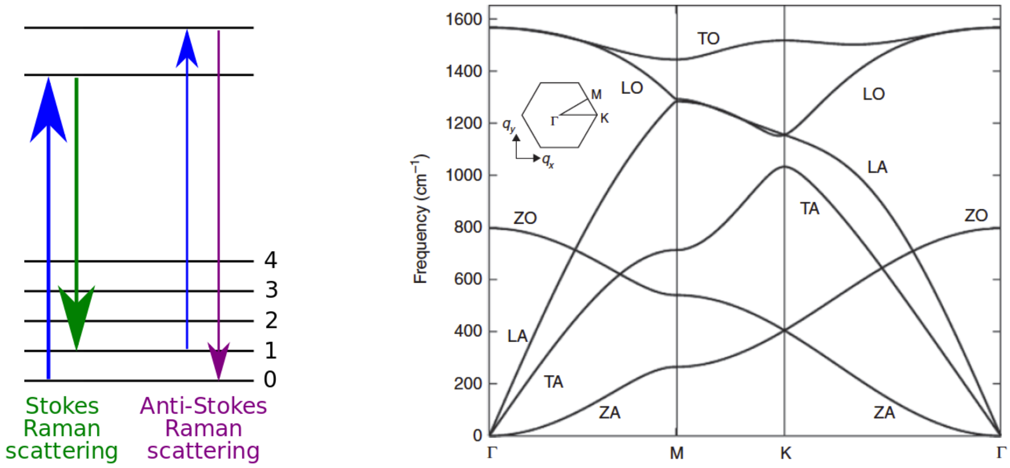

(a) Representation of the Raman effect

(b) Theoritical phonon dispersion of graphene according to [77]

Figure 4.13: Illustration of the Raman effect and the phonon dispersion in graphene

parameter). But the case of graphene is a bit more complicated, and the reason why will be briefly expounded hereafter.

It is not possible to experimentally get the whole phonon dispersion curve of graphene since there are not enough atoms in graphene flakes for inelastic neutron scattering experiment. However, it is possible to calculate it theoretically (see figure 4.13b).

On this figure, we can see six branches. They are called ZA, TA, LA, ZO, LO, TO. A is for acoustic, while O is for optics. Z stands for the flexural modes (out of plane) whereas L and T correspond to the in-plane Longitudinal and Transverse modes respectively. Only some of those modes are Raman active, and the theory predicts that the LO and TO branches are active [154] in a single layer of graphene. Then, looking at the Figure 4.13b, it is possible to predict that we should have a single peak around 1580 cm^{-1}, when performing a Raman experiment (Γ point in abscisse).

This peak, called G (G stands for "Graphite"), is clearly visible in Fig. 4.14. Because of the strong interaction electron-phonon in this zero-gap semiconductor near the centre of the Brillouin zone, the G peak is strongly dependent upon doping.

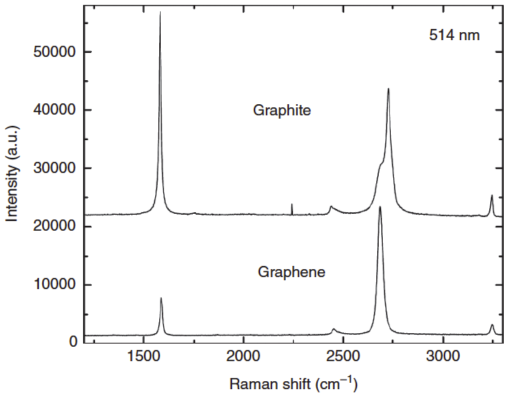

Figure 4.14: Raman spectra of graphite and graphene probed at a light wavelength of 514 nm [131]

However, the graphene shows a second peak, usually called 2D (also called G' sometime, because always present in graphene), around 2700 cm^{-1}. It has been interpreted [131] as a two phonon-interaction.

In fact, the inelastic scattering of the light is responsible for the emission of two phonon having opposite wavevectors, such as the momentum is conserved. This is the reason why they are always active in any graphene layer. This 2D peak is the second order of a D peak (therefore called 2D), that means that there is a D peak which involve only one phonon, and take place at a frequency $2700/2=1350 cm^{-1}$. This is due to the breathing modes of six-atom rings and requires a defect (D for defect) for its activation. Therefore, this particular peak is really sensitive to defect, grain boundary or edge (not present in the Figure 4.14). The ratio between the intensities of the D peak and the G peak provide a parameter that can be used to quantify the amount of disorder.
Several others peaks exist, mostly for defected graphene sheet. Reading and interpreting properly a Raman spectrum is not trivial, as valuable informations can be deduced from the position, the height, the area, the FWHM (full-width at half-maximum) and the dispersion (shift of energy as a function of the excitation wavelength) of each peak. In the following, we will focus only on the three peaks shown above, the G peak, the 2D peak and the D peak.

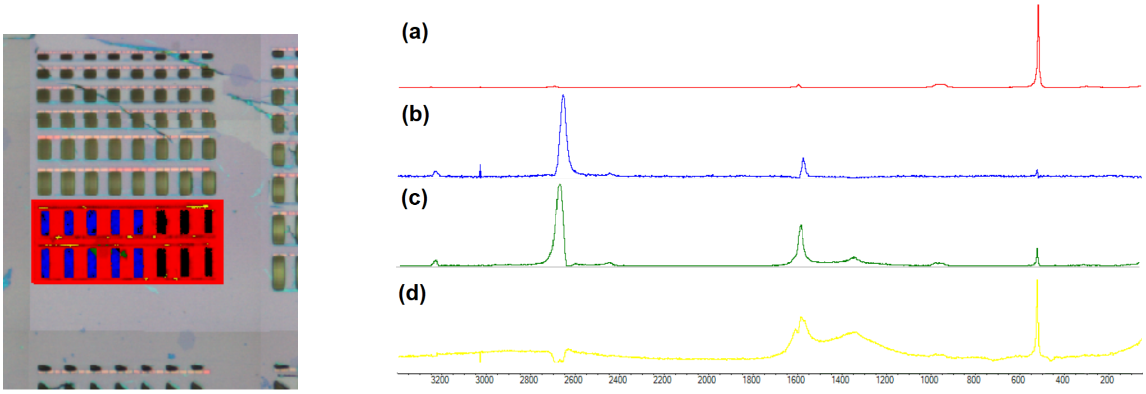

(a) Hyper-spectral Raman mapping

(b) Raman spectra corresponding to each color

Figure 4.15: Results of a raman spectra on top right part of the pattern represented Figure 4.12

It has been possible to use an hyper-spectral Raman tool (Thermofisher), which makes a Raman mapping of the sample possible. Its high spatial resolution (a few hundreds of nanometers), its fast scanning as well as its image processing tools make it a powerful equipment to identify suspended graphene on the sample. Figure 4.15 shows the results of a Raman mapping of one part of the pattern, using a discretization with four colour. The software categories four different type of Raman response via an algorithm. The four colors represent four Raman spectra illustrated Figure 4.15b, that can overlap each others.

The red color spectrum is relatively close to the Silicon response, with a peak around 520 cm^{-1}, and is present everywhere on the mapping, except in the deep holes (20 microns deep). The blue color is mainly present on the gold structure and in the holes. The green color appears everywhere except in the holes and finally the yellow color appears mainly on the gold structures.

The red Raman response is therefore coming from the substrate, made of silicon and silicon oxide. The blue and the green Raman spectra have a shape which is characteristic of the graphene response. However, when we look at them carefully, it is possible to distinguish them. The position of the blue peaks, related to graphene G and 2D modes, appear at lower energy, as compared to the green spectrum. Finally, the blue response of the 2D mode is much higher than the green one. According to [16], the blue colored raman spectra corresponds to suspended graphene, whereas green colored raman spectra corresponds to supported graphene. Therefore, the graphene have successfully been suspended on holes. Other parts of the sample also show suspended graphene.

The next step is to characterize the gold nanoantenna.

4.2.2 Characterisation of the gold nano-antenna

As it has been explained in Section 3.3, the gold nano-antennas are used for launching plasmons through graphene. In section 2.3.3, it has been shown that the lowest plasmons damping on SiO_2 lie around a wavelength of 11 microns. That is also a typical optical frequency used in a home-made Scanning Near-field Optical Microscope (SNOM) that has been developped at UTT. Therefore, as a first try, the nanorods have been designed in order to have a resonance frequency in this range (see Section 3.3). The numerical simulation that we performed shows that rod length should be in the 3.8-4 microns range (Figure 3.11), which is the case for the sample presented above (see Figure 4.4, 4.5, 4.6). Therefore, the last step was to characterize the rods response to an infrared excitation.

For this purpose, Fourier Transform InfraRed spectroscopy (FTIR) technique has been used. This technique enables to record simultaneously data on a large range of frequencies. Figure 4.16 shows two spectra. In blue, a spectrum showing the response of SiO_2 in reflectivity, with gold as a reference, as a function of the wave-number. This curve has been inserted on the graph for further discussion (therefore, the corresponding intensity is not correct). In red, the response of the sample substrate+nanorods+graphene as a function of the wave number. The intensity (y axis) is obtained by taking a ratio of : the reflectivity given by the sample with a polarisation along the long axis of the rods, over the reflectivity given by the sample with a polarisation along the width axis of the rods.

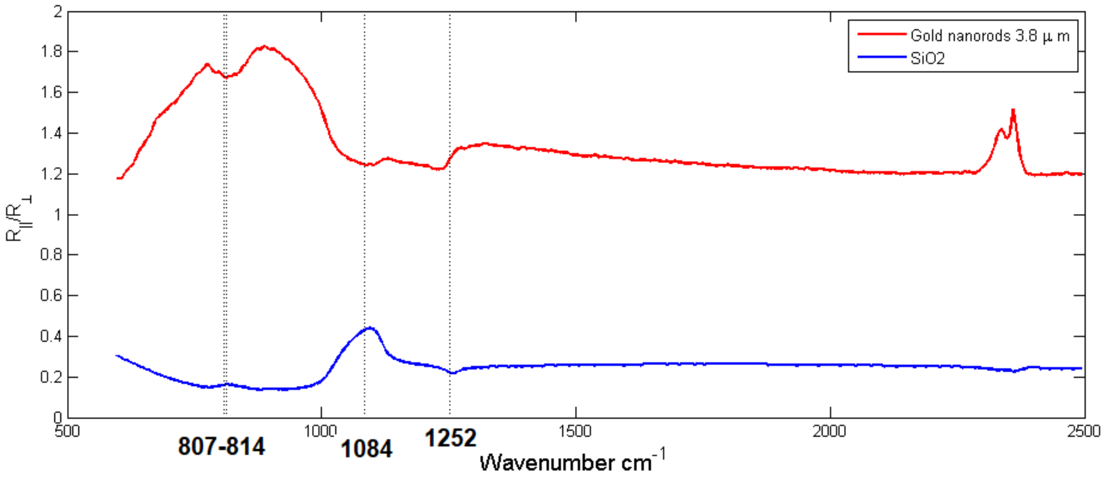

Figure 4.16: FTIR spectrum in reflectivity for SiO2 alone (gold reference) in blue, and substrate+nanorods+graphene with a ratio between two polarisation in red

Let's focus on the blue curve. The response of the SiO_2 is interesting because it is possible to observe its different infrared active modes. According to [138], it is possible to distinguish on the blue curve the optical transverse phonons modes at 807 cm^{-1} and 1084 cm^{-1}, as well as the optical longitudinal phonons modes at 814 cm^{-1} and 1252 cm^{-1}.

Let's now look at the red curve. Two main features appear: one is centered around 900 cm^{-1}, which is the response of the nanoantenna, and one is around 2300cm^{-1}, which is related to the CO_2.

Then, the different infrared modes of the SiO_2 are also appearing. This result is a confirmation that the gold structure resonance is around 11 microns, which fits well the available set up. It is therefore possible to analyse the samples in the near-field using the home made SNOM.

4.3 Optical measurement using Scanning Near-field Optical Microscopy

At the beginning of the previous century, it was believed, according to the theory, that the resolution of classical microscopy was limited to about 250 nm [168], corresponding to half light wavelength. In the eighties, in order to break this diffraction limit, it was proposed to use a little aperture as a light source which would be able to confine the excitation at subwavelength scale. Later, another kind of probes have been proposed, named "apertureless tips", which has been used in this study. Generally speaking, Near-field Scanning Optical Microscopy (SNOM or NSOM) is a local probe microscopy where a tip is placed near the surface of the material ($< \lambda/2$) to interact with matter within the near-field, well before progagation and diffraction of light issued from the sample, which allows one to break the diffraction limit. Therefore, it is possible to get nanometric resolution that is no longer imposed by the wavelength of light. Several types of SNOM exist, classified into two main families : aperture and apertureless probes. For more information about the different systems, see [152].

In this section, the home made apertureless SNOM set up will be introduced. It works in the mid-infrared. Then, the fabrication process of aperturless tips will be presented. Finally, some of the results obtained will be shown.

4.3.1 Introduction to apertureless SNOM and related approaches of signal detection

Apertureless SNOM (also named "scattering-type SNOM: s-SNOM") using a metallic tip is based on the principle that the extremity of a laser-illuminated sharp tip can locally enhance/perturb the electromagnetic field at the sample surface. In general , the near field on the sample interact with the tip. The rather complex local interaction between sample and tip results in a scattered radiative wave that can be detected in the far-field. This radiation carries the local informations (as detected by the tip's extremity) of the sample near field such as its optical phase and amplitude. To some extent, an apertureless scattering-type SNOM picks up the evanescent waves and converts them into propagating waves via a metallic tips that can been considered as an optical nanoantenna. The resulting propagating fied is recorded by a detector in far field.

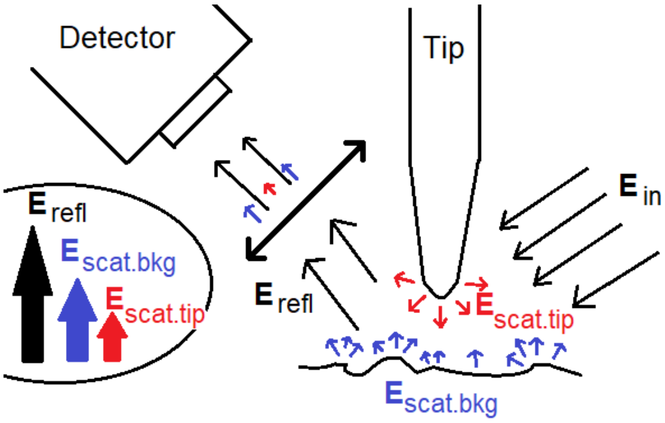

Figure 4.17: Illustration of the different contribution to the field detected by the infrared photo-detector in far field

Figure 4.17 illustrates a SNOM tip probing a sample, and the different electromagnetic fields involved [90]. The excitation field is represented by incident black arrows and noted E_{in}. A scattered background, $E_{scat.bkg}$ represented in blue, occurs on the sample everywhere within the laser spot of the excitation. The scattered field, resulting from the complex interaction between tip, sample and incident field, is represented by $E_{scat.tip}$ with a red color. A specular reflection of the excitation is also represented in black by E_{refl} toward the detector. Therefore, the detector is recording three different contributions. The reflection E_{refl} is stronger than the scattered light $E_{scat.bkg}$, the latter which is stronger than the tip diffusion $E_{scat.tip}$.

First, the specular reflection must be filtered out. A good way do so is to tilt the sample and to record the signal from the same path than the excitation (back scattering configuration). Higher is the tilt of the sample, lower is the reflection from the sample. For the SNOM in infrared at UTT, the tilt is kept higher than 45°.

Then, a second source of problem come from the strong sample scattering (where tip is not involved) that constitutes a background $E_{scat.bkg}$. It is important to remind that our s-SNOM is working in the MID-infrared. Therefore, the spot illuminating both the tip and the sample is about the size of the wavelength, typically here 10 μm. It is interesting to compare, in term of area, the spot of the laser to the zone of interest where the near field is collected by the tip. This zone corresponds to the dimension of apex of the tip, which is typically around 20 nm. Compared to the size of the spot, it is much smaller and the near field signal is likely to be hidden of the background $E_{scat.bkg}$. It must be filtered.

An efficient way to remove it is to drive periodically the tip perpendicular to the sample so that the tip works in AFM tapping mode [11, 87, 12]. It modulates the field scattered at the tip frequency. As a matter of fact, the near field is strongly confined at the surface of the sample. As the tip get closer, the near field radiated into the far-field gets bigger. Once the tips is withdrawn, the signal gets weaker. The field is therefore modulated at a frequency Ω of the tip. The scattering background being unmodulated (or poorly modulated), it is therefore suppressed post-treating the signal. The signal recorded is demodulated at Ω. The signal coming from the probe is therefore recovered.

Technically, a Lock-in Amplifier (LIA) is used. It acts as a filter that record only the field that is modulated at the oscillation frequency Ω of the tip. The frequency of the fork used in the lab is about $\Omega = 29kHz$. This approach of detection (ie direct lock-detection of the scattered light at the tip oscillation frequency Ω), is called ""homodyne detection and is illustrated Figure 4.18 (a).

Homodyne detection

The homodyne system of detection is the simplest one, where there are only three optical arms in the microscope and an only incident electromagnetic pulsation. The first arm is the laser excitation arm. The second arm is the signal arm involving tip and sample. The third arm is the detection one. A lock-In Amplifier is used to record the signal modulated at the tip frequency (or its harmonics [13]) Ω.

At the detector, interferences occur between the different radiative fields: The back-scattering acts as a background that interferes with the near-field signal, which can be translated into equations by :

$$\begin{aligned} I_{det} &= |E_{scat.bkg} + E_{scat.tip}|^2 \\ &= |E_{scat.bkg}|^2 + |E_{scat.tip}|^2 + |E_{scat.bkg}||E_{scat.tip}|cos(\omega t + \phi_{scat.bkg} + \phi_{scat.tip}) \end{aligned} \tag{4.6}$$

Here, $|E_{scat.bkg}|^2$ is not modulated at the tip frequency Ω and is therefore filtered. On the other hand, the two others terms, namely $|E_{scat.tip}|^2$ and $|E_{scat.bkg}||E_{scat.tip}|cos(\omega t + \phi_{scat.bkg} + \phi_{scat.tip})$ are both modulated at Ω and recorded. $|E_{scat.tip}|^2$ being really small, it is the interference term that will be observed. Let us stress that the term $|E_{scat.bkg}|$ can act as an amplification term with regards to $|E_{scat.tip}|$
However, this amplifier is not controlled because the background diffusion is not homogeneous on the sample. Moreover, this amplitude detection can be perturbed by the respective phases of $E_{scat.bkg}$ and $E_{scat.tip}$ which are not controlled. Fringes generally appear on the image, hiding the signal of interest. Finally, although phase information is contained (due to interferences) within the signal, it is difficult to make a distinction between phase and amplitude informations. In order to recover the phase and get a clean signal, heterodyne detection is used.

Heterodyne detection

In this case, a reference signal is added (see Figure 4.18(b)). The laser beam is split into two arms, one will target the sample+tip, and one will be used as a reference signal. An Acoustic-Optical-Modulators (AOM) is added in the path of the reference beam, which is shifting the signal frequency by a $\Delta\omega$. We

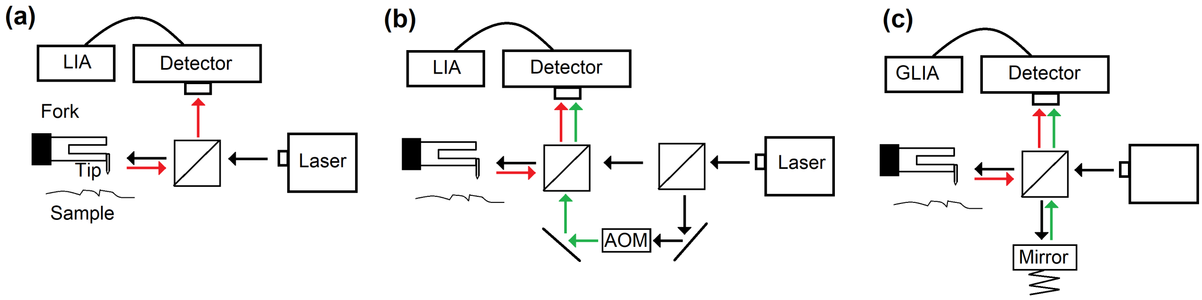

Figure 4.18: Illustration of the different system of detection. Homodyne in (a), Heterodyne in (b) and Pseudo-heterodyne in (c). The black arrows represent the excitation beam path, in red the SNOM signal path, and in green the reference signal path

have then two different electromagnetic frequencies, explaining the term "heterodyne"[144].

We have now three different beam hitting the detector : $|E_{scat.back}|$, $|E_{scat.tip}|$ and $|E_{ref}|$.Each of them will have a different modulation characteristic. $|E_{scat.bkg}|$ is not modulated. $|E_{scat.tip}|$ is modulated at the frequency of oscillation of the tip Ω. Finally, $|E_{ref}|$ is modulated at the frequency of the AOM $\Delta\omega$. All these fields will interfere with each others but only the interference between $|E_{ref}|$ and $|E_{scat.tip}|$ will be modulated at $\Omega \pm \Delta\omega$. This is the field that will be recorded by the LIA system.
Hence, the carrier signal becomes E_{ref}, instead of $E_{scat.bkg}$. Unlike $E_{scat.bkg}$, E_{ref} is controlled: both its amplitude and phase can be controlled.

More precisely, similarly to Equation 4.6, the field $|E_{scat.tip}|$ is amplified by a strong signal, here $|E_{ref}|$. The difference is that the reference signal is cleaned, constant, and do not depend on the position of the tip on the sample. The recorded image become therefore clear of background signal and it is possible to have the optical amplitude as well as the optical phase.

However, some experimental problems arise with this method [21]. Acoustic-Optical-Modulators (AOM) are usually expensive, and not always available in a wide range of frequency. Also, the Michelson interferometer layout mentioned above is not well adapted to the implementation of an AOM. A less stable Mach-Zehnder configuration is used. An alternative to this method is the pseudo-heterodyne detection, that is presented below.

Pseudo-heterodyne detection

The last method, illustrated Figure 4.18(c), is not using a frequency shift as it is done for the heterodyne detection. Instead, a periodic oscillation of the reference arm length is performed. The phase of the reference is therefore periodically shifted. The reference beam recombining with the SNOM signal create the interferences which will be exploit for the detection. The main advantage of this method is that it can be applied to any frequency range of excitation.

In fact, mirrors are mounted on a piezo material driven by a periodic signal. A mathematical signal treatment is then performed, including a lock in amplifier process, to treat the signal and recover the phase and the amplitude of the signal. This method is called "General Lock-In Amplifier", and more informations can be found in [21].

4.3.2 Experimental details about the scattering-type SNOM

The experimental set up at UTT uses three lasers that cover a spectral range running from 9.5 μm to 11.4 μm. At the exit of the lasers, an isolator is placed in order to avoid any reflected beam back to the lasers. A coupler, made of a lense mounted on a stage, drives the beam to the fiber. A collimator is placed at the exit of the fiber to conduct the laser beam to the core of the set up. This core is represented in Figure 4.19.

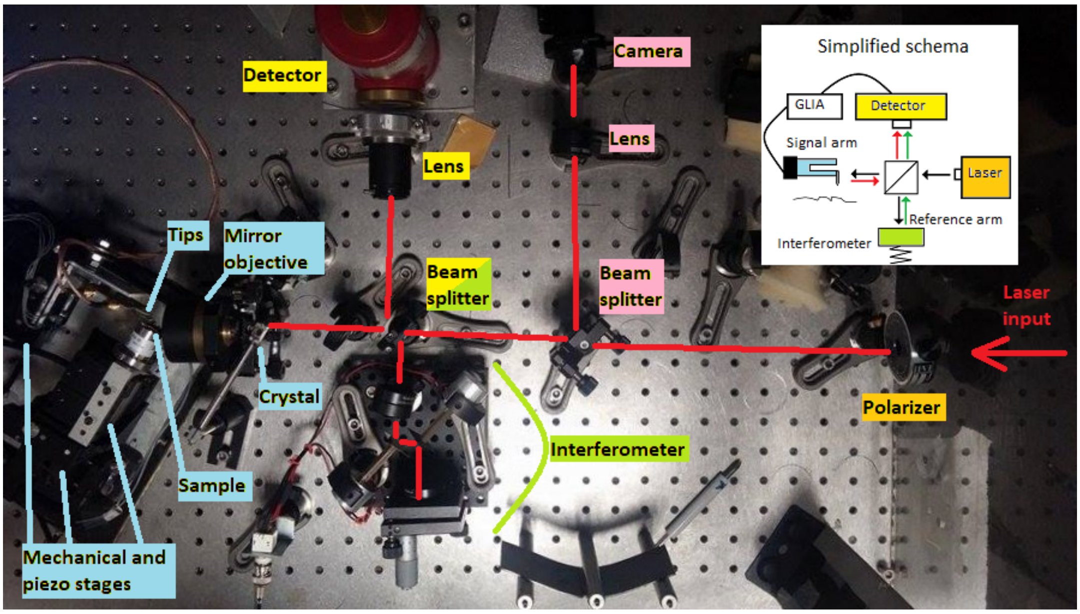

Figure 4.19: Picture of the SNOM setup. In inset, a simplified schema representing the set up

The core of the set up is composed of four arms detailed in the inset of Figure 4.19 :

1. Both incident and back scattered paths are represented in red.
2. The "signal arms" with the stage, the tip and the sample, a mirror objective and a anti-reflection crystal are hilighted in blue
3. The refererence interferometric arm is in green
4. The detection arm with a lens and a detector are indicated in yellow

Finally, another arm, parallel to the detection arm, is added in order to visualize the sample and the tip. It is represented in pink in Figure 4.19.

More in details, the signal arm includes the stages supporting the tip and the sample, and an objective to focus the beam. This is where the near field signal is converted into a far field signal. The sample and the tip are hold by a platform that is made of several mechanical and piezoelectric stages. The mechanical stages enable rough movement, whereas piezoelectric stages enable fine approach and scanning. The tip is placed at the beam focal point and does not move once scanning. Instead, it is the sample which is moving. A anti-reflection crystal is added at the objective entrance to avoid back-reflection to the detector.

The detection arm includes a HgCdTe detector and a lens. The detector is cooled with liquid nitrogen. It is linked to a Generalized Lock-In Amplifier (GLIA). In parallel, it is possible to observe on Figure 4.19 a visualization arm, which is composed of a beam splitter, a camera(webcam), and a lens for a magnification. It is used to focus the beam on the apex of the tip and to visualize the location of the scan.

Finally, the interferometric arm is made of three mirrors. Two of them are mounted on piezo materials and provide a shift in phase of the beam (modulating the length of the arm), whereas the last one is mounted on a mechanical stage, and reflects the beam back to the detector. The latter is used for alignment.

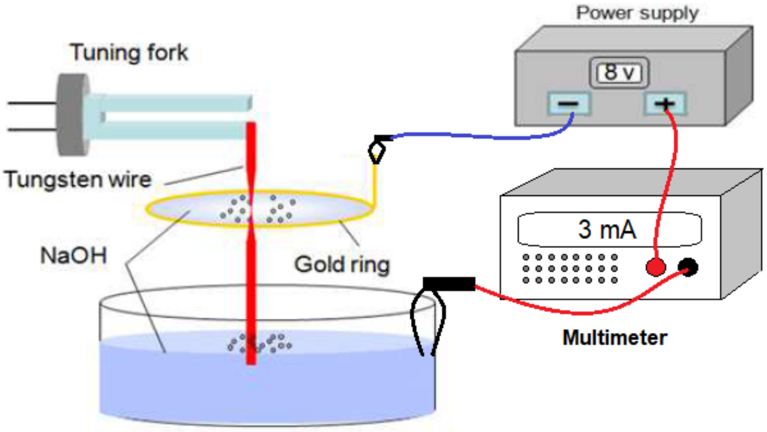

Figure 4.20: Schema representing the electro-chemical set up for the fabrication of SNOM apertureless tips

4.3.3 Fabrication of the tips

Tips are crucial for detecting evanescent waves. In particular, the apex of the tips should be as small as possible in order to act as an electric dipole that picks up the near-field. The incident field from the laser beam can be converted by the tip to local source, and excite surface plasmons. Reciprocally, the evanescent wave of a surface plasmons can be converted into a radiative wave via the tip apex.

In order to accurately record plasmons in graphene, the diameter of the tip extremity should be at least of the same order of magnitude than the expansion of the phenomenon in air. For graphene plasmons, it has been shown [44] that the diameter of the apex should be around few tenths of nanometers.

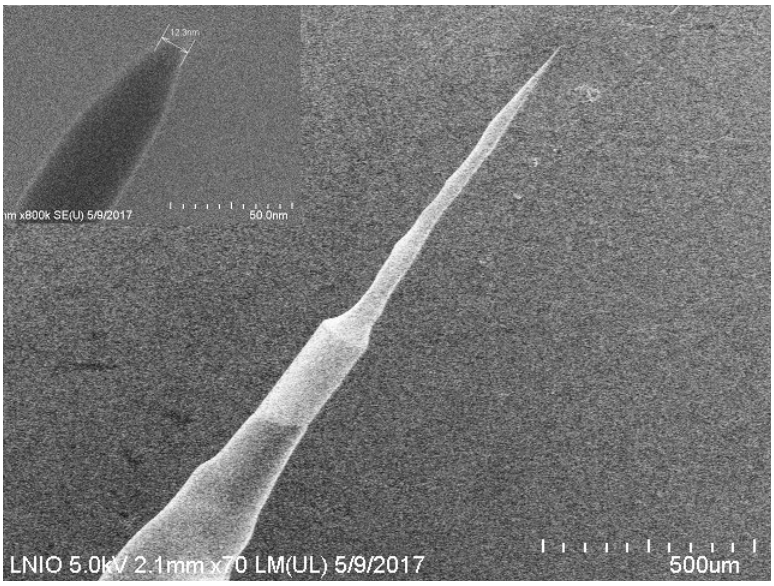

Figure 4.21: Picture of a SNOM tip tooken via an electronic microscope. The apex diameter is around 10nm.

Our probes are home-made probes produced at UTT. The method consists of etching electrochemically a tungsten wire. It is called the double lamellae dropoff technique, and has been inspired from [85]. It is based on the etching of a tungsten wire through a golden ring used as electrode, as illustrated Figure 4.20. A 2.5 cm long tungsten wire is first glued at the extremity of one arm of a tuning fork. This tuning fork is used for tapping-mode distance regulation (see sub-section 4.3.1).

Then, the fork is clamped horizontally to a stage, with the glued wire head down. Meanwhile, an electro-chemical circuit is installed. It is made of a generator, where the positive terminal is linked to a multimeter and a beaker, and the negative terminal is linked with a golden ring. The beaker and the golden ring are filled with a solution of NaOH (2.5 mol/L). The ring is attached to a stage and stand on the top of the beaker. The circuit is turned off.
Once the tungsten wire, glued to the fork, is dipped from the ring into the beaker solution, the circuit is turned on. A current pass through the circuit and a chemical reaction occurs between the tungsten and the NaOH solution in the ring. Eventually, the tungsten wire will be electrochemically cut at the ring plane and the current will goes to zero.

It has been a real issue to obtain probe with tenth of nanometers diameter. A study has been performed to find the best parameter toward thinest tip apex. The influence of the following parameters has been investigated:

1. The applied voltage (V)
2. The solution concentration (NaOH in mol/L)
3. The current (in mA)
4. The length of the tungsten wire (in cm)
5. The distance between the gold ring and the surface of the NaOH solution in the beaker (in cm).

The diameter of the gold ring was 0.8 cm. The applied voltage has been set at 8V. Both parameters have not been varied. The solution concentration has been varied from 1 mol/L to 4.5 mol/L. The current which is going through the system when the generator is turned on is of the first importance. It is related to two main parameters : the concentration of the solution, and the amount of liquid inside the ring. Since the concentration is controlled, the targeted current were reached managing the volume of liquid inside the ring. The liquid inside the ring can be suck out with paper towel in order to set the correct starting current. The length of the tungsten is an important parameter because it is directly related to the gravitational force pulling down the wire. At the etching site, this force will tear apart the two side of the tungsten wire. As well, the distance in between the ring and the NaOH solution in the beaker has to be taken into account. It shows how long tungsten wire is outside the liquid, pulling down the wire stronger. The wire length used were chosen between 0.5 to 4 cm. The distance in between the ring and the beaker solution was chosen as a consequence of the length of the wire.

The concentration has been varied at first and 2.5mol/L gave the best results. Then, the starting current has been investigated, and 3 mA gave the thinest apex. Finally, the length of tungsten wire giving the best results is about 2cm long and for a distance ring-beaker solution of 1.5cm.

Optimizing these parameters did not lead to good enough distributions of tip size, which were centred around 60 nm. The best achieved tip's diameter was around 30nm. In fact, the quality of the NaOH pallets used for the fabrication of the solution turned out to be the critical factor. Once it has been renew, a tip's distribution centred around 25 nm was obtained and reproduced (see Figure 4.22). The best tip obtained was about 10 nm (see figure 4.21).

4.3.4 First optical measurement

At first, preliminary measurements have been performed to record plasmons in CVD-fabricated graphene. The 2D layer was deposited on the top of a typical wafer of SiO2/Si. Optical and electronic microscope image of the sample are shown Figure 4.23. We can observe the graphene on both pictures as it appears darker than the bear substrate. Some impurities are also present.

In the optical image, Figure 4.23a, a red cross indicate the location from where a raman spectra have been obtained. The result is shown in the inset. We can see here that the graphene is clean, with really few defects (low defect peak). In the electronic image, Figure 4.23b, a green square have been drawn

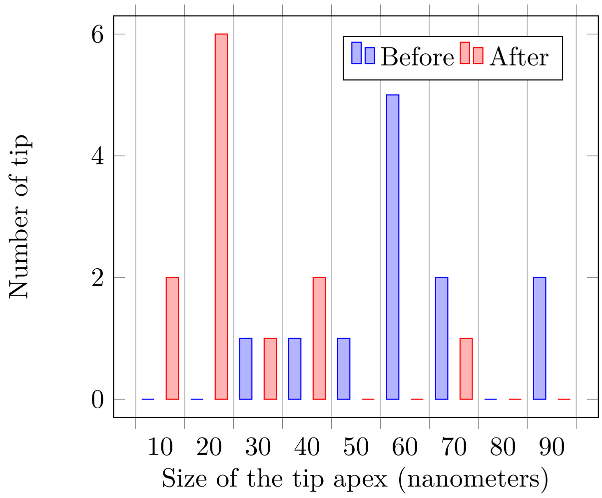

Figure 4.22: Two typical distribution of size of tip apex before and after the change of NaOH chemical (12 tips each)

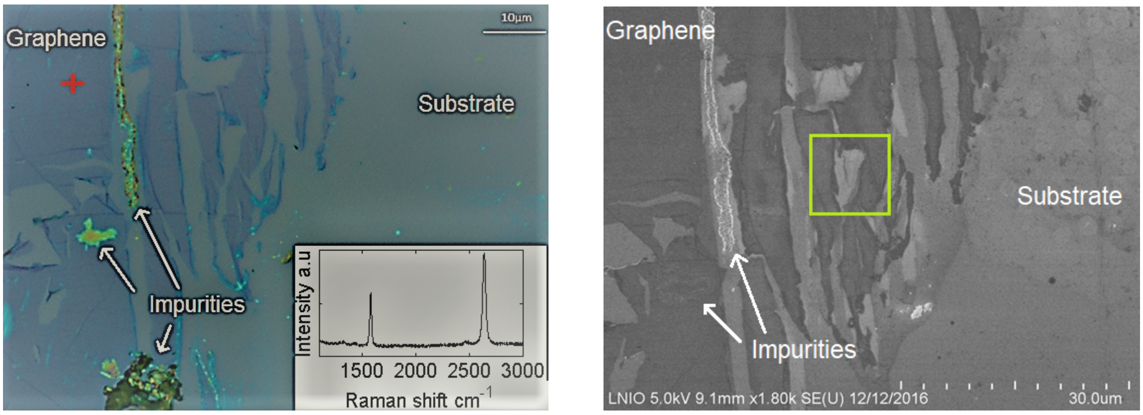

(a) Image of a sample from an optical microscope. In inset, a Raman spectra of the graphene layer taken at the red cross (top left).

(b) Image of the same zone of the sample, taken from an electronic microscope. The green square is delimiting the image obtained by SNOM, Figure 4.24.

Figure 4.23: Optical and electronic images of a sample where graphene CVD layer have been deposited non uniformly on a substrate of SiO_2/Si. The images are taken with two different microscopes at the same location. It is possible to observe the presence of graphene, which appears darker than the substrate.

representing more precisely the place where the optical measurement using SNOM have been made (see Figure 4.24).

Preliminary SNOM images are shown in Figure 4.24. The excitation wavelength was 11 μm, which in the range of low damping for graphene plasmons (see section 2.3.3). A linear polariser was used, as shown on Figure 4.19: the polarisation of the incident beam was horizontal. The long axis of the tip is also horizontal. The polarisation follows the excursion of the oscillation of the tip (tapping mode) too. Therefore, this set up enable a strong excitation of the tip, which is more likely to excite plasmons in the graphene layer.

Using our scanning probe microscope in pseudo-heterodyne mode (see section 4.3.1), it is possible to get different kinds informations simultaneously. The first one is the topography of the sample, as the is working as an AFM (Figure 4.24a). The second information is the optical amplitude that we can observe Figure 4.24b. It is the main information we are looking for in SNOM measurement, and it is really sensitive to the discontinuity of graphene (see section 2.2.2). The third picture, Figure 4.24c, is the mechanical phase of the fork. It is sensitive to the change of the underneath material. In fact, phase contrast can be used for determining physical and chemical differences in scanned materials [79]. Graphene looks in this case darker than SiO2. The last picture, Figure 4.24d, gives the difference of mechanical amplitude during the scan. This amplitude is expected to be constant during scanning, which is not exactly the case, despite the feedback loop. The feedback may have a delay, related to a physical step encounter by the fork. This contrast in the amplitude image has to be taken into account for interpretation of SNOM images. Indeed, SNOM images can contain artifact corresponding to the AFM error signal [18].

We can observe on Figure 4.24b an optical response of graphene at the edges of different flakes, that is probably related to graphene plasmons. In order to have better resolution, another scan zooming on a different area is presented in Figures 4.25 and 4.26.

On the Figure 4.26b, it is possible to observe oscillations in the graphene that are not present on the substrate. Those oscillations are peak to peak a bit higher than 100nm, which has also been reported in [42]. It correspond to the effective wavelength of graphene plasmons in this condition. The graphene intrinsic doping, deduce from this wavelength, is of the order of what is expected from the CVD synthesis method used here [113]. Unfortunately, due to technical problem, variation of the doping by injection of charge couldn't be perform, and no further evidence are available.

4.4 Conclusion

This chapter presents experimental results as the last step of this research work. It shows the fabrication, characterization and optical measurements with the introduction of Scanning Near Field Optical Microscopy technique. These experimental results are the last part of this study. The obtained results are preliminary and more experiments should be conduct in the future in order to show the true signature of plasmons in graphene. This chapter has also been showing the complexity to manipulate 2D material, and to record such confined phenomenon.

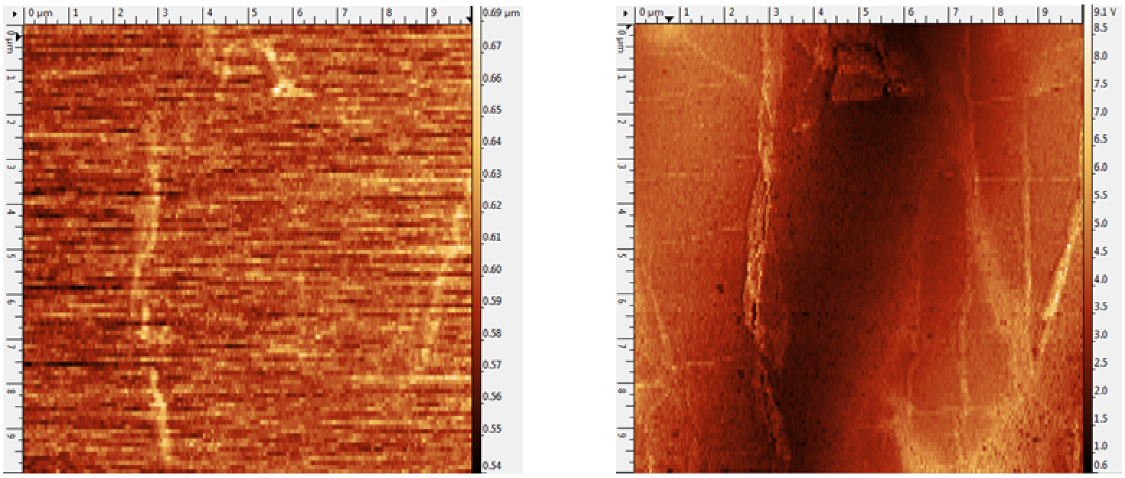

(a) AFM topography (10×10 microns)

(b) Optical amplitude

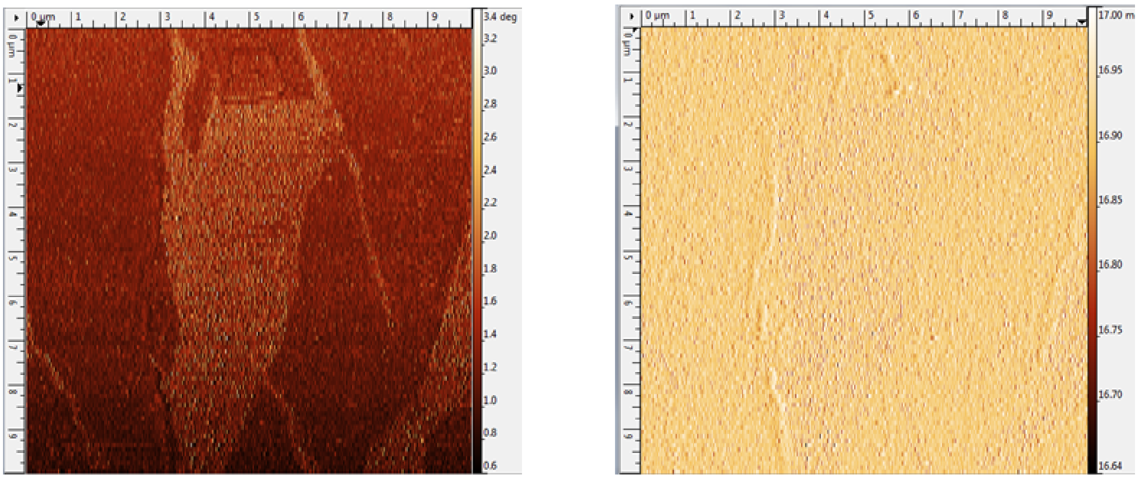

(c) AFM mechanical phase of the fork

(d) AFM mechanical amplitude of the fork

Figure 4.24: s-SNOM images : topography, optical amplitude, AFM phase and AFM amplitude

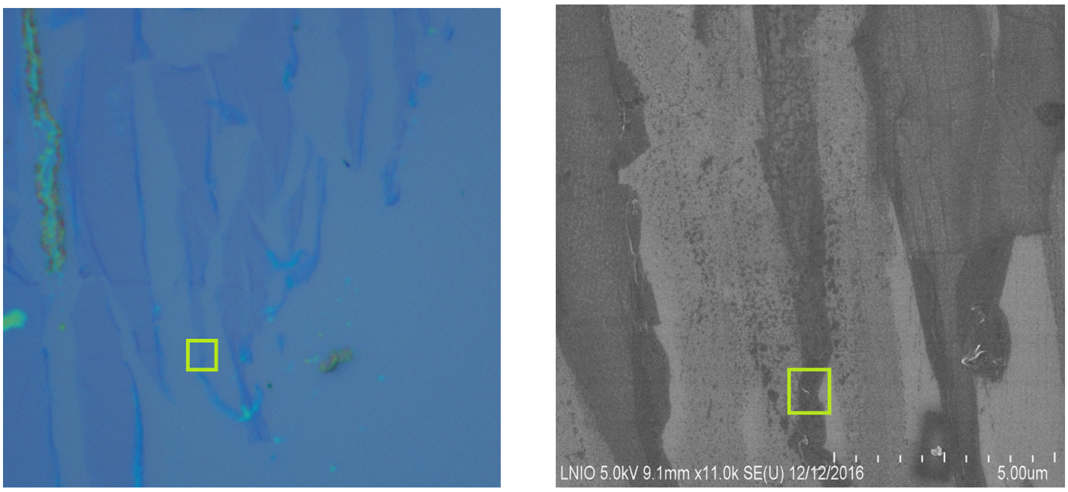

(a) Image of a sample from an optical microscope. Graphene CVD layer have been deposited non uniformly on a substrate of SiO2/Si. In inset, a Raman spectra of the graphene layer tooken at the red cross.

(b) Image of the same zone of the sample than Figure 4.23a, taken from an electronic microscope. The green square is delimiting the image obtained by SNOM, Figure 4.24.

Figure 4.25: Optical and electronic image of the sample study. It is possible to observe the presence of graphene, darker than the bear substrate.

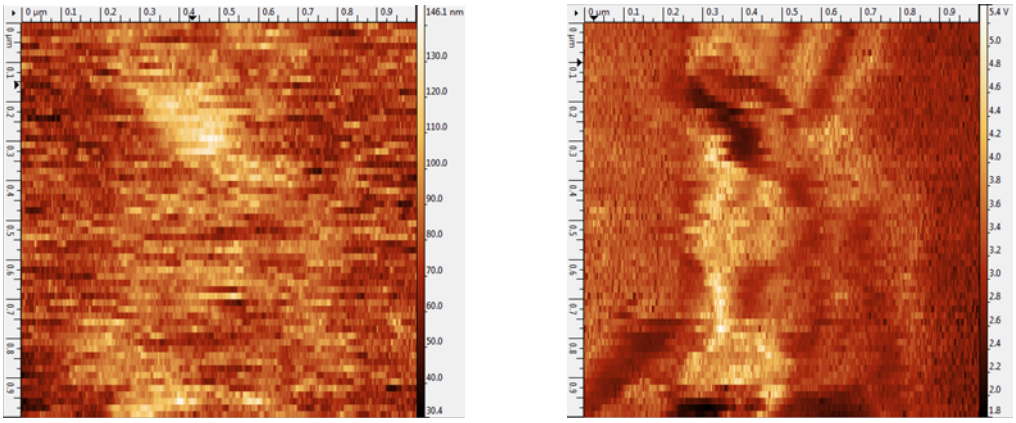

(a) AFM topography (1×1 microns)

(b) Optical amplitude

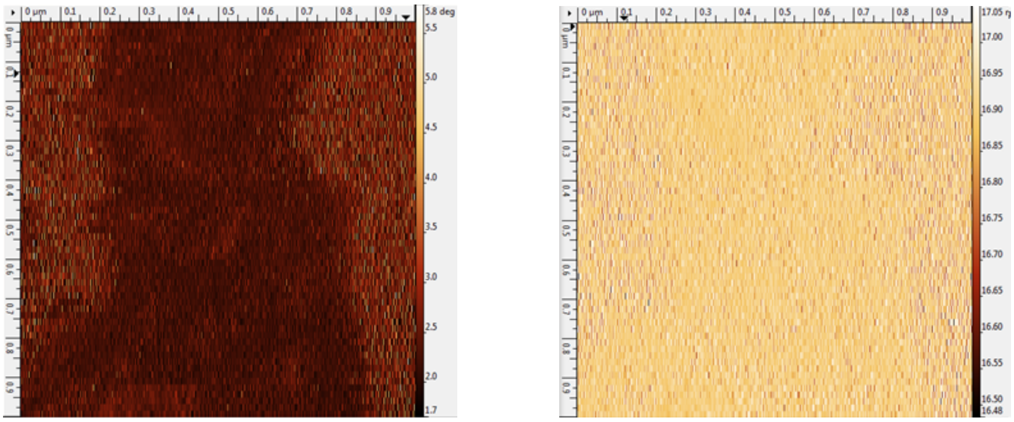

(c) AFM mechanical phase of the fork

(d) AFM mechanical amplitude of the fork

Figure 4.26: s-SNOM images : topography, optical amplitude, AFM phase and AFM amplitude

Conclusion and outlook

In this research work, new studies in the graphene plasmonics field have been done. A particular attention has been paid on the explanation of graphene plasmons phenomena using mostly classical physics.

In chapter one, the basis of plasmonics have been reviewed from the Maxwell's equations. The graphene structures has been discussed and the electrons behavior has been rose up through a tight binding model. This chapter set the foundation necessary to the understanding of Graphene plasmonics physics.

The second chapter has aimed at giving a literature review and analysis covering briefly the discovery of graphene as well as the one of graphene plasmons. It gives some glimpse on the challenge remaining in order to achieve active graphene-based electronic devices. In particular, it introduces the problematic of the propagation of plasmons, and the need to find out a suitable platform in order to get the first active device based on graphene plasmons. Finally, graphene plasmons physics is duscussed through the dispersion curve, providing the necessary key parameters for a further numerical and experimental research work.

The third chapter is dedicated to a full numerical study, based on the Finite Difference Time Domain method. This method is shortly introduced with an history and the resolution of 1D wave problem. The 3D case is then given accordingly with the key parameter to conduct a numerical study. The problem of simulating a 2D material in a 3D grid has been extensively addressed. Finally, a design of sample has been proposed. It uses gold antenna as launcher of graphene plasmons. The propagation in suspended graphene has been shown and propagation length has been discussed. Compared to supported plasmons, surface plasmon progagation length in suspendend graphene turns out to be significant and could be exploited in the near-future in the context of 2-D nanophotonics. A final discussion has given the limits of this experiment proposal, where a vacuum chamber is probably required.
The fourth chapter has been dealing with preliminary experimental achievements. At first, a sample fabrication process has been descrided. First samples have been obtained and characterized. Some issues faced during the process hace been addressed, which could be useful for students and researchers who will carry on this work. Then, the characterization of antenna as well as graphene are given. Finally, Scanning Near field Optical Microscopy technique has been introduced. It is based on a heterodyne apertureless configuration. The home-made set up has been presented and some preliminary results have been shown.

Perspectives: the case of diamond Given the challenges met to study plasmons in suspended graphene, an other research path have been explored. As already mentioned, Graphene plasmons lake of propagation length L_p when researcher think about using its properties for applications purposes (section 2.2.1). Although progress have been made recently [114, 38], the propagation length L_p remains too short to be used in active opto-electronic devices. Several parameters [98] must be therefore considered in order to obtain high GPs propagation (see Equation(2.27) for the following). Firstly, L_p is function of the scattering rate of the charge carriers, which should be kept as low as possible. Secondly, L_p is proportional to the squared value of the Fermi energy in the infrared range, which should therefore be as high as possible (following the DC approximation of the relaxation time, section 2.1.2). Finally, L_p is very sensitive to the imaginary part of the permittivity of the substrate ϵ'', the optical energy dissipation ($\mathrm{Im}(\epsilon)$).

Armed with these parameters, we can draw a picture of the ideal platform for high propagation of GPPs, which should have the following properties:

1. High dielectric strength and k-dieletric constant in order to inject high density of charges into graphene.
2. Low Im(ϵ), in order to have low plasmonics losses.
3. Possibility to fabricate within the same process than graphene, using CVD system.
4. Use of sustainable material.

SiO_2, which is the most common substrate used to study graphene [117], induces external and/or internal scattering [7, 78, 28, 110]. Then, the relatively low k-dielectric constant (3.9) associated to the dielectric strength of 0.5GV/m doesn't enable to reach high enough Fermi energy. Finally, the optical dissipation of SiO_2 induces significant damping in GPPs [42].

Soon after, studies on encapsulated graphene in h-BN, a substrate known to be suitable for graphene [145, 53], showed promising results [34, 114]. h-BN high dielectric strength property (up to 1.2GV/m when exfoliated) [60], as well as its good lattice matching with graphene [162], make it a good candidate. Moreover, thin films of h-BN have been synthesis through CVD process conserving good dielectric properties (0.4 GV/m) [74]. However, h-BN optical properties induce severe damping in graphene plasmons [153], as Im(ϵ) is of the same order of magnitude than the one of SiO_2 [157]. Moreover, Boron is rather rare on earth.

Comparatively, Diamond fulfills all the criteria cited above. Its dielectric strength is ideally higher than the h-BN one [51, 156]. It can be synthesis through the unique and same CVD process [165]. It has no optical energy dissipation in infrared region and carbon is a material that is continuously growing on earth surface in stocks, creating environmental issues. It would be also interesting to look at the behavior of plasmons in graphene transferred onto UNCD and SCD by changing the surface termination (H-termination vs O-termination) of underlying diamond. Intercalate nano-spacer between graphene and SiO2 substrate has been already studied [38], and has shown improvement of the plasmons propagation. Therefore, the combination of diamond and graphene would definitively give important results that could eventually lead to efficient active opto-electronic devices.

Bibliography

[1] Graphene 2d Interband term.

[2] FDTD Basics, October 2013.

[3] Ahmad Abbas, Mustafa Karabiyik, and Nezih Pala. Graphene-based field-effect transistor structures for terahertz applications. pages 83630S–83630S–8, May 2012.

[4] Shaffique Adam, E. H. Hwang, V. M. Galitski, and S. Das Sarma. A self-consistent theory for graphene transport. *Proceedings of the National Academy of Sciences*, 104(47):18392–18397, 2007.

[5] P. Alonso-Gonzalez, A. Y. Nikitin, F. Golmar, A. Centeno, A. Pesquera, S. Velez, J. Chen, G. Navickaite, F. Koppens, A. Zurutuza, F. Casanova, L. E. Hueso, and R. Hillenbrand. Controlling graphene plasmons with resonant metal antennas and spatial conductivity patterns. *Science*, 344(6190):1369–1373, June 2014.

[6] Stamatios A. Amanatiadis, Nikolaos V. Kantartzis, and Theodoros D. Tsiboukis. A Loss-Controllable Absorbing Boundary Condition for Surface Plasmon Polaritons Propagating Onto Graphene. *IEEE Transactions on Magnetics*, 51(3):1–4, March 2015.

[7] Tsuneya Ando. Screening Effect and Impurity Scattering in Monolayer Graphene. *Journal of the Physical Society of Japan*, 75(7):074716, July 2006.

[8] Tsuneya Ando. The electronic properties of graphene and carbon nanotubes. *NPG asia materials*, 1(1):17–21, 2009.

[9] Hideo Aoki and Mildred S. Dresselhaus, editors. *Physics of Graphene*. NanoScience and Technology. Springer International Publishing, Cham, 2014.

[10] Neil W. Ashcroft, N. David Mermin, and Wei Dan. *Solid state physics.* 2016.

[11] R. Bachelot, P. Gleyzes, and A. C. Boccara. Apertureless near field optical microscopy by local perturbation of a diffraction spot. *Ultramicroscopy*, 61(1-4):111–116, 1995.

[12] R. Bachelot, P. Gleyzes, and A. C. Boccara. Reflection-mode scanning near-field optical microscopy using an apertureless metallic tip. *Applied optics*, 36(10):2160–2170, 1997.

[13] R. Bachelot, G. Wurtz, and P. Royer. An application of the apertureless scanning near-field optical microscopy: Imaging a GaAlAs laser diode in operation. *Applied Physics Letters*, 73(23):3333–3335, December 1998.

[14] Qiaoliang Bao and Kian Ping Loh. Graphene photonics, plasmonics, and broadband optoelectronic devices. *ACS Nano*, 6(5):3677–3694, May 2012.

[15] Qiaoliang Bao, Han Zhang, Bing Wang, Zhenhua Ni, Candy Haley Yi Xuan Lim, Yu Wang, Ding Yuan Tang, and Kian Ping Loh. Broadband graphene polarizer. *Nature Photonics*, 5(7):411–415, May 2011.

[16] Stéphane Berciaud, Sunmin Ryu, Louis E. Brus, and Tony F. Heinz. Probing the Intrinsic Properties of Exfoliated Graphene: Raman Spectroscopy of Free-Standing Monolayers. *Nano Letters*, 9(1):346–352, January 2009.

[17] Claire Berger, Zhimin Song, Tianbo Li, Xuebin Li, Asmerom Y. Ogbazghi, Rui Feng, Zhenting Dai, Alexei N. Marchenkov, Edward H. Conrad, Phillip N. First, and Walt A. de Heer. Ultrathin Epitaxial Graphite: 2d Electron Gas Properties and a Route toward Graphene-based Nanoelectronics. *The Journal of Physical Chemistry B*, 108(52):19912–19916, December 2004.

[18] L. Billot, M. Lamy de la Chapelle, D. Barchiesi, S.-H. Chang, S. K. Gray, J. A. Rogers, A. Bouhelier, P.-M. Adam, J.-L. Bijeon, G. P. Wiederrecht, R. Bachelot, and P. Royer. Error signal artifact in apertureless scanning near-field optical microscopy. *Applied Physics Letters*, 89(2):023105, July 2006.

[19] K.I. Bolotin. Electronic transport in graphene: towards high mobility. In *Graphene*, pages 199–227. Elsevier, 2014.

[20] F. Bonaccorso, Z. Sun, T. Hasan, and A. C. Ferrari. Graphene photonics and optoelectronics. *Nature Photonics*, 4(9):611–622, September 2010.

[21] Aurélien Bruyant, Julien Vaillant, Tzu-Heng Wu, Yunlong Zhu, Yi Huang, and Abeer Al Mohtar. Interferometry Using Generalized Lock-in Amplifier (G-LIA): A Versatile Approach for Phase-Sensitive Sensing and Imaging. In Alexandr A. Banishev, Mithun Bhowmick, and Jue Wang, editors, *Optical Interferometry*. InTech, February 2017.

[22] Eduardo V. Castro, H. Ochoa, M. I. Katsnelson, R. V. Gorbachev, D. C. Elias, K. S. Novoselov, A. K. Geim, and F. Guinea. Limits on Charge Carrier Mobility in Suspended Graphene due to Flexural Phonons. *Physical Review Letters*, 105(26), December 2010.

[23] A. H. Castro Neto, F. Guinea, N. M. R. Peres, K. S. Novoselov, and A. K. Geim. The electronic properties of graphene. *Reviews of Modern Physics*, 81(1):109–162, January 2009.

[24] You-Chia Chang, Che-Hung Liu, Chang-Hua Liu, Siyuan Zhang, Seth R. Marder, Evgenii E. Narimanov, Zhaohui Zhong, and Theodore B. Norris. Realization of mid-infrared graphene hyperbolic metamaterials. *Nature Communications*, 7:10568, February 2016.

[25] V. V. Cheianov, V. Fal'ko, and B. L. Altshuler. The Focusing of Electron Flow and a Veselago Lens in Graphene p-n Junctions. *Science*, 315(5816):1252–1255, March 2007.

[26] Fang Chen, Duanzheng Yao, and Yanan Liu. Graphene-metal hybrid plasmonic switch. *Applied Physics Express*, 7(8):082202, August 2014.

[27] J.-H. Chen, C. Jang, S. Adam, M. S. Fuhrer, E. D. Williams, and M. Ishigami. Charged-impurity scattering in graphene. *Nature Physics*, 4(5):377–381, May 2008.

[28] Jian-Hao Chen, Chaun Jang, Shudong Xiao, Masa Ishigami, and Michael S. Fuhrer. Intrinsic and extrinsic performance limits of graphene devices on SiO2. *Nature Nanotechnology*, 3(4):206–209, April 2008.

[29] Jianing Chen, Michela Badioli, Pablo Alonso-Gonzalez, Sukosin Thongrattanasiri, Florian Huth, Johann Osmond, Marko Spasenovic, Alba Centeno, Amaia Pesquera, Philippe Godignon, Amaia Zurutuza Elorza, Nicolas Camara, F. Javier García de Abajo, Rainer Hillenbrand, and Frank H. L. Koppens. Optical nano-imaging of gate-tunable graphene plasmons. *Nature*, June 2012.

[30] Jianing Chen, Maxim L. Nesterov, Alexey Yu. Nikitin, Sukosin Thongrattanasiri, Pablo Alonso-González, Tetiana M. Slipchenko, Florian Speck, Markus Ostler, Thomas Seyller, Iris Crassee, Frank H. L. Koppens, Luis Martin-Moreno, F. Javier García de Abajo, Alexey B. Kuzmenko, and Rainer Hillenbrand. Strong Plasmon Reflection at Nanometer-Size Gaps in Monolayer Graphene on SiC. *Nano Letters*, 13(12):6210–6215, December 2013.

[31] Mohammad Choucair, Pall Thordarson, and John A. Stride. Gram-scale production of graphene based on solvothermal synthesis and sonication. *Nature Nanotechnology*, 4(1):30–33, January 2009.

[32] Hong-Son Chu and Choon How Gan. Active plasmonic switching at mid-infrared wavelengths with graphene ribbon arrays. *Applied Physics Letters*, 102(23):231107, 2013.

[33] Johann Coraux, Alpha T. N'Diaye, Carsten Busse, and Thomas Michely. Structural Coherency of Graphene on Ir(111). *Nano Letters*, 8(2):565–570, February 2008.

[34] S. Dai, Q. Ma, M. K. Liu, T. Andersen, Z. Fei, M. D. Goldflam, M. Wagner, K. Watanabe, T. Taniguchi, M. Thiemens, F. Keilmann, G. C. A. M. Janssen, S-E. Zhu, P. Jarillo-Herrero, M. M. Fogler, and D. N. Basov. Graphene on hexagonal boron nitride as a tunable hyperbolic metamaterial. *Nature Nanotechnology*, 10(8):682–686, June 2015.

[35] Susbhan Das, Alessandro Salandrino, Judy Z. Wu, and Rongqing Hui. Near-infrared electro-optic modulator based on plasmonic graphene. *Optics Letters*, 40(7):1516, April 2015.

[36] V. Despoja, D. Novko, K. Dekanić, M. Šunjić, and L. Marušić. Two-dimensional and π plasmon spectra in pristine and doped graphene. *Physical Review B*, 87(7), February 2013.

[37] Vincent E. Dorgan, Ashkan Behnam, Hiram J. Conley, Kirill I. Bolotin, and Eric Pop. High-Field Electrical and Thermal Transport in Suspended Graphene. *Nano Letters*, 13(10):4581–4586, October 2013.

[38] Alexander M. Dubrovkin, Jin Tao, Xue Chao Yu, Nikolay I. Zheludev, and Qi Jie Wang. The reduction of surface plasmon losses in quasi-suspended graphene. *Scientific Reports*, 5:9837, May 2015.

[39] T. Eberlein, U. Bangert, R. R. Nair, R. Jones, M. Gass, A. L. Bleloch, K. S. Novoselov, A. Geim, and P. R. Briddon. Plasmon spectroscopy of free-standing graphene films. *Physical Review B*, 77(23), June 2008.

[40] L A Falkovsky. Optical properties of graphene. *Journal of Physics: Conference Series*, 129:012004, October 2008.

[41] L. A. Falkovsky and S. S. Pershoguba. Optical far-infrared properties of a graphene monolayer and multilayer. *Physical Review B*, 76(15), October 2007.

[42] Z. Fei, A. S. Rodin, G. O. Andreev, W. Bao, A. S. McLeod, M. Wagner, L. M. Zhang, Z. Zhao, M. Thiemens, G. Dominguez, M. M. Fogler, A. H. Castro Neto, C. N. Lau, F. Keilmann, and D. N. Basov. Gate-tuning of graphene plasmons revealed by infrared nano-imaging. *Nature*, June 2012.

[43] Z. Fei, A. S. Rodin, W. Gannett, S. Dai, W. Regan, M. Wagner, M. K. Liu, A. S. McLeod, G. Dominguez, M. Thiemens, Antonio H. Castro Neto, F. Keilmann, A. Zettl, R. Hillenbrand, M. M. Fogler, and D. N. Basov. Electronic and plasmonic phenomena at graphene grain boundaries. *Nature Nanotechnology*, 8(11):821–825, October 2013.

[44] Zhe Fei, Gregory O. Andreev, Wenzhong Bao, Lingfeng M. Zhang, Alexander S. McLeod, Chen Wang, Margaret K. Stewart, Zeng Zhao, Gerardo Dominguez, Mark Thiemens, Michael M. Fogler, Michael J. Tauber, Antonio H. Castro-Neto, Chun Ning Lau, Fritz Keilmann, and Dimitri N. Basov. Infrared Nanoscopy of Dirac Plasmons at the Graphene–SiO $_2$ Interface. *Nano Letters*, 11(11):4701–4705, November 2011.

[45] A. C. Ferrari, J. C. Meyer, V. Scardaci, C. Casiraghi, M. Lazzeri, F. Mauri, S. Piscanec, D. Jiang, K. S. Novoselov, S. Roth, and A. K. Geim. Raman Spectrum of Graphene and Graphene Layers. *Physical Review Letters*, 97(18), October 2006.

[46] Andrea C. Ferrari and Denis M. Basko. Raman spectroscopy as a versatile tool for studying the properties of graphene. *Nature Nanotechnology*, 8(4):235–246, April 2013.

[47] Andrea C. Ferrari and Jf Robertson. Interpretation of Raman spectra of disordered and amorphous carbon. *Physical review B*, 61(20):14095, 2000.

[48] S. Fratini and F. Guinea. Substrate-limited electron dynamics in graphene. *Physical Review B*, 77(19), May 2008.

[49] F. J. Garcia de Abajo. Graphene Plasmonics: Challenges and Opportunities. *ACS Photonics*, 1(3):135–152, March 2014.

[50] A. K. Geim and K. S. Novoselov. The rise of graphene. *Nature Materials*, 6, March 2007.

[51] M. W. Geis. Growth of device-quality homoepitaxial diamond thin films. In *MRS Proceedings*, volume 162, page 15. Cambridge Univ Press, 1989.

[52] V. Geringer, M. Liebmann, T. Echtermeyer, S. Runte, M. Schmidt, R. Rückamp, M. C. Lemme, and M. Morgenstern. Intrinsic and extrinsic corrugation of monolayer graphene deposited on SiO 2. *Physical Review Letters*, 102(7), February 2009.

[53] Gianluca Giovannetti, Petr A. Khomyakov, Geert Brocks, Paul J. Kelly, and Jeroen van den Brink. Substrate-induced band gap in graphene on hexagonal boron nitride: *Ab initio* density functional calculations. *Physical Review B*, 76(7), August 2007.

[54] M. O. Goerbig. Electronic properties of graphene in a strong magnetic field. *Reviews of Modern Physics*, 83(4):1193–1243, November 2011.

[55] J. S. Gomez-Diaz and J. Perruisseau-Carrier. Graphene-based plasmonic switches at near infrared frequencies. *Optics Express*, 21(13):15490, July 2013.

[56] David J. Griffiths. *Introduction to electrodynamics*. Prentice Hall, Upper Saddle River, N.J., 1999.

[57] A. N. Grigorenko, M. Polini, and K. S. Novoselov. Graphene plasmonics. *Nature Photonics*, 6(11):749–758, November 2012.

[58] V. P. Gusynin, S. G. Sharapov, and J. P. Carbotte. Unusual Microwave Response of Dirac Quasiparticles in Graphene. *Physical Review Letters*, 96(25), June 2006.

[59] George W. Hanson. Dyadic Green's functions and guided surface waves for a surface conductivity model of graphene. *Journal of Applied Physics*, 103(6):064302, 2008.

[60] Yoshiaki Hattori, Takashi Taniguchi, Kenji Watanabe, and Kosuke Nagashio. Anisotropic Dielectric Breakdown Strength of Single Crystal Hexagonal Boron Nitride. *ACS Applied Materials & Interfaces*, 8(41):27877–27884, 2016.

[61] Yenny Hernandez, Valeria Nicolosi, Mustafa Lotya, Fiona M. Blighe, Zhenyu Sun, Sukanta De, I. T. McGovern, Brendan Holland, Michele Byrne, Yurii K. Gun'Ko, John J. Boland, Peter Niraj, Georg Duesberg, Satheesh Krishnamurthy, Robbie Goodhue, John Hutchison, Vittorio Scardaci, Andrea C. Ferrari, and Jonathan N. Coleman. High-yield production of graphene by liquid-phase exfoliation of graphite. *Nature Nanotechnology*, 3(9):563–568, September 2008.

[62] Jason Edward Hill. *One-dimensional electron systems on graphene edges*. PhD thesis, The University of Texas, Austin, August 2007.

[63] Min Hu, Jingyi Chen, Zhi-Yuan Li, Leslie Au, Gregory V. Hartland, Xingde Li, Manuel Marquez, and Younan Xia. Gold nanostructures: engineering their plasmonic properties for biomedical applications. *Chemical Society Reviews*, 35(11):1084, 2006.

[64] Pinshane Y. Huang, Carlos S. Ruiz-Vargas, Arend M. van der Zande, William S. Whitney, Mark P. Levendorf, Joshua W. Kevek, Shivank Garg, Jonathan S. Alden, Caleb J. Hustedt, Ye Zhu, Jiwoong Park, Paul L. McEuen, and David A. Muller. Grains and grain boundaries in single-layer graphene atomic patchwork quilts. *Nature*, 469(7330):389–392, January 2011.

[65] E. H. Hwang, S. Adam, and S. Das Sarma. Carrier Transport in Two-Dimensional Graphene Layers. *Physical Review Letters*, 98(18), May 2007.

[66] E. H. Hwang and S. Das Sarma. Dielectric function, screening, and plasmons in two-dimensional graphene. *Physical Review B*, 75(20), May 2007.

[67] E. H. Hwang and S. Das Sarma. Acoustic phonon scattering limited carrier mobility in two-dimensional extrinsic graphene. *Physical Review B*, 77(11), March 2008.

[68] Masa Ishigami, J. H. Chen, W. G. Cullen, M. S. Fuhrer, and E. D. Williams. Atomic Structure of Graphene on SiO $_2$. *Nano Letters*, 7(6):1643–1648, June 2007.

[69] Marinko Jablan, Hrvoje Buljan, and Marin Soljacic. Plasmonics in graphene at infrared frequencies. *Physical Review B*, 80(24), December 2009.

[70] Marinko Jablan, Marin Soljacic, and Hrvoje Buljan. Plasmons in graphene: fundamental properties and potential applications. *Proceedings of the IEEE*, 101(7):1689–1704, July 2013.

[71] John David Jackson. *Classical electrodynamics.* Wiley, New York, 1975.

[72] Prashant K. Jain, Kyeong Seok Lee, Ivan H. El-Sayed, and Mostafa A. El-Sayed. Calculated Absorption and Scattering Properties of Gold Nanoparticles of Different Size, Shape, and Composition: Applications in Biological Imaging and Biomedicine. *The Journal of Physical Chemistry B*, 110(14):7238–7248, April 2006.

[73] Jamesina Simpson. FDTD Lecture 8b: Stability (Max Times Step Permitted in 1-D, 2-D, and 3-D).

[74] Sung Kyu Jang, Jiyoun Youn, Young Jae Song, and Sungjoo Lee. Synthesis and Characterization of Hexagonal Boron Nitride as a Gate Dielectric. *Scientific Reports*, 6:30449, July 2016.

[75] Luis A. Jauregui, Helin Cao, Wei Wu, Qingkai Yu, and Yong P. Chen. Electronic properties of grains and grain boundaries in graphene grown by chemical vapor deposition. *Solid State Communications*, 151(16):1100–1104, August 2011.

[76] Long Ju, Baisong Geng, Jason Horng, Caglar Girit, Michael Martin, Zhao Hao, Hans A. Bechtel, Xiaogan Liang, Alex Zettl, Y. Ron Shen, and Feng Wang. Graphene plasmonics for tunable terahertz metamaterials. *Nature Nanotechnology*, 6(10):630–634, September 2011.

[77] L.J. Karssemeijer and Annalisa Fasolino. Phonons of graphene and graphitic materials derived from the empirical potential LCBOPII. *Surface Science*, 605(17-18):1611–1615, September 2011.

[78] M.I Katsnelson and A.K Geim. Electron scattering on microscopic corrugations in graphene. *Philosophical Transactions of the Royal Society A: Mathematical, Physical and Engineering Sciences*, 366(1863):195–204, January 2008.

[79] G. Kaupp. *Atomic force microscopy, scanning nearfield optical microscopy and nanoscratching: application to rough and natural surfaces.* Nanoscience and technology. Springer-Verlag, Berlin ; New York, 2006.

[80] Eun-Ah Kim and A. H. Castro Neto. Graphene as an electronic membrane. *EPL (Europhysics Letters)*, 84(5):57007, December 2008.

[81] Kwanpyo Kim, Zonghoon Lee, William Regan, C. Kisielowski, M. F. Crommie, and A. Zettl. Grain Boundary Mapping in Polycrystalline Graphene. *ACS Nano*, 5(3):2142–2146, March 2011.

[82] Charles Kittel, Paul McEuen, and John Wiley & Sons. *Introduction to solid state physics.* John Wiley & Sons, New Delhi, 2015.

[83] Aniruddha Konar, Tian Fang, and Debdeep Jena. Effect of high-κ gate dielectrics on charge transport in graphene-based field effect transistors. *Physical Review B*, 82(11), September 2010.

[84] O.V. Kotov, M.A. Kol'chenko, and Yu. E. Lozovik. Ultrahigh refractive index sensitivity of TE-polarized electromagnetic waves in graphene at the interface between two dielectric media. *Optics Express*, 21(11):13533, June 2013.

[85] M. Kulawik, M. Nowicki, G. Thielsch, L. Cramer, H.-P. Rust, H.-J. Freund, T. P. Pearl, and P. S. Weiss. A double lamellae dropoff etching procedure for tungsten tips attached to tuning fork atomic force microscopy/scanning tunneling microscopy sensors. *Review of Scientific Instruments*, 74(2):1027–1030, February 2003.

[86] N Kumada, R Dubourget, K Sasaki, S Tanabe, H Hibino, H Kamata, M Hashisaka, K Muraki, and T Fujisawa. Plasmon transport and its guiding in graphene. *New Journal of Physics*, 16(6):063055, June 2014.

[87] A. Lahrech, R. Bachelot, P. Gleyzes, and A. C. Boccara. Infrared-reflection-mode near-field microscopy using an apertureless probe with a resolution of λ/600. *Optics letters*, 21(17):1315–1317, 1996.

[88] Antti Laitinen, Mika Oksanen, Aurélien Fay, Daniel Cox, Matti Tomi, Pauli Virtanen, and Pertti J. Hakonen. Electron-Phonon Coupling in Suspended Graphene: Supercollisions by Ripples. *Nano Letters*, 14(6):3009–3013, June 2014.

[89] Ji Eun Lee, Gwanghyun Ahn, Jihye Shim, Young Sik Lee, and Sunmin Ryu. Optical separation of mechanical strain from charge doping in graphene. *Nature Communications*, 3:1024, August 2012.

[90] LEMOINE Paul-Arthur and DE WILDE Yannick. La nano-imagerie par microscopie optique en champ proche. *Techniques de l'ingénieur Nanosciences : concepts, caractérisation et aspects sécurité*, base documentaire : TIB194DUO(ref. article : nm7100), October 2007.

[91] Hong-Ju Li, Ling-Ling Wang, Jian-Qiang Liu, Zhen-Rong Huang, Bin Sun, and Xiang Zhai. Investigation of the graphene based planar plasmonic filters. *Applied Physics Letters*, 103(21):211104, 2013.

[92] Hong-Ju Li, Ling-Ling Wang, Han Zhang, Zhen-Rong Huang, Bin Sun, Xiang Zhai, and Shuang-Chun Wen. Graphene-based mid-infrared, tunable, electrically controlled plasmonic filter. *Applied Physics Express*, 7(2):024301, February 2014.

[93] X. Li, W. Cai, J. An, S. Kim, J. Nah, D. Yang, R. Piner, A. Velamakanni, I. Jung, E. Tutuc, S. K. Banerjee, L. Colombo, and R. S. Ruoff. Large-Area Synthesis of High-Quality and Uniform Graphene Films on Copper Foils. *Science*, 324(5932):1312–1314, June 2009.

[94] Zhaoyi Li and Nanfang Yu. Modulation of mid-infrared light using graphene-metal plasmonic antennas. *Applied Physics Letters*, 102(13):131108, 2013.

[95] Yu Liu and R. F. Willis. Plasmon-phonon strongly coupled mode in epitaxial graphene. *Physical Review B*, 81(8), February 2010.

[96] Yu Liu, R. F. Willis, K. V. Emtsev, and Th. Seyller. Plasmon dispersion and damping in electrically isolated two-dimensional charge sheets. *Physical Review B*, 78(20), November 2008.

[97] Tony Low and Phaedon Avouris. Graphene plasmonics for terahertz to mid-infrared applications. *ACS Nano*, 8(2):1086–1101, February 2014.

[98] Xiaoguang Luo, Teng Qiu, Weibing Lu, and Zhenhua Ni. Plasmons in graphene: recent progress and applications. *Materials Science and Engineering: R: Reports*, 74(11):351–376, November 2013.

[99] Ye Luo, Maysamreza Chamanzar, Aniello Apuzzo, Rafael Salas-Montiel, Kim Ngoc Nguyen, Sylvain Blaize, and Ali Adibi. On-Chip Hybrid Photonic-Plasmonic Light Concentrator for Nanofocusing in an Integrated Silicon Photonics Platform. *Nano Letters*, 15(2):849–856, February 2015.

[100] Isaac John Luxmoore, Choon How Gan, Peter Qiang Liu, Federico Valmorra, Penglei Li, Jérôme Faist, and Geoffrey R. Nash. Strong Coupling in the Far-Infrared between Graphene Plasmons and the Surface Optical Phonons of Silicon Dioxide. *ACS Photonics*, 1(11):1151–1155, November 2014.

[101] Stefan A. Maier. *Plasmonics: fundamentals and applications*. Springer, New York, NY, 2007.

[102] Eros Mariani and Felix von Oppen. Flexural Phonons in Free-Standing Graphene. *Physical Review Letters*, 100(7), February 2008.

[103] Eros Mariani and Felix von Oppen. Temperature-dependent resistivity of suspended graphene. *Physical Review B*, 82(19), November 2010.

[104] J. Martin, N. Akerman, G. Ulbricht, T. Lohmann, J. H. Smet, K. von Klitzing, and A. Yacoby. Observation of electron-hole puddles in graphene using a scanning single-electron transistor. *Nature Physics*, 4(2):144–148, February 2008.

[105] Jannik C. Meyer, A. K. Geim, M. I. Katsnelson, K. S. Novoselov, T. J. Booth, and S. Roth. The structure of suspended graphene sheets. *Nature*, 446(7131):60–63, March 2007.

[106] S. A. Mikhailov and K. Ziegler. New Electromagnetic Mode in Graphene. *Physical Review Letters*, 99(1), July 2007.

[107] Mario Miscuglio, Davide Spirito, Remo Proietti Zaccaria, and Roman Krahne. Shape Approaches for Enhancing Plasmon Propagation in Graphene. *ACS Photonics*, 3(11):2170–2175, November 2016.

[108] E. G. Mishchenko, A. V. Shytov, and P. G. Silvestrov. Guided Plasmons in Graphene p-n Junctions. *Physical Review Letters*, 104(15), April 2010.

[109] Naomi Mizuno, Bent Nielsen, and Xu Du. Ballistic-like supercurrent in suspended graphene Josephson weak links. *Nature Communications*, 4, November 2013.

[110] S. V. Morozov, K. S. Novoselov, M. I. Katsnelson, F. Schedin, D. C. Elias, J. A. Jaszczak, and A. K. Geim. Giant Intrinsic Carrier Mobilities in Graphene and Its Bilayer. *Physical Review Letters*, 100(1), January 2008.

[111] AYATO Nagashima, K. Nuka, H. Itoh, T. Ichinokawa, C. Oshima, S. Otani, and Y. Ishizawa. Two-dimensional plasmons in monolayer graphite. *Solid state communications*, 83(8):581–585, 1992.

[112] Vahid Nayyeri, Mohammad Soleimani, and Omar M. Ramahi. Modeling Graphene in the Finite-Difference Time-Domain Method Using a Surface Boundary Condition. *IEEE Transactions on Antennas and Propagation*, 61(8):4176–4182, August 2013.

[113] Van Luan Nguyen, Bong Gyu Shin, Dinh Loc Duong, Sung Tae Kim, David Perello, Young Jin Lim, Qing Hong Yuan, Feng Ding, Hu Young Jeong, Hyeon Suk Shin, Seung Mi Lee, Sang Hoon Chae, Quoc An Vu, Seung Hee Lee, and Young Hee Lee. Seamless Stitching of Graphene Domains on Polished Copper (111) Foil. *Advanced Materials*, 27(8):1376–1382, February 2015.

[114] G. X. Ni, L. Wang, M. D. Goldflam, M. Wagner, Z. Fei, A. S. McLeod, M. K. Liu, F. Keilmann, B. Ozyilmaz, A. H. Castro Neto, J. Hone, M. M. Fogler, and D. N. Basov. Ultrafast optical switching of infrared plasmon polaritons in high-mobility graphene. *Nature Photonics*, 10(4):244–247, March 2016.

[115] Denis L Nika and Alexander A Balandin. Two-dimensional phonon transport in graphene. *Journal of Physics: Condensed Matter*, 24(23):233203, June 2012.

[116] Kentaro Nomura and Allan H. MacDonald. Quantum Hall Ferromagnetism in Graphene. *Physical Review Letters*, 96(25), June 2006.

[117] K. S. Novoselov. Electric Field Effect in Atomically Thin Carbon Films. *Science*, 306(5696):666–669, October 2004.

[118] K S Novoselov and A H Castro Neto. Two-dimensional crystals-based heterostructures: materials with tailored properties. *Physica Scripta*, T146:014006, January 2012.

[119] K. S. Novoselov, D. Jiang, F. Schedin, T. J. Booth, V. V. Khotkevich, S. V. Morozov, and A. K. Geim. Two-dimensional atomic crystals. *Proceedings of the National Academy of Sciences of the United States of America*, 102(30):10451–10453, 2005.

[120] C. Nützenadel, A. Züttel, D. Chartouni, G. Schmid, and L. Schlapbach. Critical size and surface effect of the hydrogen interaction of palladium clusters. *The European Physical Journal D*, 8(2):245–250, 2000.

[121] H. Ochoa, Eduardo V. Castro, M. I. Katsnelson, and F. Guinea. Temperature-dependent resistivity in bilayer graphene due to flexural phonons. *Physical Review B*, 83(23), June 2011.

[122] H. Ochoa, Eduardo V. Castro, M.I. Katsnelson, and F. Guinea. Scattering by flexural phonons in suspended graphene under back gate induced strain. *Physica E: Low-dimensional Systems and Nanostructures*, 44(6):963–966, March 2012.

[123] Zhun-Yong Ong and Massimo V. Fischetti. Theory of remote phonon scattering in top-gated single-layer graphene. *Physical Review B*, 88(4), July 2013.

[124] Kelvin J. A. Ooi, Lay Kee Ang, and Dawn T. H. Tan. Waveguide engineering of graphene's nonlinearity. *Applied Physics Letters*, 105(11):111110, September 2014.

[125] Kelvin J. A. Ooi, Hong Son Chu, Ping Bai, and Lay Kee Ang. Electro-optical graphene plasmonic logic gates. *Optics Letters*, 39(6):1629, March 2014.

[126] Sungjin Park and Rodney S. Ruoff. Chemical methods for the production of graphenes. *Nature Nanotechnology*, 4(4):217–224, April 2009.

[127] N. M. R. Peres, F. Guinea, and A. H. Castro Neto. Electronic properties of disordered two-dimensional carbon. *Physical Review B*, 73(12), March 2006.

[128] J M Pitarke, V M Silkin, E V Chulkov, and P M Echenique. Theory of surface plasmons and surface-plasmon polaritons. *Reports on Progress in Physics*, 70(1):1–87, January 2007.

[129] Alessandro Principi, Matteo Carrega, Mark B. Lundeberg, Achim Woessner, Frank H. L. Koppens, Giovanni Vignale, and Marco Polini. Plasmon losses due to electron-phonon scattering: The case of graphene encapsulated in hexagonal boron nitride. *Physical Review B*, 90(16), October 2014.

[130] H. Raether. *Surface plasmons on smooth and rough surfaces and on gratings.* Springer-Verlag, Berlin; New York, 1988.

[131] Hassan Raza, editor. *Graphene Nanoelectronics.* NanoScience and Technology. Springer Berlin Heidelberg, Berlin, Heidelberg, 2012.

[132] S. Reich, J. Maultzsch, C. Thomsen, and P. Ordejón. Tight-binding description of graphene. *Physical Review B*, 66(3), July 2002.

[133] Alfonso Reina, Hyungbin Son, Liying Jiao, Ben Fan, Mildred S. Dresselhaus, ZhongFan Liu, and Jing Kong. Transferring and Identification of Single- and Few-Layer Graphene on Arbitrary Substrates. *The Journal of Physical Chemistry C*, 112(46):17741–17744, November 2008.

[134] C. Riedl, C. Coletti, T. Iwasaki, A. A. Zakharov, and U. Starke. Quasi-Free-Standing Epitaxial Graphene on SiC Obtained by Hydrogen Intercalation. *Physical Review Letters*, 103(24), December 2009.

[135] G. M. Rutter, J. N. Crain, N. P. Guisinger, T. Li, P. N. First, and J. A. Stroscio. Scattering and Interference in Epitaxial Graphene. *Science*, 317(5835):219–222, July 2007.

[136] R. Saito, G. Dresselhaus, and M. S. Dresselhaus. *Physical properties of carbon nanotubes.* Imperial College Press, London, 2007.

[137] JC Sancho-García and AJ Pérez-Jiménez. Electronic Properties and Transport in Finite-Size Two-Dimensional Carbons. In *Graphene Science Handbook*, pages 91–104. CRC Press, April 2016.

[138] I. I. Shaganov, T. S. Perova, R. A. Moore, and K. Berwick. Spectroscopic characteristics of SiO and SiO2 solid films: Assignment and local field effect influence. *Journal of Materials Science: Materials in Electronics*, 12(4-6):351–355, 2001.

[139] S. Y. Shin, N. D. Kim, J. G. Kim, K. S. Kim, D. Y. Noh, Kwang S. Kim, and J. W. Chung. Control of the π plasmon in a single layer graphene by charge doping. *Applied Physics Letters*, 99(8):082110, 2011.

[140] Ergun Simsek. A closed-form approximate expression for the optical conductivity of graphene. *Optics Letters*, 38(9):1437, May 2013.

[141] J. Slawinska, P. Dabrowski, and I. Zasada. Doping of graphene by a Au(111) substrate: Calculation strategy within the local density approximation and a semiempirical van der Waals approach. *Physical Review B*, 83(24), June 2011.

[142] H. S. Song, S. L. Li, H. Miyazaki, S. Sato, K. Hayashi, A. Yamada, N. Yokoyama, and K. Tsukagoshi. Origin of the relatively low transport mobility of graphene grown through chemical vapor deposition. *Scientific Reports*, 2, March 2012.

[143] Kandammathe Valiyaveedu Sreekanth, Shuwen Zeng, Jingzhi Shang, Ken-Tye Yong, and Ting Yu. Excitation of surface electromagnetic waves in a graphene-based Bragg grating. *Scientific Reports*, 2, October 2012.

[144] Ilan Stefanon, Sylvain Blaize, Aurélien Bruyant, Sébastien Aubert, Gilles Lerondel, Renaud Bachelot, and Pascal Royer. Heterodyne detection of guided waves using a scattering-type scanning near-field optical microscope. *Optics express*, 13(14):5553–5564, 2005.

[145] K. Suenaga, C. Colliex, N. Demoncy, A. Loiseau, H. Pascard, and F. Willaime. Synthesis of Nanoparticles and Nanotubes with Well-Separated Layers of Boron Nitride and Carbon. *Science*, 278(5338):653, October 1997.

[146] Allen Taflove and S C. Hagness. *Computational Electrodynamics: The Finite-Difference Time-Domain Method, 3rd edition.*, volume 2062. June 2005.

[147] Andrea Toma, Gobind Das, RemoProietti Zaccaria, Manohar Chirumamilla, Francesco Gentile, Federico Mecarini, MariaLaura Coluccio, Marco Leoncini, Carlo Liberale, Marco Francardi, Francesco De Angelis, and Enzo Di Fabrizio. Nanostructures for Plasmonics. In *Nanoantenna*, pages 267–296. Pan Stanford Publishing, January 2013.

[148] Ashkan Vakil and Nader Engheta. Transformation Optics Using Graphene. *Science*, 332(6035):1291–1294, June 2011.

[149] Guoxi Wang, Xueming Liu, Hua Lu, and Chao Zeng. Graphene plasmonic lens for manipulating energy flow. *Scientific Reports*, 4, February 2014.

[150] Haidong Wang, Xing Zhang, and Hiroshi Takamatsu. Ultraclean suspended monolayer graphene achieved by *in situ* current annealing. *Nanotechnology*, 28(4):045706, January 2017.

[151] P.R. West, S. Ishii, G.V. Naik, N.K. Emani, V.M. Shalaev, and A. Boltasseva. Searching for better plasmonic materials. *Laser & Photonics Reviews*, 4(6):795–808, November 2010.

[152] Roland Wiesendanger, Klaus von Klitzing, and Roland Wiesendanger, editors. *Scanning Probe Microscopy*. NanoScience and Technology. Springer Berlin Heidelberg, Berlin, Heidelberg, 1998.

[153] Achim Woessner, Mark B. Lundeberg, Yuanda Gao, Alessandro Principi, Pablo Alonso-González, Matteo Carrega, Kenji Watanabe, Takashi Taniguchi, Giovanni Vignale, Marco Polini, James Hone, Rainer Hillenbrand, and Frank H. L. Koppens. Highly confined low-loss plasmons in graphene-boron nitride heterostructures. *Nature Materials*, 14(4):421–425, December 2014.

[154] E. L. Wolf. *Graphene: a new paradigm in condensed matter and device physics*. Oxford University Press, Oxford, United Kingdom ; New York, NY, United States of America, first edition edition, 2014. OCLC: ocn864784879.

[155] Hon-Sum Philip Wong and Deji Akinwande. *Carbon nanotube graphene device physics*. Cambridge University Press, Cambridge ; New York, 2011.

[156] Chris JH Wort and Richard S. Balmer. Diamond as an electronic material. *Materials Today*, 11(1):22–28, 2008.

[157] Jipeng Wu, Leyong Jiang, Jun Guo, Xiaoyu Dai, Yuanjiang Xiang, and Shuangchun Wen. Tunable perfect absorption at infrared frequencies by a graphene-hBN hyper crystal. *Optics Express*, 24(15):17103, July 2016.

[158] Xiangyu Wu, Inge Asselberghs, Maria Politou, Antonino Contino, Iuliana Radu, Cedric Huyghebaert, Zsolt Tokei, Bart Soree, Stefan De Gendt, Steven De Feyter, and Marc Heyns. Doping of graphene for the application in nano-interconnect. *Microelectronic Engineering*, 167:42–46, January 2017.

[159] B Wunsch, T Stauber, F Sols, and F Guinea. Dynamical polarization of graphene at finite doping. *New Journal of Physics*, 8(12):318–318, December 2006.

[160] Hugen Yan, Xuesong Li, Bhupesh Chandra, George Tulevski, Yanqing Wu, Marcus Freitag, Wenjuan Zhu, Phaedon Avouris, and Fengnian Xia. Tunable infrared plasmonic devices using graphene/insulator stacks. *Nature Nanotechnology*, 7(5):330–334, April 2012.

[161] Hugen Yan, Tony Low, Wenjuan Zhu, Yanqing Wu, Marcus Freitag, Xuesong Li, Francisco Guinea, Phaedon Avouris, and Fengnian Xia. Damping pathways of mid-infrared plasmons in graphene nanostructures. *Nature Photonics*, 7(5):394–399, April 2013.

[162] Matthew Yankowitz, Jiamin Xue, Daniel Cormode, Javier D. Sanchez-Yamagishi, K. Watanabe, T. Taniguchi, Pablo Jarillo-Herrero, Philippe Jacquod, and Brian J. LeRoy. Emergence of superlattice Dirac points in graphene on hexagonal boron nitride. *Nature Physics*, 8(5):382–386, March 2012.

[163] Yu Yao, Mikhail A. Kats, Patrice Genevet, Nanfang Yu, Yi Song, Jing Kong, and Federico Capasso. Broad Electrical Tuning of Graphene-Loaded Plasmonic Antennas. *Nano Letters*, 13(3):1257–1264, March 2013.

[164] Morteza Yarahmadi, Mohammad K. Moravvej-Farshi, and Leila Yousefi. Subwavelength Graphene-Based Plasmonic THz Switches and Logic Gates. *IEEE Transactions on Terahertz Science and Technology*, 5(5):725–731, September 2015.

[165] Jie Yu, Guanxiong Liu, Anirudha V. Sumant, Vivek Goyal, and Alexander A. Balandin. Graphene-on-Diamond Devices with Increased Current-Carrying Capacity: Carbon sp ^{2} -on-sp ^{3} Technology. *Nano Letters*, 12(3):1603–1608, March 2012.

[166] Qingkai Yu, Jie Lian, Sujitra Siriponglert, Hao Li, Yong P. Chen, and Shin-Shem Pei. Graphene segregated on Ni surfaces and transferred to insulators. *Applied Physics Letters*, 93(11):113103, 2008.

[167] Renwen Yu, Valerio Pruneri, and F. J. Garcia de Abajo. Active modulation of visible light with graphene-loaded ultrathin metal plasmonic antennas. *Scientific Reports*, 6:32144, August 2016.

[168] A. V. Zayats and David Richards, editors. *Nano-optics and near-field optical microscopy*. Artech House nanoscale science and engineering. Artech House, Boston ; London, 2009. OCLC: ocn233547461.

[169] Yi Zhang, Luyao Zhang, and Chongwu Zhou. Review of Chemical Vapor Deposition of Graphene and Related Applications. *Accounts of Chemical Research*, 46(10):2329–2339, October 2013.

[170] Yuanbo Zhang, Victor W. Brar, Caglar Girit, Alex Zettl, and Michael F. Crommie. Origin of spatial charge inhomogeneity in graphene. *Nature Physics*, 5(10):722–726, October 2009.

[171] L. Zhao, K.T. Rim, H. Zhou, R. He, T.F. Heinz, A. Pinczuk, G.W. Flynn, and A.N. Pasupathy. Influence of copper crystal surface on the CVD growth of large area monolayer graphene. *Solid State Communications*, 151(7):509–513, April 2011.

[172] Jinfeng Zhu, Qing Huo Liu, and Timothy Lin. Manipulating light absorption of graphene using plasmonic nanoparticles. *Nanoscale*, 5(17):7785, 2013.

[173] K. Ziegler. Robust Transport Properties in Graphene. *Physical Review Letters*, 97(26), December 2006.

[174] P. J. Zomer, S. P. Dash, N. Tombros, and B. J. Van Wees. A transfer technique for high mobility graphene devices on commercially available hexagonal boron nitride. *Applied Physics Letters*, 99(23):232104, 2011.

Appendices

Appendix A

Example of application : infrared spectrometer

One of the direct application of graphene plasmons is that it could lead to optoelectronic transistors, already demonstrated experimentally. Others theoretical devices have been also study numerically. An infrared spectrometer concept is presented below.

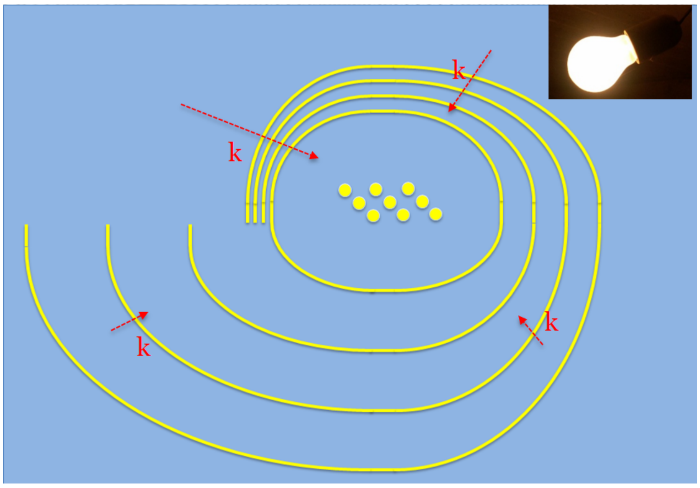

Figure A.1: Illustration of a golden snail shape structure that is possible to fabricate through e-beam lithography. In the center, golden diffusers are placed.

It is based on the grating effect which is presented Section 4.1.4. Periodic structures have the property to diffract the light. As well as antenna (see Section 3.3), periodic structures can excite graphene plasmons. They also show a particularity : they can enhance a near field with a particular angular momentum.

At normal incidence, the momentum of the near field enhanced by the periodic structures is inversely proportional to the spacing between the different periodic structures (see Equation 4.5). Therefore, the wavelength enhanced by the periodicity of the grating is proportional to the distance between two periodic structure.

Hence, it is possible to fabricate a grating with a defined space between the periodic structure which select a wavelength (momentum) to be enhanced. As well, it should be possible theoretically to design a periodic structure with a variable spacing, that could be able to enhance near fields with a pre-defined range of wavelength (pre-defined range of momentum). Figure A.1 shows a snail shape periodic structure, with a distance in between golden line which vary steadily. This kind of structure can be seen as a many grating, drawing lines from the center of the snail to the edges. In each direction, a different spacing between the rods enhanced a different wavelength. In the center is placed diffusers.

Let's assume a beam of light with a broad frequency spectrum. When this beam is hitting the structure, the different period of the shape would enhanced a range of near field associated with a range of angular momentum, depending on the spacing between the different rod. Therefore, all the plasmons related to those angular momentum would be launched. In the case of graphene, above the intrinsic graphene phonon taking place around $6\mu m$, plasmons are theoretically propagating (in the case we have a suitable platform for propagation of plasmons, with graphene doped electrostatically).

Then, the plasmon will travel toward the center of the snail, exciting the golden diffusers. The diffusers would transfer the energy of plasmons to radiative light out of the plane, that could be eventually recorded. This is general principle of this infrared spectrometer. In the following, we will now take the case where we have a beam made of three frequencies. The spectrum of the beam is shown on the right of the Figure A.2. The case of a beam hitting the sample with a normal angle (on the left of the Figure A.2) is taken in this example. Finally, the spectrometer will work thanks to the tunability of graphene plasmons, that is presented below.

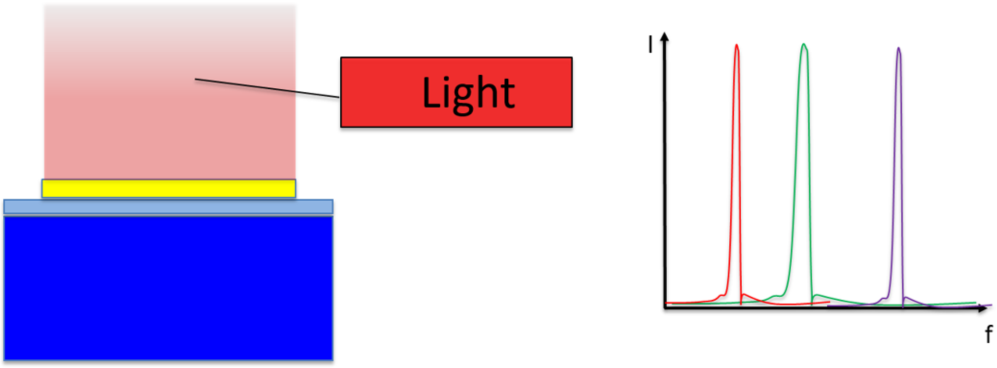

Figure A.2: On the left, a beam of light hit the snail (in yellow) perpendicularly to its plane. The substrate is represented by two different blue color. On the right is shown the spectrum of the beam combining three distinct frequencies.

Let's start from undoped graphene, which means that no potential is applied to the graphene (Figure A.3 left). Its Fermi level approach zero (Figure A.3 center left) and no plasmons would be able to propagate to the diffusers (Figure A.3 center right), due to high Laundau damping (see Section 1.3.3). No signal would be detected (Figure A.3 right).

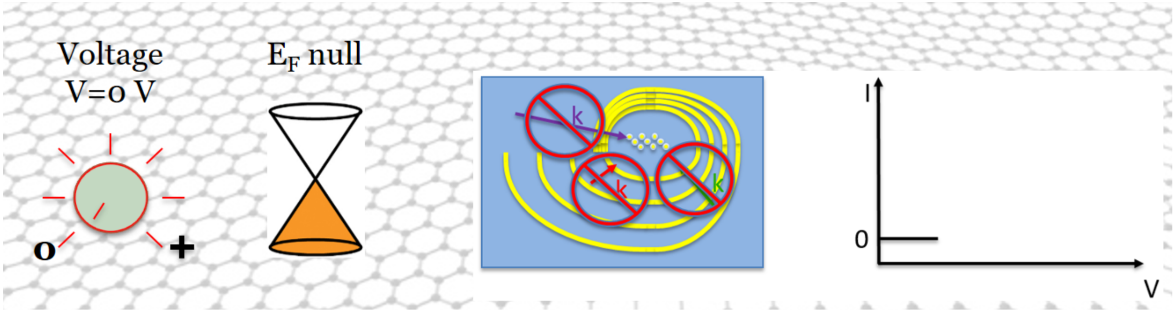

Figure A.3: Illustration of the first step of the spectrometer concept. The graphene is undoped (0V applied), no plasmons are propagating, and no signal is broadcast.

Let's now rise slowly the potential (Figure A.4 left). The graphene is electrostaticaly doped. Its Fermi energy will rise also slowly (Figure A.4 center left). Energetically low plasmons (long wavelength) would be able to propagate through graphene. Therefore, the related small angular momentum corresponding to low energy plasmons would be launched and propagate to the diffusers (Figure A.4 center right). The diffusers would transform plasmons energy into farfield signal, that can be recorded. Intensity increase at the photodetector (Figure A.4 right). Referring to our three frequency beam, the lower frequency would be then recorded at the photodetector (red small arrow).

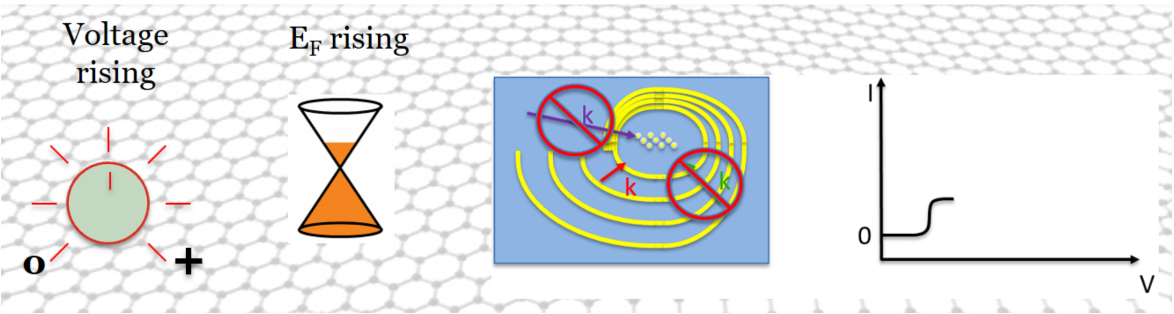

Figure A.4: Illustration of the second step of the spectrometer concept. The graphene is weakly doped by an applied voltage, low energy plasmons are propagating, and a signal is recorded.

Rising again the backgate potential would allowed higher energy plasmons to propagate to the diffusers. In this case, the central frequency of the beam would be recorded (green arrow). That would increase the intensity recorded at the detector (Figure A.5).

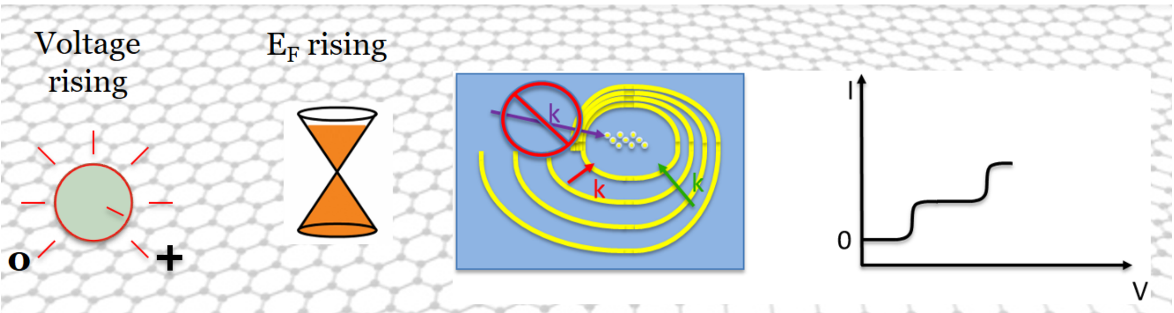

Figure A.5: As the applied voltage is rising, the Fermi energy in graphene is rising, enabling higher energetical plasmons to propagate to the diffusers. A corresponding energy is transfered to the photodetector.

Eventually, all the permitted graphene plasmons (above $6\mu m$) would be allowed to travel to the diffusers and be recorded to the photodetector (Figure A.6 left). Because each plasmons correspond to a wavelength, it is possible, from the intensity spectrum recorded, to recover the incident beam spectrum. In fact, each intensity step, corresponding to a distinct applied potential, would be interpreted as a frequency (Figure A.6 right). A transfer function would actually exist in between the potential and the frequency. As well, the intensity of a peak will depend on the height a a step.

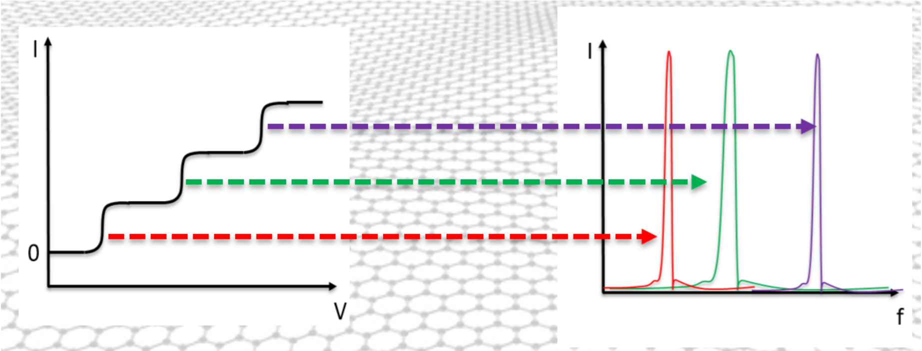

Figure A.6: On the left, the intensity finally recorded at the photodetector. It is a step function with in x-axis the intensity versus the potential in y-axis. Each step is therefore characterized by a different of intensity, and a potential (ΔI, V). On the right, the recovered frequency spectrum of the beam.

Appendix B

French summary

Introduction

Au cours du siècle dernier, le domaine de l'infiniment petit a commencé à être étudié, au fur et à mesure que les outils ont été développé et ont été disponible dans les centres de recherche. Les nanosciences ont porté les promesses de révolution dans de nombreux domaines. Entre autres, d'énormes efforts ont été mis en place dans les domaines de la médecine et des technologies de l'information, où des progrès sont fortement demandés. La nanoscience est présente dans notre vie quotidienne à travers tous les dispositifs électroniques qui nous entourent. En effet, la taille du composant a été réduite de façon régulière jusqu'à l'échelle nanométrique. Cependant, le nanomonde ne fonctionne pas avec les mêmes règles physiques, où d'autres phénomènes ont lieu. Beaucoup de recherches sont orientées vers la résolution des problèmes qui se posent, avec deux stratégies. La première est de faire fonctionner les nano-dispositifs de la même façon que les macro dispositifs marchent à notre échelle. La seconde stratégie est de mener des recherches afin de tirer avantage de ces nouvelles règles, de ces nouveaux phénomènes. Cette thèse vise à montrer quelques résultats récents sur les ondes électromagnétiques apparaissant à l'échelle atomique. Ce travail prend place à l'intersection de deux disciplines, la plasmonique et le graphène, en tant que nouveau matériau.

La plasmonique fait partie du domaine général des plasmas. Le plasma est un état de la matière, où les ondes collectives de densité d'électrons peuvent être manipulées. Il en existe plusieurs formes, et l'une d'entre elles est l'oscillation collective en 2D des électrons de surface des matériaux conducteurs. A l'interface entre un métal et un isolant, des plasmons de surface peuvent être trouvés. Ces ondes électromagnétiques peuvent être couplées à la lumière, et cette dernière pouvant se retrouver confinée. Le confinement de la lumière est un sujet de recherche important car les appareils photoniques souffrent de leur taille, en grande partie due à la taille de la longueur d'onde à laquelle ils fonctionnent. Ce phénomène plasmonique a été récemment observé dans un matériau 2D, plus particulièrement dans le graphène.

Dans la quête de comprendre et de manipuler l'infiniment petit, le graphène apparaît comme un trésor. Il est en effet infiniment mince : c'est la première couche d'un atome d'épaisseur à être découverte. La liaison forte carbone-carbone permet au scientifique de le manipuler avec des outils macroscopiques. En plus de cela, il est possible d'isoler une couche de graphène par la technique d'exfoliation mécanique avec du scotche. Cette technique a un gros avantage : elle est si simple et bon marché qu'elle peut être reproduite par n'importe quelle équipe de recherche dans le monde entier. Enfin, ses propriétés particulières ouvrent de nouveaux champs de recherche. Pour avoir une idée de l'importance de la découverte, il n'a fallu que six ans à Andrei Geim et Kostya Novoselov pour obtenir leur prix Nobel après leur célèbre publication. Dans ce contexte apparaît le domaine de la plasmonique dans le graphène.

Le domaine de la plasmonique dans le graphène émerge quelques années après les prix Nobel. Les plasmons de graphène ont montré leur potentiel grâce à leur confinement élevé et leur tunabilité. Ce domaine est détaillé dans cette thèse. Dans le premier chapitre, quelques connaissances de base sur les propriétés plasmoniques en général, et sur les propriétés principalement électroniques du graphène, sont exposées. Le deuxième chapitre est une revue de la littérature sur le graphène et la plasmonique dans le graphène, ainsi que la démonstration d'un modèle de base expliquant les propriétés des plasmons de graphène. Dans le troisième chapitre, une étude numérique sur les plasmons se propageant dans le graphène suspendu est présentée. Dans le quatrième chapitre, la fabrication d'échantillons ainsi que les mesures optiques à travers un SNOM (scanning near-field optic microscope) fait maison sont introduites. Enfin, les principaux résultats de cette thèse sont résumés, ainsi que la direction de recherche possible à prendre en compte à la suite de ce travail.

Contexte théorique

Cette thèse s'inscrit dans le cadre d'un champ scientifique large et peu intuitif, généralement appelé nanotechnologie. Le nom se réfère directement à la taille (le nanomètres) des systèmes étudiés. De nouvelles propriétés découlent du confinement dans une ou plusieurs dimensions des matériaux. A titre d'exemple, le rapport entre les atomes de surface et les atomes de cœur varie considérablement lorsque l'on réduit les dimensions d'un objet à l'échelle nanométrique. En fait, les atomes de surface présentent des propriétés différentes des atomes de coeur, car les forces appliquées sur eux ainsi que leur terminaisons chimiques diffèrent. Par conséquent, les atomes de surface donnent à la structure de nouvelles propriétés chimiques, car ils construisent l'interface physique entre le solide et son environnement. Le confinement de la structure donne également de nouvelles propriétés physiques, mécaniques, électromagnétiques. En particulier, on y trouve de nouvelle propriétés plasmoniques remarquables. C'est notoirement le cas pour les matériaux à deux dimensions découverts assez récemment [119], et parmi eux le graphène.

Afin d'aller plus loin dans le domaine de la plasmonique dans le graphène, le premier chapitre vise à exposer les bases de la plasmonique et du graphène. Par conséquent, dans une première partie, les équations de Maxwell et le modèle de Drude sont introduits, ce qui donnera les clés pour traiter la deuxième partie de ce chapitre, c'est-à-dire les plasmons de surface polaritons (SPP). Enfin, certaines des propriétés électronique du graphène seront expliquées.

Les équations de Maxwell et le modèle de Drude

Les équations de Maxwell sont les bases d'une révolution en physique [56, 71]. Ces équations couplent le champ magnétique $\mathbf{H}(\mathbf{r}, t)$ et le champ électrique $\mathbf{E}(\mathbf{r}, t)$. Dans le domaine spatial et temporel, les 6 fonctions scalaires de ces champs sont reliées entre elles par les équations de Maxwell, qui donnent naissance à l'équation de l'onde électromagnétique. Cet ensemble d'équations différentielles partielles fait partie des lois de la science. Il y a quatre équations qu'il est possible de définir en fonction des milieux environnants. Grâce à ces équations, il est possible d'obtenir la relation de dispersion suivante :

$$k^2 = \epsilon \frac{w^2}{c^2} \quad \text{ie} \quad k = \sqrt{\epsilon} \frac{w}{c} \tag{B.1}$$

Cette relation de dispersion décrit la dynamique d'une onde plane dans un milieu avec k le nombre d'onde, ϵ la permittivité du milieu, w la pulsation et c la vitesse de la lumière dans le vide. Si le milieu est dit dispersif, sa fonction diélectrique est fonction de la longueur d'onde de la lumière. La fonction diélectrique est habituellement notée $\epsilon(w)$. Dans le vide, $\epsilon(w) = 1$ et la relation de dispersion linéaire devient:

$$k = \frac{w}{c} \tag{B.2}$$

Conditions aux limites

Les équations de Maxwell sont valables pour un milieu continu. Cependant, ils peuvent être utilisés dans le cas d'interfaces, où ils contraignent le comportement des champs électromagnétiques conduisant à ce que l'on appelle les conditions aux limites. En conséquence, une partie de l'énergie est généralement réfléchie, et une autre transmise. Il est également possible d'en déduire les directions et les angles des champs résultants, en fonction du faisceau incident, de sa polarisation ainsi que des propriétés des milieux. Plus spécifiquement pour cette étude, la relation de dispersion des plasmons de graphène provient des conditions aux limites appliquées sur le champ magnétique.

Les conditions aux limites pour les champs électromagnétiques peuvent être dérivées des formes intégrales des équations de Maxwell exposées dans l'introduction de la section. Quatre conditions aux limites proviennent des 4 équations de Maxwell.

Révision du modèle de Drude et des équations du mouvement des électrons libres

Le modèle Drude a été construit trois ans après la découverte des électrons par Thomson. Dans un métal, Drude considère une mer d'électrons et utilise la théorie des gaz pour décrire les conductions électriques et thermiques. Dans ce modèle, il est supposé que les électrons sont des solides sphériques se déplaçant à l'identique le long d'une ligne droite. Une moyenne temporelle ($t = \tau$) connue sous le nom de temps de collision est définie pour délimiter deux collisions. Les électrons émergeront avec une direction et une vitesse aléatoire après chaque collision (pas de condition initiale particulière). Il n'y a pas de force appliquée sur les électrons sauf celles qui se produisent quand ils entrent en collision : pas d'interaction électron-électron (approximation indépendante des électrons), pas d'interaction électron-ion (approximation des électrons libres).

Fonction diélectrique du gaz d'électrons. La réponse optique d'un métal Drude, en l'absence de force de traînée, peut être établie :

$$\epsilon(\omega) = 1 - \frac{ne^2}{\epsilon_0 m\omega^2} = 1 - \frac{\omega_p^2}{\omega^2} \tag{B.3}$$

avec n la densité de charge, e la charge élementaire, ϵ_0 la permittivité du vide, m la masse de la charge et ω_p la fréquence du plasma. A cette fréquence angulaire, le mouvement collectif des électrons dans un milieu conducteur, tel qu'un métal, résonne. Sous cette fréquence, le milieu réfléchit l'onde électromagnétique, tandis qu'au-dessus, l'onde se propage à travers le milieu.

Équations de mouvement pour un porteur de charge libre. Il est possible de décrire la dynamique d'un porteur de charge libre en ajoutant un terme d'amortissement.

On définit donc la conductivité optique $\sigma(w)$ en fonction de la pulsation par :

$$\sigma(w) = \frac{ine^2}{m(w + i/\tau)} \tag{B.4}$$

De la conductivité optique à la permittivité. La permittivité est une propriété intrinsèque vraiment intéressante des matériaux car elle donne accès à la réponse optique d'un matériau sous perturbations. Malheureusement, cette propriété n'est utile que pour la modélisation de matériaux 3D. Le graphène étant une feuille de carbone d'un atome d'épaisseur, nous utiliserons plus probablement la conductivité 2D. Cependant, dans une première approche, le modèle de Drude peut convertir la conductivité 2D en une permittivité 3D, ce qui nous donne une bonne idée de la réponse optique du graphène dans l'infrarouge. Ses propriétés optiques via la permittivité des matériaux ont été largement utilisées au début pour le graphène, permettant ainsi la simulation FDTD.

Cette approche 3D implique de modéliser des matériaux avec un ensemble arbitraire d'épaisseur finie de $2a$. Dans ce modèle, l'environnement du graphène, caractérisé par une permittivité $epsilon_s$, joue également un rôle crucial:

$$\epsilon_g(\omega) = \epsilon_s(\omega) + \frac{i\sigma_{2D}(w)}{\omega 2a\epsilon_0} \tag{B.5}$$

Dans le cas du graphène suspendu, $\epsilon_1 = \epsilon_2 = \epsilon_{air} = 1$ et ainsi $\epsilon_s = 1$. L'équation (B.5) mène à :

$$\epsilon_g(\omega) = 1 + \frac{i\sigma_{2D}(w)}{\omega 2a\epsilon_0} \tag{B.6}$$

Plasmons de surface polariton

Dans le cadre de l'étude des ondes électromagnétiques, les plasmons de Surface polaritons peuvent être considérés comme un résultat particulier des équations de Maxwell à l'interface de deux milieux aux propriétés spécifiques [101, 128, 130]. Pour donner une explication plus imagée de la plasmonique, il est intéressant de revenir à son origine physique. Le plasmon peut être vu comme un mouvement collectif d'électrons réagissant à un champ électrique. Cependant, ces mouvements collectifs ont tendance à se déplacer un peu trop loin et, par conséquent, une force de rappel les tire vers l'arrière. Ceci en réaction à la perturbation de charge créée par leur excès de déplacement. Ce premier mouvement collectif est répété de sorte qu'une oscillation faiblement amortie se produit. Par conséquent, un plasmon peut être défini comme une oscillation collective cohérente d'électrons libres. Lorsque l'excitation du plasmon est légère, un couplage entre les plasmons et l'onde électromagnétique se produit, aboutissant à un plasmon de surface polariton (SPP).

Plasmon de surface polariton sur une seule interface en absence de courant libre

Dans notre cas, nous nous intéressons aux plasmons de surface n'apparaissant qu'en mode TM (pour le cas TE, voir [101]). La relation de dispersion d'un SPP dans un système à une seule interface est :

$$k_x = k_p = k_0\sqrt{\frac{\epsilon_1\epsilon_2}{\epsilon_1+\epsilon_2}} \tag{B.7}$$

k_p est le vecteur d'onde de plasmon de surface. Cette grandeur k_p peut donner des informations intéressantes telles que la longueur de propagation:

$$L = \frac{1}{2Im[k_p]} \tag{B.8}$$

aussi bien que la longueur d'onde effective du plasmon dans le matériau :

$$\lambda_p = \frac{2\pi}{Re[k_p]} \tag{B.9}$$

La longueur de propagation est la longueur à laquelle l'intensité, proportionnelle au carré du module du champ électromagnétique, tombe à 1/e. La longueur d'onde des plasmons est la longueur d'onde efficace qui peut être mesurée, par exemple, par la microscopie optique en champ proche (SNOM). Cette dernière grandeur physique peut être normalisée par le champ d'excitation et s'appelle dans ce cas le facteur de localisation. Il donne aussi, indirectement, une bonne idée du confinement du champ électromagnétique dans les matériaux.

Polariton de plasmon de surface dans un système multicouche

Un système multicouche est défini lorsqu'une interaction/couplage entre des plasmons de surface de différentes interfaces a lieu. Cela signifie que l'épaisseur du métal est comparable ou inférieure à la décroissance du plasmon de surface.

Il existe deux modes possible, représentés par deux équations de dispersion. Le modes antisymétrique tend à devenir radiatif, car il suit la relation de dispersion de la lumière dans l'air. Par conséquent, pour le graphène qui est un matériau d'un atome d'épaisseur, seule la relation de dispersion symétrique subsiste. Dans ce mode, la profondeur de pénétration devient petite, ce qui conduit à un très fort confinement .

L'étude réalisée dans ce chapitre a été menée de façon a comprendre la plamonique appliquée dans le cas d'un métal extrêmement mince. Le graphène, qui est un semi-métal, a un comportement plasmonique remarquablement proche des SPP provenant d'une couche extrêmement mince de métal noble commun. Cependant, sa structure cristalline 2D ainsi que la dynamique de ses électrons rendent les Plasmons du Graphène un peu différents. Dans la section suivante, nous nous intéresserons donc aux propriétés cristallines et électroniques du graphène, avant d'approfondir la plasmonique graphène.

Propriétés du graphène

Une feuille d'atome de carbone

Le graphène est la mère de toutes les formes graphitiques: c'est une feuille d'atomes de carbone dans un réseau en nid d'abeille. Il possède des propriétés physiques uniques: le graphène est le matériau connu le plus fort et le plus flexible, il a l'enregistrement de la conductivité thermique la plus forte, et est complètement imperméable [50, 8]. De plus, du point de vue optoélectronique, ses porteurs (électrons et trous) présentent une très grande mobilité et un long chemin libre moyen. Le graphène a des densités de porteur de charge tunable par l'application d'un potentiel électrique. De plus, cette membrane épaisse d'un atome est un exemple parfait d'un système d'électrons bidimensionnel pour les physiciens. Selon [62], "Quand la théorie quantique des solides a été développée, le graphite a été l'un des premiers matériaux auxquels cette théorie a été appliqué. Les premiers calculs de la structure en bande d'énergie du graphite semblent avoir été faits par Hund et Mrowska en 1937 en tant qu'exercice académique. "

Afin d'étudier en détail les propriétés opto-électroniques du graphène, il est important de regarder sa structure cristalline. C'est une monocouche d'atomes de carbone bornés sp_2 dans un réseau en nid d'abeille. Chaque atome de carbone est attaché à trois voisins par des liaisons covalentes d'une longueur d'environ $a_0 = 0,142nm$. Cette configuration provient des interférences orbitales atomiques entre atomes de carbone voisins (hybridation orbitale).

Faisons d'abord un zoom sur la plus petite unité de sa structure: l'atome de carbone. Cet élément chimique a six électrons, quatre des électrons sont dans sa couche de valence (la couche extérieure). La configuration de l'état fondamental de l'atome de carbon est $1S^2 2S^2 2P^2$ qui peut aussi être écrite afin de faire ressortir les électrons de valence $[He]2S^2 2P^2$. De façon schématique :

$$\boxed{\uparrow\downarrow}_{1S}\quad\boxed{\uparrow\downarrow}_{2S}\quad\boxed{\uparrow}\boxed{\uparrow}\boxed{}_{2P} \tag{B.10}$$

Ici, nous pouvons voir les six électrons représentés par des flèches (la direction de la flèche représente le spin électronique). Les électrons situés les plus proches du noyau se trouvent dans l'orbitale 1s. Ces électrons sont généralement considérés comme "gelés" dans l'approximation pseudo-potentielle, qui a lieu dans de nombreux modèles. Le modèle de pseudopotentiel est un moyen de remplacer les effets compliqués du mouvement des électrons de noyau d'un atome et de son noyau par un potentiel effectif, ou pseudopotentiel. Ces électrons ne sont pas impliqués dans les liaisons inter-atomiques. Les deux électrons suivants sont dans l'orbitale 2s. Les autres seront dans deux orbitales 2p distinctes. Les orbitales p ont la même énergie et donc les électrons seraient plutôt dans des orbitales séparées.

Dans le graphène, l'atome de carbone réarrange ses électrons de valence de manière à créer des liaisons avec ses trois voisins. En fait, créer une liaison diminue l'énergie du système. On se retrouve donc avec des atomes de carbone dont les états électronique sont décrit de la manière suivante :

$$\left\{\begin{matrix} s \\ p_x \\ p_y \\ p_z \end{matrix}\right\} \text{ with a electronic configuration : } \boxed{\uparrow}_{2S}\quad\boxed{\uparrow}\boxed{\uparrow}\boxed{\uparrow}_{2P} \tag{B.11}$$

De cette manière, il est possible de reconstruire la structure en nid d'abeille avec des liaisons hybrides de type sp_2

Le modèle des liaisons fortes : une étude sur la dynamique des électrons

Modélisation de la dynamique des électrons, un ensemble d'hypothèses

Afin d'étudier en détail les propriétés opto-électroniques du graphène, donnant lieu à des plasmons, il est important de se pencher sur la dynamique des électrons dans ce matériau 2D.

Ce problème est bien connu et peut être résolu en mélangeant la physique des états solides avec la mécanique quantique. Le premier point est de réaliser qu'un tel système de n-corps ne peut pas être résolu exactement, en raison des interactions et des degrés de liberté importants. En effet, les électrons et les trous sont des porteurs de charge, donc leur dynamique dépend de toutes les autres particules (électrons, trous, noyaux et défauts) dans les milieux. Le calcul exact sur de tels systèmes nécessite une puissance de calcul qui n'est pas disponible de nos jours. C'est la raison pour laquelle les physiciens mettent en place des méthodes de calcul basées sur des approximations qui permettent d'obtenir des résultats proches des observations expérimentales.

Ici, le but est de comprendre les propriétés électroniques du graphène via le modèle des liaisons fortes qui donne un résultat sous forme de structures d'énergie de bande [23, 54]. Dans cette approche, les électrons se déplacent à travers un potentiel périodique très fort au voisinage des atomes du réseau. En regardant la dynamique des électrons dans un réseau, on regarde la délocalisation des électrons causée par les atomes voisins. On en déduit une équation de dispertion décrivant la dynamique des électrons, qui est représenté pour les petites énergies sur la Figure B.1a.

La structure de bande La bande de valence et la bande de conduction se touchent en deux points dans la zone de Brillouin (Figure B.1a), K_1 et K_2. En conséquence, le graphène est souvent considéré comme un semi-conducteur à intervalle nul ou un semi-métal. Il est intéressant d'observer qu'à faible énergie, la relation de dispersion autour des points K est linéaire (Figure B.1b), ce qui donne à la structure de bande électronique du graphène cette forme particulière de cône au voisinage du point de Dirac .

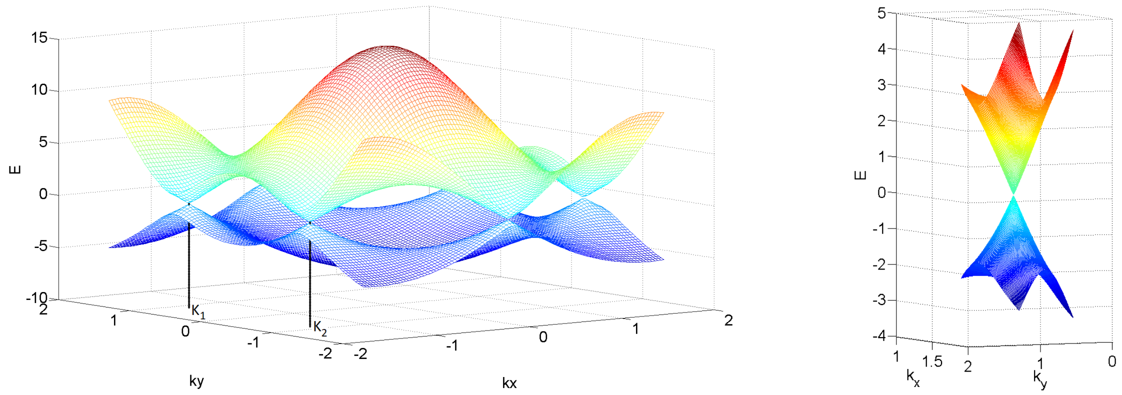

(a) Relation de dispersion électronique d'une seule couche de graphène tracée dans la première zone brillouin.

(b) Zoom sur le point de haute symétrie K. Dans les faibles énergies, nous avons une dispersion linéaire

Figure B.1: Illustration de la relation de dispersion des électrons du graphène (a) dans la première zone brillouin et (b) au voisinage du point de symétrie élevé K.

Au voisinage des K points, la relation de dispersion peut être approchée comme étant :

$$E^{\pm} = \pm\gamma_0|f(\mathbf{q})| = \pm\gamma_0\frac{3a_0}{2}|\delta\mathbf{k}| = \pm\hbar v_F|\delta\mathbf{k}| \tag{B.12}$$

où la vitesse de Fermi a été définie comme $v_F = \ gamma_0\ frac3a_02\ hbar\ approx 10^6 m.s^{-1}$. De plus, la vitesse de Fermi ne dépend pas de la masse. Nous parlerons donc de l'électron sous forme de fermions de Dirac sans masse dans le graphène. L'une des conséquences est la mobilité ultra-élevée des charges dans le graphène, conduisant à une conductivité élevée de ce matériau même à température ambiante.

Spectre d'excitation électron-trou du graphène

Les excitations de trous d'électrons dans la plage de basse énergie peuvent être expliquées en regardant attentivement la structure de bande en forme de cône (Figure B.1b). Ces excitations sont très importantes dans l'étude de la plasmonie du graphène, car il existe une possibilité de transfert d'énergie entre les plasmons et les électron-trous entraînant l'amortissement des plasmons. Cet amortissement s'appelle l'amortissement de Landau, qui est une perte de mouvement électronique collectif des plasmons pour l'excitation de paires électron-trou.

Conclusion

Dans ce premier chapitre, des principes fondamentaux ont été présentés afin de couvrir à la fois les domaines de la plasmonique et du graphène. Les principes de la physique de l'électromagnétisme ont été utilisés pour comprendre la base de la plasmonique, aussi bien dans le cas général que dans le cas des couches minces. Ensuite, les principales propriétés du graphène sont introduites. En particulier, le modèle des liaisons fortes fournit une compréhension du comportement des électrons dans le graphène

Dans le chapitre suivant, les connaissances recueillies ici seront utilisées pour étudier le domaine de la plasmonique dans le graphène.

Plasmonique de graphène

Les dispositifs électroniques, utilisés dans les télécommunications et le traitement de l'information, présentent des limitations inhérentes dues aux pertes et aux bruits électroniques des matériaux qui ont des conséquences sur leur conductivité et la consommation d'énergie associée. Pour supprimer ces barrières et continuer à augmenter les performances des dispositifs électroniques, la tendance technologique est de trouver d'autre support d'informations capable de remplacer ou de compléter les électrons, parmi lesquels les photons semblent être le candidat idéal. Jusqu'à présent, cependant, malgré les récentes démonstrations prometteuses de confinement fort en champ proche dans des structures hybrides Silicon on Insulator, par exemple [99], les dispositifs photoniques ont été limités par la longueur d'onde de la lumière. réduit à l'échelle nanométrique.

Récemment, le graphene [50] a été proposé comme candidat pour combler le fossé entre les électrons et les photons pour une nouvelle génération de dispositifs optoélectroniques [14]. Alors que de nombreuses propriétés prometteuses du graphène telles que son épaisseur ultime, sa transparence, la mobilité de ses électrons ou sa force mécanique concentrent les efforts de nombreux groupes, quelques groupes pionniers ont récemment commencé à étudier le graphène pour ses propriétés optoélectroniques [20] et plasmoniques [57], ouvrant de nouvelles voies vers des nanodispositifs optoélectroniques basés sur des interactions électron-photon.

De toutes les études théoriques pionnières [159, 58, 66, 59] et expérimentales [117, 114], il semble maintenant possible d'utiliser la lumière comme support d'information en la manipulant à travers des Plasmons de graphène polaritons.

Les promesses de la plasmonique dans le graphène résident dans le confinement élevé et l'amortissement faible de ces plasmons ainsi que la possibilité de les ajuster électrostatiquement simplement en appliquant une tension. Le principal atout serait de permettre la miniaturisation du composant photonique sans faire face aux limitations thermiques habituelles, grâce à de faibles pertes électroniques dans le graphène. Les applications pourraient donc être nombreuses.

Ce chapitre vise à exposer une revue de la littérature sur le graphène et la plasmonique dans le graphène. Dans un premier temps, la découverte du graphène sera retracée ainsi que ses limites en terme de propriétés de transport électronique. Ensuite, les propriétés optiques du graphène seront introduites et une vue d'ensemble de l'état de l'art de la plasmonique dans le graphène sera présentée. Par la suite, la relation de dispersion des plasmons de graphène sera démontrée. Ensuite, les propriétés plasmoniques du graphène seront examinées en détail et enfin, une conclusion à travers les objectifs de cette étude sera faite.

Revue de la littérature sur le graphène et ses propriétés de transport électronique

La découverte du graphène et le processus de synthèse

En octobre 2004, deux articles ont été publiés [17, 117] et ont montré quelques propriétés remarquable de couches de carbone sur différents substrats.

Malgré la pensée commune [105], de tels films extrêmement minces sont thermodynamiquement stables aux conditions ambiantes. Deux méthodes de fabrication différentes ont été utilisées: sur carbure de silicium par désorption thermique de Si [17], et par exfoliation mécanique [117].

Le comportement des propriétés du gaz d'électrons 2D dans un tel film mince a été démontré, ouvrant un énorme champ de recherche dans un domaine tel que la mécanique quantique. Il a également été démontré que le graphène est un semi-métal et qu'il peut supporter un courant énorme. Le transport d'électrons dans ce milieu montre une petite résistivité électrique (transport balistique), limitée par l'effet de diffusion, et donc une mobilité importante. Enfin, la caractéristique la plus importante découverte est la possibilité d'injecter des porteurs de charge dans le graphène (dopage) qui modifie sa conductivité / résistivité et présente un effet de champ électrique ambipolaire (conductivité portée par électron ou trou en fonction de la tension appliquée). Cette découverte a conduit à un prix Nobel de physique.

Limites sur les propriétés de transport du graphène

Les propriétés de transport du graphène sont limitées par différents mécanismes de diffusion. L'ampleur de la diffusion des porteurs de charge peut être exprimée en termes de mobilité μ, qui relie la vitesse de dérive moyenne d'un porteur de charge à un champ électrique appliqué. Le substrat de graphène sur SiO_2 présente une mobilité de plus de 1 $m^2V^{-1}s^{-1}$, un ordre de grandeur plus élevé que le silicium qui est le matériau électronique le plus commun [57] . Cependant, le taux de diffusion reste un obstacle et limite les applications potentielles en opto-électronique, ainsi qu'en physique fondamentale [19].

La diffusion peut être divisée en deux catégories. Le premier concerne les mécanismes de diffusion intrinsèque, tels que les défauts du graphène, les joints de grains, les ondulations intrinsèques ou les phonons de graphène, émergeant du graphène lui-même. La seconde implique les mécanismes extrinsèques, issus des matériaux environnants, comme les impuretés chargées dans le substrat ou piégées sous / au-dessus du graphène, les ondulations et les déformations induites par le substrat, et les phonons d'interface.

Revue de littérature sur les propriétés optiques et plasmoniques du graphène

Comme cela a été vu précédemment, le graphène présente des propriétés exotiques. Entre autres, le comportement de particule de Dirac sans masse conduit à une très grande mobilité des porteurs chargés. De plus, la possibilité de tuner le niveau de Fermi du graphène, et donc de modifier ses propriétés optiques, conduit à un large intérêt dans la communauté scientifique. En fait, les porteurs de charge peuvent être injectés jusqu'à 0,01 par atome de carbone en utilisant un système à effet de champ ($1 \times 10^{13} cm^{-2}$), et jusqu'à 0,1 par atome pour l'électrolyte en gel solide [97]. Bien que très inférieure à la concentration de dopage que l'on peut atteindre en métal noble (jusqu'à 1 par atome), l'injection de charges dans le graphène entraîne un changement significatif de ses propriétés optiques.

La tunabilité des propriétés optiques du graphène comparé à celle d'un métal volumique peut être comprise comme suit. Quand une masse de métal se trouve dans un fort champ électrique, les électrons s'accumulent le long de la surface. Cela entrain un décalage de l'état de tous les électrons à l'intérieur du volume. Cependant, le niveau total de Fermi n'est pas modifié et par conséquent, la propriété du métal n'est pas modifiée. Au contraire, dans une seule couche d'atomes de carbone, il y a un changement effectif de la densité des électrons / trous dans le matériau, ce qui change la conductivité et ensuite la réponse optique [69]. Par conséquent, il est possible de moduler la relation de dispersion des plasmons, qui suscite un intérêt considérable dans le monde scientifique.

Dans la section suivante, nous introduirons la théorie des propriétés optiques du graphène, puis nous exposerons les dispositifs opto-électroniques prédits par simulation. Dans une seconde partie, un aperçu de ce qui a été expérimenté dans le domaine de la plasmonique dans le graphène sera présenté.

Théorie des propriétés optiques et simulation des dispositifs à base de graphène

Le graphène est un matériau prometteur pour l'optoélectronique, mais reste difficile à manipuler et à contrôler, en raison de son épaisseur d'un atome. Cependant, les applications possibles ont suscité un grand intérêt et de nombreux groupes ont travaillé sur la théorie et simulé des dispositifs à base de graphène pour concevoir les futures plateformes opto-électroniques. Dans cette sous-section, une méthode semi-classique est proposée pour traiter les propriétés optiques du graphène, basée sur la formule de Kubo [59]. Par la suite, les dispositifs basés sur le graphène, prédits par différentes méthodes de simulation, seront énumérés.

Les propriétés optiques du graphène

Les besoins de compréhension du comportement électro-optique particulier du graphène à travers la théorie ont été motivés très tôt par la découverte et la caractérisation d'une feuille de graphène monocouche [17, 117]. L'approche des liaisons fortes appliqué à ce réseau en nid d'abeille 2D permet de comprendre la plupart des propriétés électroniques inhabituelles [54]. Cependant, l'interaction du graphène avec la lumière n'est pas triviale et de nombreux groupes de recherche ont travaillé sur différentes approches pour le modéliser [58, 40, 59, 106]. Une introduction est faite sur le formalisme semi-classique, à partir de la formule de Kubo [59], qui représente le graphène comme surface conductrice. Ryogo Kubo a introduit un formalisme de transport électronique pour décrire la conductivité, basé sur la théorie de la réponse linéaire. Il donne la conductivité en fonction du champ électrique appliqué.

Observation expérimentale des plasmons dans le graphène

Plusieurs techniques permettent aux chercheurs d'accéder à une preuve directe de l'existence de plasmons dans le graphène. La première preuve expérimentale montrant le phénomène a été réalisée par Electrons Energy Loss Spectroscopy (EELS) [111, 39, 96], où les électrons sont utilisés pour sonder les propriétés du graphène.

Dans cette méthode, un faisceau incident d'électrons heurte la feuille de carbone. Certains des électrons vont transférer une partie de leur énergie, par diffusion inélastique, aux plasmons de graphène. Leur énergie sera éventuellement enregistrée après la réflexion ou la transmission à travers l'échantillon, et un spectre de perte d'énergie des électrons est obtenu. Dans le graphène, on sait qu'il existe deux sortes d'électrons de valence: les électrons π responsables des bornes covalentes entre les atomes de carbone, et les électrons σ, quasi libres, qui créent des liaisons sur les orbitales p_z. Par conséquent, plusieurs types de plasmons peuvent exister [36]:

- Les plasmons de basse énergie, habituellement appelés plasmons 2D, avec une énergie inférieure à 3 eV, qui est le champ d'intérêt de cette thèse.
- Les plasmons de haute énergie, correspondant aux plasmons π (environ 4,7 eV) et $\pi + \sigma$ (environ 14,6 eV).

Cependant, les plasmons 2D sont difficiles à sonder car ils apparaissent avec un dopage relativement élevé (niveau de Fermi), étant très dépendants de celui-ci. Ils dépendent aussi d'autres paramètres comme le substrat et les températures [98].

En 2012, deux articles [42, 29] ont été publiés simultanément décrivant la première imagerie en espace réel de plasmons de surface se propageant sur un substrat Si / SiO_2 pour le premier, et sur le graphène nanoribbon sur le dessus du substrat 6H-SiC pour le second. Il a été difficile d'enregistrer la signature d'une telle onde en raison de sa nature non radiative. Afin de visualiser ces ondes évanescentes, un microscope optique à champ proche a été utilisé dans la région infrarouge.

Propriétés des Plasmons de Graphène

Il est intéressant de noter deux choses quand on parle de plasmons dans le graphène. Ils montrent beaucoup de similitudes avec les plasmons de surface à une interface entre un diélectrique et un métal. Cependant, deux propriétés du système impliquent différentes caractéristiques du plasmon dans le graphène. Le premier est que les électrons sont gelés perpendiculairement à la surface, et le second concerne la relation de dispersion des électrons dans le graphène, comparée à celle parabolique dans les métaux [70]. Ces deux différences majeures conduisent à des relations de dispersion différentes entre ces deux systèmes.

Cette étude vise à mettre l'accent sur les modes longitudinaux, où le champ électrique associé aux plasmons est dans le plan, parallèle au vecteur d'onde. Ces modes sont connus sous le nom de modes magnétiques transversaux. Ils apparaissent à une fréquence inférieure à l'énergie de blocage de Pauli. Un mode transverse électrique de plasmon existe également dans le graphène, où l'on peut trouver une oscillation collective d'électrons transversaux au plan de graphène [15]. Cependant, la courbe de dispersion de ces modes semble être trop proche de celle de la lumière. En conséquence, du point de vue du confinement énergétique, ils semblent moins intéressant que les modes TM [70].

En 2007, il a été proposé plusieurs façons d'étudier les modes plasmoniques transverses électriques et magnétiques sur le graphène. [66, 106]. Dans les sections suivantes, deux approches semi-classiques seront proposées pour obtenir la relation de dispersion du plasmon dans le graphène. L'un est basé sur une approche de volume, et l'autre consiste en une approche de surface. Ensuite, les différents paramètres importants dans la propagation des plasmons de graphène seront analysés.

Relation de dispersion par l'approche volumique

Dans cette section, le graphène sera considéré comme un matériau d'épaisseur finie. Par conséquent, le graphène sera décrit comme une plaque métallique extrêmement mince avec une permittivité complexe ϵ_m. Le système peut être décrit comme une multicouche et le graphène est intégré dans un milieu diélectrique avec une perméabilité diélectrique ϵ_d. Le graphène étant un matériau dont l'épaisseur est d'un atome, l'épaisseur $\Delta = 2a$ peut être approchée comme tendant vers 0. On trouve la relation de dispersion suivante :

$$k_p \approx k_0 \sqrt{1 - \left(\frac{2}{\eta \sigma_{2D}}\right)^2} \tag{B.13}$$

avec $k_0 = w/c$ et $\eta = \sqrt{\mu_0/\epsilon_0}$ l'impédance de l'environnement.

Une introduction à la simulation de l'interaction matériau-lumière sera donnée afin d'étudier le graphène à l'aide d'outils numériques. En conséquent, un modèle matériel est nécessaire. En première approche, les résultats obtenus ci-dessus ont été implémentés dans le logiciel Lumerical FDTD, où le graphène a été traité comme un matériau 3D, avec une épaisseur finie.

Cependant, le maillage requis est très petit par rapport à la longueur d'onde infrarouge, et une certaine aberration peut se produire. Par conséquent, un deuxième modèle a été développé, avec du graphène vu comme un matériau 2D, défini par sa conductivité 2D. Cette deuxième approche est démontrée ci-après.

Relation de dispersion par l'approche de surface

Une autre façon d'obtenir la relation de dispersion des plasmons dans le graphène est de décrire le système comme une interface de deux milieux diélectriques, avec un courant libre entre les deux. Le même mode TM sera considéré. La relation de dispersion peut s'écrire :

$$\frac{\epsilon_2}{\sqrt{k_p^2 - \epsilon_2 k_0^2}} + \frac{\epsilon_1}{\sqrt{k_p^2 - \epsilon_1 k_0^2}} = -\frac{i\sigma}{w\epsilon_0} \tag{B.14}$$

Cette équation est plus facilement implémentable, et plus flexible. C'est celle ci qui sera utilisé par la suite dans les simulations FDTD.

Graphene plasmons propagation and damping rate

La relation de dispersion des plasmons dans le graphène peut-être simplifier sous la forme :

$$k_p = \frac{1}{\lambda_0}\frac{\pi\hbar}{2\alpha\tau E_F}(\epsilon_1 + \epsilon_2)(\omega\tau + i) \tag{B.15}$$

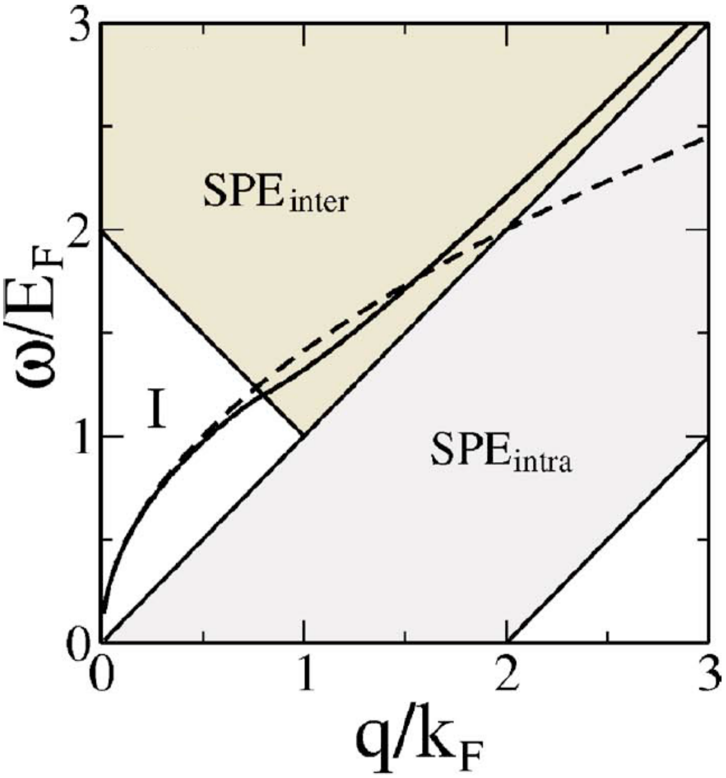

Figure B.2: Relation de dispersion du plasmon de graphène calculée par RPA (ligne continue), et par le modèle classique (ligne pointillée). Le graphène repose sur le substrat de SiO2. Les deux types de zone SPE sont dessinés en arrière-plan.

La longueur d'onde du plasmon dans le graphène peut être obtenue en utilisant l'équation (B.9). Il est également possible d'obtenir la distance de propagation avec l'équation (B.8). Toutes ces grandeurs physiques peuvent être dérivées des parties réelles et imaginaires du vecteur d'onde k_p (voir Equation (B.15)). Prenons le cas d'une couche de graphène prise en sandwich entre un diélectrique et l'air. Par conséquent, nous pouvons définir $\epsilon_1 = \epsilon_{sous} = \epsilon' + i\epsilon''$ et $\epsilon_2 = \epsilon_{air} = 1$. La longueur d'onde des plasmons λ_p^{sup} peut donc être établie, ainsi que sa distance de propagation L_p^{sup} pour le graphène supporté comme suit:

$$\lambda_p^{sup} = \lambda_0 \frac{4\alpha\tau E_F}{\hbar((\epsilon' + 1)\omega\tau - \epsilon'')} \tag{B.16}$$

$$L_p^{sup} = \lambda_0 \frac{\tau\alpha E_F}{\pi\hbar(\epsilon' + 1 + \epsilon''\omega\tau)} \tag{B.17}$$

Le taux d'amortissement peut être écrit comme:

$$\gamma = \frac{Im(k_p)}{Re(k_p)} = \frac{\epsilon' + 1 + \epsilon''\omega\tau}{(\epsilon' + 1)\omega\tau - \epsilon''} \approx \frac{1}{\omega\tau} + \frac{\epsilon''}{\epsilon' + 1} \tag{B.18}$$

But de cette étude

L'objectif initial de cette étude est de jeter les bases de la propagation des plasmons pour le développement de futurs dispositifs optoélectroniques à base de graphène. Idéalement, les plasmons de graphène dans l'infrarouge subissent de faibles pertes métalliques par rapport aux métaux nobles. Cela est dû à ses excellentes propriétés électroniques. Cependant, le substrat implique des impuretés et des défauts qui affectent les propriétés de transport du graphène. En outre, l'utilisation d'un substrat induit un fort amortissement dû à une dissipation d'énergie optique élevée. Dans ce contexte, le graphène suspendu semble être une voie prometteuse pour la conception de futurs dispositifs opto-électroniques.

La portée de ce travail est l'étude des plasmons dans le graphène suspendu. Le graphène suspendu permet de se débarrasser de l'interaction des charges du substrat. Sous des conditions spéciales, les plasmons de graphène pourraient atteindre une longueur de propagation intéressante. Par conséquent, une étude numérique est détaillée dans le chapitre 3. Dans le chapitre 4, les résultats expérimentaux sont présentés. La fabrication des échantillons, les caractérisations ainsi que les mesures optiques sont introduites dans le chapitre 4. Les mesures optiques sont réalisées avec un microscope optique à champ proche (SNOM) à balayage dans l'infrarouge.

FDTD Simulation de la propagation des plasmons dans le graphène en suspension

Le travail d'un chercheur consiste à entreprendre des recherches créatives sur une base systémique et organisée. Par conséquent, des outils numériques ont été développés pour aider les scientifiques à prédire les routes intéressantes à explorer, avant les démonstrations expérimentales. La méthode FDTD est une technique d'analyse numérique qui donne à la communauté de l'optique la possibilité de simuler diverses interactions entre la lumière et la matière. L'excitation des Plasmons de Surface est un phénomène qui se produit dans le cadre de ces interactions, apparaissant d'un point de vue théorique après avoir réarrangé les équations de Maxwell. Ces équations sont à la base de la méthode FDTD, qui vise à les résoudre dans les domaines d'espace et de temps discrétisés. Par conséquent, les plasmons peuvent être calculés et étudiés grâce à cette méthode numérique.

Tout d'abord, l'idée de base de la méthode FDTD sera introduite brièvement. Ensuite, la modélisation du graphène à travers la FDTD sera discutée. Enfin, le cas de la propagation des plasmons dans le graphène en suspension sera détaillé: dans un premier temps, l'utilisation d'une nano-antenne dans le plan pour l'excitation des Plasmons Graphène (GP) sera étudiée. Ensuite, un système est conçu en prenant en compte les contraintes induites avec pour objectif une longue propagation. Enfin, certaines remarques et critiques sont abordées.

Idée de base de la méthode FDTD

La méthode FDTD est basée sur un algorithme proposé par Kane Yee [146]. Les étapes clés de l'algorithme sont résumées ci-après, avec quelques références au cas 1D qui sera développé ultérieurement.

1. Remplacer toutes les dérivées temporelles et spatiales des équations de Maxwell par des différences finies. Ce faisant, l'espace et le temps sont discrétisés et les champs électriques et magnétiques sont décalés dans les quatre dimensions.

2. Résoudre les différentes équations de Maxwell, en utilisant l'équation différentielle centrale du second ordre, et exprime les champs inconnus futurs en termes de champs passés connus (Equation (B.19)).

3. Évaluer les champs magnétiques à la première itération future afin qu'ils soient maintenant connus .

4. Évaluer les champs électriques à la première itération future afin qu'ils soient maintenant connus .

5. Répéter les deux étapes précédentes jusqu'à ce que les champs aient été obtenus pendant la durée désirée.

Regardons de plus près le cas le plus simple: le cas à une dimension.

1-D FDTD

En utilisant les étapes décrites précédemment, on peut trouver l'équation du champ u suivant :

$$u_i^{n+1} \backsimeq \left(\frac{v\Delta t}{\Delta x}\right)^2 (u_{i+1}^n - 2u_i^n + u_{i-1}^n) + 2u_i^n - u_i^{n-1} \tag{B.19}$$

avec n représentant l'indexe temporel présent et connu. n-1 représente donc l'indexe temporel passé et n+1 représente l'indexe temporel futur. De la même manière, i représente l'indexe spatial. L'équation (B.19) est dite entièrement explicite. Du côté droit de l'équation, toutes les valeurs des champs sont à l'étape de temps n ou $n-1$, donc déjà calculées parce que se référant aux itérations de temps présentes et passées respectivement. Sur le côté gauche, la valeur du champ correspond au futur, à l'instant t_{n+1}. L'équation entièrement explicite permet de calculer la valeur future du champ à partir des valeurs précédentes, déjà stockée dans l'ordinateur (à l'instant n actuel et au pas passé n-1).

FDTD in 3 dimensions

En 3 dimensions, la technique FDTD, qui est une méthode temporelle, résout les équations de Maxwell dans un espace discrétisé. Cela donne lieu à un ensemble de 6 équations scalaires pour 6 composantes de champ vectoriel, $\mathbf{E_x}$, $\mathbf{E_y}$, $\mathbf{E_z}$, $\mathbf{H_x}$, $\mathbf{H_y}$, $\mathbf{H_z}$, qui sont calculés dans une cellule Yee. La cellule Yee, du nom de son inventeur, est une grille décalée et non-affectée, ce qui signifie que **E** et **H** ne sont pas échantillonnés au même endroit, et chacune des 3 composantes vectorielles des deux champs ne sont pas calculés sur le même emplacement.

En 40 ans d'existence, de nombreuses autres structures en maillage ont été proposées, mais aucune n'a pu remplacer celle de Yee. Certaines des raisons sont énumérées par la suite. Dans un premier temps, l'algorithme de Yee résout simultanément le champ électrique et le champ magnétique, plutôt que de résoudre seulement l'un d'entre eux par l'équation d'onde (Equation (B.19)). Par conséquent, il rend le calcul plus robuste et élargit le champ des simulations possibles, y compris au niveau des singularités près des bords et des coins.

Deuxièmement, les composantes des champs E et des champs H sont placées de façon particulières, de sorte que chaque composante du champ E est entourée de quatre composantes du champ H en cercle, et inversement. Cela facilite le maintien des conditions aux limites, où la loi de Faraday et la loi de l'Ampère sont liées. La seule exigence est de définir les propriétés optiques des différents matériaux à une interface. L'interface sera définie parallèlement à une face de cellule Yee. Par conséquent, l'interface aura une forme d'escalier avec une résolution d'espace de la taille du maillage. Enfin, en l'absence de charges et de courants, la localisation du champ E et du champ H, combinée aux différences de second ordre, impose les lois de Gauss, rendant les simulations exemptes de divergence.

Enfin, les 6 composantes des champs magnétiques et électriques sont également centrées dans le temps. Le processus de progression temporelle est centré et le second ordre précis. Il est robuste parce que les champs ne se dissipent pas en raison de l'algorithme de temps d'où pourrait provenir des artefacts numériques. Il est également appelé "entièrement explicite", évitant ainsi à nouveau des erreurs et des aberrations. Pour plus d'informations, voir [146].

Pour une même quantité d'erreur, la cellule de Yee permet d'utiliser un plus petit nombre de cellules, comme l'ont fait les autres possibilités, à savoir les cellules co-localisées non décalées et décalées [73].

Modélisation du graphène dans FDTD

Le graphène est un matériau 2D, et en tant que tel, il n'est pas trivial de le simuler en utilisant FDTD. Tout d'abord, la théorie qui nous donne l'équation de dispersion pour les propriétés optiques du graphène est basée sur la formule de Kubo. La formule de Kubo donne deux termes intégraux à résoudre, qui représentent le terme intrabande et le terme interbande. Le premier est résolu analytiquement tandis que le second peut seulement être résolu numériquement avec précision. Parce que le terme interbandes ne peut être résolu que numériquement, plusieurs approximations existent.

Deuxièmement, les propriétés optiques du graphène, habituellement présentées en termes de conductivité optique 2D, ne sont pas triviales à résoudre pour la simulation numérique FDTD 3D. Deux méthodes existent: une approche 3D basée sur une permittivité virtuelle 3D, définissant le graphène avec une épaisseur finie très faible, et une approche 2D utilisant la conductivité optique 2D, utilisant un algorithme spécial pour modéliser le graphène comme matériau 2D [1]

En fait, dans le cas de l'approche 3D, le maillage d'une couche de graphène d'une épaisseur de l'ordre de l'ordre de l'Angstrom donne une quantité significative de cellules de Yee à calculer. L'excitation électromagnétique est l'infrarouge, ce qui rend les structures du système de l'ordre du micromètre. Couplé avec la longueur d'onde effective des plasmons de graphène qui est vraiment petite, il rend la région de calcul énorme, relative au maillage.

Cette méthode de graphène 3D nécessite une discrétisation spatiale locale de l'ordre de ou plus mince que le nanomètre, tandis que nos simulations impliquent des longueurs d'onde et des structures plus grandes que le micron, conduisant à d'énormes domaines de calcul et à un maillage non-uniforme. De plus, le critère de stabilité de la FDTD nécessite alors une discrétisation temporelle extrêmement courte, et un nombre important d'itérations est donc nécessaire pour compléter une seule simulation. Par conséquent, cette méthode nécessite beaucoup de ressources en terme de processeur et des aberrations numériques peuvent se produire.

La modélisation de matériaux 2D, qui est la deuxième approche vue plus haut, vise à décrire le graphène comme une surface chargée, où les conditions aux limites ne sont appliquées qu'à une fraction d'une cellule Yee [6]. En tant que tel, il n'y a pas besoin de discrétiser l'espace (et le temps) à des tailles extrêmes, et cela s'est avéré conduire à une stabilité accrue de nos simulations. De plus, cela conduit à des résultats qui correspondent bien à la théorie des plasmons de graphène. C'est la méthode qui sera utilisée ci-après. L'étude numérique du graphène a été rendue possible grâce à l'utilisation du super calculateur Romeo à Reims, en France.

Utilisation d'une antenne plasmonique pour l'excitation GPPs

A l'origine, l'excitation des GPP était obtenue par l'utilisation d'une pointe métallique éclairé par laser dans la configuration de microscopie optique en champ proche à balayage [42, 29]. Bien que la dispersion du spectre angulaire résultant ait été large, une petite partie a été exploitée pour lancer avec succès les GP.

Dans nos simulations, nous utilisons des nano-antennes d'or pour étudier les GPP lancés perpendiculairement à l'axe principal du nanorod. Ceci afin d'anticiper la possibilité de maximiser la puissance des GPP lancés à l'aide d'un réseau. Il est en effet possible de placer côte à côte de nombreuses nano-antennes ensemble, et d'obtenir un effet d'amplification grâce à la configuration du réseau.

En tant qu'étude préliminaire, une nano-antenne d'or d'une longueur L est considéré agissant comme un dipôle résonant le long de L. La section des nano-antennes est rectangulaire, 80nm de large et 50nm de haut. La forme est en aiguille, pour s'adapter à la fabrication par lithographie par faisceau d'électrons. Le nanorod a été illuminé avec une impulsion qui se propage perpendiculairement au plan de l'échantillon, le long de z. La lumière incidente est polarisée linéairement, parallèle à l'axe long de la tige (axe x). Ce pulse a un spectre large bande allant de 8 μ m à 12 μ m, avec une longueur d'onde centrale d'environ 10 μ m.

La géométrie utilisée dans [5, 107] permet une efficacité de couplage GPP non négligeable. Pourtant, cette géométrie avait une largeur de tige fixe, qui pourrait être optimisée. En fin de compte, notre travail a montré qu'une optimisation précise de l'efficacité du couplage nécessite de simuler le système complet, et d'étudier l'énergie que le plasmon porte réellement à travers les transformées de Fourier du champ proche. Quantitativement parlant, cette méthode est supérieure à l'étude du champ moyen seulement, car le champ proche moyen contient de nombreux composants k qui ne peuvent pas être couplés à un GPP.

Cependant, le critère de champ moyen ne doit pas être entièrement rejeté. Comme nous l'avons montré ici, il conduit toujours à une bonne approximation au premier ordre. Contrairement à notre critère qui nécessite des méthodes numériques pour calculer le système complet, le critère de champ moyen peut être utilisé avec des modèles analytiques ou pseudo-analytiques, ou des méthodes numériques avec des logiciels incapables de simuler le système complet, le graphène étant assez difficile à simuler.

Un troisième paramètre qui n'a pas été exploré est l'épaisseur de nanoantenne, mais ce paramètre affecte également la distance entre la feuille de graphène et le substrat, et peut alors non seulement affecter le comportement de l'antenne, mais aussi les propriétés du graphène lui-même.

Système conçu basé sur GPP

En conséquence, nous proposons la conception (voir Fig. B.3) d'un échantillon réaliste prenant en compte les différents paramètres expérimentaux discutés ci-dessus. Sur un substrat de SiO_2 (300nm) / Si reposent des structures en or, qui joueront le rôle de support de suspension pour le graphène, et également un nanorod (antenne) pour le lancement de GPP. L'épaisseur du support en or et de l'antenne en or est fixée à 100 nm. L'antenne d'or est intégrée dans un système de nano-fentes d'or perpendiculaire à l'axe longitudinal de la tige. Les fentes dorées, d'une largeur de 300 nm, sont conçues pour suspendre le graphène et guider les GPP perpendiculairement à l'axe long de la tige, ouvrant ainsi la voie aux futurs circuits nanophotoniques basés sur le graphène en suspension.

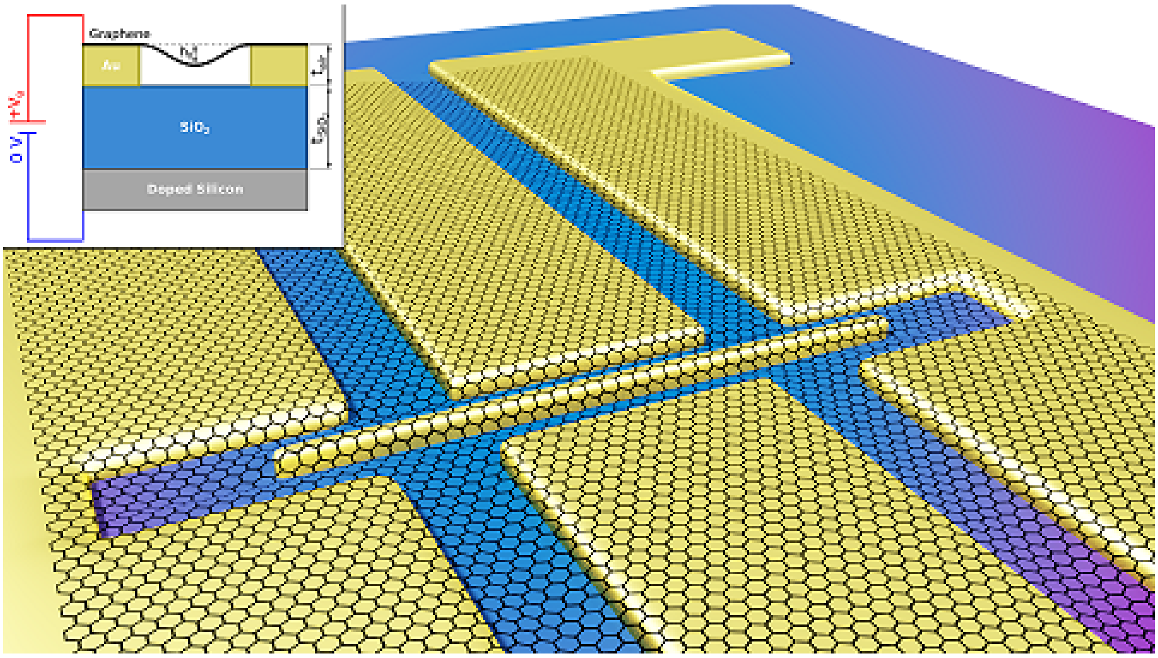

Figure B.3: Illustration du système étudié. Une antenne plasmonique repose sur un substrat SiO_2 / Si. Les nano-slots d'or rassemblent et propagent les plasmons sur le graphène en suspension. La dalle a également une fonction d'électrode pour le dopage du graphène en suspension. Or, Si et $Si0_2$ sont représentés respectivement en jaune, gris et bleu. Encart: une vue de côté schématique le long de l'axe x du graphène, de la fente dorée et du substrat. La hauteur de déflexion h_0 est également représentée.

Discussion sur le champ électrique appliqué

Un problème non couvert par cette étude peut survenir à l'étape expérimentale. En effet, le FDTD ne prend pas en compte les phénomènes électrostatiques. Pour implémenter l'injection de charge dans le graphène, le niveau de Fermi doit être modifié. Cependant, les champs électriques et magnétiques dans les différents matériaux ne sont pas pris en compte.

Afin d'injecter des charges dans le graphène, le champ électrique effectif appliqué au graphène est énorme. Par conséquent, les matériaux diélectriques entre le graphène et la couche conductrice de la grille arrière doivent tolérer une amplitude de champ électrique élevée. La propriété liée au champ électrique maximal qu'un matériau peut supporter sans rupture est appelée résistance diélectrique. La rigidité diélectrique de l'air est d'environ 3MV / m. Pour un bon film mince de SiO_2, il est possible d'avoir 500MV / m. La dégradation diélectrique de H-BN a été enregistrée aussi haut que 1GV / m [60, 74]. Le diamant peut théoriquement atteindre une valeur plus élevée [51, 156]. Et enfin, le vide idéal résisterait à un champ électrique aussi élevé que 10^{9} GV / m.

Conclusion

Dans ce chapitre, une étude numérique a été présentée. Après un bref historique de la méthode FDTD, la solution pour un problème d'onde unidimensionnel a été résolue, puis appliquée au cas 3D. La technique de modalisation du graphène dans une simulation 3D a été discutée. Enfin, un plan est proposé, utilisant une antenne, pour étudier la propagation des plasmons dans le graphène en suspension.

Certaines préoccupations concernant la faisabilité d'une telle expérience à l'état ambiant donnent lieu à une discussion finale. Une installation utilisant une chambre à vide serait probablement nécessaire pour obtenir la mesure attendue en laboratoire.

Procédure expérimentale

Dans ce chapitre, les réalisations expérimentales sont décrites. Chronologiquement, la fabrication des premiers échantillons a été faite en parallèle avec le travail de simulation numérique présenté précédemment. Par conséquent, une partie du travail expliqué ci-dessous était en fait un premier essai pour enregistrer les plasmons dans du graphène en suspension et la conception peut être légèrement différente de celle montrée dans le chapitre précédent. En outre, il n'a pas abordé certains problèmes évoqués plus haut, où il est expliqué pourquoi une configuration de microscope optique à champ proche à balayage sous vide (SNOM) est nécessaire pour enregistrer des plasmons sur du graphène en suspension.

Par conséquent, dans un premier temps, le processus de fabrication d'un échantillon avec du graphène en suspension est décrit, ainsi que les différentes conceptions que nous voulions étudier. Ensuite, la caractérisation du graphène basé sur la spectroscopie Raman est discutée. Enfin, les résultats préliminaires SNOM seront affichées et commentées.

Fabrication de l'échantillon

Les échantillons avec du graphène suspendu ont été fabriqués à Singapour, au Centre for Advanced 2D Materials.

Processus de fabrication des échantillons de graphène en suspension

Ci-après sont présentés les motifs fabriqués dans le but d'observer et de mesurer la distance de propagation des Plasmons dans le Graphène.

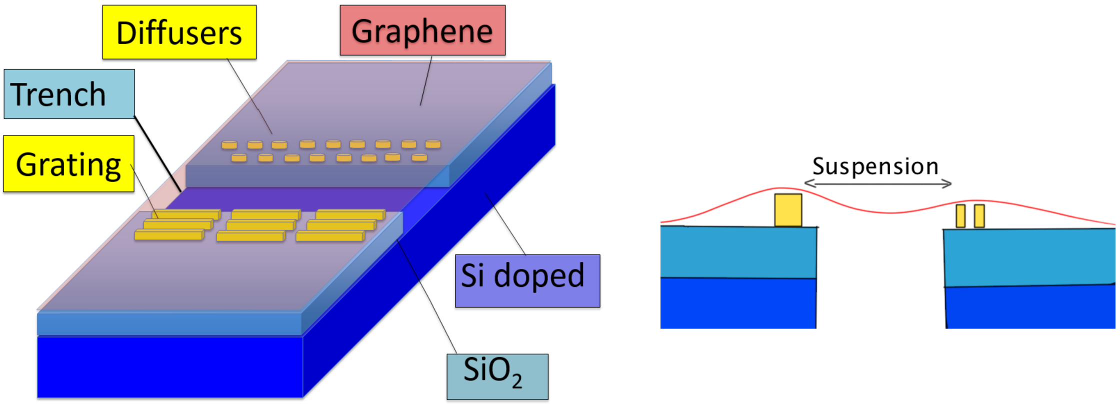

(a) A perspective view of the sample

(b) Cross-section view of the sample

Figure B.4: Illustration de la conception pour l'étude des plasmons de graphène à travers le graphène en suspension. La monocouche de graphène (rouge) est sur le dessus du système. Les nanostructures d'or sont en jaune et le substrat est fait de wafer dopé SiO_2 (300 nm, bleu clair) / Si (bleu foncé).

Patterns pour l'étude de la propagation GPs

Différents modèles ont été fabriqués afin d'étudier différentes plates-formes pour la propagation des plasmons de graphène. Plusieurs conceptions de trous ont été faites. La forme de la tranchée a été rendue triangulaire (figures B.5a et B.5b), circulaire (B.5c et B.5d) et rectangulaire (B.6a et B.6b).

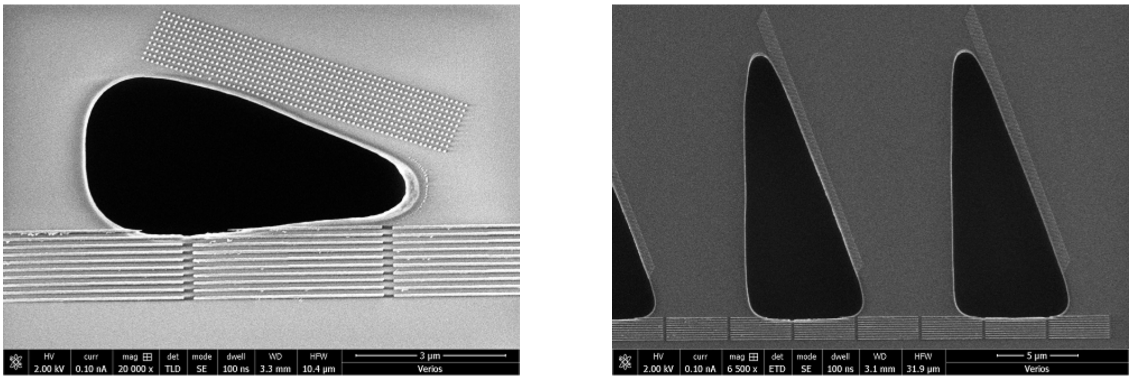

(a) Hole with small trianglular shape

(b) Hole with large trianglular shape

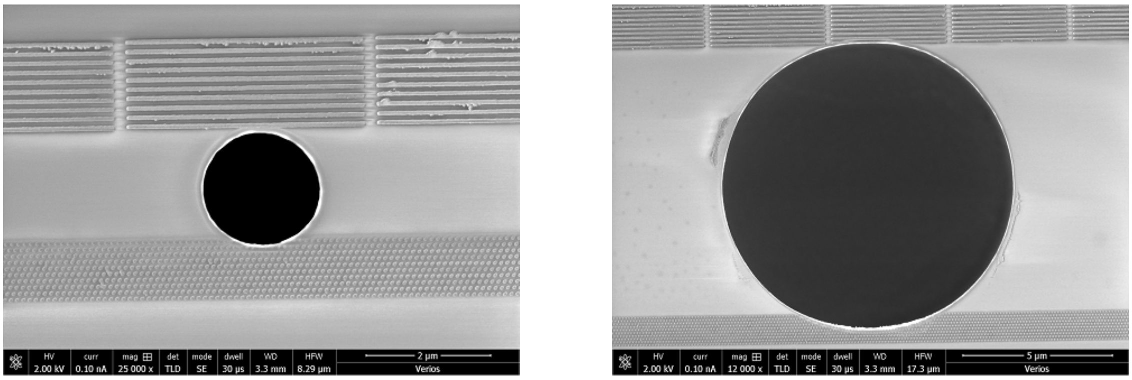

(c) Hole with small circular shape

(d) Hole with large circular shape

Figure B.5: Images SEM des échantillons fabriqués dans la salle blanche après la mise en place de la simulation. On peut voir sur les différentes images des nano-tiges d'or de 4 μm d'un côté des trous, et des diffuseurs d'or, de forme tubulaire, de l'autre côté des trous.

Ces trous sont conçus pour suspendre le graphène sur eux. Grâce à un alignement très précis entre la lithographie par faisceaux d'électrons et la photolithographie, les nano-tiges et les diffuseurs de plasmons sont placés très près des bords des trous. Comme déjà souligné, l'une des parties les plus difficiles de la fabrication consistait à déposer les nanostructures aussi près que possible des trous. En effet, une fois le graphène déposé sur l'ensemble de la structure, représenté sur l'image ref FRFig::susp, il est important que la monocouche ne touche pas le substrat entre les structures d'or et les trous. Comme nous pouvons le voir sur les différentes images SEM (Figures B.5a, B.5b, B.5c, B.5d, B.6a, B.6b, B.7a, B.7b), les résultats finaux sont prometteurs et on peut s'attendre à ce que le graphène soit suspendu sur l'ensemble des structures.

Patterns pour étudier la longueur d'onde des SPP

Un second ensemble de modèles a été réalisé pour étudier la longueur d'onde des SPP à travers le graphène via des phénomènes d'interférences. Avec les motifs représentés Figures ref FRInter1 et ref FRInter3, nous avons la possibilité de lancer deux plasmons à partir de deux points différents.

Ces ondes à deux surfaces interfèrent entre elles et un motif d'interférence peut apparaître sur les diffuseurs. En fait, nous nous attendrions à avoir un modèle d'interférence qui serait échantillonné par

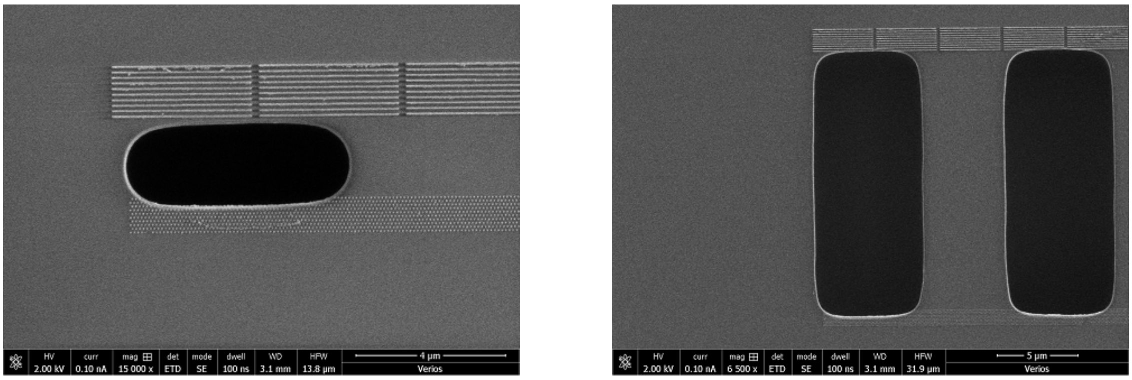

(a) Hole with small rectangular shape

(b) Hole with large rectangular shape

Figure B.6: Images SEM des échantillons fabriqués en salle blanche suivant les données de simulation. On peut voir sur les différentes images des nano-tiges d'or de 4 μm d'un côté des trous, et des diffuseurs en or, de forme circulaire, de l'autre côté des trous.

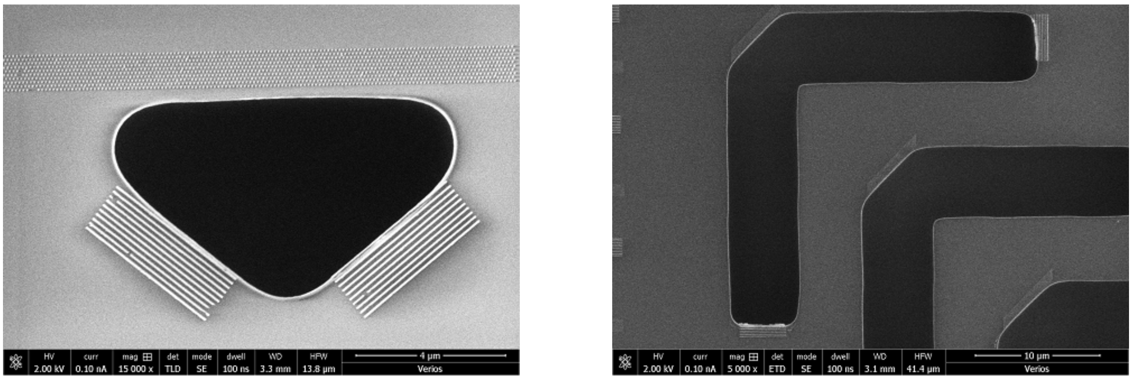

(a) Small trianglular shape of hole

(b) Small trianglular shape of hole

Figure B.7: Images SEM des échantillons fabriqués en salle blanche après la mise en place de la simulation. On peut voir sur les différentes images des nanorods d'or de 4 μm d'un côté des trous, et des diffuseurs d'or, de forme circulaire, de l'autre côté des trous.

les diffuseurs, montrant des points chauds intenses à l'emplacement d'interférences constructives, et une réponse faible à l'emplacement d'interférences destructives, de manière similaire à l'expérience à double fente (appelée expérience de Young).

Modèle pour étudier l'effet de réseau

Enfin, afin d'avoir l'intensité des plasmons la plus élevée possible, il serait prometteur d'exploiter le phénomène de réseau, en plus du phénomène de résonance des nano-tiges. Pour cette raison, il a été fabriqué pour chaque échantillon 4 motifs différents avec des espacements différents entre les nano-tiges. En fait, la période de réseau de nano-tiges peut être calculée pour avoir une amélioration du champ proche pour un vecteur d'onde particulier, ce qui donne en termes d'impulsion (voir Figure B.8):

$$k_{SPP} = k_0 \sin\theta + n\frac{2\pi}{d} \tag{B.20}$$

Comme nous l'avons vu précédemment dans notre simulation, nous prévoyons d'éclairer nos échantillons perpendiculairement à celui-ci. Par conséquent, $\sin\theta = 0$ et nous trouvons:

$$d = \frac{n2\pi}{k_{SPP}} = n\lambda_{SPP} \approx n300nm \tag{B.21}$$

Donc, pour un multiple de 300 nm, nous devrions obtenir un effet de réseau qui devrait améliorer la force des plasmons lancés à travers le graphène. Il a donc été décidé de fabriquer plusieurs échantillons de conceptions différentes modifiant l'espacement entre les nanotiges qui sont d'environ 150 nm, 300 nm, 450 nm et enfin 600 nm.

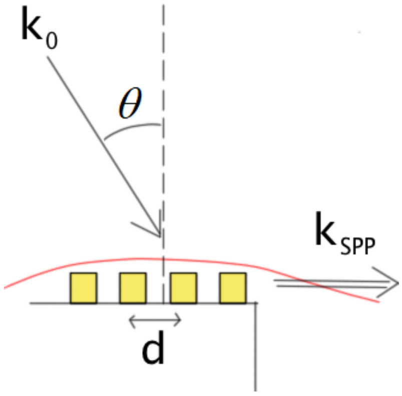

Figure B.8: Illustration of the nano rods grating

Dépôt de graphène et caractérisation des échantillons

Il a été choisi d'utiliser le graphène CVD qui a été prouvé pour soutenir des plasmons de graphène [43]. Comme cela a été expliqué précédemment, les plasmons de graphène sont très sensibles à l'environnement. L'un des principaux problèmes est d'obtenir du graphène très pur et propre pour de faibles pertes optiques et une grande mobilité des électrons. Au début, le graphène CVD a été déposé à Singapour.

Présentation générale des spectres Raman dans le graphène

Avec la microscopie à faisceau d'électrons (MEB) et la microscopie à force atomique (AFM), la spectroscopie Raman est une technique de routine utilisée pour caractériser le graphène [155]. Alors que MEB et AFM peuvent donner des images physiques du graphène, la spectroscopie Raman peut fournir beaucoup plus d'informations basées sur la vibration de réseau du matériau. En fait, la spectroscopie

Raman est basée sur la diffusion inélastique des photons par la matière, la différence d'énergie étant enregistrée comme la vibration du réseau, ou phonons. Il s'agit donc d'un transfert d'énergie entre les modes photoniques et les modes phononiques dans un réseau particulier, c'est-à-dire une sorte de signature de chaque cristal. Parce que les spectres Raman fournissent des informations sur la vibration du réseau, c'est une technique qui est vraiment sensible à la structure du réseau et à la cristallinité [47], le nombre de couches de graphène [45], la déformation, le défaut et la densité de charges [89], entre autres [46]. De plus, c'est une technique qui peut être réalisée à température ambiante, qui est fiable et non destructive.

Il a été possible d'utiliser un outil Raman hyperspectral (Thermofisher), ce qui permet une cartographie Raman de l'échantillon. Sa haute résolution spatiale (quelques centaines de nanomètres), son balayage rapide ainsi que ses outils de traitement d'image en font un équipement performant pour identifier le graphène en suspension sur l'échantillon.

Caractérisation de la nano-antenne d'or

Comme cela a été expliqué précédemment, les nano-antennes d'or sont utilisées pour lancer des plasmons à travers le graphène.Il a été montré que les plasmons les moins amorties sur du SiO_2 se situent autour d'une longueur d'onde de 11 microns. C'est aussi une fréquence optique typique utilisée dans un microscope optique à champ proche (SNOM) à balayage qui a été développé à l'UTT. Donc, dans un premier temps, les nanorods ont été conçus pour avoir une fréquence de résonance dans cette gamme. La simulation numérique que nous avons effectuée montre que la longueur de la tige doit être comprise entre 3,8 et 4 microns, ce qui est le cas pour l'échantillon présenté ci-dessus (voir Figure B.5, B.6, B.7). Par conséquent, la dernière étape consistait à caractériser la réponse des bâtonnets à une excitation infrarouge.

A cet effet, la technique de spectroscopie infrarouge à transformée de Fourier (FTIR) a été utilisée. Cette technique permet d'enregistrer simultanément des données sur une large gamme de fréquences. Les résultats ont confirmé que la résonance de la structure d'or est d'environ 11 microns, ce qui correspond bien à la configuration SNOM disponible. Il est donc possible d'analyser les échantillons en champ proche en utilisant le SNOM fait maison.

Mesure optique à l'aide de la microscopie optique à champ proche à balayage

Au début du siècle précédent, on croyait, selon la théorie, que la résolution de la microscopie classique était limitée à environ 250 nm, ce qui correspond à la demi-longueur d'onde de la lumière. Dans les années quatre-vingt, afin de casser cette limite de diffraction, il a été proposé d'utiliser une petite ouverture comme source de lumière qui serait capable de confiner l'excitation. Plus tard, un autre type de sondes a été proposé, appelé "pointe sans ouvertures", qui a été utilisé dans cette étude. D'une manière générale, la microscopie optique à balayage de champ proche (SNOM ou NSOM) est une microscopie locale à sonde où une pointe est placée près de la surface du matériau ($< \lambda/2$) pour interagir avec la matière dans le champ proche. Par conséquent, il est possible d'obtenir une résolution nanométrique qui n'est plus imposée par la longueur d'onde de la lumière. Plusieurs types de SNOM existent, classés en deux familles principales: les sondes à ouverture et sans ouverture. Pour plus d'informations sur les différents systèmes, voir [152].

Dans cette section, la mise en place d'un SNOM sans ouverture sera introduit. Il fonctionne dans l'infrarouge moyen. Ensuite, le processus de fabrication des pointes sera présenté. Enfin, certains des résultats obtenus seront affichés.

Introduction au SNOM sans ouverture et aux approches de détection du signal associées

Le SNOM sans ouverture (également appelé SNOM: s-SNOM "à diffusion") utilisant une pointe métallique est basé sur le principe que l'extrémité pointu de la sonde est éclairé par laser. Il peut localement améliorer / perturber le champ électromagnétique à la surface de l'échantillon. En général, le champ proche de l'échantillon interagit avec la pointe. L'interaction locale plutôt complexe entre l'échantillon et l'extrémité produit une onde radiative dispersée qui peut être détectée dans le champ lointain. Ce rayonnement porte les informations locales (telles que détectées par l'extrémité de la pointe) du champ proche de l'échantillon, telles que sa phase optique et son amplitude. Dans une certaine mesure, un SNOM de type diffusion sans ouverture capte les ondes évanescentes et les convertit en ondes propagatives via des pointes métalliques qui peuvent être considérées comme une nanoantenne optique. Le champ de propagation résultant est enregistré par un détecteur dans le champ lointain.

Détails expérimentaux sur le SNOM

Le dispositif expérimental de UTT utilise trois lasers qui couvrent une gamme spectrale allant de 9,5 μm à 11,4 μm. A la sortie des lasers, un isolateur est placé afin d'éviter tout retour de faisceau réfléchi vers les lasers. Un coupleur, constitué d'une lentille montée sur une platine, entraîne le faisceau vers la fibre. Un collimateur est placé à la sortie de la fibre pour conduire le faisceau laser au cœur de l'installation. Ce dernier est représenté dans la figure B.9.

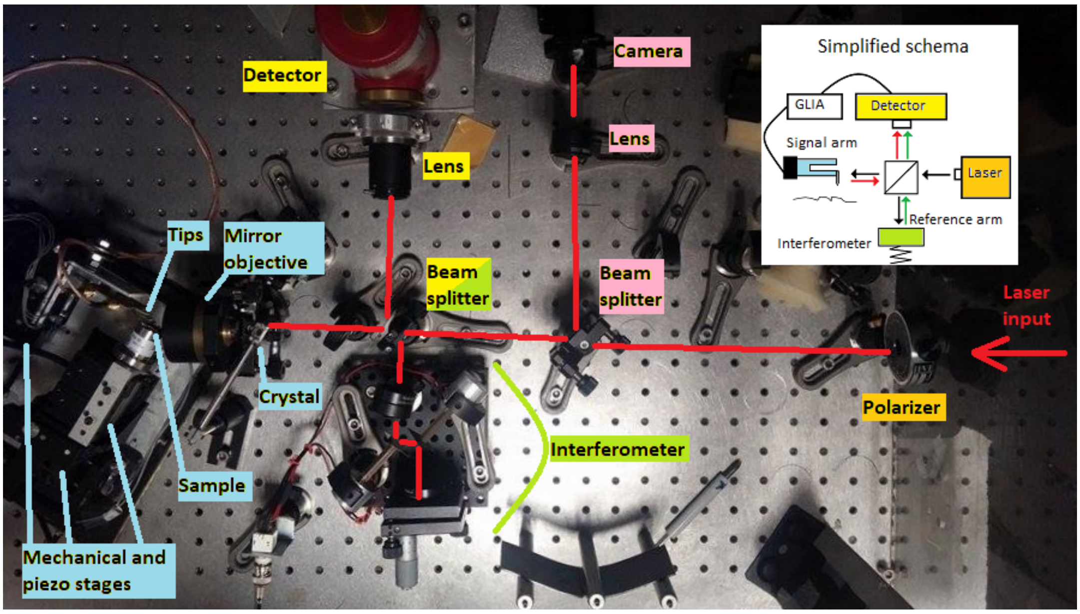

Figure B.9: Image de la configuration SNOM. En encart, un schéma simplifié représentant la disposition des éléments principaux

Fabrication des pointes SNOM

Les astuces sont cruciales pour détecter les ondes évanescentes. En particulier, l'extrémité des pointes doit être aussi petit que possible pour agir comme un dipôle électrique qui capte le champ proche. Le champ incident du faisceau laser peut être converti par la pointe en source locale et exciter les plasmons de surface. Réciproquement, l'onde évanescente d'un plasmons de surface peut être convertie en une onde radiative via l'apex de la pointe.

Afin d'enregistrer précisément les plasmons dans le graphène, le diamètre de l'extrémité de la pointe doit être au moins du même ordre de grandeur que l'expansion du phénomène dans l'air. Pour les plasmons de graphène, il a été montré [44] que le diamètre de l'apex devrait être de l'ordre de quelques dixièmes de nanomètres.

First optical measurement

Les images SNOM préliminaires sont représentées sur la figure B.10. La longueur d'onde d'excitation est de 11 μm, ce qui se trouve dans la plage de faible amortissement des plasmons de graphène. Un polariseur linéaire a été utilisé, comme indiqué sur la figure B.9: la polarisation du faisceau incident est horizontale. Le grand axe de la pointe est également horizontal. La polarisation suit également l'excursion de l'oscillation de la pointe (mode de tapotement). Par conséquent, cette configuration permet une forte excitation de la pointe, qui est plus susceptible d'exciter les plasmons dans la couche de graphène.

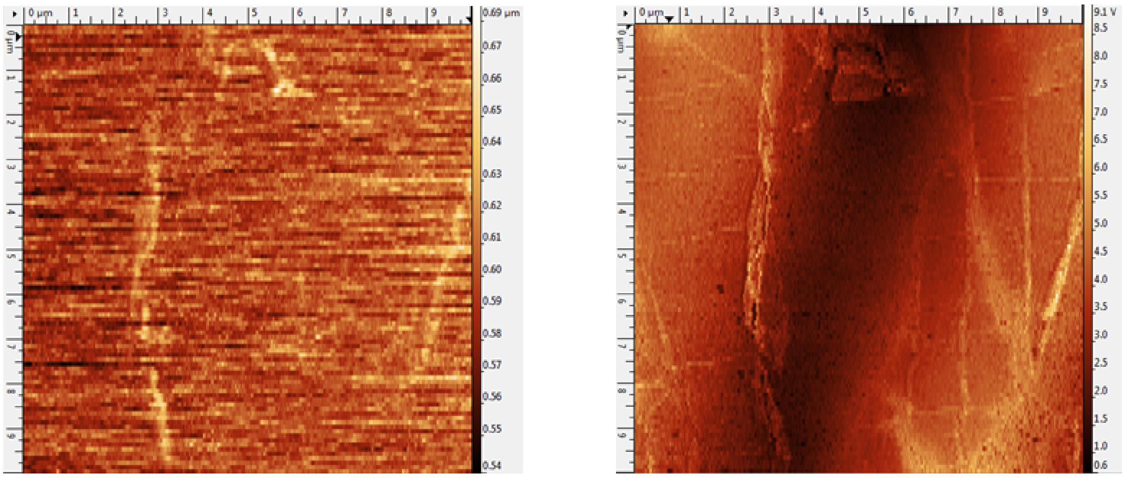

(a) AFM topography (10×10 microns)

(b) Optical amplitude

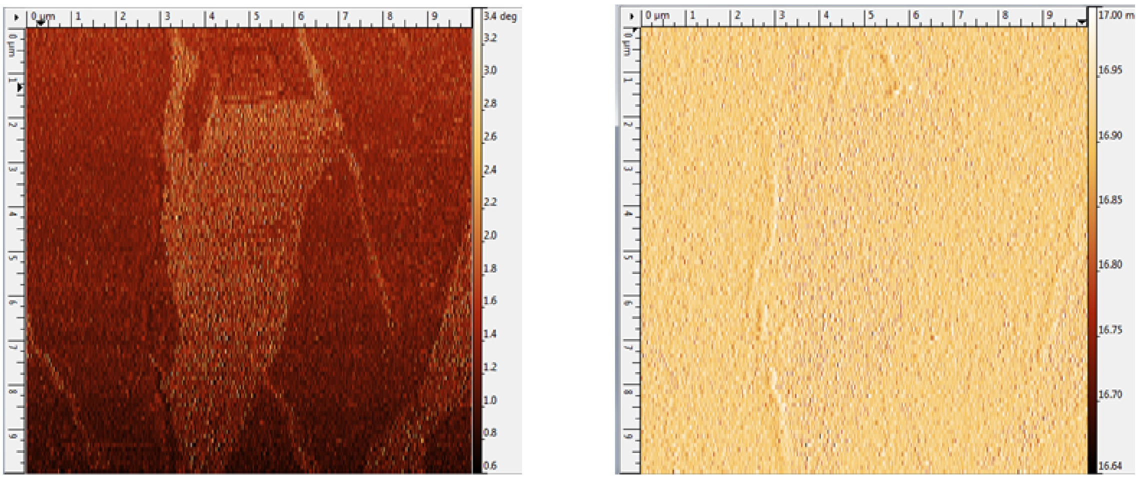

(c) AFM mechanical phase of the fork

(d) AFM mechanical amplitude of the fork

Figure B.10: Images SNOM : topographie, amplitude optique, phase AFM and amplitude AFM

Conclusion

Ce chapitre présente les résultats expérimentaux comme la dernière étape de ce travail de recherche. Il montre la fabrication, la caractérisation et les mesures optiques avec l'introduction de la technique de microscopie optique en champ proche. Ces résultats expérimentaux constituent la dernière partie de cette étude. Les résultats obtenus sont préliminaires et d'autres expériences devraient être conduites dans le futur afin de montrer la véritable signature des plasmons dans le graphène. Ce chapitre a également montré la complexité de manipuler ce matériau 2D, et d'enregistrer ce phénomène très confiné.

Conclusion et perspectives

Au cours de cette thèse, une exploration du champ de la plasmonique dans le graphène est donnée. Une attention particulière a été accordée à l'explication des phénomènes de plasmons de graphène en utilisant principalement la physique classique.

Dans le premier chapitre, les bases de la plasmonique ont été examinées à partir des équations de Maxwell. De plus, les structures de graphène sont montrées et le comportement des électrons est augmenté à travers un modèle de liaison étroite. Ce chapitre a posé les bases nécessaires à la compréhension de la physique des plasmoniques au graphène.

Le deuxième chapitre vise à donner une revue de la littérature couvrant brièvement la découverte du graphène ainsi que celle des plasmons de graphène. Il donne un aperçu du défi qui reste à relever pour obtenir des dispositifs électroniques actifs à base de graphène. En particulier, il introduit la problématique de la propagation des plasmons, et la nécessité de trouver une plateforme adaptée pour obtenir le premier dispositif actif à base de plasmons de graphène. Enfin, la physique des plasmons de graphène est expliquée à travers la courbe de dispersion, fournissant les paramètres clés nécessaires pour un autre travail de recherche numérique et expérimental.

Le troisième chapitre est consacré à une étude numérique, basée sur la méthode du domaine temporel des différences finies. Cette méthode est brièvement introduite avec un historique et la résolution du problème des ondes 1D. Le cas 3D est alors donné en conséquence avec le paramètre clé pour conduire une étude numérique. Le problème de la simulation d'un matériau 2D dans une grille 3D est abordé. Enfin, une conception d'échantillon est proposée en utilisant l'antenne comme lanceur de plasmons. La propagation dans le graphène suspendu est montrée ainsi que la longueur de propagation attendue. Une discussion finale donne la limite de cette proposition d'expérience, où une chambre à vide est probablement nécessaire.

Le quatrième chapitre concerne les travaux de recherche préliminaires. Au début, un processus de fabrication d'échantillon est montré. Il se compose du processus de fabrication, ainsi que d'une image au microscope des résultats. Certains problèmes rencontrés au cours du processus sont également abordés. Ensuite, la caractérisation de l'antenne ainsi que le graphène sont donnés. Enfin, une introduction à la technique de microscopie optique à champ proche à balayage est affichée. L'installation faite maison est présentée et quelques résultats préliminaires sont montrés.

Perspective : le cas du diamant Compte tenu des défis rencontrés pour étudier les plasmons dans le graphène en suspension, un autre chemin de recherche a été exploré. Comme déjà mentionné, les plasmons graphène lac de longueur de propagation L_p lorsque le chercheur pense à utiliser ses propriétés à des fins applicatives. Bien que des progrès aient été faits récemment [114, 38], la longueur de propagation L_p reste trop courte pour être utilisée dans les dispositifs opto-électroniques actifs. Plusieurs paramètres [98] doivent donc être considérés afin d'obtenir une propagation de GPs élevée (voir Equation (B.17) pour ce qui suit). Premièrement, L_p est fonction du taux de diffusion des porteurs de charge, qui devrait être maintenu aussi bas que possible. Deuxièmement, L_p est proportionnel à la valeur quadratique de l'énergie de Fermi dans l'infrarouge, qui doit donc être aussi élevée que possible (après l'approximation DC du temps de relaxation). Enfin, L_p est très sensible à la partie imaginaire de la permittivité du substrat *epsilon*$''$, la dissipation d'énergie optique (Im(*epsilon*)).

Armés de ces paramètres, nous pouvons dessiner une image de la plate-forme idéale pour la propagation de GPPs, qui devrait avoir les propriétés suivantes:

1. Rigidité diélectrique élevée et constante k-diélectrique afin d'injecter une forte densité de charges dans graphène.
2. Faible Im(ϵ), afin d'avoir de faibles pertes plasmonique.
3. Possibilité de fabriquer dans le même processus que le graphène, en utilisant le système CVD.
4. Utilisation de matériel durable.

SiO_2, qui est le substrat le plus commun utilisé pour étudier graphene [117], induit une diffusion externe et / ou interne [7, 78, 28, 110]. Ensuite, la constante k-diélectrique relativement faible (3.9) associée à la rigidité diélectrique de 0.5GV / m ne permet pas d'atteindre une énergie de Fermi suffisamment élevée. Enfin, la dissipation optique de SiO_2 induit un amortissement important dans les GPPs [42].

Peu de temps après, des études sur le graphène encapsulé dans h-BN, un substrat connu pour être adapté au graphène [145, 53], ont montré des résultats prometteurs [34, 114]. La propriété de haute rigidité diélectrique de h-BN (jusqu'à 1.2GV / m quand exfoliée) [60], ainsi que sa bonne correspondance de réseau avec graphene [162], en font un bon candidat. De plus, les films minces de h-BN ont été synthétisés par un procédé CVD conservant de bonnes propriétés diélectriques (0,4 GV / m) [74]. Cependant, les propriétés optiques h-BN induisent un amortissement sévère dans les plasmons de graphène [153], car Im(ϵ) est du même ordre de grandeur que celui de SiO_2 [157] . De plus, le bore est plutôt rare sur terre.

Comparativement, Diamond remplit tous les critères cités ci-dessus. Sa rigidité diélectrique est idéalement plus élevée que la valeur h-BN one [51, 156]. Il peut être une synthèse à travers le même processus CVD [165]. Il n'a pas de dissipation d'énergie optique dans la région infrarouge et le carbone est un matériau qui croît continuellement sur la surface de la terre dans les stocks, ce qui crée des problèmes environnementaux. Il serait également intéressant de regarder le comportement des plasmons dans le graphène transféré sur UNCD et SCD en changeant la terminaison de surface (H-terminaison vs O-terminaison) du diamant sous-jacent. Le nano-espaceur intercalé entre le graphène et le substrat SiO2 a déjà été étudié [38], et a montré une amélioration de la propagation des plasmons. Par conséquent, la combinaison du diamant et du graphène donnerait définitivement des résultats importants qui pourraient éventuellement conduire à des dispositifs optoélectroniques actifs.

David LEGRAND

Doctorat : Matériaux, Mécanique, Optique, Nanotechnologie

Année 2018

Etude de plasmons propagatifs dans le graphène par méthodes de simulation et spectroscopie infrarouge

La physique du graphène et la plasmonique sont deux domaines qui, une fois combinés, promettent une variété d'applications intéressantes. Une de ces applications est l'intégration de dispositifs nanooptoélectroniques actifs dans des systèmes électroniques, en utilisant le fait que les plasmons dans le graphène sont accordables, fortement confinés et faiblement amortis. Avant de réaliser ces dispositifs actifs, un défi crucial demeure : trouver une plateforme permettant une forte propagation des Polaritons Plasmons Graphène (GPP).

Dans ce cadre, une étude complète de la propagation des plasmons à travers le graphène en suspension est abordée. Cette étude commence par examiner les résultats de la recherche théorique et expérimentale liés au domaine émergent de la plasmonique du graphène. Une étude numérique par méthode FDTD est présentée, et les conditions pour la réalisation de l'étude des plasmons de graphène dans le graphène en suspension sont analysées. Une conception de l'échantillon avec un processus expérimental est proposée. Enfin, une étude expérimentale, de la fabrication en salle blanche, puis la caractérisation de la structure graphène et plasmonique, à la mesure optique par microscopie optique à champ proche à balayage, est présentée.

Mots clés : résonance plasmonique de surface – simulation, méthodes de – spectroscopie infrarouge – graphène – microscopie en champ proche.

Propagative Plasmons in Graphene Investigated by Simulation Method and Infrared Spectroscopy

Graphene physics and plasmonics are two fields which, once combined, promise a variety of exciting applications. One of those applications is the integration of active nano-optoelectronic devices in electronic systems, using the fact that plasmons in graphene are tunable, highly confined and weakly damped. Before achieving these active device, a crucial challenge remains: finding a platform enabling a high propagation of Graphene Plasmons Polaritons (GPPs).

In this framework, a full study of the propagation of plasmons through suspended graphene is addressed. This study starts by reviewing the theoretical and experimental research achievement related to the really recent emerging field of graphene plasmonics. A numerical investigation by FDTD method is presented, and the conditions for a realisation of the study of graphene plasmons in suspended grapheme are analysed. A design of the sample with an experimental process is proposed. Finally, an experimental study from the fabrication in clean room, then the characterisation of graphene and plasmonics structure to the optical measurement through Scanning Near-field Optical Microscopie is presented.

Keywords: surface plasmon resonance – simulation methods – infrared spectroscopy – graphene – near, field microscopy.

Thèse réalisée en partenariat entre :

NANYANG TECHNOLOGICAL UNIVERSITY
School of Electrical and Electronic Engineering

utt
UNIVERSITÉ DE TECHNOLOGIE
TROYES

Ecole Doctorale "Sciences pour l'Ingénieur"